ASTES

Advances in Science, Technology & Engineering Systems Journal

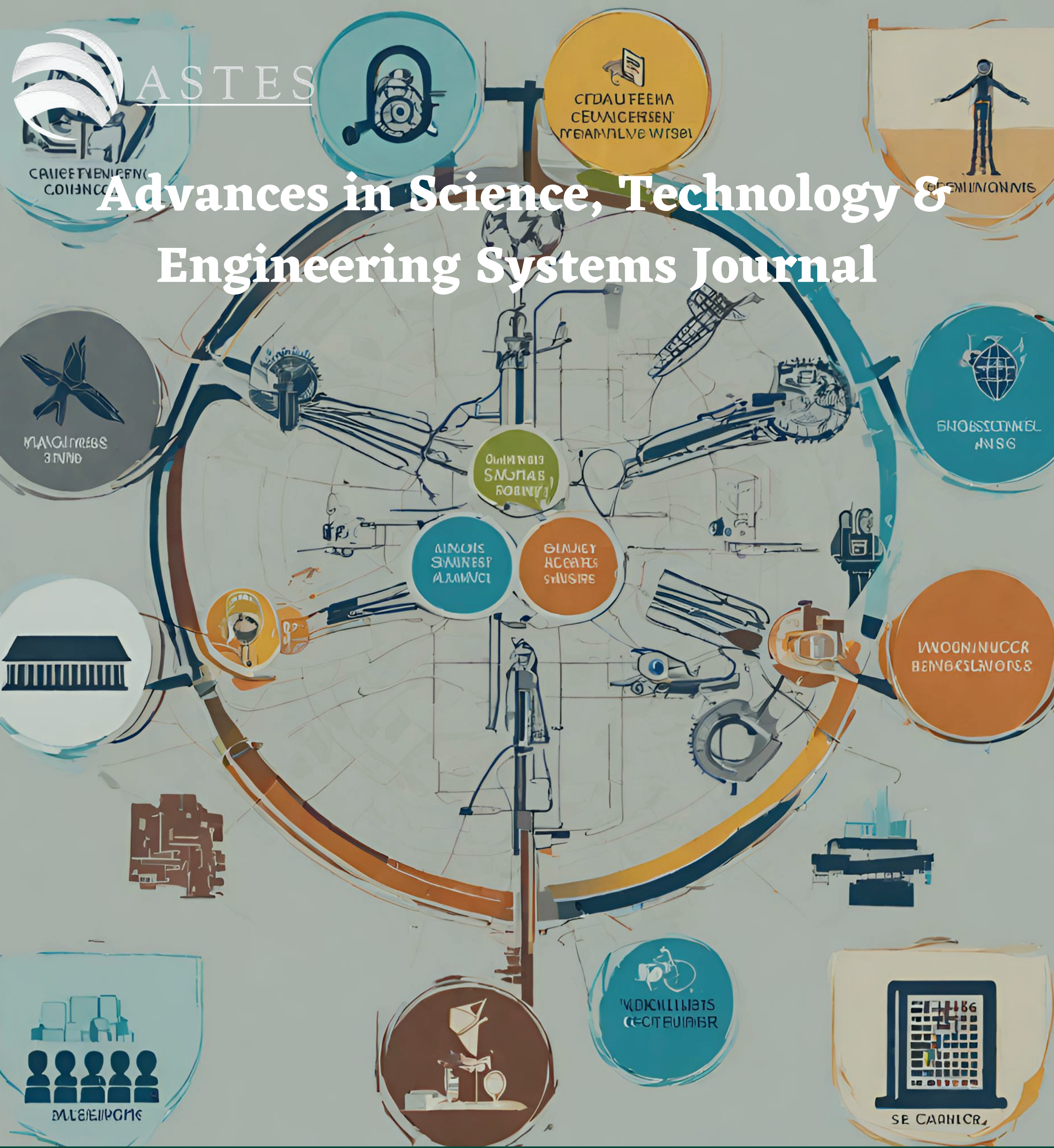

VOLUME 8-ISSUE 2|MAR-APR 2023

www.astesj.com
ISSN: 2415-6698

EDITORIAL BOARD
Editor-in-Chief

Prof. Passerini Kazmerski
University of Chicago, USA

Editorial Board Members

Dr. Jiantao Shi
Nanjing Research Institute of Electronic Technology, China

Dr. Tariq Kamal
University of Nottingham, UK
Sakarya University, Turkey

Dr. Hongbo Du
Prairie View A&M University, USA

Dr. Nguyen Tung Linh
Electric Power University, Vietnam

Prof. Majida Ali Abed Meshari
Tikrit University Campus, Iraq

Dr. Mohmaed Abdel Fattah Ashabrawy
Prince Sattam bin Abdulaziz University, Saudi Arabia

Mohamed Mohamed Abdel-Daim
Suez Canal University, Egypt

Dr. Omeje Maxwell
Covenant University, Nigeria

Mr. Muhammad Tanveer Riaz
School of Electrical Engineeirng, Chongqing University, P.R. China

Dr. Heba Afify
MTI university, Cairo, Egypt

Mr. Randhir Kumar
National University of Technology Raipur, India

Dr. Serdar Sean Kalaycioglu
Toronto Metropolitan University, Canada

Dr. Daniele Mestriner
University of Genoa, Italy

Regional Editors

Dr. Hung-Wei Wu
Kun Shan University, Taiwan

Dr. Maryam Asghari
Shahid Ashrafi Esfahani, Iran

Dr. Shakir Ali
Aligarh Muslim University, India

Dr. Ahmet Kayabasi
Karamanoglu Mehmetbey University, Turkey

Dr. Ebubekir Altuntas
Gaziosmanpasa University, Turkey

Dr. Sabry Ali Abdallah El-Naggar
Tanta University, Egypt

Mr. Aamir Nawaz
Gomal University, Pakistan

Dr. Gomathi Periasamy
Mekelle University, Ethiopia

Dr. Walid Wafik Mohamed Badawy
National Organization for Drug Control and Research, Egypt

Dr. Abhishek Shukla
R.D. Engineering College, India

Mr. Abdullah El-Bayoumi
Cairo University, Egypt

Dr. Ayham Hassan Abazid Jordan University of Science and Technology, Jordan

Mr. Manu Mitra
University of Bridgeport, USA

Dr. Qichun Zhang
University of Bradford, United Kingdom

Editorial

In this issue, we present 16 accepted papers of diverse array addressing crucial challenges and advancements in various domains of technology and engineering. These papers contribute valuable insights and propose innovative solutions to contemporary issues. The following paragraphs provide a brief overview of each paper, outlining its objectives, methodologies, and key findings.

Globally, road transportation plays a pivotal role in modern civilization, but the presence of road anomalies poses a significant threat to safety. The author addresses this concern by introducing an intelligent road anomaly detection system for autonomous vehicles. The system utilizes a modified Histogram Oriented Gradient (HOG) and Fuzzy Logic Control (FLC), presenting promising results in the identification of speed bumps and potholes [1].

The author, focus to risk analysis for soft targets, particularly cultural events like music concerts. The authors employ a multi-criteria decision-making method, fuzzy TOPSIS, to objectively assess the risk of violent attacks. The study demonstrates that this approach provides consistent and practical results for enhancing security measures [2].

The author tackles the critical issue of battery fires caused by overcharge. Introducing a temperature-compensated overcharge protection measurement technology, the authors propose a wireless-enabled Battery Management System (BMS) that enhances stability while maximizing convenience [3].

Moving on to the education sector, the author introduces a multiplatform application for the automatic recognition of personality traits in learning environments. The application employs machine learning models to personalize and adapt content based on the dominant personality traits of students, enhancing the overall learning experience [4].

Despite the favorable conditions for renewable energy in Qatar, the adoption of solar panels faces challenges. The author explores these challenges through a two-phase study, offering insights that can inform stakeholders, policymakers, and future researchers in enhancing the deployment of solar panels in the region [5].

In the realm of cybersecurity, the author introduces a hybrid intrusion detection system utilizing the Activity and Event Network (AEN) graph model. The system effectively identifies threats through signature-based and anomaly-based detection mechanisms, showcasing promising results in intrusion detection datasets [6].

The author presents an omnidirectional multi-view image measurement system designed for 3D reconstruction and multi-view imaging. Utilizing four cameras in a co-sphere framework, the system demonstrates versatility in capturing comprehensive multi-view images for various applications [7].

The author introduces a multi-camera system for measuring the movement of a pilot's body during flight operations. This system records and analyzes the pilot's body reactions in real-time, providing valuable insights into human-computer interaction and enhancing cockpit design [8].

Power loss minimization in electrical power systems is the focus, where an Extreme Learning Machine (ELM) method is proposed for solar irradiation forecasting. The results demonstrate the efficacy of the ELM algorithm in reducing power losses, contributing to more efficient power system operations [9].

The author addresses the automatic detection of olive trees in RGB images using a RetinaNet model and the DeepForest Python package. The proposed approach shows significant improvements over pretrained models, highlighting its potential for accurate tree detection in unmanned aerial vehicle (UAV) imagery [10].

Moving into decision-making under uncertainty, The author introduces the multistage one-shot decision-making approach (MOSDMA). Applied to reevaluate a technology project decision problem, MOSDMA incorporates salience information, offering a promising alternative for multistage decision-making under uncertainty [11].

A hybrid machine learning model is developed to enhance IT project cost and duration prediction accuracy. The MLR-DNN model outperforms traditional predictive project management tools, demonstrating its reliability and effectiveness [12].

Job performance prediction is the focus, where a hybrid neural network and particle swarm optimization approach is employed. The study emphasizes the significance of Particle Swarm Optimization (PSO) in improving model performance, presenting promising results for recruitment screening [13].

This paper delves into optical fiber displacement sensors, specifically addressing scattered-bend loss. The presented sensor utilizes a multimode polymer optical fiber and side coupling technique, offering a simple, comprehensive, and cost-effective solution with potential applications in industrial settings [14].

Addressing cybersecurity concerns in the Internet of Medical Things (IoMT), the author introduces a deep learning approach to detect Covert Timing Channel (CTC) attacks. The proposed pipeline, incorporating Convolutional Neural Network (CNN), Siamese Neural Network (SNN), and K-Nearest Neighbors (K-NN), demonstrates high accuracy in identifying covert messages [15].

A triple-band MIMO antenna design for 5G/Wi-Fi 6 applications is presented. The proposed design incorporates a symmetric parasitic structure, significantly improving isolation between radiation elements. With compact dimensions and wide bandwidths, the MIMO antenna design shows promise for high-performance wireless communication systems [16].

In summary, this special issue encompasses a wide range of cutting-edge research, from intelligent road anomaly detection and risk analysis to renewable energy challenges, personality trait recognition in learning environments, and advanced technologies in cybersecurity, decision-making, and wireless communication systems. Each paper contributes valuable insights and solutions, advancing our understanding and capabilities in these diverse fields.

References:

[1] P.M. Udah, A.I. Suleiman, J.A. Bala, A.A. Sadiq, T.A. Folorunso, J. Eichie, A.P. Adedigba, A.M. Aibinu, “Development of an Intelligent Road Anomaly Detection System for Autonomous Vehicles,” Advances in Science, Technology and Engineering Systems Journal, **8**(2), 1–13, 2023, doi:10.25046/aj080201.

[2] D. Kotkova, L. Kralik, L. Kotek, J. Valouch, “Multiple Criteria Decision-making: Risk Analyses for the Soft Target,” Advances in Science, Technology and Engineering Systems Journal, **8**(2), 14–23, 2023, doi:10.25046/aj080202.

[3] J.U. Yeon, J.W. Noh, I. Oh, “Temperature-Compensated Overcharge Protection Measurement Technology,” Advances in Science, Technology and Engineering Systems Journal, **8**(2), 24–29, 2023, doi:10.25046/aj080203.

[4] V.M.B. Beltrán, R.Z. Cabada, M.L.B. Estrada, H.M.C. López, H.J. Escalante, “A Multiplatform Application for Automatic Recognition of Personality Traits in Learning Environments,” Advances in Science, Technology and Engineering Systems Journal, **8**(2), 30–37, 2023, doi:10.25046/aj080204.

[5] A. Banibaqash, Z. Hunaiti, M. Abbod, “Challenges Facing Solar Panel Energy Deployment within Qatari Homes and Businesses,” Advances in Science, Technology and Engineering Systems Journal, **8**(2), 38–43, 2023, doi:10.25046/aj080205.

[6] P.G. Quinan, I. Traoré, I. Woungang, U.R. Gondhi, C. Nie, “Hybrid Intrusion Detection Using the AEN Graph Model,” Advances in Science, Technology and Engineering Systems Journal, **8**(2), 44–63, 2023, doi:10.25046/aj080206.

[7] Y.-H. Chen, J.H. Huang, “Omni-directional Multi-view Image Measurement System in the Co-sphere Framework,” Advances in Science, Technology and Engineering Systems Journal, **8**(2), 64–70, 2023, doi:10.25046/aj080207.

[8] Y.-H. Chen, J.H. Huang, “Omni-directional Multi-view Image Measurement System in the Co-sphere Framework,” Advances in Science, Technology and Engineering Systems Journal, **8**(2), 64–70, 2023, doi:10.25046/aj080207.

[9] A.B. Rehiara, S. Setiawidayat, F.H. Sumbung, “Day-Ahead Power Loss Minimization Based on Solar Irradiation Forecasting of Extreme Learning Machine,” Advances in Science, Technology and Engineering Systems Journal, **8**(2), 78–86, 2023, doi:10.25046/aj080209.

[10] I. Marin, S. Gotovac, V. Papić, “Development and Analysis of Models for Detection of Olive Trees,” Advances in Science, Technology and Engineering Systems Journal, **8**(2), 87–96, 2023, doi:10.25046/aj080210.

[11] M. Al-Shanfari, “The First Application of the Multistage One-Shot Decision-Making Approach to Reevaluate a Technology Project Decision Problem,” Advances in Science, Technology and Engineering Systems Journal, **8**(2), 97–107, 2023, doi:10.25046/aj080211.

[12] D.-J. Pang, “Hybrid Machine Learning Model Performance in IT Project Cost and Duration Prediction,” Advances in Science, Technology and Engineering Systems Journal, **8**(2), 108–115, 2023, doi:10.25046/aj080212.

[13] T.K. Yassine, A. Said, L. Lamia, F. Mohammed, “Hybrid Discriminant Neural Networks for Performance Job Prediction,” Advances in Science, Technology and Engineering Systems Journal, **8**(2), 116–122, 2023, doi:10.25046/aj080213.

[14] L.S. Supian, D.H.M. Razali, C.S. Ping, N.S. Suhaimi, S.A.S. Ali, N.F. Naim, H. Ramza, “Assessment of Scattered-Bend Loss in Polymer Optical Fiber (POF) Displacement Sensor,” Advances in Science, Technology and Engineering Systems Journal, **8**(2), 123–129, 2023, doi:10.25046/aj080214.

[15] M. Cuomo, F. Massimi, F. Benedetto, “Detecting CTC Attack in IoMT Communications using Deep Learning Approach,” Advances in Science, Technology and Engineering Systems Journal, **8**(2), 130–138, 2023, doi:10.25046/aj080215.

[16] N. Van Tan, D.T.T. Tu, N.V. Hung, H.M. Duc, “Achieving a High Isolation for the Triple-band MIMO Antenna in 5G/ Wi-Fi 6 Applications using Symmetric Parasitic Structure,” Advances in Science, Technology and Engineering Systems Journal, **8**(2), 139–147, 2023, doi:10.25046/aj080216.

Editor-in-chief

Prof. Passerini Kazmersk

ADVANCES IN SCIENCE, TECHNOLOGY AND ENGINEERING SYSTEMS JOURNAL

Volume 8 Issue 2 **March-April 2023**

CONTENTS

Advances in Science, Technology and Engineering Systems Journal Vol. 8, No. 2, 1-13 (2023)

www.astesj.com

Special Issue on Innovation in Computing, Engineering Science & Technology

ASTESJ

ISSN: 2415-6698

Development of an Intelligent Road Anomaly Detection System for Autonomous Vehicles

Paul Miracle Udah*[,1], Ayomide Ibrahim Suleiman[1], Jibril Abdullahi Bala[1], Ahmad Abubakar Sadiq[2], Taliha Abiodun Folorunso[1], Julia Eichie[3], Adeyinka Peace Adedigba[1], Abiodun Musa Aibinu[1]

[1]*Department of Mechatronics Engineering, Federal University of Technology, Minna,920101, Nigeria*

[2]*Department of Electrical and Electronics Engineering, Federal University of Technology, Minna,920101, Nigeria*

[3]*Department of Physics, Federal University of Technology, Minna,920101, Nigeria*

ARTICLE INFO

Article history:
Received: 24 August, 2022
Accepted: 08 January, 2023
Online: 11 March, 2023

Keywords:
Image Processing
Autonomous Vehicle
Road Anomaly
Fuzzy Logic
Speed Control
Maneuvering

ABSTRACT

Globally, road transportation has become one of the most reliable means of moving goods and services from one place to the other. It has contributed immensely to the standard of living and modern civilization. However, this means of transportation is characterised by some issues which are poised to be harmful to the human population if not properly addressed. One of such issues is the presence of potholes, bumps, and other road anomalies. Unfortunately, the late identification of road anomalies (Speedbumps and Potholes) and the inability of drivers to detect and slow down while approaching such road anomalies has also been a big challenge faced by many nations. Therefore, there is a need for an automatic and intelligent approaches to be built into vehicles to mitigate the number of road accidents caused by these anomalies. In this work, the development of an intelligent road anomaly identification and manoeuvring system for autonomous vehicle is presented. The developed system focuses on the detection of road anomalies specifically speedbumps and potholes; and the regulation of the vehicular speed when these anomalies are detected. A modified Histogram Oriented Gradient (HOG) and Fuzzy Logic Control (FLC) have been proposed in this work. Furthermore, promising results have been obtained and presented which depicts the proposed HOG algorithm outweigh other techniques in the identification and detection of speedbumps and potholes. In addition, the developed FLC was able to regulate the speed of the vehicle in the presence of speedbumps as well as navigate the vehicle accordingly in the presence of potholes.

1. Introduction

Road travel has facilitated the flow of goods and services in both developed and emerging countries, increased the quality of living, and has also led to global economic development. This goods and service distribution medium has now become one of the most important element of human society and may be one of the most dangerous elements for the human race if adequate steps are not enforced [1].

As since the advent of automobiles and other road vessels, traffic collisions have become the cumulative consequence of the adverse externalities of public transport [2]. Road accidents occur worldwide but are more frequent in dev eloping countries, triggered by over-speeding, traffic indifference, unfavorable weather, lack of vehicle maintenance and bad road conditions [2]. Some of such events are caused by human negligence or an unexpected natural phenomenon, which may be stopped with the correct precautionary measure. According to the World Health Organization (WHO), bad road conditions, especially in Nigeria, are the most unpredictable and the most prevalent cause of road accidents, and for every 100,000 vehicles accident, there are 1042 deaths worldwide in a year [3]. Another report found that in 2009 the annual road traffic fatality figure in Nigeria was 5,000. Poor roads condition and anomalies were the key contributors to these numbers, forcing drivers to swerve or loss control, which place them, and other road users at risk [3].

A study between the years 2000 and 2004 shows that about 36,000 Nigerians died and 125,000 were injured as a result of road crashes, increasing the death rate from traffic injuries in Nigeria as compared to other countries worldwide [4]. These accidents are

---

*Corresponding Author: Paul Miracle Udah, Federal University of TechnologyMinna, (+234)09097883956 , paulmiracle2014@gmail.com

https://dx.doi.org/10.25046/aj080201

usually caused by several factors such as inexperience, congestion, intoxication, intersection bottlenecks, distraction, drowsiness, and over speeding in the presence of road anomaly (Speedbumps and Potholes) [5] [6]. Speed bumps are structures that are built on the highways to limit traffic travel speeds in sensitive road areas, such as hospitals and schools [7], while a pothole is a bowl shaped deformity on a road surface that ranges from 150mm and above [8]. There are different types and sizes of potholes and they have harmful effects on pedestrians and cars regardless of their type or style. These road conditions account for damages to vehicles parts and causes drivers to lose control of their cars as they drive past them, which can result in a fetal road accident. Hence, the use of an advanced driver assistance systems (as found in autonomous vehicles) for the precise and timely identification of these anomalies would be idea to reduce and mitigate road accidents in developed and developing countries. Furthermore, this inclusion would also help provide driver with adequate information to aid navigation and speed control. [9].

Autonomous vehicles can be described as vehicles that that autonomously drives to the desired location without requiring any manual control [10]. Autonomous vehicles also have the capability to sense their surroundings and navigate around without the help of an external factor when subjected to different terrains [11]. The concept of autonomous vehicle (AV) involves computer vision (Perception), map navigation (Localization and Planning) and control integration. Each of these concepts must be present to ensure a vehicle is completely autonomous [12]. Regardless of the wide range of usage and nature of AV, human performance has proven to be reliable in driving ground vehicles, for instance, when overtaking another vehicle [13]. The implementation of computer vision and image recognition is very critical in facilitating proper object detection and self-navigation.

The application of computer vision is critically important in the development of AV as it is required for the acquistion of images of road and environment for ease of navigation and protection and safety of users [1]. Generally, computer vision provides machines with the functionality and ability to detect,analyse, interpret and comprehend videos and image information using techniques such as gradient, neutral network and edge detection [14]. Mostly, the technique involves viewing images as a two-dimensional signal, and then applying the traditional technique of image processing. When combined with an embedded device, highly efficient, low memory and robust solutions can be obtained [1]. In recent times, self-driving has been a topic of wide interest for Artificial Intelligence and the Automotive Industries. The irregularity detection on the road surface is a task with great challenges. In developing countries, it is very common to find un-marked speedbumps on road surfaces, which reduces the security and stability of self-driving cars [15]. In AVs, speedbump detection and other road anomalies can be achieved by using a number of techniques one of such is the use of mulitple cameras and microcontroller systems [16].

Some of the major limitations observed in the design and development of autonomous vehicle are blurriness and ineffectiveness in the detection of anomalies, as well as an absent or unsuitable control mechanism for vehicles to move over or around such anomalies. Therefore, the development of an intelligent road anomaly detection system, speed control and maneuvering system for autonomous vehicles is presented in this paper. The system analyses images of the surface of the road using image processing techniques (HOG and BRISK Features) for the detection of road anomalies (Speedbumps and potholes). The use of Fuzzy Logic Controller is used to regulate the speed and also the direction of the vehicle in the presence of r road anomalies (speedbumps and potholes).

In 2010, the number of vehicles used worldwide was estimated to be over 1 billion, and according to [17], AVs are widely anticipated to alleviate road congestion through higher throughput, and also reduce human errors to improve road safety and ease the stress of driving. Also, in [18], a review of previous work done on the effect of Artificial Intelligence on AVs was carried out. The use of intelligent transportation systems and artificial intelligence was employed in the improvement of the working of an autonomous vehicle, which was aimed at decreasing the possible error which can be encountered in AV development. The use of an artificial intelligence approach was used to show the possible setbacks in autonomous vehicles and an effective method using artificial intelligence in solving most of the problems in the autonomous vehicle was also proposed. This approach was proven to be possible and achievable with a low failure rate than the conventional approach used in other works reviewed. Although the algorithm employed in the development and improvement of an AV was effective, it was also time-consuming, difficult and ambiguous in development and implementation.

The remainder of this paper is organized as follows. Section 2 presents a review of related past works with respect to the identification of speedbumps and road anomalies specifically potholes. Also, presented in this section is the summary of the findings and gaps in the reviewed literatures. In section 3, the detailed methodology adopted for the research is presented with emphasis on the mathematical modelling of Avs, the Identification and detection of road anomalies using computer vision and AI. The technique for the speed control and navigation of the AV using fuzzy logic control system is also presented in this section. Section 4, presents and discusses the results obtained from the implementation of the proposed methodology as well as the performance evaluation of the methodology vis-à-vis standard metrics of evaluation. Section 4 presents the summary of findings, conclusion of the work and further research opportunities.

2. Literature Review

2.1. Related works in Pothole Detection

There exists in literature several works in the area of pothole identification and avoidance. In [19] the development of an image-based pothole detection system for intelligent transport system (ITS) service and road management system was proposed. In this work, , a pothole detection method based on two-dimensional (2D) images was proposed for improving the existing method and to be applied to ITS service and road management systems. The use of Modified Histogram Shaped-Based Thresholding (MHST) improved the accuracy of the system to 73% and the precision to 80%. However, the system exhibited a long image processing time

(46s average), which limits the practical application of the approach. Furthermore, the vibration of the vehicle also has effect on affects the detection unit of the proposed system

In addition, [20] developed a real-time pothole detection and road monitoring system. The work introduces a system to detect the potholes and informs the concerned authority about the pothole. The proposed system used an ultrasonic sensors and accelerometers to measure the depth of the pothole and jerking respectively. The system captures the geographical location of potholes using a Geograhic Position System (GPS) module. The acquired information is also stored in a cloud database. This serves as a valuable source of information to the vehicle drivers and Government authorities, through a web server with public access. The proposed system provides precautionary measures that can be taken to evade accidents. However, due to the placement of the Ultrasonic sensors, the system is unable to detect a pothole before the vehicle goes over it.

Furthermore, [21] implemented an android based pothole detection system using ultrasonic sensors. The system makes use of an integrated mobile app with the pothole detection system (Ultrasonic Sensor and Microcontroller) for monitoring the road path and anomalies. The system helps users monitor road paths and associated anomalies remotely with the aid of the mobile app. However, the system is limited in its capability to detected all types of road anomalies due to shortcomings of the ultrasonic sensors used. Another limitation of the proposed system is the quality of service of the internet/ communication network.

In a related development, [21] designed a real-time pothole detection technique using image processing and dimension estimation. The proposed system uses image processing and edge detection (Canny, Zero Cross) techniques identify and detect potholes in realtime. The proposed methodology ensures the estimation of the depth and width of potholes for the purpose of remediation such as filling and patching. The system applies a high level of image processing, filtering of images and application of scaling factors to accurately determine and calculate the area of the potholes.

Similarly, [22] designed an automatic pothole detection system using laser technology. The system captures the geographical location coordinates of the potholes and humps.. The developed system effectively detects humps and potholes without any huma intervention before the vehicle actually hits the potholes or the humps. With the use of laser technology, the system can calculate the distance between vehicles and potholes faster than an Ultrasonic Sensor. A major limitation of this system, however, is that it does not possess the ability to control the vehicles when maneuvering potholes.

In , [23] an intelligent system for pothole and hump identification on roads using Internet of Things (IoT) was proposed. The proposition makes use of a database to keep records of identified potholes and also sends the data to the appropriate authorities. The system is also capable of alerting the driver of a pothole ahead so that the vehicle maneuver or slowed down accordingly. However, the system does not assist the driver maneuvering potholes but only detects the potholes.

2.2. Related works in Speedbump Detection

There also exist a number of works in the literature as it relates to speedbumps . In 2010, the number of vehicles used worldwide was estimated to be over 1 billion, and according to [24], AVs are widely anticipated to alleviate road congestion through higher throughput, and also reduce human errors to improve road safety and ease the stress of driving.

In [25], a survey on possible production errors and security challenges faced by Autonomous Vehicles was carried out. The use of road segmented remedy, intersection-based solution, active & passive countermeasure was employed in carrying out the survey on possible production error and security challenges faced in autonomous vehicles.

In a related development a road surface condition monitoring and database system with the aid of a programmed accelerometer sensor was proposed by [26]. The system identifies different road conditions with the aid of vehicular vibrations due to their acceleration on road anomalies.. The proposed approach was reliable, durable and not time-consuming which makes it suitable for the development of road monitoring systems. The proposed approach offers a reliable and fast medium for the detection of road surface profiles. In the system acquired profiles are stored to form a robuost database for future references. Regardless of the benefit the system offers, the mechanism for the protection of the stored data on the database was not provided which pose a security risk to user data and this limits the application in AV systems as reagrds vehicle to vehicle communication [26].

Also, a smartphone road anomaly detection system was proposed and developed in [27]. The proposed system adopted a modified fuzzy logic guassian model for analysing and classification of road anomalies. The developed system employed a K-nearest neighbour (KNN) algorithm to classify the sensed anomalies into Potholes and Bumps. The proposed system demonstrated versatility, effectiveness with a 94% to 96% accuracy rate in the recognition of road anomaly and compatiblilty with different types of vehicles and its low cost-effectiveness. Regardless of the effectiveness, versatility and accuracy of the technique used in the recognition of road conditions, the technique is only applicable to only two types of road conditions namely potholes and bumps[27].

[13], proposed the use of a fuzzy logic controller for the development of a vision and control system for autonomous vehicles. The fuzzy logic controller comprises a steering controller and a speed controller. One of the added advantages of this method was its ability to add human knowledge and experience via the fuzzy decision tree language into the system to achieve higher accuracy and precision. Although the method is capable of performing automatic driving on straight roads, the scheme is challenging to implement in AV development [13].

The image processing was used in the development of a speed breaker and road marking detection system in [28]. The technique involved using image processing for speed breaker and road marking detection. The authors also integrated Optical character recognition and Hough transform alogrithms to recognize traffic signs and detect line markings respectively. An accuracy rate of 79.97% for optical character recognition and 100% for the local binary patterns was obtained after analysis. One of the limitation of the system was the inability to detect speed breaker and road marking in the absence of light which made the system not fully functional at night.

2.3. Summary of findings and research gaps

In the light of the above, it is evident the application of image processing and computer vision have aided the identification and detection of road anomalies on motorways. Albeit, the blurriness of the road anomalies images as identified from the perspective of the moving vehicle and the inability to regulate the speed of vehicle when approaching anomalies are another issues. These and other issues identified in literature have resulted in the ineffectiveness of developed solution. Thus, to proffer solutions to these challenges, this work proposes the development of a improved Histogram of Oriented Gradient (HOG) image processing algorithm to detect road anomalies as well as estimate their locations. Furthermore, to control the speed and effectively navigate AVs, this work proposes the adoption of a modified fuzzy logic controller to regulate the speed of a vehicle when approaching a road anomaly. Table 1 shows some of the related work carried out in autonomous vehicle and pothole detection.

Table 1: Related works on Pothole and Autonomous vehicle

S/N	Author(s)	Work	Year	Description	Strength(s)	Weakness(es)
1	Seung-ki, R., Taehyeong, K. & Young-RO, K.	Image-Based Pothole Detection System for ITS Service and Road Management System.	2015	ITS (Intelligent Transportation System) service and road management system. A pothole detection method based on two dimensional (2D) images is proposed for improving the existing method and designing a pothole detection system to be applied to ITS service and road management system.	The use of a Modified Histogram Shaped-Based Thresholding (MHST) improved the Accuracy to 73% and Precision of 80%.	Long image processing time (46s average), accuracy can be improved with the use of more than one optical sensor, the vibration of vehicle affects the detection unit.
2	Ashwini, K., Kore, K., Akshada, K., & Ashwini, M.	Pothole Detection System Based on Android Device and Ultrasonic Sensor.	2018	The system makes use of an integrated mobile app with the pothole detection system (Ultrasonic Sensor and Microcontroller) for monitoring of the road path.	the mobile app helps the users monitor the road path remotely.	The use of just an ultrasonic sensor causes the system to be inefficient in detecting all forms of potholes. The system would be ineffective where there is poor or no network reception.
3	Rahul, H., Ashish, Z., & Nilesh, P.	Real time pothole detection technique using image processing and dimension estimation.	2019	The proposed system uses image processing and edge detection (Canny, Zero Cross) techniques to take real time data of potholes. It uses this data to estimate the depth and width of potholes for filling and patching purposes.	The system applies high level of image processing, filtering of images and application of scaling factors to accurately calculate the area of the pothole.	The processing time of the system will be relatively slow when applied to self driving cars for pothole detection due to the fact that self driving cars need only fast estimations of the pothole perimeters and not the depth.
4	Shivaleelavathi, B. G., Veeramma, Y., Yamini, V. S., & Spoorthi, T.	Design and Development of an Intelligent System for Pothole and Hump Identification on Roads.	2019	This project aims at identifying the potholes using image processing technology with the help of a camera. The system sends the location of these potholes to authorities using GPS. The humps are detected using the ultrasonic sensors and the electronics system alerts the driver about the humps and the driver can accordingly slow down the vehicle and hence avoid the accidents. The alert is provided in the form of voice through speakers and displayed on the LCD and using GSM, SMS is sent to the driver.	The system makes use of an IOT database to keep records of identified potholes and also sends the data to the appropriate authorities. The system is also capable of alerting the driver of a pothole ahead so that the vehicle can be manoeuvred or slowed down accordingly.	The system does not assist the driver manoeuvring potholes but only detect the potholes.
5	Youngtae, J., & Seungki, R.	Enhanced Pothole Detection Algorithm for Blurry Images.	2015	This system comprises of a pothole detection algorithm using various features in 2D images that improved the existing methods and accurately detected a pothole. The System implemented the use of	The major strength of this system is the ability of the system to be accurate enough to detect real potholes on the road with the aid of	There is a little the system can do if the image blur is caused by vibrations or shake in the camera. The restoration rate in

				image sharpening algorithms to prevent wrong detection of potholes.	a de-Blurring image sharpening algorithm.	situations like this is still very low.
6	Akshatha, P. , Chaitra, P. , Lakshmi, S. , & Richard, L.P.	Automatic Detection of Potholes	2019	Automatic detection of potholes is a human safety based project. This system provides cost effective solution for detection of potholes on the road by using ultrasonic sensors. The microcontroller fetches the location of the pothole using GPS and the GPS locations are sent with the help of GSM. The GSM at the vehicle part takes that location and sends the location to the concerned person and that person can see pothole on the map of that area.	This system provides cost effective solution for detection of potholes and humps on the road and indicate the road maintenance authority for maintenance. This system also provides the driver an indication that there is a pothole ahead and the desired action can be taken	The system does not possess the ability aid the vehicle in control. The alert system does not provide exact location of pothole on the road path to aid avoidance of the pothole.

3. Research Methodology

3.1. System Description

The design and development of the speedbump detection and speed control system for an autonomous vehicle involve numerous components. These components include Raspberry pi 3 microprocessor, speed sensor (LM 390), Pi camera, Model Car, Direct Current (DC) motors, servo motor, power supply.. The Raspberry pi microcontroller is the brain of the system. The inputs to the microcontroller are the images acquired from the camera as well as the speed of the vehicle at that instant. The outputs of the system are the speed of the DC motor and the angle of the servo motor. These outputsrl indicates the status of the vehicle in terms of speed and direction in the presence of road anomalies (Speedbumps and potholes). The raspberry pi microcontroller carries out all major processing and also houses the HOG and Fuzzy Logic Control algorithms.

When an anomaly is detected, the system will evaluate the distance of the vehicle from the anomaly, based on the data obtained from the camera, the fuzzy logic controller determines the appropriate speed and direction to be used when approaching an anomaly. When the vehicle is close to an anomaly, the speed will be reduced by the controller, and maneuver the vehicles in the appropriate direction. The vehicle will revert to its original speed and position after it has successfully passed the anomaly.

The block diagram representing system architecture is shown in Figure 1 and the flowchart of the system operation is shown in Figure 2.

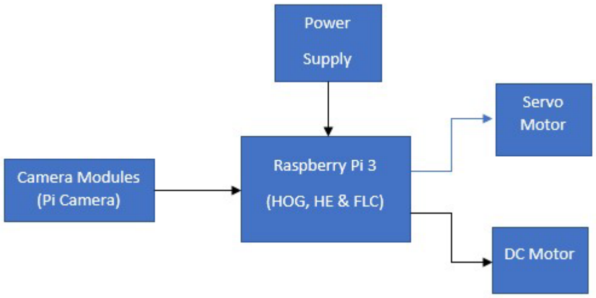

Figure 1: System Architecture

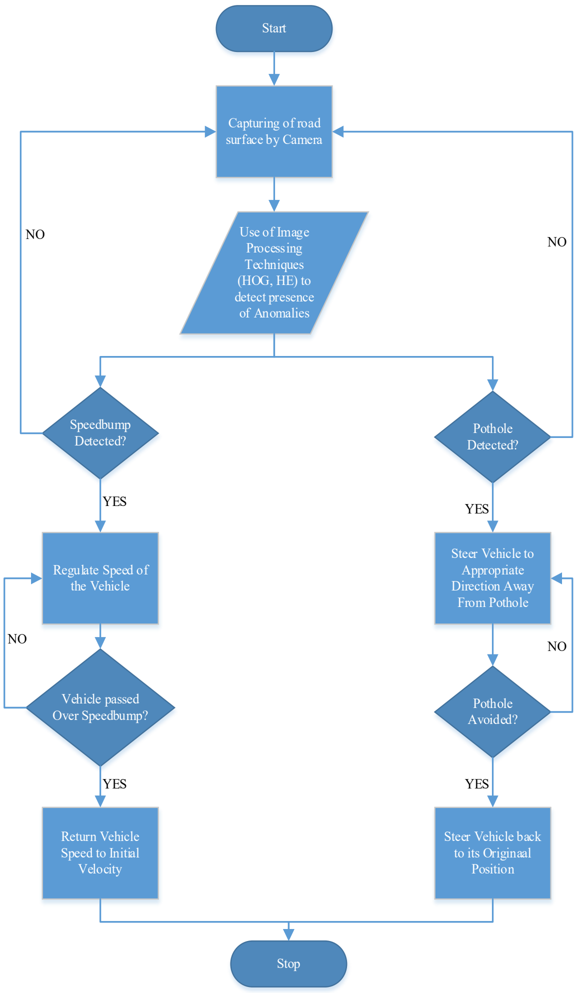

Figure 2: System Flowchart

Figure 2 shows the process of how information is being acquired, gathered, processed, and transmitted from one section of the system to the other. The image of the anomaly (speedbump or pothole) is captured by the camera by extracting the features of the road surface using the histogram of oriented gradient technique and Histogram Equalization respectively. When the road anomaly has been detected, a command is sent to the microcontroller which regulates the speed of the vehicle, when the anomaly is a speedbump, and in the presence of a pothole, a command/ signal is sent to the system to change the direction of the vehicle by changing the angle of the servo motor. When the vehicle has successfully passed or steered passed the anomaly, the speed and the direction of the vehicle is returned to the original velocity and position respectively. This process continues the vehicle is in motion.

In this work, MATLAB software was used for the realization of the vehicle model, development and implementation of the image processing and fuzzy logic algorithms . MATLAB is an acronym for “Matrix Laboratory” which is a high-level programming language and an Integrated Development Environment (IDE) used for numeric computations, simulations and programming. MATLAB is used in different fields for data analysis, algorithm development and the development of system models. It has a vast variety of tools and commands essential to almost all engineering applications.

3.2. Mathematical Model

In this work, the autonomous vehicle was modelled in terms of the longitudinal dynamics of the vehicle. The external longitudinal forces acting on the vehicle include aerodynamic drag forces, gravitational forces, longitudinal tire forces and rolling resistance forces.

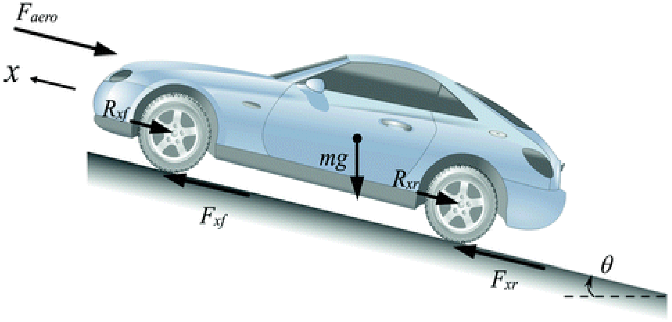

Figure 3: Longitudinal Vehicle Dynamics [29]

Figure 3 shows a diagram representing the longitudinal dynamics of the vehicle. The diagram shown in Figure 3 highlights the forces considered when modelling the longitudinal dynamics of a vehicle. F_{xr}, F_{aero}, F_{xf}, R_{xf}, mg, and R_{xr} represent the longitudinal tire forces at the rear, aerodynamic drag force, rolling resistive force at front tires, mass of the vehicle, and rolling resistive force at front tires, respectively [29]. The force balance along the vehicle longitudinal axis yield is showed in (1).

$$m\ddot{x} = F_{xf} + F_{xr} - F_{aero} + R_{xf} - R_{xr} - mgsin(\theta) \qquad (1)$$

Where:

F_{xf} = longitudinal tire force at front tire
F_{xr} = longitudinal force at rear tire
F_{aero} =equivalent longitudinal aerodynamic drag force
R_{xf} = rolling resistance at front tire
R_{xr} =rolling resistance at rear tire
m = mass of the vehicle
g = acceleration due to gravity
θ = angle of inclination of the road the vehicle travels θ

The aerodynamic drag force on the vehicle can be represented as equation 5.

$$F_{aero} = \frac{1}{2}\rho C_d A_f (Vx + Vwind)^2 \qquad (2)$$

Where:

ρ is the mass density of air.
C_d is the aerodynamic drag coefficient.
A_f is the frontal area of the vehicle which is the projected area of the vehicle in the direction of travel.
$V_x = \dot{x}$ is the longitudinal vehicle velocity, V_{wind} is the wind velocity (positive for a headwind and negative for a tailwind) [29].

3.3. Road Anomaly Detection

a) Image Acquisition

This process entails acquiring the image from the surface of the road, which will be used in determining the presence or absence of anomalies by applying image processing techniques. Image processing has become one of the main aspects of automation and safety-related applications in the electronic industries and these images can either be in a digital or analog form [15]. This process of acquiring the image will be carried out using a Pi camera with a resolution of 8 Megapixels, when the vehicle is moving with a speed of 5 to 10 m/s.

b) Image Preprocessing (Color space conversion, HE, HOG noise removal)

Images of road surfaces are captured using the Pi camera. The captured images are sent to the microcontroller to carry out image processing to detect and extract both speedbump and pothole features. The next process is done by the microcontroller to convert the image’s colour space from RGB to grayscale, filter all distortion and blurriness using the median filter, crop out the Region of Interest (ROI) of the image, and HOG and HE respectively is applied on the image to enhance the image. The mathematical representation of the histogram equalization (HE) is in (3) and Histogram of Oriented Gradient (HOG) in (4) to (8).

Equation for HE:

$$h(v) = floor\ ((CFD(v) - \frac{CFDmin}{(Mxn) - CFDmin} x\ (L-1) \qquad (3)$$

Where:

h = new grayscale value.

v = pixel number.

CDF(v)= Cumulative Density Function at v.

CDFmin = minimum Cumulative Density Function.

M x n = image rows & columns.

L = current grayscale level.

After histogram equalization, a feature extraction process is used to identify features on the image that are relevant to the scope of this project (potholes). This process is done by using the BRISK (Binary Robust Invariant Scalable Key points) points algorithm. The BRISK points represent the metric data on the region of interest with the most significant value. Pothole elements in images have more distinct metric values due to the disparity in pixel contrast compared to the road surface. This process is used to retrieve the location of the strongest metric data representing the pothole features recognized in the segmented image. The point's locations are then stored in an array.

Equation for HOG:

Using the 1st order differential coefficient, $f_x\ (x, y)$ and $f_y\ (x, y)$

$$fx\,(x,y) = f\,(x+1,y) - f\,(x-1,y) \quad (4)$$

$$fy\,(x,y) = f\,(x,y+1) - f\,(x,y-1) \quad (5)$$

where $f\,(x, y)$ *in (1) and (2) is luminance at* (x, y)

The magnitude and direction of the gradient (m & θ) can be calculated using (6) and (7)

$$(x, y) = \sqrt{}fx(x, y)^2 + fy(x, y)^2 \quad \textit{(Magnitude)} \quad (6)$$

$$(x, y) = arctan \frac{fx(x,y)}{fy(x,y)} \quad \textit{(Direction)} \quad (7)$$

After computation of (6) and (7), the HOG is generated by the following steps:

- determining the class which $\theta(x, y)$ belongs to.
- increasing the value of the class using the first step.
- repeating the above operation for all the gradients belonging to the cell.

Equation (8) can be used in finding the final HOG feature.

$$v = Vk \quad (8)$$

Where Vk = vector corresponding to a combined histogram for a block and V = normalize Vector.

c) Image Segmentation

Image segmentation entails the use of Sobel edge detection in identifying the edges present in an image, which is carried out based on the characteristics of the pixels in the image. The Sobel filter works by calculating the gradient of image intensity at each pixel within a given image. From the result gotten from the input of the Pi camera, the edges of the images were obtained by finding the approximate absolute gradient magnitude at each point in the image.

d) Feature Extraction (HOG and BRISK)

Feature extraction involves the identification and selection of the desired data from an image, and converting that data obtained into useful information The feature extracted provides the coordinate of the speedbump on the road surface when present with the use of the HOG Technique, while the feature and coordinate of the pothole of are provided using the Brisk points. These features are used in training the system in detecting the presence or absence of road anomalies (Speedbump and Potholes) respectively. During the feature extraction, the HOG points converge around or on the surface of the anomaly (i.e., Speedbump) and also during that of the BRISK points. Equation 9 was used in crrying out the HOG technique.

$$\boldsymbol{v} = \frac{\boldsymbol{Vk}}{\sqrt{||\boldsymbol{Vk}||2+1}} \quad (9)$$

e) Feature Recognition (ANN, DT, and SVM)

The use of Artificial Neural Network (ANN), Support Vector Machine (SVM) and Decision Tree techniques were applied in training and testing of the designed system in recognizing the presence or absence of road anomaly (speedbump and potholes). The presence and absence of anomalies on the road surface were used as the target in training the system, where the presence of anomalies was represented by an output one (1), and the absence of anomalies was represented as an output zero (0).

3.4. Speed and Steering Control

a) Fuzzy Logic Design for Steering

Fuzzy Logic is a method from imprecise and ambiguous knowledge, which provides a definite solution. When using a series of statistical rules used to describe expertise dependent on membership degrees, this is achieved. Fuzzy Logic has widespread applications in control engineering, signal processing, and artificial intelligence.

The fundamental type of fuzzy logic control modelling, known as the fuzzy inference system (FIS), is a rule-based structure composed of three conceptual components:

- A rule base composed of a set of fuzzy if-then rules.
- A database describing the membership function (MF) used in these fuzzy rules.
- A reasoning process incorporating such rules into a mapping routine from inputs to the outputs of the system to drive a reasonable output.

There are essentially two types of base rule structures, namely Mamdani and Takagi-Sugeno-Kang (TSK). The fuzzy rule is expressed in language form in the Mamdani type. In this work, the fuzzy rule was represented using the Takagi-Sugeno-Kang rule structure as a logical function of the input variables which is more suitable for neuro-fuzzy systems. The fuzzy logic approach is made up of five steps:

- Define all input and output variables.
- Define the subset interval.
- Choose the membership function.
- Define the IF-THEN rules.
- Perform calculations and adjust the rules.

Due to its simplicity, ease of interpretation, acceptance of imprecise data and ability to integrate with other traditional control methods, this study will employ the use of a Fuzzy Logic Controller. Figure 4 presents a fuzzy logic control system.

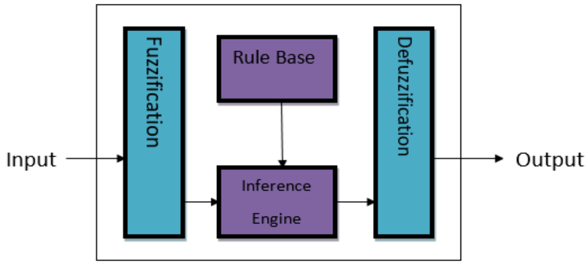

Figure 4: Fuzzy Logic System.

In this work , the steering of the vehicles in the presence of a pothole anomaly is determined by the rule base of the fuzzy system, the rule base is the representation of the IF-AND-THEN rules used in the implementation of the fuzzy controller. These rules are stated below, with the diagram representation shown in Figure 5:

i. If (POA is PRESENT) and (DTA is LEFT) then (STEERING is RIGHT)
ii. If (POA is PRESENT) and (DTA is RIGHT) then (STEERING is LEFT)
iii. If (POA is ABSENT) then (STEERING is MIDDLE).

where

POA : Presence of Abnormaly
DTA: Distance to Abnormaly
STEERING: Control of vehicle

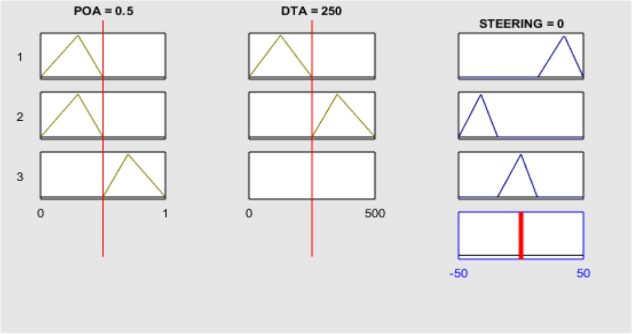

Figure 5: Rule Base for FIS.

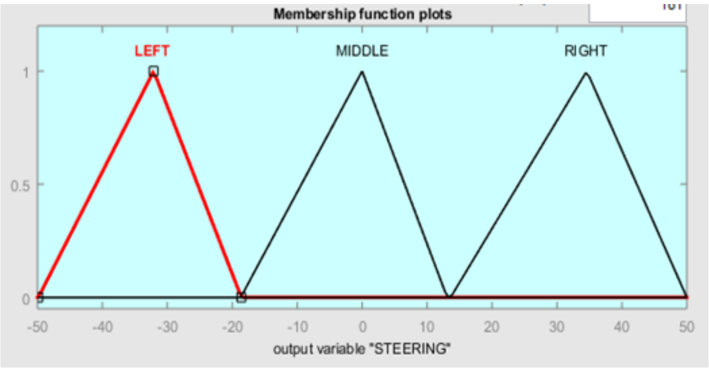

Figure 6: Output Membership Function for Steering.

The fuzzy logic controller uses the output membership function from the FIS in Figure 6 to determine the direction to control the autonomous vehicle in the presence or absence of road anomaly (pothole). The surface diagram describing the fuzzy logic controller's FIS is shown in Figure 7.

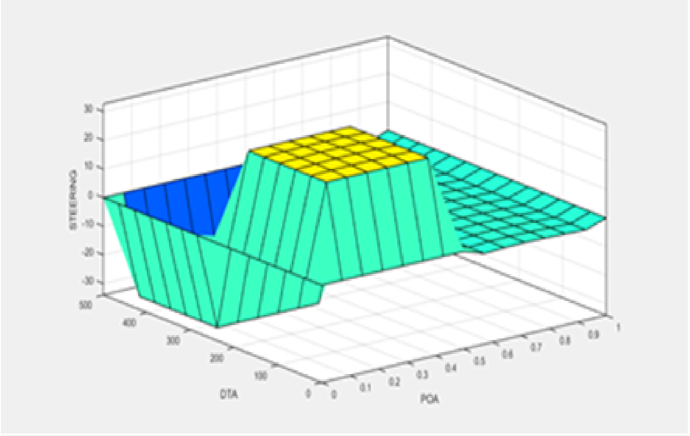

Figure 7: Surface Diagram of Fuzzy Logic Controller

b) Fuzzy Logic Design for Speed

The use of a surface diagram was employed to represent the relationship between the input and output parameters of the designed FLC system. Figure 8 shows the surface diagram of the design FLC system, by representing the relationship between the input membership parameter to the output membership parameters in a three-dimensional graphical representation, which was generated from the design of the FLC controller.

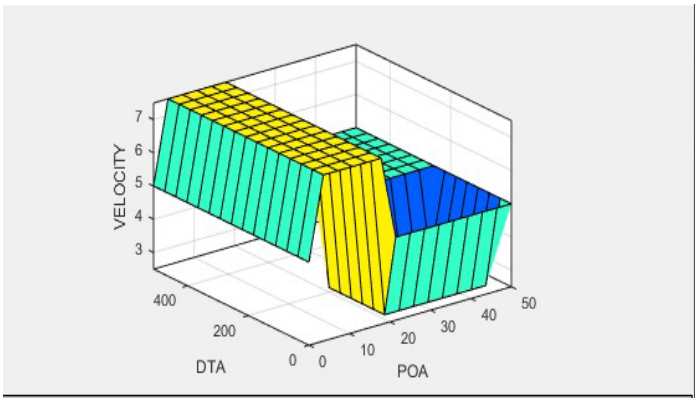

Figure 8: System Surface Diagram

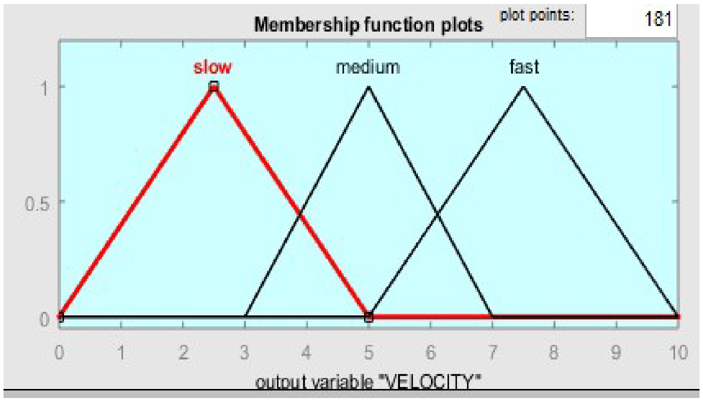

Figure 9: Output Membership Function for Speed Control.

The fuzzy logic controller uses the output membership function from the FIS in Figure 9 to determine the direction to control the autonomous vehicle in the presence or absence of road anomaly (speedbump).

In the design of the FLC system, rules were generated in order to provide the needed condition (rules) on which the FLC depend in controlling the speed of the vehicle in the presence or absence of speedbumps. Table 2 shows the rules generated by FLC in a graphical format. Where

POA : Presence of Anomaly

DOA: Distance of Anomaly

Table 2: FLC Rule Base

POA DOA	Present	Absence
Close	Slow	Fast
Far	Med	Fast

3.5. Testing and Performance Evaluation

The performance evaluation of the system is carried out to determine the effectiveness, accuracy, precision and efficiency of the method and techniques used in the development of this project. The intelligent speedbump detection system is tested and evaluated based on precision, recall and accuracy in detecting the presence of speedbumps on the road. The metrics are represented mathematically as:

$$\text{Precision} = TP / (TP + FP) \qquad (10)$$

$$\text{Accuracy} = TP / (TP + FN) \qquad (11)$$

$$\text{Sensitivity} = FP / (TN + FP) \qquad (12)$$

where:

TP = true positive (number of abnormally classified correctly).

FP = false positive (number of negative cases of abnormally classified correctly).

TN = true negative (number of correct cases of abnormally classified wrongly). FN = false negative (number of incorrect cases of abnormally classified wrongly).

The fuzzy logic model was also evaluated based on the response of the system to the rules generated by the fuzzy inference system in regulating the speed and direction of the vehicle when there is the presence of road anomaly. In carrying out the performance evaluation of the system, the accuracy rate which indicates how well the system was able to correctly detect the positive cases of a speedbump.

4. Results

This section presents the result gotten from the detection of road anomaly, i.e. speedbumps detection system in section 4.1 and that of the pothole detection system in section 4.2 respectively.

4.1. Road Anomaly Detection

a) Speedbump

The results obtained from the development of an intelligent speedbump and speed control system for autonomous vehicle, with the use of the HOG technique is shown in Figure 10. The result was obtained with the implementation of the HOG feature extraction technique in order to extract the needed data from the image acquired by the camera (i.e., speedbump). The feature extracted provides the coordinate of the speedbump on the road surface when present, and it's also used in training the system in detecting the presence or absence of road anomaly. During the feature extraction, the HOG points converge around or on the surface of the anomaly (i.e., Speedbump).

The use of Artificial Neural Networks (ANN) and Decision Tree techniques was applied in training and testing of the designed system in recognizing the presence or absence of road anomaly (speedbump). The results obtained from the training the system with the use of ANN and Decision Tree are presented in Figure 11 to Figure 14.

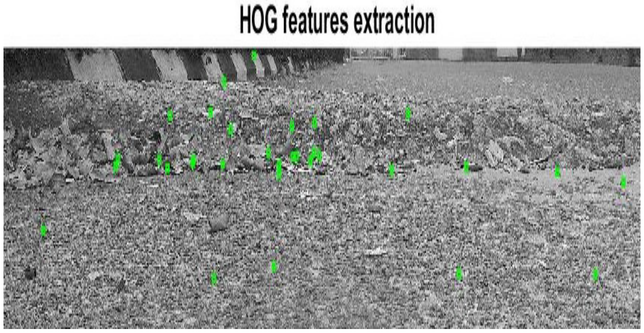

Figure 10: Feature Extraction using HOG

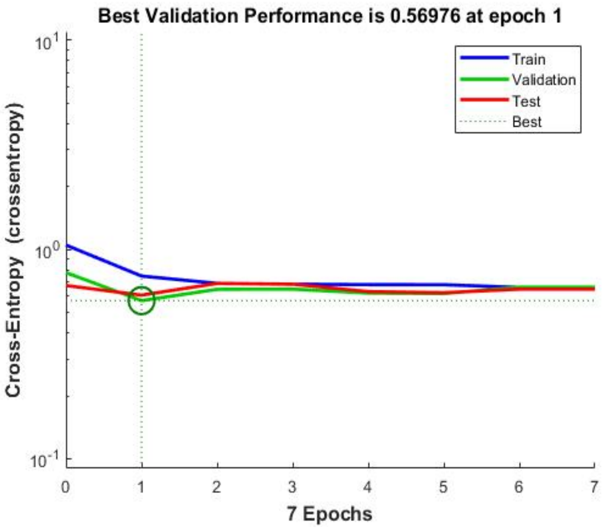

Figure 11: Performance Validation of System (ANN)

From Figure 11, it is shown that the best performance of the trained model occurred at a value of 0.56976 before the occurrence of overfitting at 7 Epochs. The confusion matrix of the system in Figure 12 presents the result in the detection of an anomaly. The confusion matrix shows that the system had a testing performance of 58.4%, a training performance of 71.4%, a validation performance of 71.4% and total performance of 62.3% for the detecting of speedbumps on road surfaces.

Figure 12: Confusion Matrix of Neural Network

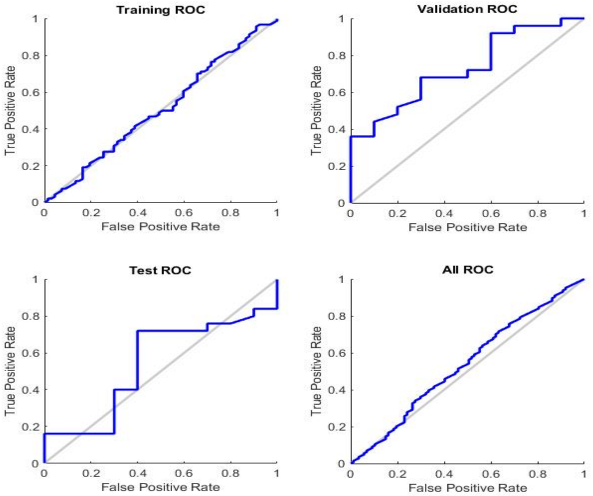

Figure 13: Receiver Operation Characteristics of Neural Network

The evaluation of the result between the output of the model to the true positive rate and false positive rate in the classification of the data. From the ROC shown in Figure 13, the system had a higher True Positive Ratio compared to the False Negative Ratio in the validation, training and testing ratio graph in the detection speedbump.

Figure 14 presents a graphical representation of the output gotten from the application of training the system with the use of a classification learner (Decision Tree). The Classifier was also provided with a dataset containing 231 road images (144 images with speedbump and 87 images without speedbump). The Decision tree classifier was also trained with 144 features extracted from the images and had an accuracy of 75.7%.

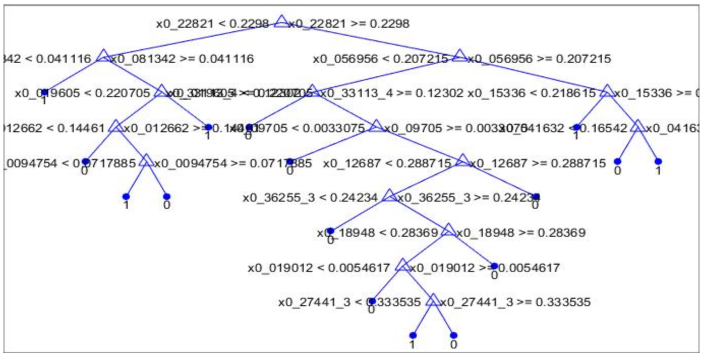

Figure 14: Classification Tree Model for Decision Tree for Speedbump

b) Pothole

The results obtained from the image processing algorithm, image acquisition, image preprocessing using Histogram Equalization, and feature extraction are shown in Figure 15.

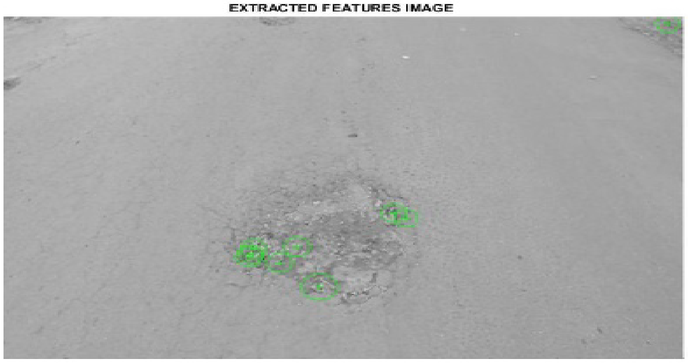

Figure 15: BRISK Points Extracted from the Image.

4.2. Vehicle Maneuvering

This section presents the result gotten from the design of the fuzzy logic system in the steering and speed control of the vehicle. The result of the steering fuzzy system is shown in section 4a and the speed control is in section 4b.

a) Steering

Table 3 presents the extracted points from the image. these points will be fed into the feature recognition (ANN) model to predict if a pothole is present in the image.

Table 3: Brisk Points Location

BRISK POINT	X AXIS	Y AXIS
1	404.0000	269.0000
2	287.3419	337.0000
3	258.8189	324.8189
4	305.3646	314.9544
5	416.9694	275.9694
6	328.2500	370.0000
7	256.0000	329.0000
8	261.0000	317.2109
9	256.4589	274.0000

Table 4: Fuzzy Logic Controller Performance results

Presence of anomaly (POA) (Meter)	Distance to Anomaly (DTA) (Meter)	Output (Velocity) (M/s)	Accuracy	Remark
0.1	0	1	Accurate	Slow Velocity
0.2	20	2	Inaccurate	Fast Velocity
0.3	40	3	Accurate	Slow Velocity
0.4	60	4	Accurate	Medium Velocity
0.5	80	5	Accurate	Medium Velocity
0.6	100	6	Inaccurate	Fast Velocity
0.7	120	7	Accurate	Slow Velocity
0.8	140	8	Accurate	Fast Velocity
0.9	160	9	Inaccurate	Fast Velocity
1	180	10	Accurate	Fast Velocity
2	200	10	Accurate	Fast Velocity
3	220	6	Inaccurate	Slow Velocity
4	240	4	Inaccurate	Slow Velocity
5	260	7	Accurate	Fast Velocity
6	280	10	Accurate	Fast Velocity
7	300	10	Accurate	Fast Velocity
8	320	8	Inaccurate	Slow Velocity
9	340	10	Accurate	Fast Velocity
10	360	9	Inaccurate	Medium Velocity
11	380	10	Accurate	Fast Velocity

b) Speed

The Fuzzy Logic Controller was used in the control of the vehicle speed in the presence of a speedbump, this was also carried out using a maximum velocity of 10M/s in controlling the speed of the vehicle. The presence the distance of the speedbump was used in the determination of the velocity at the vehicle moves at. Table 4 present the response of the FLC in regulating the speed of the vehicle in relation to the presence and distance of rod anomaly (speedbump) to the vehicle.

Figure 16: Developed MATLAB Application for Speedbump Analysis on Images.

4.3 Testing and Performance Analysis

a) Developed Application Interface

The feature recognition system was evaluated by developing a GUI application in testing the detection accuracy of the ANN model to that of the Decision Tree model and the SVM for both speedbump and pothole anomaly as shown in Figure 16 and Figure 17 respectively. Also, the results obtained from the ANN, SVM and Decision Tree model displayed on the MATLAB application used for the image analysis are shown in Figure 16.

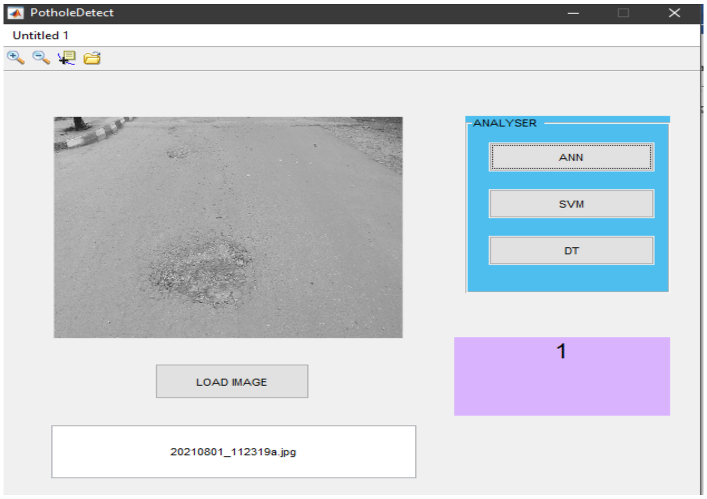

1

20210801_112319a.jpg

Figure 17: Developed MATLAB Application for Pothole Analysis on Images.

From the results presented in the application in Figure 17, an output of 1 was achieved signifying that an anomaly (pothole) is present in the image.

b) Comparative Analysis

The ANN, SVM and DT models' performance was evaluated based on accuracy, precision and sensitivity using Equations (9), (10), and (11). The evaluated performances are shown in Table 4 and Table 5 for both speedbump and pothole respectively.

After the two models have been designed, trained and tested, a comparison between both techniques was carried out, based on the accuracy, recall and precision of their results. Table 2 shows the comparative analysis between the ANN and Decision Tree models. The Precision, Accuracy and Recall of both trained models were calculated using (9), (10) and (11). The aim of the result shown in Table 5, is to determine the most optimal and suitable prediction technique for detecting speedbumps on the road surface. From Table 5, it was seen that the Decision Tree model produces a higher accuracy, precision and recall, with a percentage of 75%, 82% and 77% respectively.

Table 5: Comparison Table of ANN and Decision Tree

Parameters/ Technique	**Artificial Neural Network (ANN)**	**Decision Tree**
Accuracy	62.3%	75.7%
Precision	70%	82%
Recall	61%	77%

From the comparison in Table 6, the SVM model provided the best performance in terms of accuracy and precision. While the ANN and Decision Tree models produced similar but optimal performances in accuracy and precision which were over 75%.

Table 6: Performance Evaluation for ANN, SVM AND DT models.

	ACCURACY (%)	**PRECISION (%)**	**SENSITIVITY (%)**
ANN	78.6	78.6	78.6
SVM	86.0	86.7	79.4
DECISION TREE	78.5	76.4	71.75

5. Conclusion

The result of the HOG ANN training model used for recognizing the presence or absence of speedbump had an accuracy of 62.3%, a precision of 0.70 and a recall of 0.61, while that of the decision tree had an accuracy of 75.7%, a precision of 0.82 and a recall value of 0.77 as shown in Table 3. The results of the HE image processing model and ANN training model showed good accuracy of 83.3% for the sample images used for testing as shown in table 5, but the model was unable to detect the presence of anomalies in low-resolution images as the algorithm could not plot 9 BRISK points on images that had low pixel quality. The trained ANN model provided a total accuracy of 78.6%.

The fuzzy logic controller was able to regulate the speed of the vehicle in the presence of a speedbump and also change the direction of the vehicle in the presence of potholes. It was also observed that the use of the decision classification tree approach in detecting speedbump detection provided more accurate results when compared to that of Artificial Neural Network (ANN) with an accuracy of 65% in testing and training of the system, while the SVM models in the detection of potholes provided the best performance in pothole detection, but the ANN model provided an optimal performance for pothole detection with an accuracy of 78.6%.

Conflict of Interest

The authors declare no conflict of interest.

Acknowledgement

The authors wish to acknowledge the Tertiary Education Trust Fund (TETFUND), Nigeria for funding this work under the National Research Fund (NRF) grant titled “Novel Road Accident Monitoring and Prevention System for Nigerian Roads and Highways” with Grant Number: TETF/ES/DR&D-CE/NRF2020/SETI/95/VOL1.

References

[1] P. U. Miracle, J. A. Bala, A. M. Aibinu, T.A. Folorunso, "Intelligent Speed Bump Identification and Speed Control System for Autonomous Vehicles: A Conceptual Design," *1st International Conference on Multidisciplinary Engineering and Applied Science (ICMEAS)*, 2021, 1-6, doi: 10.1109/ICMEAS52683.2021.9692403.

[2] J.A. Afolabi, K.T. Gbadamosi, (2017). “Road Traffic Crashes in Nigeria: Causes and Consequences.” Transport & Logistics: The International Journal, **17**(42), 41.

[3] N.C. Onyemachi, U.R. Ofoma, “The Public Health Threat of Road Traffic Accidents in Nigeria: A Call to Action.” Annals of Medical and Health Science Research, **6**(4), 199-204, 2016, doi: 10.4103/amhsr.amhsr_452_15.

[4] G.F. Pepple, C.S. Ejimadu, “Relationship between Road Traffic Accidents and Visual Status of Commercial Motor Vehicle Drivers in an Urban Area of Niger Delta Region of Nigeria.” Ophthalmology Research: An International Journal, 1-7, 2019.

[5] M. Bashiri, C.H. Fleming, “A platoon-based intersection management system for autonomous vehicles.” In IEEE Intelligent Vehicles Symposium, Proceedings **4**, 667–672, Redondo Beach, CA, USA, 2017. https://doi.org/10.1109/IVS.2017.7995794

[6] W. Zhang, E. Jenelius, H. Badia, “Efficiency of semi-autonomous and fully autonomous bus services in trunk-and-branches networks.” Journal of Advanced. Transportation, 2019. https://doi.org/10.1155/2019/7648735

[7] S. Adarsh, Real-Time Speed Bump Detection Using Image Segmentation for Autonomous Vehicles. Intelligent Computing, Information and Control System (ICICCS). 1039, 308, 2019.

[8] J. Youngtae, R. Seungki, “Enhanced Pothole Detection Algorithm for Blurry Images.” Journal of Emerging Trends in Computing and Information Sciences, **6** (5), 245, 2015.

[9] H.S. Yun, T.H. Kim, T.H. Park, “SpeedBump Detection for Autonomous Vehicles by Lidar and Camera.” Journal of Electrical Engineering & Technology, **14**(5), 2155-2162, 2019. https://doi.org/10.1007/s42835-019-00225-7.

[10] H.S. Yun, T.H.. Kim, T.H. Park, “Speed-Bump Detection for Autonomous Vehicles by Lidar and Camera." Journal of Electrical Engineering & Technology, **14**(5), 2155- 2162, 2019, https://doi.org/10.1007/s42835-019-00225-7.

[11] H. Bello-Salau, A.M. Aibinu, A.J. Onumanyi, S. Ahunsi, E.N. Onwuka, J.J. Dukiya, “Development of a road surface condition monitoring and database system.” In 2nd International Conference on Information and Communication Technology and Its Applications (ICTA 2018), Federal University of Technology, Minna, Nigeria, 6, 2018.

[12] A.B. Saeed, Madjid, T, “Autonomous Vehicles: Challenges, Opportunities and Implications.” Journal on Modern Transportation, **24**(8), 287, 2016, https://doi.org/10.1007/s40534-016-0117-3.

[13] U. Anand, “Fuzzy logic vision and control of autonomous vehicles.” *IPASJ Int. J. Comput. Sci*, **4**(1), 1-7, 2016.

[14] J.A. Bala, S.A. Adeshina, A.M. Aibinu, "Advances in Road Feature Detection and Vehicle Control Schemes: a Review," *2021 1st International Conference on Multidisciplinary Engineering and Applied Science (ICMEAS)*, 2021, pp. 1-6, doi: 10.1109/ICMEAS52683.2021.9692414.

[15] L.B. Ana, O. Ivan, O.J. Arturo, “Speedbump Detection on Roads using Artificial Vision.” Research in Computer Science, **148**(9),71-82, 2019.

[16] Y. Hyeong-Seok, K. Tae-Hyeong, P. Tae-Hyoung, ”Autonomous Vehicle by Lidar and Camera.” Journal of Electrical Engineering & Technology, **14**(5), 2155-2162, 2019, https://doi.org/10.1007/s42835-019-00225-7.

[17] H. Ziaul, “Basic Concept of GPS and Its Applications.” IOSR Journal of Humanities and Social Science, **21**(3), 31, 2016.

[18] R. Seung-ki, K. Taehyeong, K. Young-RO, “Image-Based Pothole Detection System for ITS Service and Road Management System.” Journal of Mathematical Problems in Engineering, **20**(15), 1-11, 2015, https://doi.org/10.1155/2015/968361.

[19] T. Amitha, J. Shiji, V. Sinu, P. Sooraj, N. Indrasena, “Real Time Pothole Detection and Road Monitoring System.” International Journal of Innovative Research in Science, Engineering and Technology, **8**(6), 6740-6744, 2019.

[20] K. Ashwini, K. Kore, K. Akshada, M. Ashwini, “Pothole Detection System Based on Android Device and Ultrasonic Sensor.” International Journal of Innovative Research in Computer and Communication Engineering, **6**(9), 7688-7692, 2018.

[21] H. Rahul, Z. Ashish, P. Nilesh, “Real time pothole detection technique using image processing and dimension estimation.” International Journal of Engineering Development and Research, **7**(2), 108-111, 2019.

[22] S. Yamuna, S. Raja, M. Pavithra, M. Ranjitha, R. Shubashni, S. Sneha, “Automatic Pothole Detection System using Laser Technology.” International Journal for Research in Applied Science & Engineering Technology (IJRASET), **5**(3), 1226-1231, 2017.

[23] Y. Wiseman, *Autonomous Vehicles*. Encyclopaedia of organizational knowledge, Administration, and Technologies, First Edition 2019.

[24] S.D. Pendleton, H. Andersen, X. Du, X. Shen, M. Meghjani, Y.H. Eng., M.H. Ang, “Perception, planning, control, and coordination for autonomous vehicles.” *Machines*, **5**(1), 6, 2017, **https://doi.org/10.3390/machines5010006** .

[25] J. Cui, L. S. Liew, G. Sabaliauskaite, F. Zhou, “A review on safety failures, security attacks, and available countermeasures for autonomous vehicles.” *Ad Hoc Networks*, *90*, 101823, 2019, https://doi.org/10.1016/j.adhoc.2018.12.006.

[26] A.M. Nascimento et al., "A Systematic Literature Review About the Impact of Artificial Intelligence on Autonomous Vehicle Safety," in IEEE Transactions on Intelligent Transportation Systems, **21**, (12), 4928-4946, Dec. 2020, doi: 10.1109/TITS.2019.2949915.

[27] R. Du, G. Qiu, K. Gao, L. Hu, L. Liu, “Abnormal Road Surface Recognition Based on Smartphone Acceleration Sensor.” *Sensors*, **20**(2), 451, 2020, **https://doi.org/10.3390/s20020451**.

[28] O. Adeyemi, M. Irhebhude, A. Kolawole, “Speed Breakers, Road Marking Detection and Recognition Using Image Processing Techniques.” *Advances in Image and Video Processing*, **7**(5), 30-42, 2019.

[29] R. Rajamani, Vehicle dynamics and control. Springer Science & Business Media, 2011.

Advances in Science, Technology and Engineering Systems Journal Vol. 8, No. 2, 14-23 (2023)

www.astesj.com

Special Issue on Innovation in Computing, Engineering Science & Technology

ASTESJ
ISSN: 2415-6698

Multiple Criteria Decision-making: Risk Analyses for the Soft Target

Dora Kotkova*, Lukas Kralik, Lukas Kotek, Jan Valouch

Department of Security Engineering, Tomas Bata University in Zlín, Zlín, 760 05, Czech Republic

ARTICLE INFO

Article history:
Received: 31 August, 2022
Accepted: 29 January, 2023
Online: 11 March, 2023

Keywords:
Soft targets
Risk analysis
TOPSIS

ABSTRACT

This article focuses on risk analysis using a multi-criteria decision-making method. Due to many performed risk analyses for soft targets, we are constantly trying to find new methods for objective risk assessment. Many risk analyses are subjective, which is a problem when planning security measures and comparing results (different events, objects, places, etc.). In this text, we present our case study, which deals with the use of fuzzy TOPSIS. As a reference object, we have chosen one of the specific categories of soft targets – cultural events. The goal was to find the location most at risk of violent attacks on a selected cultural event - a music concert. We then established cooperation with three experts. The completed data in the risk analysis was then compared with practice. The selected fuzzy TOPSIS method was chosen as presumably more objective. Our hypothesis was confirmed. The results were objective and consistent with practical experiences.

1. Introduction

The article aims to present our research, which we have worked on for several years [1-12]. The goal is to research the protection of soft targets and find new methods to strengthen security. In this article, we focus on one necessary step, risk analysis. The biggest problem is selecting the appropriate method and minimalizing subjective view. Currently, many risk analysis methods exist, but none are specifically designed for soft targets. Our effort is to explore these methods and choose one or develop a new one that will provide objective results.

This article extends the contribution from The IEEE International Carnahan Conference on Security Technology 2021, where we presented an essential and necessary introduction and case study with the applied Fuzzy TOPSIS method [1]. In this extended version, we provide additional information on why we selected Fuzzy TOPSIS and a more detailed risk analysis of the whole workflow. Also, the introduction offers more detailed information about previous research and project on soft targets protection [1-12].

Our research is mainly concerned with the area of soft target protection. *"The term "Soft Targets" can be referred to those objects (buildings), (open) spaces, or events characterized by the accumulation of many people, the absence or low level of security measures against violent assaults, and their omission among critical infrastructure and hard target objects"* [13].

The protection of soft targets is a relatively new phenomenon in the geopolitical space of Europe. This issue became relevant after the events in 2014 when the so-called Islamic State declared a caliphate and began carrying out terrorist attacks worldwide [13], [14]. As the first figure (Fig. 1) shows, the number of terrorist attacks almost doubled. The data is obtained from our database created for our research[7], [9], [11], where violent attacks against soft targets are recorded from Europe and parts of Russia and Turkey. The existence and updating of the database are crucial for our research because we need to register this information and add details such as the location of the attack, time, modus operandi (Fig. 2), type of soft target (Fig. 3), and other information about the attack [14], [15].

This paper describes a significant part of our research. It is focused on security measures and, above all, on risk analysis. Nowadays, there are many risk analysis methods but just a few of them suits soft targets. The central lack of those methods is objectiveness. Some complex methods, such as Failure Mode and Effects Analysis (FMEA), are claimed as objective methods. But the result of this method depends on one evaluator's opinion [16]. The section 3 specifies some methods that are mostly used in security issues. Following section 4 goes into more detail about methods verified and tested in our research.

We asked three security managers to participate in our case study by finding the most exposed and weakest point in protecting soft targets at cultural events. Our previous research has shown the utility of multi-criteria decision-making (MCDM) in identifying

---

*Corresponding Author: Dora Kotkova, kotkova@utb.cz

https://dx.doi.org/10.25046/aj080202

soft targets. This case study aimed to verify the hypothesis that some methods of MCDM should be used for risk analysis, especially risk assessment. One of the significant parts of risk analysis is proposing security measures and making a plan of necessary activities; however, we focused just on the part of risk assessment and compared the final risk ranking from MCDM and typical risk analysis.

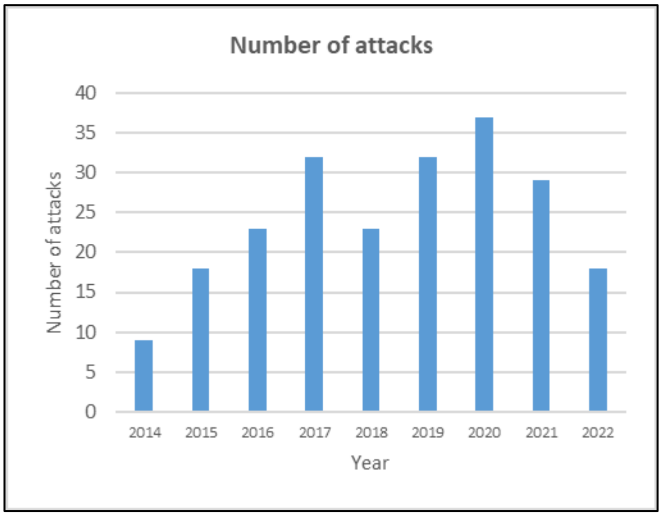

Figure 1: Number of terrorist attacks from 2014 to 2022 [15]

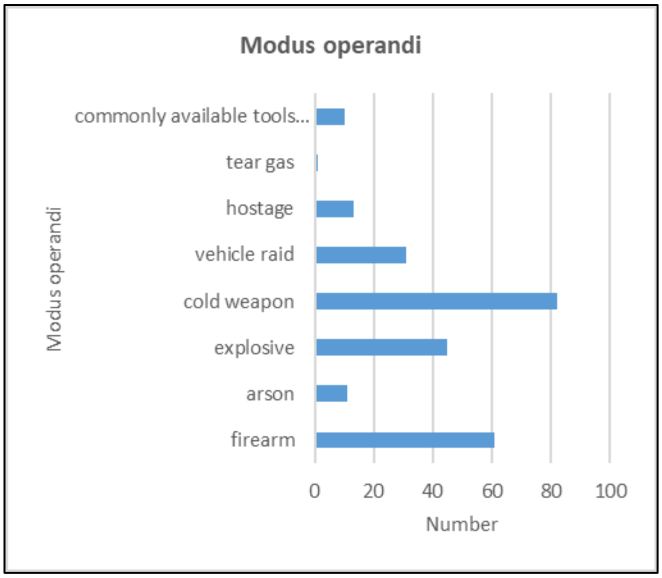

Figure 2: Modus operandi of terrorist attacks from 2014 to 2022 [15]

For this purpose, we selected some MCDM methods described deeply in section 4. Lately, we added the Fuzzy TOPSIS method to the list because this method perfectly fits our problem of objectives. Based on information from several publications [17 – 19], we decided to use the standard fuzzy TOPSIS version due to the existence of many hybrid approaches [20], [21], or updated methods [22], [23]. Some efforts are known to use Fuzzy TOPSIS for risk assessment [24], [25]. Classic fuzzy TOPSIS is only a segment of the developed methodology.

Soft targets has many categories and each category has own specifications. Cultural events is a category that we selected for our research and case study. As Fig. 3 depicts, cultural events are not targeted mostly, however they are very diverse. The quality of security measures that are highly variable, is the main reason for our choise.

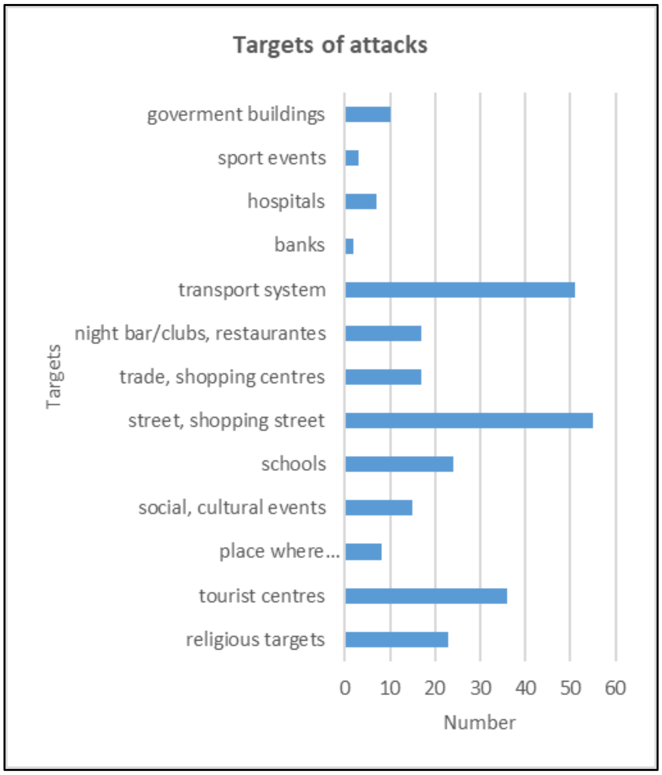

Figure 3: Targets of terrorist attacks from 2014 to 2022 [15]

2. Cultural events

Cultural events are one of the soft targets categories. *"Cultural events can be defined based on a combination of two words - culture and event or based on a combination of their defining concept. By combining these formulations, the following definition can be reached: cultural events are pre-planned events with a clearly defined place and time, the main goal of which is the presentation of spiritual and material values created by man."* [26]

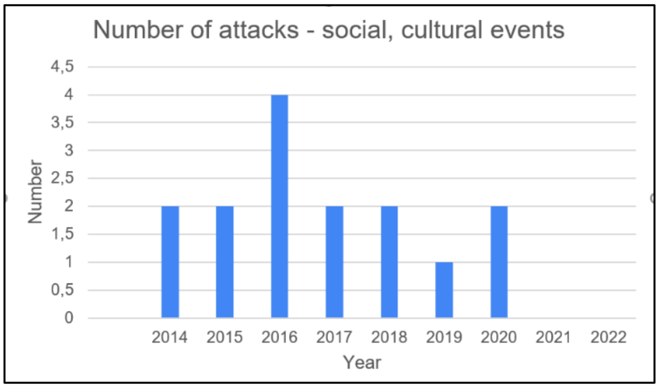

Figure 4: Number of terrorist attacks on social and cultural events from 2014 to 2022 [15]

Each mass event has its own specification, conditions and needs. Safety is a vital part of these mass events or gatherings. Differentiation of essential characteristics is absolutely necessary to establish proper safety. Every successful terrorist attack on mass gathering may take many causalities. This is the reason why all mass gatherings must be well protected. The following figure (Fig. 4) shows that the average number of attacks is 2 and a half per year with a peak in 2016 [15].

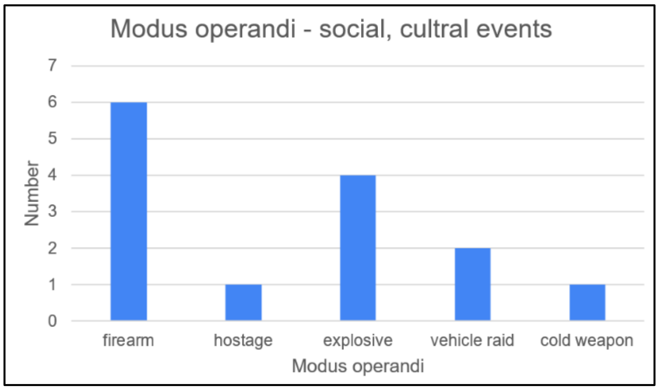

Figure 5: Modus operandi of terrorist attacks on social and cultural events from 2014 to 2022 [15]

3. Risk management

One of the integral parts of security planning is handling threats and their probability. We need to know what threats are in our facility. The objective of security planning is to take measures that lower the probability of emerging threats. The probability is also labeled as a risk.

Risk management (RM) is an endless process that subsists of three steps (fig. 6). Each step is described in more detail in the following sub-sections.

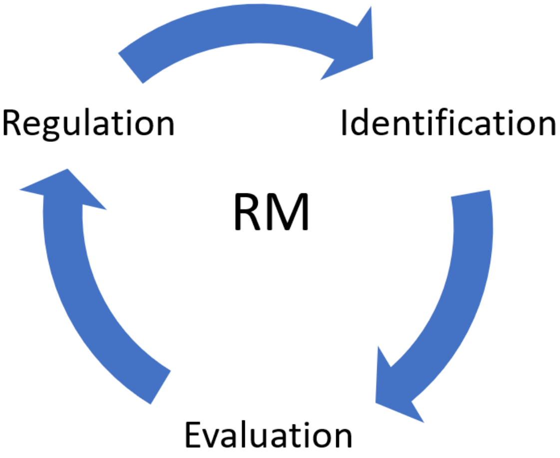

Figure 6: Risk Management steps [15]

3.1. Risk identification

Risk identification is ensured through risk analysis. The risk identification step usually includes the following activities:

1) Identification of sources of risk – this part includes:
   a) Determination of initial data – data on the analyzed entity, description of operation, location, etc.
   b) Identification of assets - definition and determination of the value of the assets owned by the subject;
2) Identification of threats – identification of events and actions that can negatively affect the value of assets;
3) Identification of vulnerabilities – every asset has its vulnerability or weakness to an identified threat. The level of this vulnerability affects the impact when a threat affects a protected asset;
4) Determining and assessment of impact.
5) Determination of risk - determination of the probability of the occurrence of threats and the degree of vulnerability of the subject [27]

There are three basic groups of risk analysis. The first one contains qualitative methods such as tree analysis – Event Tree Analysis (ETA), or Fault Tree Analysis (FTA). One of the most used and elemental methods is Safety/Security review. The group of quantitative methods stands on the other side, Failure Mode and Effect Analysis. (FMEA) is one of the well-known methods in this category. The last category is the combination of the two previous. It is a group of semi-quantitative methods that combine experience and numerical expression of risk [15].

3.2. Risk evaluation

Risk evaluation is an activity determined to enumerate risks and assign them to the correct category. The risks scale from the lowest negligible to the highest critical (Fig. 7). When planning security measures, we start with the necessary risk and need to spend the most funds in this category.

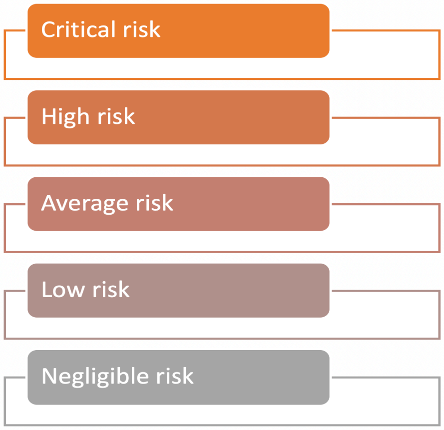

Figure 7: Risk scale

3.3. Risk regulation

The last step in risk management is risk regulation. This step includes six different approaches. Each approach has its own positives and negatives. It is very complicated to say which one is the best. It depends on the point of view. The possible approaches are:

- Ignoring the risk – conscious or unconscious
- Acceptance of the risk – this approach covers also issues with residual risk.
- Reduction of the risk – this is the most logical approach that implements corresponding security measures or reduces the severity of the impact.

- Risk avoidance
- Transfer of risk – transferring risk to another entity (e.g., outsourcing)
- Risk monitoring – the risk is not static, but it is variable and might change over time.

4. Methods

MCDM is a very complex field and provides many different methods and procedures. The most well-known methods such as the Analytic Hierarchy Process (AHP) [28], Technique for Order of Preference by Similarity to Ideal Solution (TOPSIS) [29], [30] or Višekriterijumsko Kompromisno Rangiranje (VIKOR) [30] has been selected for our research.

4.1. AHP

Tasks, the number of elements (variants and criteria), and the complexity in more complicated decision-making increase exceptionally. Due to this, the decision-maker has a problem getting his bearings in the task. Therefore, in the 1970s, Professor Thomas L. Saaty created the AHP method, which he and his colleagues developed into a practical tool for solving these complicated tasks. [28]

AHP can be described as a method of breaking down a complex unstructured situation into simpler parts – the establishment of a hierarchical system (Fig. 8). The following part uses the subjective assessment of pairwise comparisons, which assigns numerical values to individual components that express their relative importance. The subsequent synthesis of these evaluations determines the element with the highest priority.

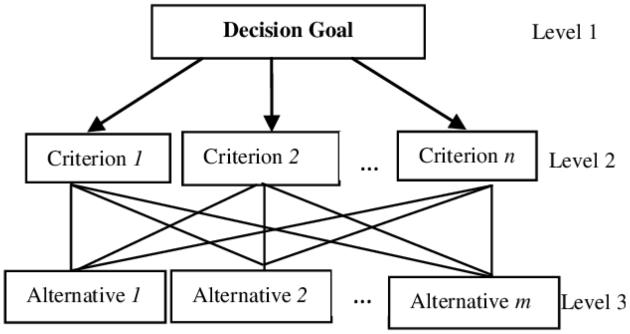

Figure 8: Structure (hierarchy) of AHP [31]

4.2. TOPSIS

The TOPSIS method, according to R.R. Venkata [32], was developed by Hwang and Yoon and is characterized by the fact that it requires only a minimum number of inputs from the user and also that the outputs are very understandable. The only subjective parameters are the weights of the criteria. The TOPSIS method is based on the idea that the optimal solution is the one that has the shortest distance from the ideal solution and is also the furthest from the solution that is negative [29], [30].

The method is based on five computational steps:

1. obtaining performance evaluation of alternatives on various criteria,
2. normalization of assessment,
3. normalized scores are assessed,
4. the distance between the ideal and negative solutions is calculated
5. the ideal solution selected based on ratios of calculated distances [29], [30]

4.3. VIKOR

The VIKOR method is another method that searches for the best solution on a set of alternatives according to the distance from the ideal solution [33]. This method was developed for multi-criteria optimization in complex systems and focused on evaluation and selection in the presence of conflicting criteria. Each alternative is evaluated according to the multi-criteria function, and the resulting compromise solution is obtained based on the proximity to the ideal alternative. The evaluation is obtained using five steps [30], [34].

1. The alternatives are labeled as $x1, x2, \ldots, xm$; where m is number of alternatives.
2. Determination of the maximum and minimum values of all criterion functions.
3. Calculation of the utility and regret measure of the respective alternative.
4. Calculation of performance evaluation of alternatives.
5. Sorting of alternatives according to performance evaluation. A lower rating value represents a better alternative [30]

4.4. Comparison and selection

The results of the above methods were compared against results from semi-quantitive risk analysis PIE. We carefully selected security issues for risk analysis and compared only cases with exactly ten threats (criteria). We asked highly renewed experts for security and safety. Each of them made a PIE analysis, and then we made a threat list ranked according to the mean value of obtained results. This list served as a “standard” for comparing our selected methods. The method with the lowest ranking difference against our PIE “standard” was selected for further research. As shown in tab. I. Fuzzy TOPSIS (FTOPSIS) presents the best results. FTOPSIS was added in the progress of research because it allows the processing of opinion of more evaluators.

Table 1: Rank Comparison

	Threat 1	**Threat 2**	**Threat 3**	**Threat 4**	**Threat 5**
TOPSIS	0.20	0.11	0.20	0.19	0.18
AHP	0.28	0.15	0.19	0.23	0.27
VIKOR	0.18	0.12	0.19	0.18	0.23
FTOPSIS	0.08	0.14	0.10	0.12	0.15
	Threat 6	**Threat 7**	**Threat 8**	**Threat 9**	**Threat 10**
TOPSIS	0.11	0.14	0.19	0.12	0.15
AHP	0.28	0.18	0.21	0.30	0.26
VIKOR	0.11	0.15	0.10	0.15	0.12
FTOPSIS	0.10	0.13	0.11	0.14	0.13

Every change of rank by one position is reflected in comparison by value 0.1. The average value for comparison of all cases is in the above table (Tab. I.)

The most significant similarity with PIE (Tab. II.) shows FTOPSIS had similar threats rank for six threats. Similar methods, TOPSIS and VIKOR, has almost identical results. (Tab. I. and Tab. II.)

Table 2: Overal Similarity

	Similarity
TOPSIS	2/10
AHP	0/10
VIKOR	2/10
Fuzzy TOPSIS	6/10

5. Fuzzy TOPSIS

FTOPSIS is a modified standard TOPSIS, which belongs to the most used techniques for MCDM. It consists of adding fuzzy logic that allows the reflection opinion of all decision-makers. This technique utilizes two ideal solutions. Those solutions are called Fuzzy Positive Ideal Solution (FPIS) and Fuzzy Negative Ideal Solution (FNIS) [29]. The aim is to find a distance from both of these ideal solutions. The longest distance from FNIS and the shortest distance from the FPIS is the best result. It is calculated as a geometric distance from these solutions [16].

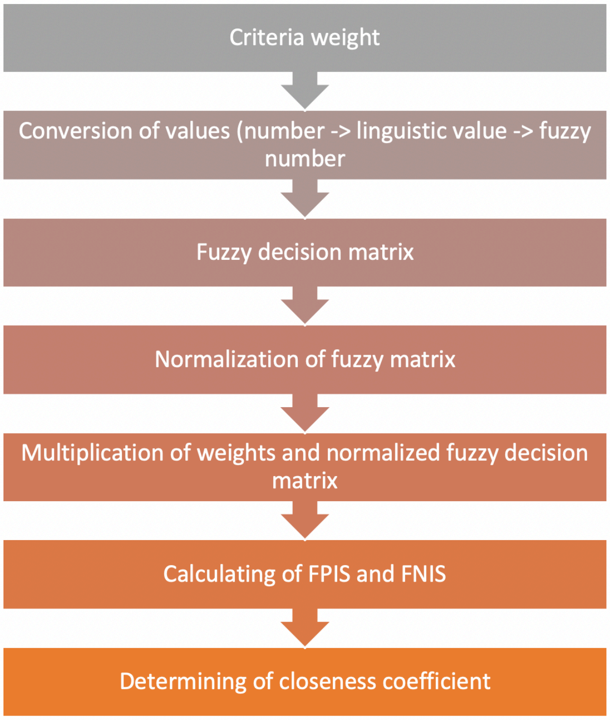

Figure 9:Seven steps of FTOPSIS [1]

Complete calculation and ordering of alternatives according to distance have seven steps (Fig. 9) [1], [16-18].

Table 3: Conversion table [1]

Numerical value	**Linguistic value**	**Fuzzy number**
1	Very low	{1, 1, 3}
2	Low	{1, 3, 5}
3	Average	{3, 5, 7}
4	High	{5, 7, 9}
5	Very high	{7, 7, 9}

Usage of linguistic values showed as a not appropriate. Each linguistic value was represented by numerical value which made it easier for our decision-makers. Consequently, we converted it into fuzzy numbers to obtain correct weights for further calculation. (Tab. III.).

Converted fuzzy numbers are used to build a corresponding fuzzy matrix for each decision-maker (three matrices, in our case). Those matrices are merged to the united fuzzy matrix. Every triangular fuzzy numbers is represented by three values (*F={a;b;c}*). Calculation of these values are based on following formulas (1):

$$a_{ij} = min_k\{a_{ij}^k\};\ b_{ij} = \frac{1}{K}\sum_{k=1}^{K} b_{ij}^k;\ c_{ij} = max_k\{c_{ij}^k\} \quad (1)$$

The uniform matrix is built from a combination of decision matrices and the above formulas. Next step is the normalization of the uniform matrix. Normalization is one of the essential activities for almost all MCDMs. The TOPSIS and also its fuzzy modification work with two types of criteria. The first group brings benefits (eg. increasing efficiency). The second group has a negative influence on the decision maker and this group is called as a cost criteria (eg. salary). Each group has slightly different formula for normalization. Benefits criteria (2) looks for maximal value and cost criteria (3) for minimal value :

$$\widetilde{r_{ij}} = \left(\frac{a_{ij}}{c_j^+}, \frac{b_{ij}}{c_j^+}, \frac{c_{ij}}{c_j^+}\right);.\ c_j^+ = max_i\{c_{ij}\} \quad (2)$$

$$\widetilde{r_{ij}} = \left(\frac{a_j^-}{c_{ij}}, \frac{a_j^-}{b_{ij}}, \frac{a_j^-}{a_{ij}}\right);\ a_j^- = min_i\{a_{ij}\} \quad (3)$$

The normalized matrix must be supplemented by criteria weight. Normalized values are simply multiplicated by reciprocal weight values of criterion (4).

$$\widetilde{A_1} \otimes \widetilde{A_2} = (a_1, b_1, c_1) \otimes (a_2, b_2, c_2) = (a_1 * a_2, b_1 * b_2, c_1 * c_2) \quad (4)$$

Multiplication results are used to find the ideal solution. There are two possible solutions: a positive solution with the “best” values and a negative solution with the worst values. Because this is fuzzy modification than solutions are called as fuzzy positive/negative solutions (FPIS (5)/ FNIS (6)), Calculation of these solution is given by:

$$A^+ = \left(\widetilde{v_1^+}, \widetilde{v_2^+}, \ldots \widetilde{v_n^+}\right);\ \widetilde{v_j^+} = max_i\{v_{ij3}\} \quad (5)$$

$$A^- = (\widetilde{v_1^-}, \widetilde{v_2^-}, \ldots \widetilde{v_n^-});\ \widetilde{v_j^-} = min_i\{v_{ij1}\} \quad (6)$$

However, it is the best or the worst situation that probably never occurs. Each involved alternative has its own solution and the distance, which is between FPIS, FNIS and this solution, (7) describes the quality of the involved alternative. The distance is given as:

$$the\ d(\tilde{x}, \tilde{y}) = \sqrt{\frac{1}{3}[(a_1 - a_2)^2 + (b_1 - b_2)^2 + (c_1 - c_2)^2]} \ (7)$$

The closeness coefficient (8) is the final step to ordering all involved alternatives.

$$CC_i = \frac{d_i^-}{d_i^- + d_i^+} \qquad (8)$$

6. Case study

We have focused on applying the TOPSIS method to one cultural event in the case study. The basic information about the event:

- Specialization: music metal concert - group Arakain
- Where: Masters of Rock Café in Zlín, Czech Republic
- Frequency: once a year (various dates)
- Number of visitors: 400 - 500 people

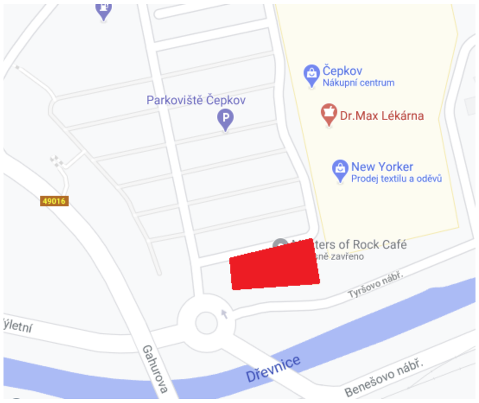

Figure 9: Localization of the Master of Rock Café. [35]

Figure 10: The main entrance of the Mater of Rock Café. [35]

6.1. Risk management

Assets are determined based on a security inspection of the given location, where we analyzed what is crucial for the owner of the building, whether from the point of view of finances, operations, or maintaining continuity. There are assets within the selected object:

- People
- Property of the club, visitors, performers
- Building
- Continuity
- Money
- Etc. [15].

The next step is to identify the threats. Several ways could do this. One possible way is again an on-site security inspection where a security professional has enough experience in the required field and can identify the most problems that may arise. The second way is to start from the threat catalog. A threat catalog is a document or, more accurately, a list of generic and most common threats. This catalog is made by some security experts to provide a tool that may help identify threats and save time.

In our case study, we combined more methods. The threat catalog was thoroughly studied, and some threats were selected as relevant. Check-list had been made from these threats, and this check-list we used for security inspection. Threats identified for our case study:

- **Assault, injury**
- Property theft, damage (vandalism), or destruction
- Pickpocketing
- Fire or flood
- Power failure, delay in the arrival of performers, cancellation of the concert
- Entrance with an invalid ticket [15].

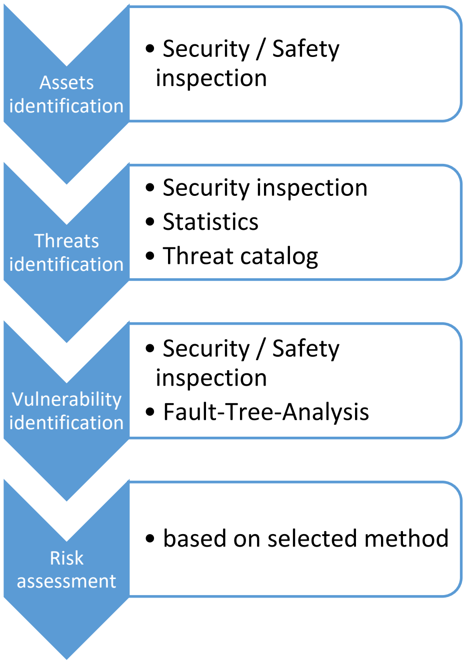

Figure 11: Risk assessment workflow

Vulnerability is always determined at a given location when existing security measures, accessibility to the facility, employee reactions, etc., are checked based on the inspection. Vulnerability identification for our case study:

- Obsolete security systems
- Absence of mechanical restraint systems
- Lack of the Visitor Regulations
- Number of glazed surfaces
- Proximity to the river

- Etc.

The whole process is outlined in the following steps (sub-processes) (fig. 11).

The final risk assessment is made with the help of the TOPSIS method. Inputs are based on the opinion of three “common” security managers. “Common” means that they are not specialized in advanced risk analysis and especially in the field of soft targets protection.

The main objective was to find the most exposed location with the highest probability of attack that may have fatal consequences. Based on experience, the location of attacks is determined by on-site inspection, security assessment, and determining which areas are attractive for the attack. This can be assessed from the point of view of their vulnerability, lack of security, or the number of people we expect at a given location. Thanks to the localization of the attack, when planning security measures, we can directly target security at a given location and thereby strengthen it.

Analyzed localizations are:

- Main entrance
- Audience space
- Stage
- Refreshments space
- Parking lot [15].

Initially, we must define the criteria for TOPSIS, which increase or decrease the risk. The criteria were determined on a similar basis to the location of the attack. Thanks to our many years of experience in planning the security of cultural events, as well as from the methodologies, books, and works of experts that have been published on this topic. Initially, it is always important to say what we want to analyze. For soft targets, one of the most critical locations are those with accumulated large numbers of people. Subsequently, we focus on how easy it is to get into the object, if someone stops the attacker, etc. When I already have security measures, I have to ask if they are effective and if they can detect and respond to an attack.

In many cases, security measures are only passive. It means that security measures serve as a monitoring tool for the occurred security situation but cannot respond. This is entirely unacceptable in the case of an attack on people. Therefore, the effort is to plan measures that will actively detect the attack and trigger some reaction (alarm). Our chosen criteria are defined in the basic document for soft target protection [13]. Those criteria are:

- A number of people – it is labeled as a benefit criterion because more people increase the risk.
- Accessibility – benefit criterion; higher accessibility = lower security -> less effective security measures such as security guards or surveillance system.
- Detectability – because this criterion decreases the risk, it is labeled as a cost criterion. Security guards are able to detect the attack in the early stage.
- Reactivity – another cost criterion. This criterion expresses the time between the start of attack and the first reaction of guards or policemen.

7. Results

There is evaluation from three professionals and security specialists in the following tables (Tab. IV, V, and VI).

Table 4: Decision maker 1 [15]

	Number of people	**Accessibility**	**Detectability**	**Reactivity**
Weight (numerical)	5	3	3	1
Main entrance	{5, 7, 9}	{7, 9, 9}	{1, 3, 5}	{5, 7, 9}
Audience space	{7, 9, 9}	{3, 5, 7}	{3, 5, 7}	{3, 5, 7}
Stage	{1, 3, 5}	{1, 1, 3}	{5, 7, 9}	{5, 7, 9}
Refreshments space	{5, 7, 9}	{3, 5, 7}	{3, 5, 7}	{3, 5, 7}
Parking lot	{1, 3, 5}	{7, 9, 9}	{1, 1, 3}	{1, 3, 5}

Table 5: Decision maker 2 [15]

	Number of people	**Accessibility**	**Detectability**	**Reactivity**
Weight (numerical)	4	4	5	4
Main entrance	{5, 7, 9}	{7, 9, 9}	{5, 7, 9}	{5, 7, 9}
Audience space	{7, 9, 9}	{3, 5, 7}	{1, 3, 5}	{1, 3, 5}
Stage	{1, 3, 5}	{1, 1, 3}	{7, 9, 9}	{5, 7, 9}
Refreshments space	{3, 5, 7}	{3, 5, 7}	{1, 3, 5}	{1, 3, 5}
Parking lot	{1, 3, 5}	{7, 9, 9}	{1, 1, 3}	{1, 1, 3}

Table 6: Decision maker 3 [15]

	Number of people	**Accessibility**	**Detectability**	**Reactivity**
Weight	5	3	4	3
Main entrance	{5, 7, 9}	{7, 9, 9}	{1, 3, 5}	{3, 5, 7}
Audience space	{7, 9, 9}	{3, 5, 7}	{1, 3, 5}	{1, 1, 3}
Stage	{1, 1, 3}	{1, 1, 3}	{7, 9, 9}	{7, 9, 9}
Refreshments space	{3, 5, 7}	{1, 3, 5}	{3, 5, 7}	{3, 5, 7}
Parking lot	{1, 3, 5}	{7, 9, 9}	{3, 5, 7}	{1, 3, 5}

When we have the results from decision makers, we combined the decision fuzzy matrix (1) (Tab. VII).

Table 7: Combined decision fuzzy matrix[15]

		Number of people	**Accessibility**	**Detectability**	**Reactivity**
weight	numerical	5	3	4	3
	linguistic	Very high	Average	High	Average
Main entrance		{5, 7, 9}	{7, 9, 9}	{1, 4.333, 9}	{3, 6.333, 9}
Audience space		{7, 9, 9}	{3, 5, 7}	{1, 3.667, 9}	{1, 3, 7}
Stage		{1, 2.333, 5}	{1, 1, 3}	{5, 8.333, 9}	{5, 7.667, 9}
Refreshments space		{3, 5.667, 9}	{1, 4.333, 7}	{1, 4.333, 7}	{1, 4.333, 7}
Parking lot		{1, 3, 5}	{7, 9, 9}	{1, 2.333, 7}	1, 2.333, 5}

Then we normalized the fuzzy matrix according to (2) and (3) (Tab. VIII).

Table 8: Normalized fuzzy matrix [15]

	Number of people	**Accessibility**	**Detectability**	**Reactivity**
weight	{7, 9, 9}	{3, 5, 7}	{5, 7, 9}	{3, 5, 7}
Main entrance	{0.556, 0.778, 1}	{0.778, 1, 1}	{0.111, 0.231, 1}	{0.111, 0.158, 0.333}
Audience space	{0.778, 1, 1}	{0.333, 0.556, 0.778}	{0.143, 0.273, 1}	{0.143, 0.333, 1}
Stage	{0.111, 0.259, 0.556}	{0.111, 0.111, 0.333}	{0.111, 0.120, 0}	{0.111, 0.130, 0}
Refreshments space	{0.333, 0.630, 1}	{0.111, 0.481, 0.778}	{0.143, 0, 1}	{0.143, 0.032, 1}
Parking lot	{0.111, 0.333, 0.556}	{0.778, 1, 1}	{0.143, 0, 1}	{0.200, 0, 1}

Then we created a weighted normalized fuzzy matrix according to (4) (Tab. IX). The A^+ and A- are according to (5) and (6).

Table 9: Weighted normalized fuzzy matrix [15]

	Number of people	**Accessibility**	**Detectability**	**Reactivity**
Main entrance	{3.889, 7, 9}	{2.333, 5, 7}	{0.556, 1.615, 9}	{0.333, 0789, 2.333}
Audience space	{5.444, 9, 9}	1, 2.778, 5.444}	{0.714, 1.909, 9}	{0.429, 1.667, 7}
Stage	{0.778, 2.333, 5}	{0.333, 0.556, 2.333}	{0.556, 0.840, 1.800}	{0.333, 0.652, 1.400}
Refreshments space	{2.333, 5.667, 9}	{0.333, 2.407, 5.444}	{0.714, 1,615, 9}	{0.429, 0.161, 7}
Parking lot	{0.778, 3, 5}	{2.333, 5, 7}	{0.714, 3, 9}	{0.600, 2.143, 7}
A+	**{5.444, 9, 9}**	**{2.333, 5, 7}**	**{0.714, 3, 9}**	**{0.600, 2.143, 7}**
A-	**0.778, 2.333, 5}**	**{0.333, 0.556, 2.333}**	**{0.556, 0.840, 1.800}**	**{0.333, 0.652, 1.400}**

Then we calculated distance FPIS and FNIS according to (7) (Tab. X).

Table 10: Final FPIS and FNIS distances [15]

	FPIS				**FNIS**			
Main entrance	1.463	0.000	0.805	3.808	3.977	3.896	4.181	0.650
Audience space	0.000	1.745	0.630	2.217	5.235	2.241	4.203	3.348
Stage	5.235	3.896	4.341	4.253	0.000	0.000	0.000	0.283
Refreshments space	2.632	2.093	0.799	3.002	3.137	2.090	4.182	3.234
Parking lot	4.959	0.000	0.000	1.929	0.385	3.896	4.341	3.433

As the results show, the riskiest area is the audience space. Many people in a small area have a crucial effect on early detection and mainly on possible reactions. A mass of people complicates and prevents the moving of security guards. The second risky area is the main entrance. It reflects practical experience from previous terrorist attacks. Many people standing in the queue are very attractive to attack by vehicles. The parking lot stands in third place. Protection of this area is a little bit complicated because people move in unpredictable directions, and installing anti-collision barriers is almost impossible. The results were calculated by using the formula (8) (Tab. XI).

Table 11: Results [15]

CC_i	**Localizations**	**rank**
0,676	Main entrance	2
0,766	Audience space	1
0,016	Stage	5
0,597	Refreshments space	4
0,636	Parking lot	3

8. Discussion

There are many different methods that should be tested in the risk management of soft targets; however, FTOPSIS shows very promising results (Tab. XI). It can easily involve "standard" security managers and specialists and reflect the opinion of all of them. Also, the results were discussed and consulted with experts for soft targets protection. Their professional view confirmed our results. The exact value of risk is not important. Important is the rank in the case of social or cultural events. It is necessary to test this method and approach for other types of soft targets and validate results with others risk analysis methods.

Used method (FTOPSIS) has provided results that are consistent and comparable with practice. Even if this case study was limited by cooperation with only three experts, the results are representative enough. This case study also validates and confirms the utilization of FTOPSIS as a risk analysis. Many other risk analyses have a problem subjective approach of an evaluator. This could be a serious problem when we have different results from different evaluators. This may bring an underestimation of risk, which means, in general, higher risk. FTOPSIS brings a certain amount of objectivity and it should be used without prominent experience in soft target protection.

This article aimed to examine one of the risk analysis methods and test it with other selected methods. As already mentioned, the intention is to find a method that will be simple for experts, quick to use, and above all, objective. But the work of a security expert does not end there. We now know what and where we are in danger and to what extent. Subsequently, it is necessary to start the process of reducing the risk, where we look for various measures to reduce the resulting value of the threat. There are several ways - security measures, insurance, avoiding a given risk, monitoring, etc. The most commonly used are technical and non-technical security measures, by which we understand various security systems, camera systems, and fire protection, but also the setting of processes for how to behave in the event of a security incident, crisis communication, detection of suspicious behavior, training of security and emergency personnel, etc.

9. Conclusion

Risk analysis is about finding and ordering risks. This process is very similar to other decision-making processes and thus, MCDM should be effectively applied to this field. The biggest challenge, as for every decision-making, is correctly defined criteria. A properly set template may save a lot of time, and usage of FTOPSIS could be faster and more time effective than other risk analysis methods based on subjective opinion. On the other hand, FTOPSIS presumes some elementary knowledge of mathematics.

Next research step is case studies and validation on upcoming events. We would like to use MCDM not only for risk analysis but also for prioritization of proposed security measures and evaluation of incidents.

Acknowledgment

This work was supported by the research project VI20192021163 "Built-up and operation development of security systems at mass events", supported by the Ministry of the Interior of the Czech Republic in the years 2019-2021.

References

[1] D. Kotkova, L. Kralik, L. Kotek, "Multiple Criteria Decision-making: Risk Analyses for Cultural Events as one of the Soft Target Categories," in 2021 IEEE International Carnahan Conference on Security Technology (ICCST) 1-6, 2021, doi: 10.1109/ICCST49569.2021.9717382.

[2] D. Lapkova, L. Kotek, J. Nevrkla, K. Jenckova, "Decision support - Tool for customization of security measures for cultural events," in 2020 11th Iberian Conference on Information Systems and Technologies (CISTI), 1-6, doi: 10.23919/CISTI49556.2020.9140917.

[3] D. Kotkova, M. Hromada, T. Sternova, K. Ljubymenko, "Methodology of identification and protection of soft targets of transport infrastructure – initial study," in 2020 Transport Means - International Conference, 1107-1112. 2020.

[4] L. Kotek, M. Hromada, D. Lapkova, "Protection of Soft Targets from Terrorism," in 2019 IEEE 6th Asian Conference on Defence Technology (ACDT), 71-78. 2019, doi: 10.1109/ACDT47198.2019.9072743.

[5] D. Lapkova, L. Kotek, D. Rozek, "Terrorism Situation and Identification of Soft Target's Attractiveness," in 2019 IEEE 6th Asian Conference on Defence Technology (ACDT), 65-70, 2019, doi: 10.1109/ACDT47198.2019.9072875.

[6] D. Lapkova, L. Kotek, D. Rozek, "Counter-terrorism Measures - Determining of Soft Target's Vulnerability," in 2019 IEEE 6th Asian Conference on Defence Technology (ACDT), 79-84, 2019, doi: 10.1109/ACDT47198.2019.9072861.

[7] L. Kotek, M. Hromada, D. Kotkova, "Educational platform for personal and community protection situations from the perspective of soft targets," in 2020 Iberian Conference on Information Systems and Technologies (CISTI), 1-4, 2020, doi: 10.1109/ICCST52959.2022.9896561.

[8] D. Kotkova, K. Jenckova, "DETERMINING OF SOFT TARGET'S VULNERABILITY," in 2019 DAAAM International Scientific Book, 205-214, 2019, doi: 10.2507/daaam.scibook.2019.16.

[9] D. Kotkova, K. Jenckova, "COMPARISON OF MODUS OPERANDI OF TERRORIST'S ATTACKS - VEHICLE RAMMING ATTACK AND FIREARM ATTACK," DAAAM International Scientific Book 2019. Vienna : DAAAM International Vienna, **2019**, s. 191-198. ISBN 978-3-902734-24-2, doi: 10.2507/daaam.scibook.2019.14.

[10] D. Kotkova, T. Sternova, Z. Kalvach, L. Kotek, "The Process to Plan Security Measures for Cultural Events," in 2021 IEEE International Carnahan Conference on Security Technology (ICCST), 1-6, 2021 doi: 10.1109/ICCST49569.2021.9717380.

[11] D. Kotkova, M. Hromada, M. Malanikova, S. Kovar, "The concept of a software tool with an interactive map for identification and determination of soft targets of transport infrastructure," in 2021 IEEE International Carnahan Conference on Security Technology (ICCST), 1-5, 2021 doi: 10.1109/ICCST49569.2021.9717375.

[12] K. Ljubymenko D. Kotkova, T. Sternova, "Use of detection of suspicious behavior in ensuring the security of persons in transport," in 2021 IEEE International Carnahan Conference on Security Technology (ICCST), 1-4, 2021, doi:10.1109/ICCST49569.2021.9717399.

[13] Z. Kalvach, "Definition of Soft Targets," Prague, 2017

[14] T. Sternova, "Vývoj teroristických útoků v období 2014 - 2017. Rozbor vybraných útoků v roce 2017 (Development of terrorist attacks in 2014-2017. Analysis of selected attacks in 2017.)," in The Conference of Security Technologies, Systems and Management, 2017.

[15] Application for database management of terrorist attacks, *DoVA* [online], Prague, 2019.

[16] L. Hofreiter, V. Berezutskyi, L. Figuli, Z. Zvakova, "Soft Target Protection-NATO Science for Peace and Security Series C: Environmental Security," Springer, ISBN: 978-94-024-1754-8.

[17] S. Nădăban, S. Dzitac, I. Dzitac, "Fuzzy TOPSIS: A General View," Procedia Computer Science, **91**, 823-831, 2016, doi: https://doi.org/10.1016/j.procs.2016.07.088.

[18] I. Mahdavi, A. Heidarzade, B. Sadeghpour-Gildeh, "A general fuzzy TOPSIS model in multiple criteria decision making," Int J Adv Manuf Technol **45**, 406 – 420, 2009. https://doi.org/10.1007/s00170-009-1971-5

[19] N. B. Kore, K. Ravi, S. B. Patil, "A simplified description of fuzzy TOPSIS method for multi criteria decision making," International Research Journal of Engineering and Technology (IRJET), **4**(5), 2047-2050, 2017, e-ISSN: 2395 -0056.

[20] G. Kannan, S. Pokharel, P. S. Kumar, "A hybrid approach using ISM and fuzzy TOPSIS for the selection of reverse logistics provider," Resources, Conservation and Recycling, **54**(1), 28-36, 2009 doi: https://doi.org/10.1016/j.resconrec.2009.06.004.

[21] E. Afful-Dadzie, “Hybridized integrated methods in fuzzy multicriteria decision making (with case studies),” PhD Thesis, Thomas Bata University in Zlin, 2013.

[22] B. Vahdani, S. M. Mousavi, R. Tavakkoli-Moghaddam, “Group decision making based on novel fuzzy modified TOPSIS method,” Applied Mathematical Modelling, **35**(9), 4257-4269, 2011, doi: https://doi.org/10.1016/j.apm.2011.02.040.

[23] P. Rani, A. R. Mishra, A. Mardani, F. Cavallaro, M. Alrasheedi, A. Alrashidi, “A novel approach to extended fuzzy TOPSIS based on new divergence measures for renewable energy sources selection,” Journal of Cleaner Production, **257**(1), 120352, 2020, doi:10.1016/j.jclepro.2020.120352.

[24] G. K. Koulinas, O. Demesouka, P. Marhavilas, A. P. Vavatsikos, D. Koulouriotis, “Risk assessment using fuzzy TOPSIS and PRAT for sustainable engineering projects,” Sustainability, **11**, 615, 2019, doi: 10.3390/su11030615.

[25] M. Nazam, J. Xu, Z. Tao, J. Ahmad, M. Hashim, “A Fuzzy AHP-TOPSIS Framework for the Risk Assessment of Green Supply Chain Implementation in the Textile Industry,” International Journal of Supply and Operations Management, **2**(1), 548-568, 2015, doi: 10.22034/2015.1.02

[26] K. Jenckova, “Zajišťování bezpečnosti kulturních akcí za účasti většího množství osob v České republice (Ensuring the safety of cultural events with the participation of a larger number of people in the Czech Republic),” diploma thesis, Police Academy of Czech Republic in Prague, 2019.

[27] D. Kotkova, L. Kralik, “Change Of Soft Target’s Resilience In Time – Case Study,” in 2019 DAAAM International Scientific Book, 199-204, 2019, doi: 10.2507/daaam.scibook.2019.15.

[28] R. F.S.M. Russo, R. Camanho, “Criteria in AHP: A Systematic Review of Literature, Procedia Computer Science,” **55**, 2015, 1123-1132, https://doi.org/10.1016/j.procs.2015.07.081.

[29] M. Behzadian, S. K. Otaghsara, M. Yazdani, J. Ignatius, “A state-of the-art survey of TOPSIS applications, Expert Systems with Applications,“ Volume **39**(17), 2012, Pages 13051-13069, ISSN 0957-4174, https://doi.org/10.1016/j.eswa.2012.05.056.

[30] T. Licek, “Vícekriteriální rozhodování agentů v ekonomických prostředích,” University of Hradec Kralove, 2015, Czechia.

[31] A. Daniel, F. E. Onuodu, “A Fuzzy AHP Model for Selection of University Academic Staff,” International Journal of Computer Applications **141** (2016), 19-26, 2016, doi: 10.5120/ijca2016908969.

[32] R. R. Venkata, “Decision making in manufacturing environment using graph theory and fuzzy multiple attribute decision making methods,“ Springer, 2013, doi: https://doi.org/10.1007/978-1-4471-4375-8.

[33] K. Mela, T.Tianen and M. Heinisuo, “Comparative study of multiple criteria decision making methods for building design,“ Advanced Engineering Informatics, **26**(4), 716-726, 2012, doi: https://doi.org/10.1016/j.aei.2012.03.001.

[34] A. Mardani, E. K. Zavadskas, K. Govindan, A. Amat Senin, A. Jusoh, “VIKOR Technique: A Systematic Review of the State of the Art Literature on Methodologies and Applications,“ Sustainability. **8**(1), 37, 2016, https://doi.org/10.3390/su8010037

[35] Google Maps Available from: https://www.google.com/maps/place/Zl%C3%ADn/@49.2284554,17.6597917,17z/data=!4m5!3m4!1s0x47130cad4c888e0d:0x418d4c16a8ac214f!8m2!3d49.2244365!4d17.6627635

Advances in Science, Technology and Engineering Systems Journal Vol. 8, No. 2, 24-29 (2023)

www.astesj.com

Special Issue on Computing, Engineering and Multidisciplinary Sciences

ASTESJ

ISSN: 2415-6698

Temperature-Compensated Overcharge Protection Measurement Technology

Jin Uk Yeon[1], Ji Whan Noh[2], Innyeal Oh[*,1]

[1]*Sunmoon University, Department of Advanced Automotive Engineering, Asan, Chungnam, 31460, Republic of Korea*

[2]*Korea Institute of Machinery & Materials(KIMM), Yuseong-gu, Daejeon, 34103, Republic of Korea*

ARTICLE INFO

Article history:
Received: 04 November, 2022
Accepted: 05 February, 2023
Online: 11 March, 2023

Keywords:
Battery
Battery Management System
Isolation
Indirect Voltage Measurement
LED

ABSTRACT

Recently, many problems have been caused by battery fires. The existing BMS(Battery Managment System) measured the voltage of each cell of the battery through the physical connection between the battery and the control module. However, if a battery with up to 1000 VDC becomes inoperable due to an external factor, the battery is damaged, and accordingly, a large current of the battery breaks the control unit of the BMS with 5 VDC to 24 VDC, putting the BMS inoperable. If the battery is operated when the bms is in trouble, it poses a risk of battery fire.Recently, as bms technology was announced with a wireless function, battery information could be easily transferred from the outside, so that convenience was maximized, but stability is still weak. This paper physically separated the battery and control module by measuring the battery voltage depending on the strength of the LED by connecting the battery and LED. and furthermore, the measurement error should be less than 1 mV even when the temperature changes. In addition, it was designed to operate at a low output level of 200 μW to 360 μW using the sub-threshold section of the LED.

1. Introduction

Recently, with the development of battery technology, it is widely used in the field of electric vehicles, such as Uninterruptible Power Supply (UPS) & Energy Storage System (ESS), etc., demand for a system using lithium-ion batteries has increased rapidly. Accordingly, the demand for battery management system (BMS), which has a function of controlling and protecting a battery, is increasing [1]. However, as battery fires have recently occurred, many issues have been raised. As a result of the analysis of electric vehicle fire accidents in 2018, about 16 accidents were reported. Fire accidents involving electric vehicles occur during a collision, but they occur during charging, driving, and even parking. Therefore, this study proposes a system to identify the main causes of electric vehicle fire and prevent fire accidents. The battery fire is caused by various factor (same, lack of choice words), such as temperature and humidity of the surrounding environment, battery fire caused by overcharging, etc. [2]. However, most of the causes are that the overvoltage of the battery affects the control unit that uses a low voltage, which destroys the control unit, and accordingly, the control unit cannot react with it, leading to a battery fire. As a representative function of BMS, it monitors the voltage between cells of the battery to support an overcharge protection function and safely performs charging and discharging through battery cell balancing. However, it is reported that the control unit is destroyed due to an imbalance between a battery capable of representing 1,000 VDC or higher and a control unit operating between 1.2 V and 2.4 V, and a fire accident of battery is ensued due to BMS failure. As a fundamental solution, a new BMS system that supports the safe operation of the overcharge protection monitoring system by isolating the high voltage battery and the control module is proposed. The overcharge protection system of the existing battery system is shown in Figure 1. In the structure of Figure 1, for voltage measurement, switch 1 is closed to charge C1, switch 1 is opened, switch 2 is closed to charge C2, and the control unit is ADC(Analog to Digital Converter) and measured with C2 voltage [3]. In this measurement method, when a problem of a high voltage unit including a battery pack occurs, insulation is destroyed in a low voltage unit. Therefore, like the existing BMS, a circuit that monitors the battery voltage without physically connecting the control unit and the battery pack is required. This study applied an indirect measurement technology that measures the voltage without the physical connection between the control part and the battery pack. A circuit that monitors the voltage between battery cells while separating the high voltage and low voltage parts was proposed and implemented using this technology. Systems with detachable structures have some cases mentioned in existing communication circuits [4]. There is also a patent for monitoring voltage by applying a photo sensor, but it was not a technology used for isolation structures [5]. This study

---

[*] Corresponding Author: Innyeal Oh, innyealoh@sunmoon.ac.kr

https://dx.doi.org/10.25046/aj080203

proposes and implements an isolated battery cell monitoring system by applying LEDs and photo sensors.

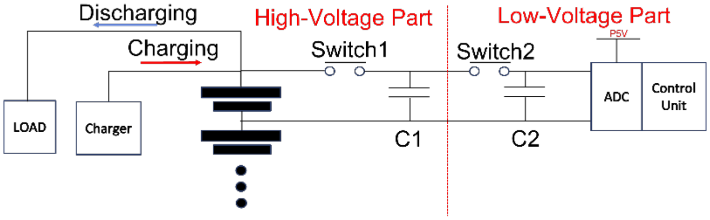

Figure 1: Existing Overcharge Monitoring Circuit [6]

2. Overcharge protection device design

2.1. Battery cell Indirect monitoring

In this paper, an indirect measurement technology of measuring the voltage through a medium without physical connection between a battery pack including a high voltage unit and a control unit is proposed and implemented. Indirect measurement technology is a technology that measures a change in the voltage of a battery by detecting a change in the brightness of an LED. To this end, the light of the LED was prevented from being emitted through the light blocker, and the light was measured using a photo sensor. A block diagram of indirect measurement technology is shown in Figure 2.

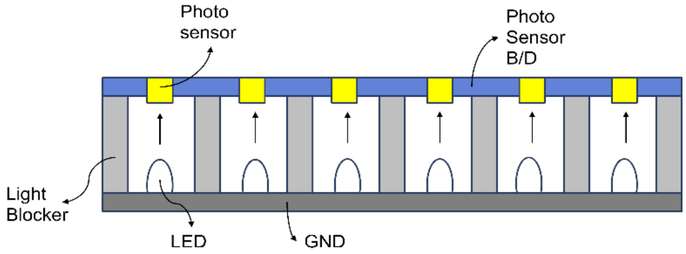

Figure 2: Block diagram of indirect measurement technology [7]

Normally, lithium-ion batteries are known to have an operating range of 3V to 4.3V. However, to measure a voltage using the indirect measurement technology in this paper, an alternative is required because the operating voltage is not matched with the lithium-ion battery. Therefore, this paper proposes an indirect measurement technology that uses a diode array to drop the voltage of the battery and measures the voltage through the corresponding change in the brightness of the LED. Figure 3 shows an indirect measurement circuit.

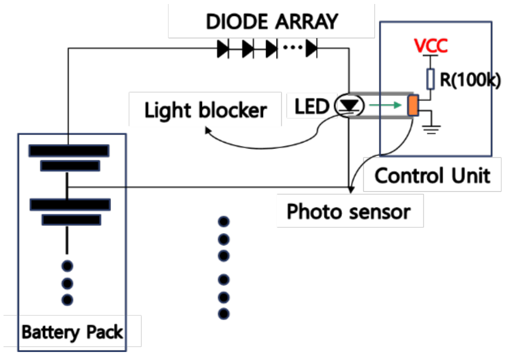

Figure 3: Indirect measurement circuit [7-8]

According to the structure shown in Figure 3, the LED connected to the battery is transmitted to the photo sensor through the light block. The resistance value of the photo sensor changes according to the brightness of light. It is connected to the VCC to measure the voltage applied to both ends of the photo sensor. Since the indirect measurement technology proposed in this paper measures the voltage using a medium, the brightness value of the existing LED is measured and stored in a memory included in the control unit. The voltage is estimated by comparing the brightness value stored in the memory with the currently measured brightness value.

2.2. Isolated LED & Photo sensor characteristics

2.2.1. Sensing characteristics for LED

The indirect battery voltage measurement method proposed in this paper measures the brightness of an LED whose brightness changes depending on battery voltage using an illuminance sensor called Cadmium sulfide (CdS). The resistance of CdS varies with the intensity of brightness. Therefore, the voltage at both ends of CdS is generated through the VCC connected to the front end of CdS, and the voltage is measured through the Analog to Digital Converter (ADC) according to the change in the resistance of CdS. In this paper, the resistance change of CdS measured through ADC is defined as Brightness. Figure 4 shows the graph of the relationship between the battery voltage and brightness measured at room temperature.

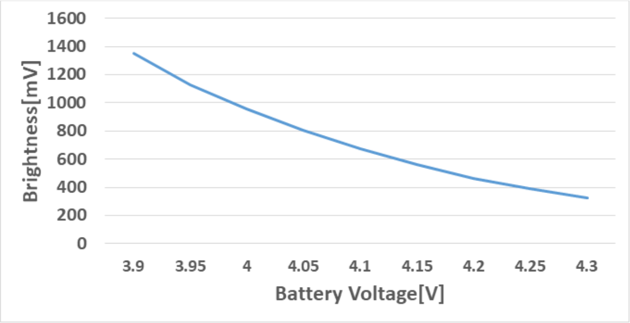

Figure 4: Relationship between Battery Voltage and Brightness

In the graph shown in Fig. 4, it can be found that the relationship between battery voltage and brightness has an inversely proportional relationship. The lithium-ion polymer used for the test in this paper has an operating range of 3.9V to 4.3V. Therefore, it can be confirmed that Brightness has an operation part of 1.3V to 0.3V from 3.9V to 4.3V, which are battery operation parts. In this paper, the voltage was estimated using the aforementioned relationship between the battery voltage and Brightens.

2.2.2 Light source wavelength

The peak spectral response of CdS used in this paper is between 500 nm and 600 nm. Therefore, it is necessary to adjust the spectrum band of the LED used to the spectrum band of the Cds used in this paper. Graphs of the spectrum band of CdS used in this paper and the spectrum band according to the color of LEDs are shown in Figures 5 and 6, respectively.

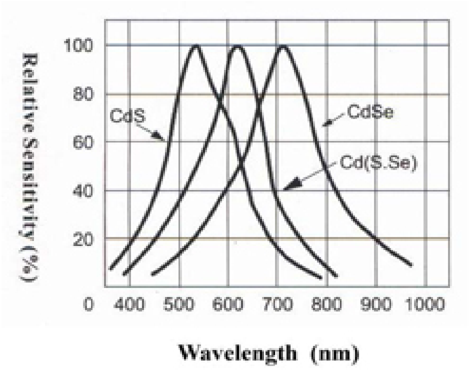

Figure 5: Spectrum band of the CdS [9]

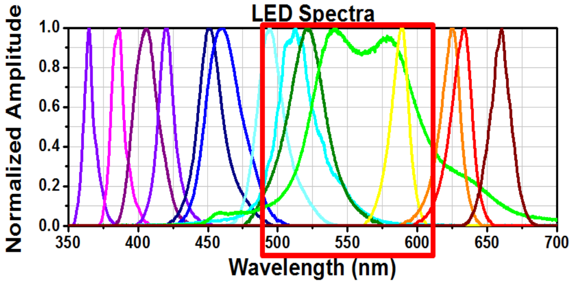

Figure 6: Color of LED according to wavelength [10]

In the graph in Figure 5, it can be seen that the wavelength of CdS is the most sensitive in the characteristics of about 500 nm to 600 nm. On the other hand, the red square box of the relationship between the wavelength length of the LED and the color of the LED in Figure 6 represents LEDs in the wavelength band of 500 nm to 600 nm, which is the wavelength of CdS. The LEDs in the red square box are green LED, blue LED, and yellow LED. Therefore, the LEDs suitable for the wavelength band of CdS, the photo sensor used in this paper, can be said to be Green, Yellow, and Blue LEDs. However, the indirect measurement technology in this paper is a circuit for cell monitoring of batteries, so it shall be possible to accurately measure the battery voltage. On the other hand, the intensity of light in an LED is determined by the current flowing through the LED. Therefore, the circuit including the LED should show a difference in current consumption that can be recognized according to the battery voltage.

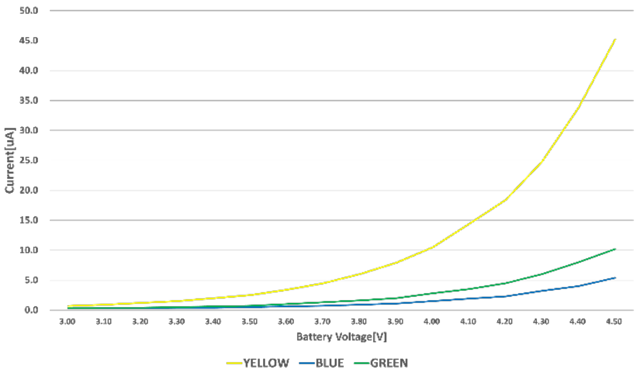

Figure 7: Current consumption according to the LED color

The current consumption graph of each LED is shown in Figure 7. Figure 7 shows the graph of measuring current by connecting 6 diodes of a diode array with LEDs in series. As shown in the figure above, it can be seen that the current of the Blue LED is 0.3 μA ~ 5.4 μA, Green LED is 0.3 μA ~ 10.2 μA, Yellow LED is 0.7 μA ~ 45.2 μA in the 3V to 4.5V Voltage range. Therefore it was confirmed that th Blue LED were not suitable for use in the indirect measurement circuit of this paper.

2.3. Low power behavior design

Since the battery voltage measurement technology operates using battery power, high power consumption leads to degradation of battery performance. Therefore, there is a need for a method to reduce power consumption due to the characteristics of indirect measurement technology that constitute a closed circuit at all times. Therefore, this paper proposes to use the sub-threshold section of LED as an operation section to reduce power consumption of indirect measurement technology. The motion graph of the sub-threshold is shown in Figure 8.

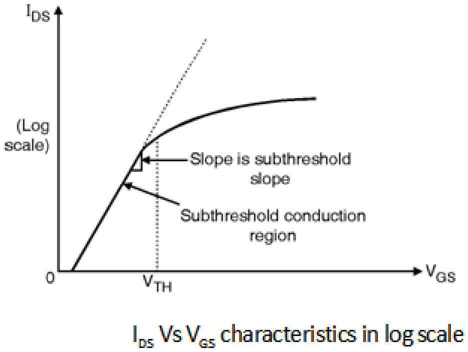

Figure 8: V-I characteristics of LEDs

The structure illustrated in Fig. 8 shows that a leakage current is generated even when a voltage smaller than an operating voltage is applied in a section operated at a point lower than the threshold voltage. The brightness of the light of the LED is proportional to the current and there is a current characteristic curve that changes according to the applied voltage. The general LED usage section is after the operating voltage, and current consumption is high in this section. However, it was confirmed that leakage current occurred even in a low voltage section of 0.7 V or less, and thus current consumption was low and LED was emitting light. It is a known technology in the field of transistor and is being used as a technology called sub-threshold swing. A recent study is also being conducted on the analysis of low-power CMOS inverters using sub-threshold swing [11]. This paper measured the voltage by adjusting the number of diode arrays and lowering the operating range of LEDs to the sub-threshold region. Figure 9 shows the voltage applied to the LEDs according to the number of diodes and the threshold voltage of the LEDs.

The LED used in this paper is the Yellow LED, and the wavelength is 590 nm. Therefore, as shown in Figure 9, the threshold voltage of the LED is about 1.75V to 1.97V [10]. If the voltage of the LED exceeds the threshold voltage, the current rises rapidly, so it should be designed so that the voltage does not exceed the threshold voltage in all sections. Therefore, in this paper, the number of diode arrays was selected and designed so that it does not exceed the Threshold Voltage in all sections, as shown in the structure of the graph in Figure 9.

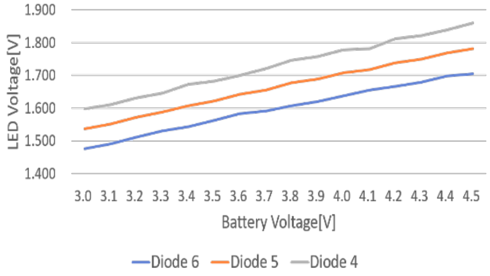

LED Wave length	Threshold Voltage
430	2.69 ± 0.3
565	1.91 ± 0.08
590	1.86 ± 0.11
627	1.83 ± 0.13
700	1.85 ± 0.05
850	1.3 ± 0.18

Figure 9: Voltage of the LED according to the number of diodes & Threshold Voltage of LED [12]

2.4. Temperature compensation

In a universal electronic circuit, the intensity of the current consumed by the elements of the circuit varies with temperature. Therefore, the indirect measurement circuit proposed in this paper also changes the current consumed according to the temperature. On the other hand, LED is a device in which the intensity of light changes according to the intensity of current consumed, so the value of brightness changes according to temperature. The change in Brightness according to temperature is shown in Figure 10.

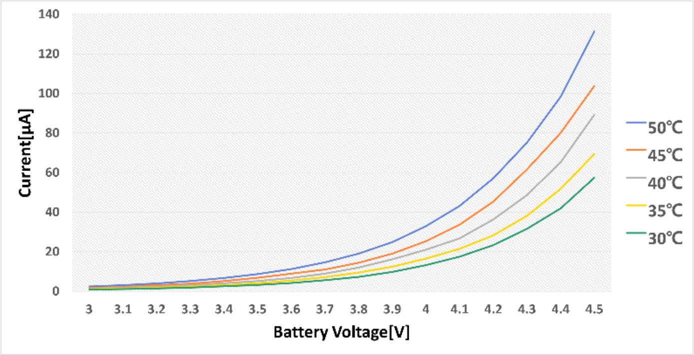

Figure 10: Brightness change according to temperature change of LED

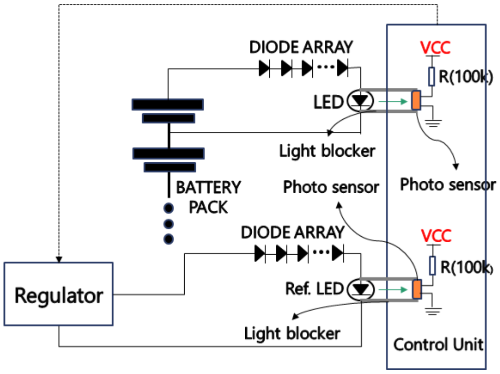

Figure 11. Temperature compensation circuit [8]

The graph illustrated in Fig. 10 shows that the difference in brightness at the same battery voltage at a low temperature and low voltage tends to be large. Therefore, an appropriate temperature compensation circuit is required. This paper measured a temperature corresponding to brightness by connecting a circuit, such as an indirect measurement circuit, with a regulator, and implemented a temperature compensation circuit by applying an offset to the brightness of each LED. The temperature compensation circuit of this paper is shown in Figure 11.

In the circuit shown in Figure 11, a regulator is the power supply that generates the corresponding voltage regardless of external factors, such as temperature, humidity, etc. Therefore, the Ref connected to the regulator. The LED emits corresponding light regardless of external factors. Measure the light using the photo sensor included in the control unit and estimate the temperature using the look-up table stored in the memory included in the control unit. The look-up table is schematized and shown in Figure 12.

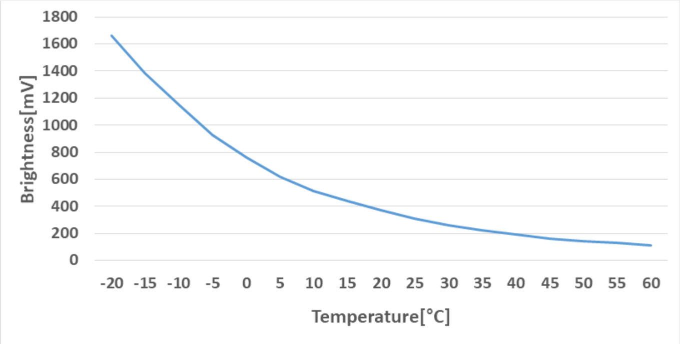

Figure 12: Change of Ref. LED's Brightness

2.5. Structure of Light blocker

With the indirect measurement technology proposed in this paper, it is very important to have a system that estimates a battery voltage by measuring the intensity of light of an LED according to a change in the battery voltage. In this paper, it is defined as a light blocker, a structure that prevents LED light from being emitted. The designed light blocker is shown in Figure 13.

Figure 13: Light blocker

The light blocker in Figure 13 is a structure designed to monitor 36 battery cells. Therefore, it is designed as a structure that can absorb light well so that it does not affect brightness measured according to external light. The light blocker is used in conjunction with the designed Printed Circuit Board (PCB) and can be secured to the PCB through a hole located at the apex of the light blocker. Therefore, it is possible to design so that light does not fade out.

3. Result & Measurement

3.1. Structure of the designed overcharge protection device

Indirect measurement systems are sensitive to the influence of external light. Therefore, it is important to solve structurally so that external light does not affect the indirect measurement system. Therefore, in this paper, the external influence was greatly reduced by designing the PCB of the system in a multilayer structure. The structure of the designed PCB is shown in Figure 14.

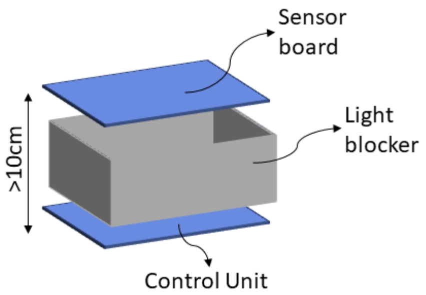

Figure 14: Structure of the designed PCB

In the structure illustrated in Fig. 15, the distance between the sensor board and the control unit was designed to be 10cm or less, so that the light of LED could be transmitted intact, and a size of PCB was designed to be small through the multilayer structure.

3.2. Measurement of overcharge protection device

The designed indirect measurement system is shown in Figure 15. The structure of Figure 15 is 36 LEDs installed in the control unit and 1 Ref. It is a system configured by combining a light blocker on an LED to block light, a photo sensor substrate on it, and a diode array substrate to a control unit. The board shown in Figure 16 is designed to measure the voltage of a total of 36 battery cells. The memory included in the control unit stores a lookup table for the brightness and voltage of the LED.

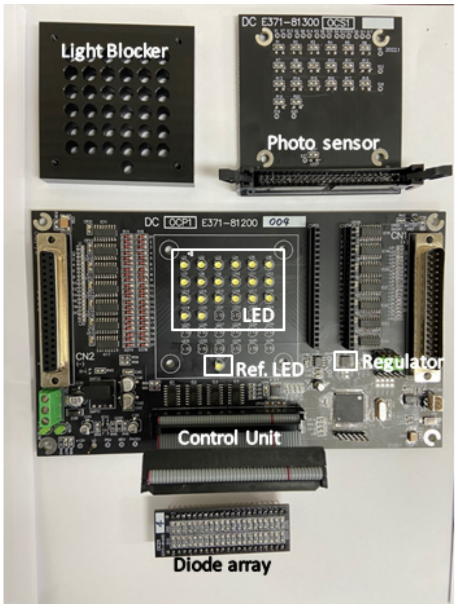

Figure 15: Designed Board

Table 1 shows the average of the values measured more than 10 times by applying a voltage from 3.9V to 4.3V to the LED channel of the designed board. It has an error value of 1 mV at a temperature change of -20°C to 60°C and the electric power amount is about 200 µW to about 360 µW.

Table 1: Results of Overcharge protection board

Battery Voltage[V]	Measured Voltage[V]	Power[㎼]	Current[㎂]
3.919	3.918	211.905	54.067
3.971	3.970	219.975	55.400
4.022	4.021	231.112	57.467
4.071	4.070	244.936	60.033
4.103	4.102	254.523	62.033
4.174	4.172	282.696	67.733
4.204	4.203	398.204	70.933
4.272	4.271	341.333	79.900
4.290	4.289	355.669	82.900

In addition, the comparison results with other papers are shown in Table 2. [4] In the case of , it is not a voltage measurement method used in BMS, but an electric line. Although it is a different application field, voltage measurement technologies in the form of isolation are compared. [13] In the case of , voltage measurement was carried out without physical connection using a wireless transceiver, and the indirect measurement method proposed in this paper measured the voltage using the brightness of light of an LED.

Table 2: Results of comparison with other papers

Paper	Error	Power	temp	Physical connection
[4]	-40~30[mV]	-	-20~40[°C]	O
[13]	5[%]	-	-	X
This work	1[mV]	200~350[㎼]	-20~60[°C]	X

4. Conclusion

This paper proposes and implements an indirect measurement technology that measures voltage without physical connection between battery pack and control unit. Recently, BMS functions for safe battery use have been emphasized [14]. However, it was announced in 2022 as representative of Infineon's BMS (TLE9012DQU) and TI's wireless BMS (BQ79616-Q1), a group that presents advanced BMS technology. Infineon announced wired BMS technology, while TI and Linear Technology implemented wireless capabilities in BMS. The above technologies and this proposed technology are compared and analyzed and shown in the Table 3.

Table 3: Results of comparison with other BMS technology

No	Factor	Infineon BMS (TLE9012DQU) [15]	TI BMS (BQ79616-Q1) [16]	This work		Remark
				Characteristics	Explanation	
1	Physical isolation of high and low	Wired connection	Wired connection	Complete physical isolation	Safed Isolated BMS	Advantage

	voltage parts				Operation	
2	Communication interface with the master board	Wired serial communication	Wireless communication	Wired serial communication	Ease of data delivery	Disadvantage
3	Battery power consumption	20mW	20mW + wireless comm	200~350 [uW]	Low power operation	Advantage

As shown in the Table 3, the existing wireless technology maximizes convenience by providing wireless communication function to the battery so that battery information can be easily received wirelessly from the outside, but it is not implemented as a solution to a battery accident. However, the BMS technology proposed in this proposal is an original technology with a completely different isolation structure and has the advantage of minimizing battery consumption through safe battery operation and low power consumption operation of BMS while implementing BMS. The implemented system can measure the voltage of a total of 36 battery cells, and the voltage used is greatly reduced using the sub-threshold section. It was verified that the voltage measurement error was 1mV or less and the power amount was approximately 200µW to 360µW. In addition, a solution to the error according to temperature was presented using the LED, which is the reference point. Therefore, it can be confirmed that the technology proposed in this paper can have a safe battery monitoring system based on a complete isolation structure and a low power operating structure at the same time.

Conflict of Interest

The authors declare no conflict of interest.

Acknowledgment

This work was supported by a Korea Evaluation Institute of Industrial Technology (KEIT) grant funded by the Korean government (MOTIE) (No. 20022473, Development of 5KWh High-Safety Expandable Battery Module for Electric Vans and Electric Utility Cart)

References

[1] "Battery Management System," https://www.innopolis.or.kr/board/view?linkId=44443&menuId=MENU00999, INNOPOLIS, 2020.03.27
[2] D. Guo, Lei Sun, "The Causes of Fire Explosion of Lithium Ion Battery for Energy Storage," 2018 2nd IEEE Conference on Energy Internet and Energy System Intergration(EI2), Oct. 2018, DOI: 10.1109/EI2.2018.8582017
[3] T. Yue, Liji Wu, "High-precision voltage measurement IP core for battery management SOC of electric vehicles," 2014 12th IEEE International Conference on Solid-State and Integrated Circuit Technology(ICSICT), Oct. 2014, DOI: 10.1109/ICSICT.2014.7021570
[4] A. Hande, S.Kamalasadan, A.Srivastava, "A Selective Voltage Measurement System for Series Connected Battery Packs," Proceeding of the IEEE SoutheastCon 2006, May 2006
[5] D.I. Kim, J.I. Kim "Battery management system," Korean Patent Office,10-2019-0055524, 2021.04.29.
[6] M. Lelie, T.Braun, M. Knips, H.Nordmann, F.Ringbeck, H.Zappen, D.U Sauer, "Battery Management System Hardware Concepts: An Overview,“ Appl. Sci 534, 2018, 8, DOI: 10.3390/app8040534
[7] J.W. Noh, S.H. Ahn, H.S Kang, J.U. Yeon "Voltage Measurement Method, Voltage Measurement Device, and Battery System," Korean Patent Office, 10-2020-0111200, 2020.09.01.
[8] J. Yeon, KunSik Kim, Innyeal Oh,"Temperature-compensated Overcharge protection Indirect measurement circuit," 2022 Thirteenth International Conference on Ubiquitous and Future Networks(ICUFN),2022.07
[9] TOKEN, "CDS LIGHT-DEPENDENT,“ wep-site,PGM5 CDS Phtoresistors, 2010
[10] M.W. Davidson, "Fundamentals of Light-Emitting Diodes (LEDs)," Carl Zeiss Microscopy Online Campus,
[11] R Sindhu, Shilpa Mehta, "Sub-threshold Inverter for Low Power Consumption," 2018 Second International Conference on Inventive Communication and Computational Technologies(ICICCT), Apr. 2018.
[12] F. Santonocito, Antonio Tornabene, Dominique Persano-Adorno, "From led light signboards to the Planck's constant," 2018 Journal of Physics Conference Series, Sept 2018
[13] X. Zhang, Bin Yue, Jian Huang, Yuchuan Ruan, Peng Zhang, "Reserch on Non-contact Voltage Measurement Technology," 2019 IEEE 2nd International Conference on Automation, Electronics and Electrical Engineering(AUTEEE), Nov. 2019, DOI: 10.1109/AUTEEE48671.2019.9033249
[14] K.W. See, Guofa Wang, Yong Zhang, Yunpeng Wang, Lingyu Meng, Xinyu Gu, Neng Zhang, K. C. Lim, L. Zhao & Bin Xie, "Critical review and functional safety of a battery management system for large-scale lithium-ion battery pack technologies," International Journal of Coal Science & Technology, **9**, 2022.05, DOI: 10.1007/s40789-022-00494-0
[15] Infineon, "TLE9012DQU, Li-Ion battery monitoring and balancing IC," Infineon web-site, 2022.02.18
[16] Texas Instruments, "BQ79616-Q1",16-S automotive precision battery monitor, balancer and integrated protector with ASIL-D compliance," Texas Instrumnets web-site, 2022.09, DOI: 10.1109/MSSC.2022.3164853

Advances in Science, Technology and Engineering Systems Journal Vol. 8, No. 2, 30-37 (2023)

www.astesj.com

Special Issue on Computing, Engineering and Multidisciplinary Sciences

ASTESJ

ISSN: 2415-6698

A Multiplatform Application for Automatic Recognition of Personality Traits in Learning Environments

Víctor Manuel Bátiz Beltrán*,[1], Ramón Zatarain Cabada[1], María Lucía Barrón Estrada[1], Héctor Manuel Cárdenas López[1], Hugo Jair Escalante[2]

[1]*Tecnológico Nacional de México campus Culiacán, Culiacán, Sinaloa, 80220, México*

[2]*Instituto Nacional de Astrofísica, Óptica y Electrónica, Tonantzintla, Puebla, 72840, México*

ARTICLE INFO

Article history:
Received: 30 December, 2022
Accepted: 12 February, 2023
Online: 11 March, 2023

Keywords:
Automatic Recognition of Personality
Deep Learning
Web Platform
Standardized Personality Tests
Intelligent Learning Environments

ABSTRACT

The present work shows the development of a data collection platform that allows the researcher to collect new video and voice data sets in Spanish. It also allows the application of a standardized personality test and stores this information to analyze the effectiveness of the automatic personality recognizers concerning the results of a standardized personality test of the same participant. Thus, it has elements to improve the evaluated models. These optimized models can then be integrated into intelligent learning environments to personalize and adapt the content presented to students based on their dominant personality traits. To evaluate the developed platform, an intervention was conducted to apply the standardized personality test and record videos of the participants. The data collected were also used to evaluate three machine learning models for automatic personality recognition.

1. Introduction

This paper is an extension of a discussion paper originally presented in [1]. One of the most widely used and accepted models for determining personality based on written tests are the trait-based models and specifically the Big-Five model. This model is usually represented by the acronym OCEAN where each letter refers to a term that represents each of the five personality traits: Openness to experience, Conscientiousness, Extraversion, Agreeableness and Neuroticism [2].

One of the most relevant efforts regarding the definition of the questions (items, as they are known in the field of psychology) to be used for the Big-Five model, is the one conducted by the International Personality Item Pool (IPIP), which we can consider as a scientific laboratory for the development of advanced measures of personality traits and other individual differences that are in the public domain thanks to its Web site (http://ipip.ori.org/). This site maintains an inventory of thousands of items and hundreds of scales for the measurement of personality traits and is generally based on the studies conducted by Goldberg [3–5].

In recent years, research has been conducted with the aim of implementing automatic personality recognizers through machine learning. These studies have focused mainly on using the Big-Five model to detect apparent personality based on text, voice, or facial features. The main challenge facing these investigations is the difficulty of having a representative dataset, the need to label the images, and the fact that these efforts are typically not in the public domain and therefore it is difficult to reproduce their results [2].

The main contribution of this work is the development of an integrated environment that allows assessing the personality traits of an individual by using a standardized test based on the Big-Five model and allows capturing video interactions in Spanish. Deep learning based automatic recognizers uses these videos and seek to determine the same personality aspects. The above, to be able to evaluate the effectiveness of such automatic recognizers with respect to the standardized test and thus have relevant information to improve the model used by the recognizers that can be integrated into different intelligent learning systems to add new features such as personalized instruction and feedback to students.

This paper is structured in the following order: Section 2 presents related works in the areas of standardized testing and automatic personality recognition; Section 3 presents an analysis of the proposed data collection platform; Section 4 describes the experiments, results, and discussion; and finally, Section 5 presents conclusions and future work.

---

*Corresponding Author: Víctor Manuel Bátiz Beltrán, Email: victor.bb@culiacan.tecnm.mx

https://dx.doi.org/10.25046/aj080204

2. Related Works

In this section we describe some research works related to the area of standardized tests and automatic personality recognition. These works, although separate efforts, are related to elements of the present research and were considered as the foundation for the development and integration of this project.

2.1. Standardized Personality Tests

Studies have shown that one of the best approaches to personality detection is the Big Five model. Its strength lies in the general acceptance that personality traits, although they may exhibit some changes, remain relatively stable throughout a person's life [6].

In recent years, several studies have been carried out that present adaptations to different languages of the items provided by the IPIP, to evaluate their applicability in different cultures, finding positive results. As an example of the above, we found the study conducted in [7] for the adaptation and contextualization of 100 items of the IPIP repository in the Argentine environment, obtaining satisfactory results in their reliability studies, and on the other hand the adaptation made by the authors in [6] for the application of a reduced version of the IPIP questionnaire in French-speaking participants. This version consisted of 20 items in total, where each of the personality traits was evaluated with 4 items, obtaining as a result the confirmation of the cross-cultural relevance of the personality indicators, of the model of the Big-Five in participants with diverse idiomatic and cultural backgrounds.

2.2. Automatic Recognition of Personality

In the field of automatic recognition, several approaches to apparent personality recognition have been proposed in recent years. Some studies have worked on automatic recognition based on textual information, such as information generated by users on social networks like Facebook, Twitter, and YouTube. Such is the case of the study presented in [8] where diverse approaches such as multivariate regression and univariate approaches such as decision trees and support vector machines are analyzed for automatic recognition.

Other studies have worked on the recognition of apparent personality based on the voice of participants. In [9] the authors propose a system based on a convolutional neural network that evaluates a voice signal and returns values for the five personality traits of the Big-Five model. They conclude that the correlation between different dimensions of a voice signal can help infer personality traits.

Likewise, research has been carried out for the detection of apparent personality based on images extracted from videos of the participants, using various models of neural networks [2]. In the research work conducted in [10], the authors present an apparent personality recognition model based on convolutional neural networks using images extracted from short video clips. They conclude that facial information plays a key role in predicting personality traits.

Renewed interest in the world of artificial intelligence and machine learning, as well as the existence of competencies such as those conducted by ChaLearn Looking at People, have helped the development of various neural network models for apparent personality detection based on first impression [2,11].

3. Data Collection Platform

As we are working with sensitive data from individuals, it is important to emphasize that participants are notified that the data collected from the standardized test and the videos are used internally for the experiments by the team of researchers. Therefore, no information that reveals or compromises their identity is published without prior consent. For this purpose, the platform always requests their registration to have their contact information.

3.1. Architecture

Data collection presents a challenge, as we must establish a system for storing and consulting the information. Nowadays, thanks to the advancement of technology, we can develop environments that make use of the Internet and thus be able to reach more people regardless of their location or the device they use to connect to the Internet. Therefore, we chose to develop a cloud platform that would work on any device and that would allow us to store the information in a repository located on the Internet to facilitate the study of the data.

We chose to use a layered architectural model on a client/server architecture. Three layers are defined: presentation, application logic and data. In Figure 1 we can appreciate the logical view of the platform.

The presentation layer shows users a graphical interface that offers them the option of registering with the system or logging in. The presentation layer uses the application logic layer to execute the operations supported by the system. The application logic layer, in turn, connects to the data layer which contains the database that stores the information regarding user identification, IPIP test and automatic recognizer results and in this layer, we have the file storage whose function is to store video files (including audio) related to the users.

The developed application is a cross-platform system hosted on the Internet cloud, using the free hosting offered by Google Firebase as part of its services.

For the development of the user interface, we decided to use React (https://es.reactjs.org/) and for the logic part of the application and storage of information and files, we opted for the free services of Google Firebase. In addition to availability, another advantage of using these services is the support in privacy and data security offered by Firebase, since it is certified in the main security and privacy standards (https://firebase.google.com/support/privacy).

In Figure 2 we can appreciate a partial view of the application of the standardized personality test in the data collection platform. Answering the test is the first step the user must take after logging into the system. The resulting scores are used as the actual values of the participant's personality traits.

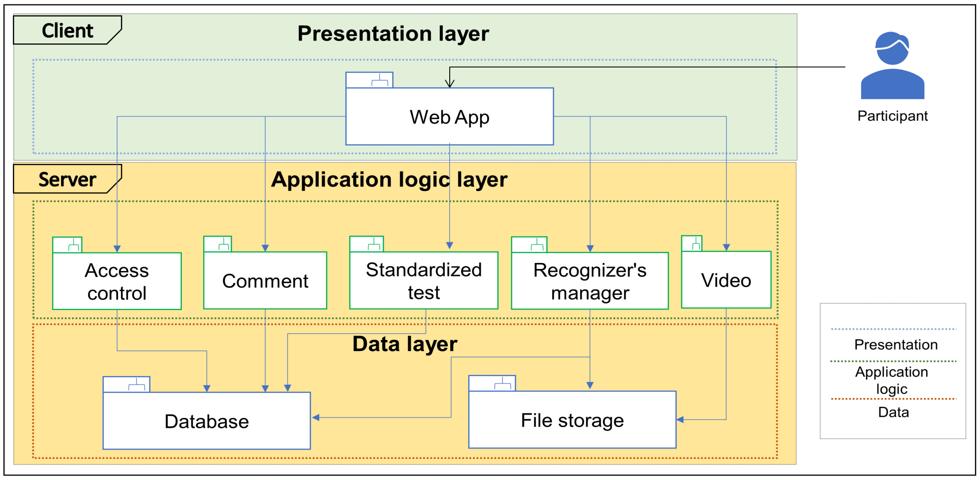

Figure 1: Logical view of the platform.

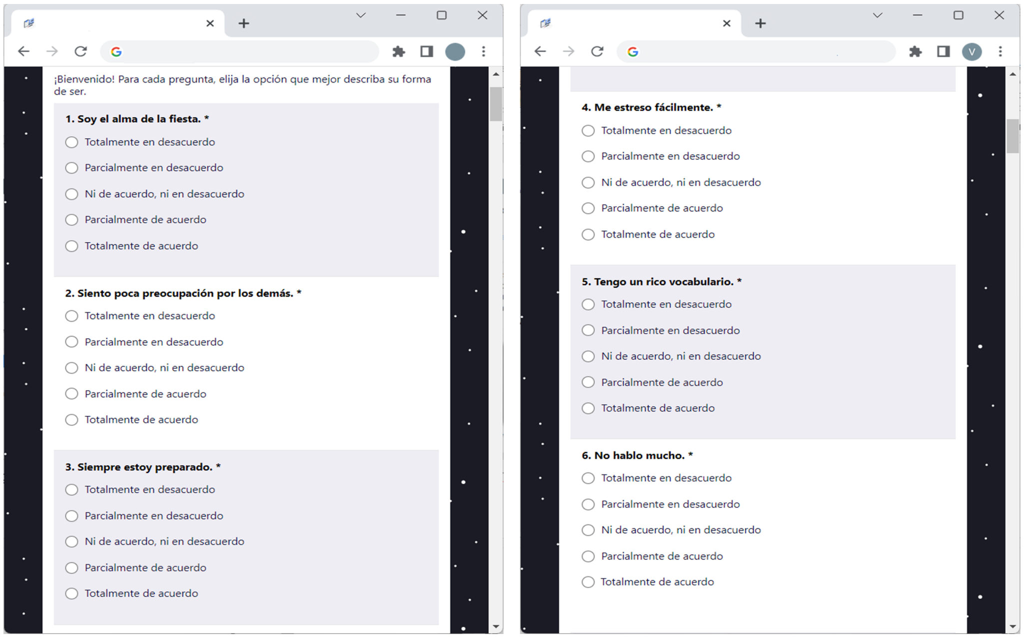

¡Bienvenido! Para cada pregunta, elija la opción que mejor describa su forma de ser.

1. Soy el alma de la fiesta. *

○ Totalmente en desacuerdo
○ Parcialmente en desacuerdo
○ Ni de acuerdo, ni en desacuerdo
○ Parcialmente de acuerdo
○ Totalmente de acuerdo

2. Siento poca preocupación por los demás. *

○ Totalmente en desacuerdo
○ Parcialmente en desacuerdo
○ Ni de acuerdo, ni en desacuerdo
○ Parcialmente de acuerdo
○ Totalmente de acuerdo

3. Siempre estoy preparado. *

○ Totalmente en desacuerdo
○ Parcialmente en desacuerdo
○ Ni de acuerdo, ni en desacuerdo
○ Parcialmente de acuerdo
○ Totalmente de acuerdo

4. Me estreso fácilmente. *

○ Totalmente en desacuerdo
○ Parcialmente en desacuerdo
○ Ni de acuerdo, ni en desacuerdo
○ Parcialmente de acuerdo
○ Totalmente de acuerdo

5. Tengo un rico vocabulario. *

○ Totalmente en desacuerdo
○ Parcialmente en desacuerdo
○ Ni de acuerdo, ni en desacuerdo
○ Parcialmente de acuerdo
○ Totalmente de acuerdo

6. No hablo mucho. *

○ Totalmente en desacuerdo
○ Parcialmente en desacuerdo
○ Ni de acuerdo, ni en desacuerdo
○ Parcialmente de acuerdo
○ Totalmente de acuerdo

Figure 2: Partial view of standardized personality test.

In Figure 3 we can see the interface where participants record a video talking about a topic of their choice.

3.2. *Automatic Recognition of Personality*

As an example of the use of our platform, we have decided to evaluate three automatic recognition models based on deep learning, using convolutional neural networks (CNN), and Long Short-Term Memory (LSTM) neural networks. These automatic recognizers were trained using ChaLearn's personality dataset which contains 10,000 videos with an approximate duration of 15 seconds each one [12]. The following is a description of the architectures of these automatic recognizers.

3.2.1. *Discrete convolutional residual neural network (TNMCUL1)*

The architecture used by this evaluated automatic recognizer (see Figure 4) is a discrete convolutional residual neural network (ResNet). We have our input layer of size 500x500x3.

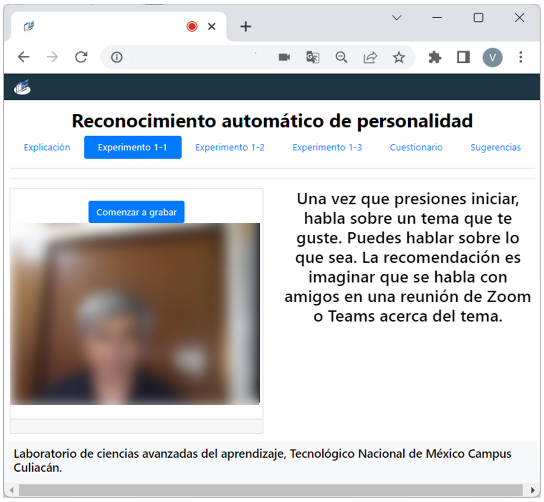

Reconocimiento automático de personalidad

Una vez que presiones iniciar, habla sobre un tema que te guste. Puedes hablar sobre lo que sea. La recomendación es imaginar que se habla con amigos en una reunión de Zoom o Teams acerca del tema.

Laboratorio de ciencias avanzadas del aprendizaje, Tecnológico Nacional de México Campus Culiacán.

Figure 3: Video Recording.

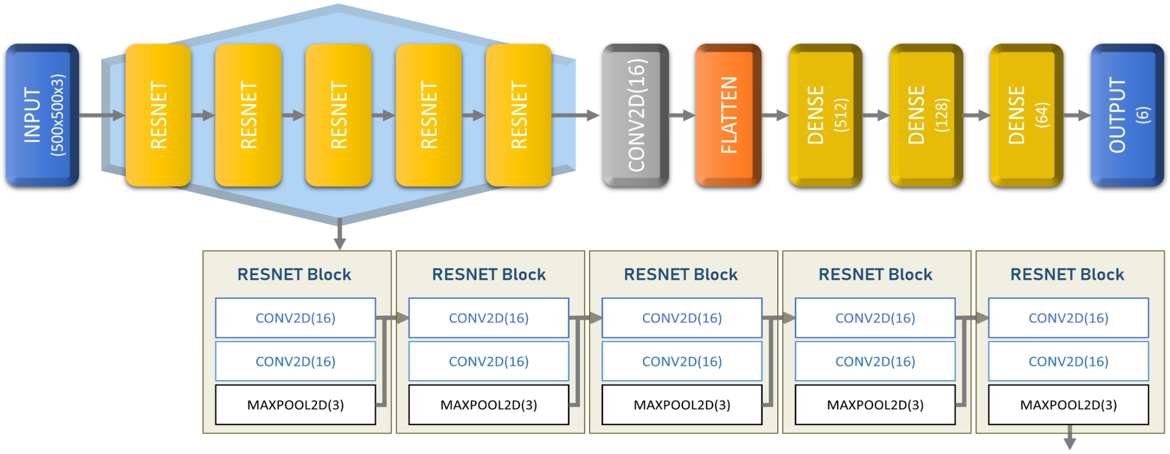

Figure 4: Discrete convolutional neural network topology.

Then we created 5 ResNet modules, where each module contains a two-dimensional convolutional layer (Conv2D) connected to another Conv2D layer, with 16 filters in 3 dimensions in both, and finally connected to a two-dimensional maximum grouping layer (Maxpool2D) with a stride of 3. A concatenation layer was used to add the characteristics of each ResNet block. Then a single Conv2D layer was used with 16 filters in 3 dimensions. We flattened the features vector and connected 4 densely connected layers, each with 512, 128, 64 and 6 neurons respectively. All layers used ReLU activation except the last one that used sigmoid activation for regression. Loss was measured using the mean absolute error (MAE).

3.2.2. Continuous convolutional residual neural network (TNMCUL2)

The second considered architecture is a time-distributed convolutional neural networks. We used sets of 30 images taken from each video creating vectors of dimensions 30x500x500x3. Then, we proceeded to use 5 ResNet modules to process the data from the image vectors and use the attribute vectors created by convolution as input for a 3 layered neural network for feature classification with a 6-neuron output layer for regression.

The full architecture is detailed in this way: first, we used an input layer of size 30x500x500x3. Then, we created a time distributed layer to wrap 5 ResNet modules with the same configuration, as explained on TNMCUL1. Finally, we used a global average pooling 3D layer, a flattening layer for the feature vector, and 4 densely connected layers, with 512, 256, 128 and 6 neurons, respectively. The hidden layers used ReLU activation, and the output layer used sigmoid activation for regression.

This architecture was designed to explore the use of time distributed layers in our study to add another dimension for the previous architecture. We aimed to use the full video image data on a full array, different to our previous architecture that only used individual frames. Figure 5 shows the topology of this neural network.

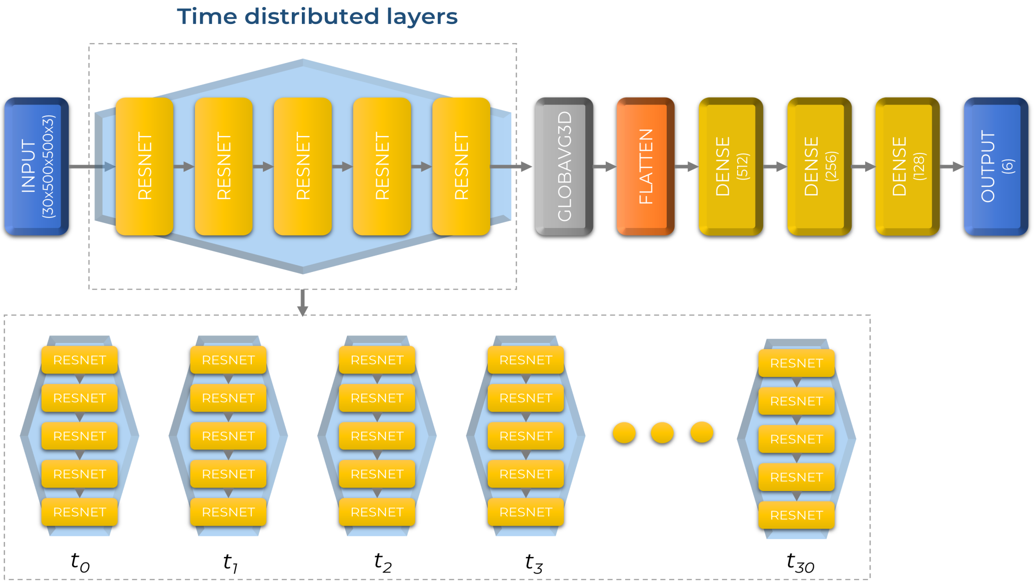

Figure 5: Continuous convolutional residual neural network topology.

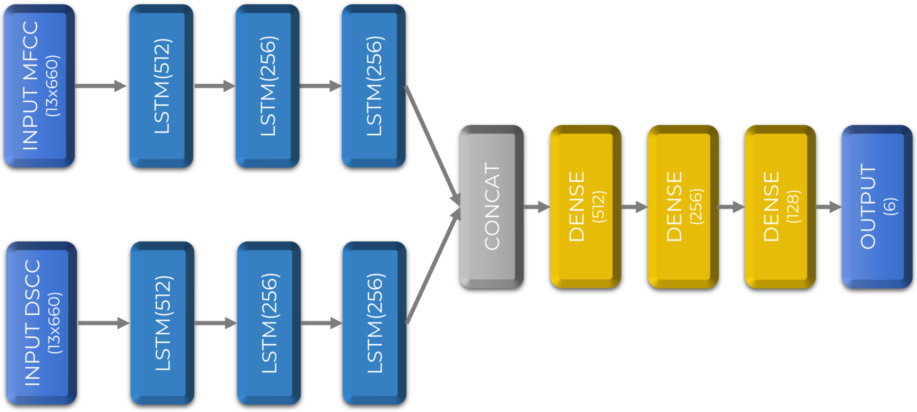

Figure 6: Speech MFCC + DSCC LSTM neural network topology.

3.2.3. Speech MFCC + DSCC LSTM neural network (TNMCUL3)

The third architecture used Long Short-Term Memory (LSTM) neural networks for audio processing. We used an audio file MFCC and DSCC vectors per video, using dual input layers connected to LSTM layers. Then, we used our two feature vectors for feature concatenation and used a 4 layered neural network for feature classification with a 6-neuron output layer for regression.

The full architecture is structured as follows: we used two twin feature extraction LSTM. First, we created input layers for MFCC and DSCC both used as input layers with a dimension of 13x660, connected to 3 LSTM layers of 512, 256 and 256 neurons, respectively. We then used a concatenation layer for the feature fusion and added 4 densely connected layers with 512, 256, 128 and 6 neurons, respectively. The hidden layers used ReLU and the output layer sigmoid activation for the final regression.

This architecture was designed to explore the use of LSTM layers in our study to explore a different modality than the ones used before. We aimed to use only audio data from the videos. Figure 6 shows the topology of this neural network.

Table 1 shows the accuracy results of the three models used (called TNMCUL1, TNMCUL2, and TNMCUL3) and its comparison against state-of-the-art approaches, included in the publications of the best participants in the apparent personality recognition contests based on First Impressions of ChaLearn [11,13]. TNMCUL2 and TNMCUL1 obtained an accuracy of 0.942215 and 0.936158 respectively, slightly surpassing the other models. TNMCUL3 obtained an accuracy of 0.864853, below the rest of the models.

Table 1: Comparison between our models and other state-of-the-art approaches (prepared with our own data and results in [13]).

Name	Technique	Accuracy
TNMCUL2	**CNN Continuos**	**0.942215**
TNMCUL1	**CNN Discrete**	**0.936158**
NJU-LAMDA	Deep Multi-Modal Regression	0.912968
evolgen	Multi-modal LSTM Neural Network with Randomized Training	0.912063
DCC	Multi-modal Deep ResNet 2D kernels	0.910933
Ucas	AlexNET, VGG, ResNet with HOG3D, LBP-TOP	0.909824
BU-NKU	Deep feature extraction with regularized regression and feature level fusion	0.909387
Pandora	Multi-modal deep feature extraction single frame and late fusion	0.906275
Pilab	Speech features 1000 forest random trees regression	0.893602
Kaizoku	Multi-modal parallel CNN	0.882571
TNMCUL3	**LSTM**	**0.864853**

3.3. Standardized Personality Test

For the standardized test we used a 50-item IPIP representation of the markers mentioned by Goldberg for the factorial structure of the Big-Five model [3]. Each of the five personality traits is evaluated by means of 10 items, which in turn are rated by the participant on a 5-element Likert scale (strongly disagree; partially disagree; neither in agreement, nor in disagreement; partially agree and fully agree) based on participant level of agreement or disagreement with respect to each statement displayed. Each option has a value of 1 to 5 points, so 50 is the maximum score per trait. In the end, we convert the score obtained to a value between 0 and 1. This information is stored in the cloud repository and registered to which user it belongs. These values are used to compare them against the results of automatic recognizers.

3.4. Workflow for Data Collection

Figure 7 shows the workflow used for data collection: as a first step, the participant must register on the platform and log in. Once inside the platform, the participant must answer the standardized 50-item IPIP test. Next, the participant must record videos with an approximate duration of one minute each.

The platform stores the recorded videos in our cloud repository. Subsequently, the collected videos are processed and evaluated using the automatic recognizers and the generated information is stored in the cloud repository, linking the corresponding data to each user.

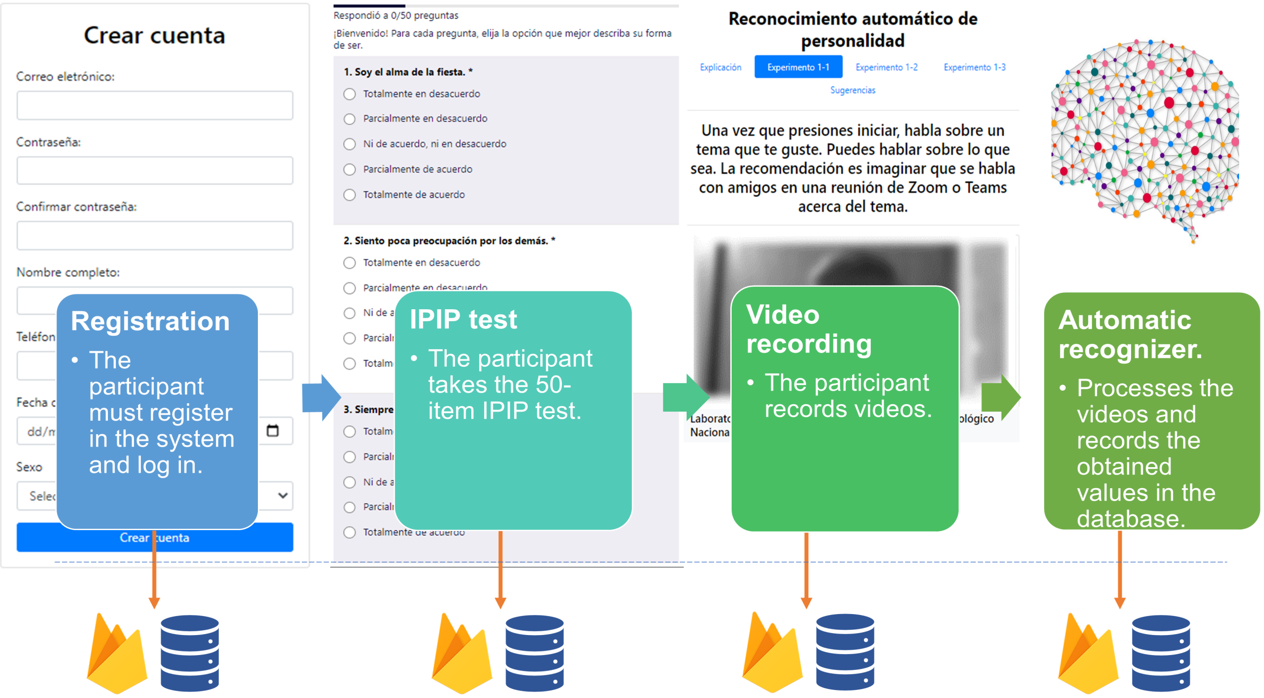

Respondió a 0/50 preguntas

¡Bienvenido! Para cada pregunta, elija la opción que mejor describa su forma de ser.

1. Soy el alma de la fiesta. *

○ Totalmente en desacuerdo
○ Parcialmente en desacuerdo
○ Ni de acuerdo, ni en desacuerdo
○ Parcialmente de acuerdo
○ Totalmente de acuerdo

2. Siento poca preocupación por los demás. *

○ Totalmente en desacuerdo
○ Parcialmente en desacuerdo
○ Ni de a
○ Parcial
○ Totalm

3. Siempre

○ Totalm
○ Parcial
○ Ni de a
○ Parcial
○ Totalmente de acuerdo

Reconocimiento automático de personalidad

Una vez que presiones iniciar, habla sobre un tema que te guste. Puedes hablar sobre lo que sea. La recomendación es imaginar que se habla con amigos en una reunión de Zoom o Teams acerca del tema.

Registration
- The participant must register in the system and log in.

IPIP test
- The participant takes the 50-item IPIP test.

Video recording
- The participant records videos.

Automatic recognizer.
- Processes the videos and records the obtained values in the database.

Figure 7: Workflow for data collection.

4. Results and Discussion

In this section we present the initial experiment, the tests, and the results obtained.

4.1. Data Collection Details

Each participant was invited to answer the IPIP test and then record, for one minute, a video where they were asked to speak freely about any topic. Each video is used to extract the images and audios that feed the automatic recognizers and the results are stored directly in the database.

Table 2: Descriptive Statistics of the IPIP Tests.

Trait	Participants	Mean	Standard deviation
Openness	32	0.7344	0.1450
Conscientiousness	32	0.6844	0.1568
Extraversion	32	0.5969	0.1750
Agreeableness	32	0.7906	0.1376
Neuroticism	32	0.5656	0.2598

4.2. Intervention Results

Thirty-two individuals participated in the intervention with the IPIP test, of whom 15 were male and 17 were female. All participants ranged from 23 to 44 years of age. Table 2 shows the descriptive statistics of the data collected for each of the personality traits. It can be observed that the personality traits with the highest mean value were agreeableness with a mean of 0.7906 and openness with a mean of 0.7344. Both traits also presented the least variation with standard deviations of 0.1376 and 0.1450, respectively. The factor with the lowest mean value was neuroticism.

For the evaluation of the selected automatic recognizers of apparent personality, 84 videos were collected. The videos were the product of the intervention of 21 participants (11 of the original participants did not record a video), of which 13 are male and 8 are female. The age range of the participants is between 23 and 40 years old. Table 3 shows the mean absolute error (MAE) values obtained by comparing each value of the personality traits predicted by the automatic apparent personality recognizers against the corresponding value for the participant based on the IPIP test.

Analyzing the results, it was possible to detect that the mean absolute error (MAE) was lower in the extraversion factor and higher in agreeableness. However, in all personality traits the value is too high, so it is not possible to consider that the automatic recognition models evaluated have made an adequate prediction. An interesting aspect is that TNMCUL3 scores better in 4 of the 5 personality traits. TNMCUL2 scores better in Extraversion.

Table 3: Mean Absolute Error (MAE) of each Personality Trait.

Model	Videos	Technique	Openness	Conscientiousness	Extraversion	Agreeableness	Neuroticism
TNMCUL1	84	CNN Discrete	0.2683	0.2684	0.1941	0.3698	0.2806
TNMCUL2	84	CNN Continuous	0.2483	0.2200	0.1786	0.2200	0.2427
TNMCUL3	84	LSTM	0.2262	0.2150	0.2087	0.2150	0.2426

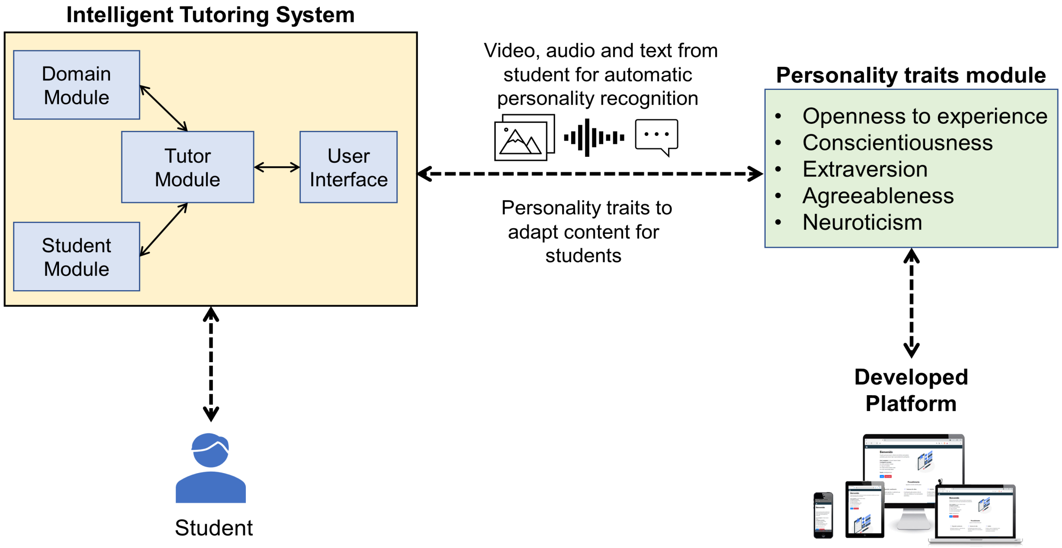

Figure 8: Platform integration with Learning and Tutoring Systems.

4.3. Personality Recognition for Intelligent Learning Environments

Our proposal is to use the information on personality traits and videos collected with the help of the developed platform to evaluate and optimize automatic personality recognition models that can be integrated into intelligent learning environments. The use of an automatic personality recognition model in an intelligent learning environment or tutoring system would allow exploring the idea of presenting adaptive content in real time to the learner based on their dominant personality traits with the goal of achieving the greatest possible impact on learners during their cognitive process.

In Figure 8 we show the proposal to combine an intelligent tutoring system with a personality traits module that makes use of the bank of automatic personality recognizers optimized with our platform.

The learning or tutoring systems communicate with the personality traits module and send it video, image, audio, or text information of the learner which will be used as input to the automatic recognizers. The personality traits module returns as output the presence or absence of the student's Big-Five personality traits. This information can be used by the intelligent tutoring system to make decisions about the content presented to the student.

5. Conclusions and Future Work

The developed platform allows quite a simple and applicable data collection through any device with Internet access from any location and supports the immediate availability of the collected data for analysis.

We have added as a secondary contribution, the evaluation of three automatic recognition models to review the functionality of the platform. In this first exercise, we have found that the evaluated recognizers present a gap in the results with respect to the IPIP test.

The construction of a dataset of Spanish language videos and personality test results is also considered a relevant contribution that can serve as a starting point for future studies.

Additionally, we presented a proposal to use our platform for improving automatic recognizers that could be integrated into tools such as intelligent learning environments or tutoring systems to personalize instruction and feedback based on the detected personality of the participant.

As future work, it is proposed to continue the improvement of the assessed recognizers using the collected dataset and the results of the IPIP tests and hyperparameter optimization techniques. It is suggested to contemplate the evaluation of automatic recognizers of apparent personality based on text to corroborate if the results are like those of the standardized test and, failing that, to work on the retraining of these models, taking advantage of the dataset that is being formed with videos in Spanish.

Another approach that can be addressed is the use of classification algorithms to determine the presence or absence of each personality trait.

Conflict of Interest

The authors declare no conflict of interest.

Acknowledgment

The authors want to thank their institutions for all the support on this research project.

References

[1] V.M. Bátiz Beltrán, R. Zatarain Cabada, M.L. Barrón Estrada, H.M. Cárdenas López, H.J. Escalante, "A multiplatform application for automatic recognition of personality traits for Learning Environments," in 2022 International Conference on Advanced Learning Technologies (ICALT), 49–50, 2022, doi:10.1109/ICALT55010.2022.00022.

[2] J.C.S. Jacques Junior, Y. Gucluturk, M. Perez, U. Guclu, C. Andujar, X. Baro, H.J. Escalante, I. Guyon, M.A.J. van Gerven, R. van Lier, S. Escalera, "First Impressions: A Survey on Vision-Based Apparent Personality Trait Analysis," IEEE Transactions on Affective Computing, **13**(1), 75–95, 2022, doi:10.1109/TAFFC.2019.2930058.

[3] L.R. Goldberg, "The development of markers for the Big-Five factor structure.," Psychological Assessment, **4**(1), 26–42, 1992, doi:10.1037/1040-3590.4.1.26.

[4] L.R. Goldberg, "A broad-bandwidth, public domain, personality inventory measuring the lower-level facets of several five-factor models," Personality Psychology in Europe, **7**(1), 7–28, 1999.

[5] L.R. Goldberg, J.A. Johnson, H.W. Eber, R. Hogan, M.C. Ashton, C.R. Cloninger, H.G. Gough, "The international personality item pool and the future of public-domain personality measures," Journal of Research in Personality, **40**(1), 84–96, 2006, doi:10.1016/j.jrp.2005.08.007.

[6] O. Laverdière, D. Gamache, A.J.S. Morin, L. Diguer, "French adaptation of the Mini-IPIP: A short measure of the Big Five," European Review of Applied Psychology, **70**(3), 100512, 2020, doi:10.1016/J.ERAP.2019.100512.

[7] M. Gross, M. Cupani, "Adaptation of the 100 IPIP items measuring the big five factors," Revista Mexicana de Psicología, **33**, 17–29, 2016.

[8] G. Farnadi, G. Sitaraman, S. Sushmita, F. Celli, M. Kosinski, D. Stillwell, S. Davalos, M.-F. Moens, M. de Cock, "Computational personality recognition in social media," User Modeling and User-Adapted Interaction, **26**(2–3), 109–142, 2016, doi:10.1007/s11257-016-9171-0.

[9] J. Yu, K. Markov, A. Karpov, Speaking Style Based Apparent Personality Recognition, 540–548, 2019, doi:10.1007/978-3-030-26061-3_55.

[10] C. Ventura, D. Masip, A. Lapedriza, "Interpreting cnn models for apparent personality trait regression," in Proceedings of the IEEE conference on computer vision and pattern recognition workshops, 55–63, 2017.

[11] V. Ponce-López, B. Chen, M. Oliu, C. Corneanu, A. Clapés, I. Guyon, X. Baró, H.J. Escalante, S. Escalera, ChaLearn LAP 2016: First Round Challenge on First Impressions - Dataset and Results, Springer International Publishing, Cham: 400–418, 2016, doi:10.1007/978-3-319-49409-8_32.

[12] H.J. Escalante, H. Kaya, A.A. Salah, S. Escalera, Y. Gucluturk, U. Guclu, X. Baro, I. Guyon, J.C.S.J. Junior, M. Madadi, S. Ayache, E. Viegas, F. Gurpnar, A.S. Wicaksana, C.C.S. Liem, M.A.J. van Gerven, R. van Lier, "Modeling, Recognizing, and Explaining Apparent Personality From Videos," IEEE Transactions on Affective Computing, **13**(2), 894–911, 2022, doi:10.1109/TAFFC.2020.2973984.

[13] A. Subramaniam, V. Patel, A. Mishra, P. Balasubramanian, A. Mittal, Bi-modal First Impressions Recognition Using Temporally Ordered Deep Audio and Stochastic Visual Features, Springer International Publishing, Cham: 337–348, 2016, doi:10.1007/978-3-319-49409-8_27.

Advances in Science, Technology and Engineering Systems Journal Vol. 8, No. 2, 38-43 (2023)

www.astesj.com

ASTESJ

ISSN: 2415-6698

Challenges Facing Solar Panel Energy Deployment within Qatari Homes and Businesses

Ayed Banibaqash[*], Ziad Hunaiti, Maysam Abbod

Department of Electronic and Electrical Engineering, Brunel University London, Uxbridge, UB8 3PH, UK

ARTICLE INFO

Article history:
Received: 11 October, 2022
Accepted: 03 December, 2022
Online: 11 March, 2023

Keywords:
Renewable Energy
Solar Energy
Gulf Corporation Council

ABSTRACT

Despite many factors conducive to renewable energy investment in Qatar (e.g., the fact that the state is a major gas exporter whose long-term prosperity depends on economic diversification), there is very low uptake of solar panel adoption among home and business owners. Major challenges implicitly face the deployment of solar and other renewables in Qatar, this research explores possible challenges. The study was conducted in two phases: interviews to identify challenges and using the outcomes from the interviews to obtain a wider response. This study identifies the key major challenges facing the deployment of solar panels in Qatar, which are very useful for diverse stakeholders, policymakers, and future researchers.

1. Introduction

Qatar is a wealthy Gulf Cooperation Council (GCC) country whose national economy is heavily over-reliant on gas exports. It is the world's largest supplier of high-quality natural gas [1]. Qatar has extreme solar exposure throughout the year, making it latently amenable to excellent Renewable Energy (RE) harvesting, particularity solar energy [2]. As shown in Figure 1, Qatar has 4380 overall sun hours annually. July has the highest exposure by month, with an average of 417 hours of sunshine, while February has the lowest, with an average of 312 hours [3]. In addition, the expected value for direct normal irradiance (DNI) is 2,008 kWh per m2 per year, which is around 200 kWh higher than the minimum threshold of 1,800 kWh per m2 per year [2].

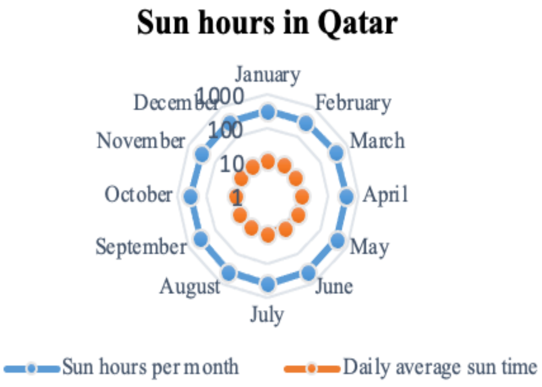

Figure 1. Daily & Monthly Sun hours in Doha, Qatar

According to Qatar 2030 vision, steps are in place to become a global leader in solar power generated RE, including the goal of achieving 2~4 GW of solar energy by 2030, in order to decrease CO2 emissions by 5 MPTA [4]. Nevertheless, the effort of moving towards clean energy in Qatar remains tentative. In 2021 Qatar deployed the first large-scale solar power plant at Al-Kharsaah, 80 km west of the capital Doha, which intends to offer sustainable, affordable, and clean energy through supplying the Qatari grid with an initial of 350 MW power, seeking to reach full capacity in 2022, covering around 10% of national electricity needs and achieving a CO2 emissions reduction of nearly 26 million tons [5].

Solar PV installation in homes and businesses in Qatar could contribute significantly to achieving the national clean energy strategy, as they are the major users of electricity in the country. They could contribute massively to sourcing 20% of energy from non-gas sources by 2030, particularly by operating air conditioning systems during daylight hours using solar panels, but related initiatives have failed to take off [6]. Therefore, this study seeks to identify challenges to solar energy deployment in Qatar's homes and businesses.

2. Solar Energy Projects in Qatar

Qatar aims to create more than 1 GW of renewable energy. It has many ongoing projects, mainly focusing on solar power. For example, the Qatari government has also built a 1000 MW solar PV plant in Doha and the Ras Lafin stadiums, which will feature solar technology cooling for the 2022 FIFA World Cup. Additionally, small-scale research on solar ponds for residential cooling was carried out at Qatar University in 1992 [7]. The Arabian Gulf's high average insolation (solar irradiation) rate of approximately 1800 kilowatts per square meter makes solar energy

---

[*] Corresponding Author: Ayed Banibaqash, ayedahmadaa.banibaqash@brunel.ac.uk

https://dx.doi.org/10.25046/aj080205

the most promising renewable option for the entire Gulf region, including Qatar.

Qatar has started an enormous initiative to develop and install solar energy globally. Qatar has several large-scale solar power projects in the works. For example, Qatar General Electricity & Water Corporation (KAHRAMAA) expects to complete a 200 MW solar power plant by 2020. Pathak and Tribune [8]. It's worth mentioning that Qatar's total power-producing capacity was 8,750 MW in 2013, which was 2,700 MW more than the total demand [9]. Furthermore, Qatar's food security programme has called for long-term water desalination utilising solar energy [9]. There have also been a handful of smaller solar panel installations on commercial building rooftops and parking lot blinds [9].

According to the International Energy Agency (IEA), photovoltaics (PV) will provide 11% of world energy consumption by 2050, resulting in a 2.3 Gt decrease in carbon dioxide emissions per year. Existing structures account for more than 40% of worldwide primary energy use. These earnings are also vulnerable to global economic fluctuations, international commerce, political, social, and environmental issues, and fiercely growing rivalry. Large-scale PV facilities for PV energy conversion are built-in arid places with lots of sunlight [10] hours of light every year, 70% of which is bright, resulting in 6 kWh/m^2 per day [11]. The peak energy consumption in the GCC occurs during the day in August and September when air conditioning usage is at its peak and GSR levels are at their maximum for the year [12].

For PV energy conversion, large-scale in 1992, Qatar University conducted small-scale research on a solar pond for domestic cooling [13]. Due to the high average insolation (solar irradiation) rate of around 1800 kilowatt/h per square metre in the Arabian Gulf, solar energy is arguably the most promising renewable alternative for the whole Gulf area, including Qatar [13]. With an estimated 2200 kWh/m^2/y Direct Normal Irradiance and 2140 kWh/m^2/y Global Horizontal Irradiance, Qatar's insolation rates are suitable for estimating PV and CSP potential which are higher than the Gulf average.

The "Siraj Solar Energy" project, scheduled to produce roughly 700 MW of power in the fourth quarter of 2021, is one of Qatar's major solar projects. According to Qatar's energy minister, in January 2020, the government inked a deal with Total, a French energy powerhouse, and Marubeni, a Japanese company, to develop a solar power plant capable of producing 800 MW, or a tenth of the country's peak energy consumption [14]. The Al-Kharsaah solar power plant, which is Qatar's first large-scale solar power plant, will use cutting-edge solar energy technology such as twin panels to conserve space, automated sun-tracking systems, and robotic solar panel cleaning to boost production efficiency and lower operating costs. It is anticipated to be finished in 2022 [14].

Al-Kharsaah Solar PV Independent Power Producer (IPP) Project is located 80 kilometres from Doha, Qatar's capital, is the country's first large-scale solar power plant (800 MWp), reducing Qatar's environmental imprint substantially. The Qatari grid will be equipped with sustainable, affordable, and clean power starting in 2021 with an initial capacity of 350 MWp before reaching its total capacity in 2022. The project will generate around 10% of Qatar's electricity peak demand and reduce the country's CO2 emissions by 26 million tons [15]. On over 1000 hectares, the solar plant will be built and equipped with 2 million bifacial solar modules with trackers, providing substantial power gains and taking advantage of the region's exceptional solar exposure [14]. The solar facility will cover over 1000 acres and feature 2 million bifacial solar modules with trackers, allowing for considerable power increases and taking advantage of the region's excellent sunshine exposure [15]. The Al-Kharsaah Solar PV IPP Project, with an output of 800 MWp, will span 10 km^2 (approximately 1400 soccer fields) and include 2 million tracker-mounted modules [16]. This will allow for significant power improvements by utilising the region's abundant sunlight.

Furthermore, using 3240 installed string inverters will increase yearly production even more by allowing for better tracking of the highest power point at the string level. A semi-automated solar module cleaning system will be installed at the factory every four days to remove dust and sand from each module. Al-Kharsaah power station has an 800 MWp and is projected to be fully operational in the second half of 2022 [17]. It will be constructed in two stages, each with a capacity of 400 MWp. In its first year of operation (P50 Year 1), it is expected to generate almost 2,000,000 MWh, enough energy to power roughly 55,000 Qatari homes [16]. The project will provide 10% of the country's peak electricity demand at total capacity and cut CO_2 emissions by 26 million metric tonnes throughout its lifetime, making it a watershed moment in the country's energy history [16].

3. Developments Barriers in GCC

This section summarizes possible challenges delaying the development of renewable energy in general and solar energy within the GCC and in particular at Qatar, based on analysing eight notable studies.

The first study comprised an up-to-date assessment of GCC solar energy efforts and listed some recommendations for the following key challenges identified: technical challenges, lack of public/private initiatives, dependency on oil and gas, lack of research and development capabilities, lack of legislation and regulatory framework, and inadequate application of building integrated RE technology [18].

The second study examined issues affecting residential rooftop solar panel adoption in Qatar, analysing public levels of awareness and knowledge towards domestic solar systems. The study reported that there was latent acceptance among the general population for using solar energy, but government initiatives were needed to improve awareness, reduce electricity price subsidies, and increase subsidies for solar energy installations [19].

The third study aimed to look at present situation of pollution and renewable energy in Saudi Arabia as per the national development plan, Vision 2030, which seeks to expand renewable energy use and to present possible obstacles facing the deployment of solar and wind energy. It identified the following major barriers to solar energy use:

3.1. Environmental Challenges

Effect of high temperature on performance of solar system, power loss due to UV rate, effect of humidity on solar panel performance, degradation of performance due to dust, possible damage to solar panels due to dust storms, strong winds, and heavy rain.

3.2. Economics / Managerial Barriers

Low price of natural gas, lack of legal and regulatory framework to support investors, low revenue from renewable energy in comparison to oil, lack of education and training on renewable energy, lack of specialized manpower and issues related to connecting generated renewable to the main grid [20].

The fourth study was conducted to assess the current electricity supply grid in Qatar and to explore the potential of incorporating different renewable energy sources (RES) into the main grid. The study simulation results presented promising possibilities to increase the share of RES in electricity production by up to 80%. Reaching 100% would require the integration of electricity storage systems into the main grid, grid stability and electricity access, availability of significant funding for investment in installations, and effective awareness campaigns [21].

The fifth study aimed to pinpoint the key gaps in the current system and the obstacles facing the development of renewable energy technologies in Kuwait. The study highlighted that Kuwait is unlikely to meet the announced target of 15% of its local energy need from RE generated sources by 2030 due to a lack of effective legal and regulatory frameworks, a lack of support for RE infrastructure, and inadequate financing policies [22].

The sixth study amid to statistically examine the challenges and requirements for renewable energy implementation in the UAE from the opinions of 94 participants. The study found positive attitudes towards governmental efforts and RE infrastructure, and solid public awareness for achieving UAE 2050 RE goals [23].

The seventh study was conducted in Qatar, with an aim to experimentally examine the ecumenical loss due to the solar panels environmental challenge associated with dust. The data from the study showed that without clearing solar panels the output power would be reduced by 43% following six months of exposure to dust with average density of 0.7 mg/m^3, which leads to economic losses if panels remain uncleaned [24].

The eighth study aimed to answer the question of why there is "almost no renewable energy in Oman" and argued that government subsidies for electricity produced from oil and gas resources are a key obstacle to RE technologies development in Oman [25].

It can be summarized from the review of the challenges facing renewable energy in the GCC that they fall within five interrelated key dimensions, as illustrated in Figure 2: technical issues related to the performance of solar panels in the local environment (i.e., dust issues); government initiatives and policies; the low return on investment from RE; low citizen awareness and willingness to adopt renewable energy; and the availability of subsidized electrical energy generated from oil and gas (provided free or at very cheap prices). The key impetus to foster renewable energy in these countries remains with governments; once the right regulations and initiatives are in place, other challenges will dissipate.

Moreover, it can be also concluded that challenges related to; monitoring the execution and sustainability of solar panels energy generation projects, to meet the national and global sited targets might emerge. Therefore, this is need further investigation.

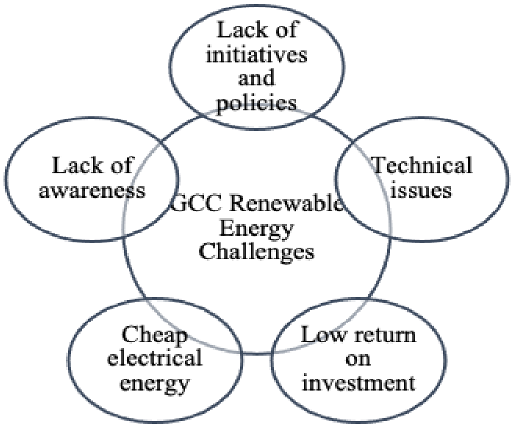

Figure 2. Five key challenges for renewable energy in the GCC countries.

4. Methodology

In order to achieve the main objective of this study, a mixed-method approach was selected, using both qualitative and quantitative methods [26], as illustrated in Figure 3.

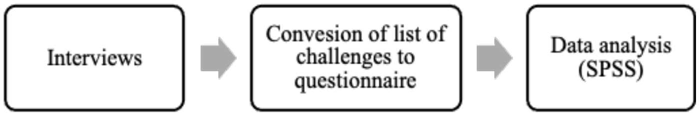

Figure 3. Study research design.

The first method was open-ended interviews conducted by phone with 10 key stakeholders; from the energy sector in Qatar to answer the main question (what the possible challenges are facing the deployment of solar panel energy within homes and businesses) [27]. Qualitative interviews enabled exploring participants' perceptions and experiences in depth, whereby common challenges could be identified from different perspectives. Moreover, the outcomes of these interviews are used to establish the quantitative questionnaire used in the second part of the study. This used Likert-type questions to elicit views from a wider sample, to obtain the opinions of different households and business owners regarding the challenges identified from the qualitative phase. The Likert items assessed participants' level of agreement with the listed challenges, facilitating data analysis [28]. SPSS v.20 is used to analyse the study data, answer its questions, and test its hypothesis [29].

5. Interview Findings

The participants in the interview had the opportunity to see the early listed Five Key Challenges for Renewable Energy in the GCC Countries as showed in Figure 2. Then have been asked two questions. The first question, if they still these challenges are valid for Qatar. While the second question was if they wanted to add any other challenges.

After that, Thematic analysis [30] was the most suitable analysis method to analyse participants' responses from different interview sessions, has been used keeping the first five main themes as listed early and new ten themes have been established, that led to identification of the following common challenges to solar panel adoption among homeowners and business owners in Qatar:

- There is a lack of awareness of renewable energy
- There are safety concerns of solar panel installation
- Solar panels give low return on investment
- The upfront cost of solar panel installation is high
- There is a lack of available solar panel technology
- There are possible cultural barriers to solar panels installation
- There is a lack of interest due to the availability of other sources of energy
- There is a lack of government initiatives
- There is fear of damaging buildings
- There is fear of changes in the look of the building due to installation
- There is a lack of technical support for solar panels
- There are barriers related to connecting generated energy to the main electrical power grid
- Unclear law and regulations governing solar panels
- There is a lack of environmental interest
- Subsidized conventional electricity makes RE uncompetitive

5.1. Findings from Questionnaire

Using SPSS [29] enabled reliability testing of the quality of responses, generating descriptive data with mean and standard deviation (SD) values, to provide a general overview of the results from each group. One-way analysis of variance (ANOVA) was used for comparative analysis between different groups, to establish any significant differences. The following statistical assumptions were used as shown in Table 1.

Table 1: Descriptive statistics of the data.

Descriptive statistics:

Frequencies and percentages: To measure the distributions of the characteristics of the sample members.

Mean: to measure the average answers of the sample members to the questions of the study questionnaire, which used a five-point Likert scale, weighted as follows:

Score	Strongly Agree	Agree	Neutral	Disagree	Strongly Disagree
Approval	5	4	3	2	1
Relative weight	81~100%	61~80%	41~60%	21~40%	1~20%

Length of the period =	Upper ~ lower	=	5 ~ 1	1.33
	The number of levels		3	

Number of levels:

Level	Period
Low	1 ~ 2.33
Medium	2.34 ~ 3.67
High	3.68 ~ 5

Standard deviation (SD): to measure the dispersion of the answers of the sample members from their arithmetic mean

Inferential statistics:

One Way ANOVA

Consistency coefficient (Cronbach Alpha) for the variability of the stability of the study instrument

5.2. Reliability of the Study Sample

To avoid the data collection method shortcomings when participants fill the questionnaire, it was essential to perform reliability of the study sample. Hence, SPSS Cronbach's alpha reliability was test conducted, its impotent that Cronbach's alpha coefficient needs to be at least 0.6, which indicates that the questions from the questionnaire measure the appropriate variables, signifying a consistent and dependable instrument. The Cronbach's alpha coefficient of the survey used in this study was 0.88, indicating good valid for study purposes [4].

5.3. Data Analysis

Participant characteristics (i.e., their status as either home or business owners, or both) are shown in Table 2. It can be seen that the majority of the same were exclusively homeowners (n = 804, 70.5%), a quarter were exclusively business owners (n = 276, 24.2%), and a small proportion (n = 60, 5.3%) owned both homes and businesses.

Table 2: Nature of the Ownership of the Study Sample.

Nature of ownership	**n**	**%**
Business owner	276	24.2
Homeowner	804	70.5
Home and business owner	60	5.3
Total	**1140**	**100.0**

Table 3 shows the means, SDs, percentages, and degrees of participant responses concerning challenges facing the deployment of solar panels in Qatar. The average score for all items (3.38) indicates a medium level of challenges, and most of these related to "a lack of interest due to the availability of other sources of energy, the availability of subsidized conventional electricity, and there is a lack of awareness about renewable energy," which received high scores. The remaining challenges were as follows: "There is a shortage of government initiatives, there is a lack of environmental concern, there is a lack of technical support for solar panels, there are barriers related to connecting the generated energy to the main electric power grid, law and regulations are unclear regarding solar panels, there is the possibility of cultural barriers to the installation of solar panels, the upfront cost of solar panel installation is too high, there is a lack of available solar panel technology, the solar panels give a low return on investment, there is a fear of changes in the appearance of the building due to installation, there is a fear of safety when considering solar panel insulation, and there is a fear of damaging buildings," which got medium degrees of agreement.

Researchers believe that, this result is due to the fact that it is natural and in any country that if there is free availability of electricity or its cost is very cheap, this will be a direct reason for not installing solar panels, so the person will not bear the burden of the cost of installing solar panels, as he will consider it unprofitable for home or business owner in the future, because electricity is available at a cheap cost, and in this case there will be no benefit from installing solar panels in terms of reducing the cost for the user.

Table 3: The Challenges Facing the Deployment of Solar Panels in Qatar.

Challenges	**Mean**	**SD**	**%**	**Degree**
Lack of interest due to availability of other sources of energy	4.03	1.261	80.6	High
Subsidized conventional electricity makes RE uncompetitive	3.74	1.401	74.7	High
There is a lack of awareness of renewable energy	3.68	1.284	73.7	High
There is a lack of government initiatives	3.62	1.275	72.4	Medium
There is a lack of environmental interest	3.52	1.231	70.3	Medium
There is a lack of technical support for solar panels	3.48	1.239	69.7	Medium
There are barriers related to connecting generated energy to the main electrical power grid	3.45	1.255	69.1	Medium
Unclear law and regulations governing solar panels	3.40	1.252	68.0	Medium
There are possible cultural barriers to solar panels installation	3.35	1.344	66.9	Medium
The upfront cost of solar panel installation is high	3.26	1.348	65.3	Medium
There is a lack of available solar panel technology	3.26	1.409	65.3	Medium
Solar panels give low return on investment	3.16	1.309	63.2	Medium
There is fear of changes in the look of the building due to installation,	2.96	1.399	59.2	Medium
There are safety concerns of solar panel installation	2.89	1.302	57.9	Medium
There is fear of damaging buildings	2.87	1.332	57.5	Medium
Average	**3.38**	**0.842**	**67.6**	**Medium**

Table 4: One-Way ANOVA to Test the Study Hypothesis.

	n	Mean	SD	df	Mean Square	F	Sig.
Business owner	276	3.37	0.824	2	0.310	0.438	0.646
Homeowner	804	3.39	0.843				
Combined	60	3.28	0.907				
Total	1140	3.38	0.842				

5.4. Test of Study Hypothesis

To test the study hypothesis (H0): There is no different due to the nature of ownership (at the level of statistical significance $p \leqslant 0.05$) in the degree of challenges facing the deployment of solar panels in Qatar. One-way ANOVA results are shown in Table 4, indicating that the F value is not statistically significant ($p \leqslant 0.05$), so we conclude that the nature of ownership does not significantly affect the degree of challenges facing the deployment of solar panel in Qatar.

The researchers believe that, the reason behind this result is that all people when taking any step towards a specific business, the first thinking will be about the material cost of it and whether there is a need for it and future results that result in financial savings, and this thinking is prevalent among everyone regardless of the nature of ownership, as everyone They will agree on the same challenges that they will face in the event of installing solar panels.

6. Conclusion

As anticipated from the main objective of this study, there are various key challenges facing the deployment of solar panels in Qatar, with no differences in degree according to the nature of ownership. The top five major challenges identified from this study are summarized in Figure 4.

It is clear that these top challenges are in line with the main challenges facing RE in other GCC countries. These and the other challenges remain to be tackled before considering deploying solar panel energy for houses and businesses in Qatar, with a national roadmap toward a sustainable energy profile within the medium to long term. In addition of setting further agenda future research. Moreover, the outcomes from this study can be useful for other stakeholders in other GCC countries to revisit their own challenges and see if new emerged ones are worth consideration.

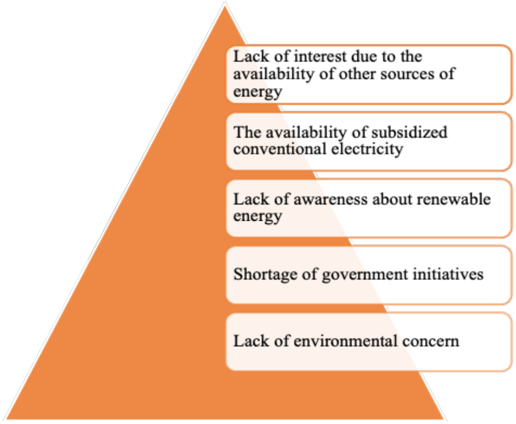

Figure 4. Five key challenges.

Conflict of Interest

The authors declare no conflict of interest.

References

[1] International Energy Agency, "Qatar: Countries & regions," International Energy Agency, 2022. [Online]. Available:

https://www.iea.org/countries/Qatar.

[2] S. Zafar, "Solar energy in Qatar," EcoMENA, 2022. [Online]. Available: https://www.ecomena.org/solar-energy-in-qatar/.

[3] Suncurves, "Sunrise and sunset times for Doha, Qatar," Suncurves, 2022. [Online]. Available: https://suncurves.com/en/v/18533/.

[4] US-Qatar Business Council, Qatar Sustainability Report: A Leader in Green Initiatives. Washington: USQBC, 2020. [Online]. Available: https://www.usqbc.org/public/documents/upload/Qatar%20Sustainability%20Report%20-%20Final.pdf.

[5] Total Energies, "Total to develop Qatar's first large-scale (800 MWp) solar plant," TotalEnergies.com, 2022. [Online]. Available: https://totalenergies.com/media/news/press-releases/total-develop-qatars-first-large-scale-800-mwp-solar-plant.

[6] O.F. Alrawi, T. Al-Siddiqi, A. Al-Muhannadi, A. Al-Siddiqi, and S. G. Al-Ghamdi, "Determining the influencing factors in the residential rooftop solar photovoltaic systems adoption: Evidence from a survey in Qatar," In 8th International Conference on Energy and Environment Research, ICEER 2021, 257-262, 2021.

[7] W.A. Kamal, "A solar pond for air conditioning a small family house in Qatar.", 1992.

[8] S. Pathak, and Q. Tribune, "200MW Solar Power Plant to Be Ready in 8 Years: KAHRAMAA. Qatar Tribune." 2013.

[9] fffB. Guo, W. Javed, B.W. Figgis and T. Mirza, T., "March. Effect of dust and weather conditions on photovoltaic performance in Doha, Qatar." In 2015 First Workshop on Smart Grid and Renewable Energy (SGRE), IEEE, 1-6, 2015.

[10] W.E. Alnaser and N.W. Alnaser, 2020. The impact of the rise of using solar energy in GCC countries. In Renewable energy and sustainable buildings. Springer, Cham. 167-183, 2020.

[11] A. Aksakal and S. Rehman, "Global solar radiation in northeastern Saudi Arabia. Renewable Energy," **17**(4), 461-472, 1999.

[12] J. Meltzer, N.E. Hultman and C. Langley, "Low-carbon energy transitions in Qatar and the Gulf cooperation council region." Brookings papers on economic activity, 2014.

[13] S. Zainaa, S. Sadaf, A. Kunjuc, M. Meraj, D. Unal and F. Touati, "Statistical Assessment of Renewable Energy Generation in Optimizing Qatar Green Buildings." arXiv preprint arXiv:2103.07881, 2021

[14] USQBC Releases, "Qatar Sustainability Report: A Leader in Green Initiatives" - US Qatar Business Council, 2022. [online] Available at: https://www.usqbc.org/news/usqbc-releases-qatar-sustainability-report-a-leader-in-green-initiatives [Accessed 8 Jun. 2022].

[15] Total Energies. "Total to develop Qatar's First Large-Scale (800 MWp) Solar Plant," 2020a [online] Available at: https://totalenergies.com/media/news/press-releases/total-develop-qatars-first-large-scale-800-mwp-solar-plant#:~:text=Qatar [Accessed 8 Jun. 2022].

[16] Total Energies. "Al Kharsaah, a pioneering solar power plant in Qatar." 2022b. [online] Available at: https://totalenergies.com/projects/renewables-electricity/al-kharsaah-pioneering-solar-power-plant-qatar.

[17] S. Riger and R. Sigurvinsdottir, "Thematic analysis. Handbook of methodological approaches to community-based research: Qualitative, quantitative, and mixed methods," 2016.

[18] A.A. Mas'ud, A.V. Wirba, S.J. Alshammari, F. Muhammad-Sukki, M.A.M. Abdullahi, R. Albarracin, and M.Z. Hoq, "Solar energy potentials and benefits in the Gulf Cooperation Council countries: A review of substantial issues," Energies, **11**(2), 372, 2018. [Online serial]. Available: http://dx.doi.org/10.3390/en11020372.

[19] O. F. Alrawi, T. Al-Siddiqi, A. Al-Muhannadi, A. Al-Siddiqi, and S. G. Al-Ghamdi, "Determining the influencing factors in the residential rooftop solar photovoltaic systems adoption: Evidence from a survey in Qatar," Energy Reports, **8**, 257-262, 2022. [Online serial]. Available: http://dx.doi.org/10.1016/j.egyr.2022.01.064.

[20] G. Al-Zohbi and F. G. Al-Amri, "Current situation of renewable energy in Saudi Arabia: Opportunities and challenges," Journal of Sustainable Development, **13**(2), 98-119, 2020. [Online serial]. Available: http://dx.doi.org/10.5539/jsd.v13n2p98.

[21] E. C. Okonkwo, I. Wole-Osho, O. Bamisile, M. Abid, and T. Al-Ansari, "Grid integration of renewable energy in Qatar: Potentials and limitations," Energy, **235**, 121310, 2021. [Online serial]. Available: https://doi.org/10.1016/j.energy.2021.121310.

[22] O.A. Alsayegh, "Barriers facing the transition toward sustainable energy system in Kuwait," Energy Strategy Reviews, 38, 100779, 2021. [Online serial]. Available: http://dx.doi.org/10.1016/j.esr.2021.100779.

[23] Al Shehhi, A., Al Hazza, M., Alnahhal, M., Sakhrieh, A. and Al Zarooni, M., "Challenges and barriers for renewable energy implementation in the United Arab Emirates: Empirical study," International Journal of Energy Economics and Policy, **11**(1), 158-164, 2021. [Online serial]. Available: https://doi.org/10.32479/ijeep.10585.

[24] A. Zeedan, A. Barakeh, K. Al-Fakhroo, F. Touati, and A.S. Gonzales, "Quantification of PV power and economic losses due to soiling in Qatar," Sustainability, **13**(6), 3364, 2021. Available: http://dx.doi.org/10.3390/su13063364.

[25] A. Al-Sarihi, "Why is there almost no renewable energy in Oman?," London School of Economics Middle East Centre Blog, 2017. [Online]. Available: https://blogsdev.lse.ac.uk/mec/2017/01/23/why-is-there-almost-no-renewable-energy-in-oman/.

[26] S.C. Weller, B. Vickers, H.R. Bernard, A.M. Blackburn, S. Borgatti, C.C. Gravlee, and J.C. Johnson, "Open-ended interview questions and saturation," PLOS ONE, **13**(6), e0198606, 2018. [Online serial]. Available: https://doi.org/10.1371/journal.pone.0198606.

[27] Hagen and D. Pijawka, "Public perceptions and support of renewable energy in North America in the context of global climate change," International Journal of Disaster Risk Science, **6**, 385-398, 2015. [Online serial]. Available: https://doi.org/10.1007/s13753-015-0068-z.

[28] P. Hinton, C. Brownlow, and I. McMurray, SPSS Explained. Hoboken: Taylor and Francis, 2014.

[29] U. Sekaran and R. Bougie, Research Methods for Business: A Skill Building Approach (Seventh Edition). London: John Wiley & Sons, 2016.

[30] A. Elrahmani, J. Hannun, F. Eljack and M.K. Kazi, "Status of renewable energy in the GCC region and future opportunities." Current Opinion in Chemical Engineering, **31**, 100664, 2021.

Advances in Science, Technology and Engineering Systems Journal
Vol. 8, No. 2, 44-63 (2023)
www.astesj.com
Special Issue on Computing, Engineering and Multidisciplinary Sciences

ASTES Journal
ISSN: 2415-6698

Hybrid Intrusion Detection Using the AEN Graph Model

Paulo Gustavo Quinan*,[1], Issa Traoré[1], Isaac Woungang[2], Ujwal Reddy Gondhi[1], Chenyang Nie[1]

[1]*University of Victoria, Department of Electrical and Computer Engineering, Victoria, B.C., Canada*

[2]*Ryerson University, Department of Computer Science, Toronto, ON, Canada*

ARTICLE INFO

Article history:
Received: 28 November, 2022
Accepted: 21 February, 2023
Online: 11 March, 2023

Keywords:
Attack fingerprint
Anomaly detection
Intrusion detection system
Subgraph matching
Unsupervised machine learning
Graph database

ABSTRACT

The Activity and Event Network (AEN) is a new dynamic knowledge graph that models different network entities and the relationships between them. The graph is generated by processing various network security logs, such as network packets, system logs, and intrusion detection alerts, which allows the graph to capture security-relevant activity and events in the network. In this paper, we show how the AEN graph model can be used for threat identification by introducing an unsupervised ensemble detection mechanism composed of two detection schemes, one signature-based and one anomaly-based. The signature-based scheme employs an isomorphic subgraph matching algorithm to search for generic attack patterns, called attack fingerprints, in the AEN graph. As a proof of concept, we describe fingerprints for three main attack categories: scanning, denial of service, and password guessing. The anomaly-based scheme, in turn, works by extracting statistical features from the graph upon which anomaly scores, based on the bits of meta-rarity metric first proposed by Ferragut et al., are calculated. In total, 15 features are proposed. The performance of the proposed model was assessed using two intrusion detection datasets yielding very encouraging results.

1 Introduction

The Activity and Event Network (AEN) is a new graph that models a computer network by capturing various network security events that occur in the network perimeter. The AEN has the purpose of providing a base for the detection of both novel and known attack patterns, including long-term and stealth attack methods, which have been on the rise but have proven difficult to detect.

This paper is an extension of work originally presented in the 3rd Workshop on Secure IoT, Edge and Cloud systems (SIoTEC) of the 22nd IEEE International Symposium on Cluster, Cloud and Internet Computing (CCGrid 2022) [1]. In the present paper, we present an unsupervised ensemble intrusion detection mechanism composed of two detection schemes, one signature-based and one anomaly-based, with the goal of leveraging the strengths of both types of detection methods and mitigating their weaknesses.

Signature-based detection, also known as rule-based detection, works by searching data for specific characteristics of previously seen attacks. This makes it good at detecting known attack patterns, but at the same time renders it ineffective when confronted with new and unseen attacks. In contrast, anomaly detection methods rely on the assumption that events deviating from normal usage patterns or behaviours are potentially malicious. This method has the potential to detect novel attack patterns but may generate a large number of false positives due to the fact that atypical events are not necessarily malicious [2, 3].

To validate the scheme, we provide a collection of attack fingerprints covering a small subset of known scanning, denial of service (DoS) and password guessing attacks.

The fingerprints are described using Property Graph Query Language (PGQL) because it provides a standardized language for describing graphical patterns, which we believe makes comprehension easier than describing the fingerprints algorithmically. We also provide a subgraph matching algorithm specifically for finding subgraphs that are isomorphic to the fingerprints.

The anomaly-based scheme, in turn, involves calculating anomaly scores based on the bits of meta-rarity metric introduced by [4] for a set of 15 statistical features and underlying distributions extracted from the AEN graph.

To evaluate the proposed intrusion detection mechanism, we conducted experiments with two datasets: the Information Security and Object Technology (ISOT) Cloud Intrusion Detection (ISOT-CID)

---

[*] Corresponding Author: Paulo Gustavo Quinan, quinan@uvic.ca

https://dx.doi.org/10.25046/aj080206

Phase 1 dataset [5] and the 2017 Canadian Institute for Cybersecurity (CIC) Intrusion Detection Evaluation Dataset (CIC-IDS2017) [6]. First, each of the two schemes were separately evaluated, and then an ensemble classification was created that fuses the two results. The obtained results were promising for both the individual detection schemes and for the combined method.

The remainder of this paper is structured as follows. In section 2, we review the literature on graph-based intrusion detection, anomaly detection and subgraph matching. In section 3 we give a brief overview of the AEN graph. In section 4, we present the fingerprint model and explain how the fingerprints are described and searched for in the graph. In section 5, we provide detail about the anomaly detection model, including a description of the anomaly score calculation and the proposed features model. In section 6, we present the experimental evaluation of the proposed scheme and discuss the obtained performance results. Finally, in section 7, we make concluding remarks.

2 Literature Review

2.1 Graph-based Intrusion Detection

Many different graphical models have been proposed for intrusion detection or forensic analysis. One traditional focus is on non-probabilistic models, such as attack graphs. These include state attack graphs [7]–[9], logical attack graphs [10] and multiple prerequisite graphs [11], each of which aims to either elucidate different aspects of the system or network's security issues or, at a minimum, fix the limitations of the previous models. In general, there are many open challenges when working with attack graphs [12].

Current approaches are plagued by the exponential growth of the graph according to its vulnerabilities and network size, making generation intractable, even for a few dozen hosts. They are limited in scope, and while they provide static information about the attack paths and the probability of a vulnerability exploitation, they do not provide any information about other effective parameters, such as current intrusion alerts, active responses or network dependencies. Furthermore, current attack graphs do not capture the dynamic and evolving nature of the long-term threat landscape. In practice, each change to the network requires a complete recreation of the graph and a restart of the analysis, which means they can only be applied for offline detection.

Another important area of research is in probability or belief-based models used for signature-based intrusion detection such as those employing Bayesian networks (BNs) [13]–[15] and Markov random fields (MRFs) [16, 17]. These models provide good results for the modelled attacks but have some important limitations. The first stems from the fact that the entity being modelled is not the network itself. Instead, the graph is constructed based on predefined features, which limits the extensibility of the models. This is because each new attack type requires the definition of more predefined features that must be incorporated into the graph as new elements. Moreover, these methods require a training phase used to define the graph's probabilities, making them fully supervised methods. Finally, like attack graphs, they need to be reconstructed whenever the graph changes, which can be time consuming, and in practice make them unable to perform online detection.

Moving to anomaly detection applied for intrusion detection, numerous models have been proposed that have used a diverse range of techniques, such as decision trees [18] and neural networks [19]–[21]. These models obtain good performance but suffer from the previously mentioned issues, including necessitating a training phase, requiring multiple rounds of training in some cases, and not supporting online detection. Moreover, despite being anomaly-based, some models have a limited capability to identify novel attacks due to their structure based on predefined features.

In our work we overcame these problems by modelling the network itself. This allows for greater extensibility in describing new attacks because, rather than attack features being predefined, they may be extracted from the graph. Moreover, the AEN graph is fully dynamic and in constant change. Each new subgraph matching operation can be performed against the graph online without the need to recreate it after every change. Finally, the proposed schemes are all unsupervised, which eliminates the need for a training phase.

2.2 Isomorphic Subgraph Matching

Isomorphic subgraph matching is used to search graphs for subgraphs that match a particular pattern. It has been employed extensively in diverse areas, including computer vision, biology, electronics and social networks. However, to the best of our knowledge, our work is the first to employ isomorphic subgraph matching for signature-based intrusion detection.

The general form of this problem is known to be NP-complete [22]; however, its complexity has been proven to be polynomial for specific types of graphs, such as planar graphs [23].

Different algorithms have been proposed for this problem. For example, Ullmann's algorithm [24] uses a depth-first search algorithm to enumerate all mappings of the pattern. Over the years, many improvements have been proposed for that algorithm, such as the VF2 algorithm [25], in attempts to more effectively prune search paths. More modern algorithms, such as the Turboiso [26] and the DAF [27], employ pre-built auxiliary indexes to accelerate searches and facilitate search-space pruning. These algorithms can perform several orders of magnitude faster than index-less algorithms like Ullmann's but require more memory to store the index and also some pre-processing time to build the indexes.

In our work, we leveraged these ideas to design a custom-made matching algorithm specifically to match fingerprints, given the specific characteristics of the AEN and the proposed fingerprints.

3 AEN Graph Overview

The AEN graph was designed to model the variety, complexity and dynamicity of network activity, along with the uncertainty of its data, something that is intrinsic to the collection process, through a time-varying uncertain multigraph. The graph is composed of different types of nodes and edges, with the nodes describing different types of network elements, such as hosts, domains and accounts, and the edges describing their relationships, such as sessions (sets of traffic between two hosts of the same protocol, ports, etc.) and authentication attempts (an account trying to authentication on a host). Furthermore, each element type has different sets of properties, including domain name, account identifier, session protocol and start and stop time. To build such a graph, data from heterogeneous sources (*e.g.* network traffic, flow data) and system and application logs (*e.g.* syslog, auditd) are used.

The graph is built online, with elements added or modified as soon as they are observed in the data and old elements removed once they are considered stale. Consequently, the graph serves as a stateful model of the network, and as such, can be used as a basis for many different types of analyses and inferences. Interested readers are referred to [28] for more details on the AEN graph model's elements and construction.

4 Attack Fingerprints in the AEN Graph Model

4.1 AEN Fingerprints Framework

4.1.1 Attack Fingerprint Visualization

As a visual example of how attack fingerprints can be mined from the AEN graph, Figure 1 shows how certain network activity can create evident patterns in the graph. Specifically, the figure shows a visualization of a subset of a graph generated from an example dataset containing a distributed password guessing attack. The hosts are represented by blue nodes at the center, accounts that were used in authentication attempts are represented by orange nodes and the attempts themselves (edges) are either blue when successful or orange when unsuccessful.

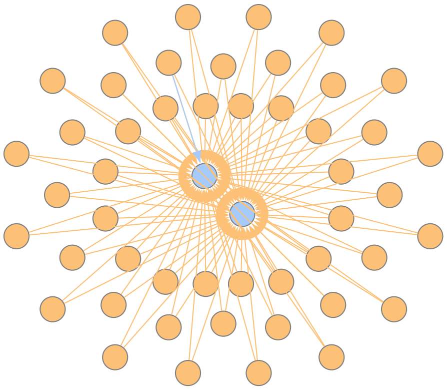

Figure 1: Visualization of an AEN graph containing a password guessing attack.

The figure shows a "cloud" of failed authentication attempts against the two central hosts using the same set of accounts. Furthermore, the majority of the edges are orange, indicating failed attempts, but there is a single blue (successful) edge. This pattern makes evident a successful combined credential stuffing and spraying attack where, after several failed attempts, one login was successful.

Likewise, other types of attacks insert their own distinct attack patterns in the graph. It follows that those patterns serve as fingerprints of these attacks and can, therefore, be mined using subgraph isomorphism matching algorithms to identify instances of an attack.

The statefulness of the AEN plays an important role here because it permits the formation of long term patterns. That is in contrast with traditional intrusion detection systems (IDSs) which can only identify short-term patterns. In the given example, the attack could have been carried out over several weeks, which would have created a challenge for traditional detection mechanisms. In contrast, because the AEN maintains the relationships over a longer term, those patterns can emerge and be identified.

4.1.2 Problem Definition

Given a graph $G = (N_G, E_G)$ where N_G is the set of nodes and $E_G : N_G \times N_G$ is the set of edges, the graph $F = (N_F, E_F)$ is isomorphic to a subgraph $G\prime$ of G if all nodes and edges of F can be mapped to nodes and edges of G. More formally, $F \cong G\prime \sqsubseteq G$ if there is a bijective function $f : N_F \mapsto N_G$ such that $\forall u \in N_F,\ f(u) \in N_G$ and $\forall (u_i, u_j) \in E_F,\ (f(u_i), f(u_j)) \in E_G$.

The definition above can easily be extended to apply to more complex graphs that contain labels and properties, such as the AEN, by applying f to those labels and properties as well.

Finally, the problem of matching a fingerprint is defined as the following: Given an AEN graph G and a fingerprint F, find all distinct subgraphs of G that are isomorphic to F.

4.1.3 Describing Attack Fingerprints

In this study, the attack fingerprints are described using the PGQL query language [29] because it provides a standardized language for describing queries, or patterns, that we wish to search for in a property graph. We believe this makes comprehension easier than when the fingerprints are described algorithmically. This is because PGQL's syntax follows SQL where possible, except that instead of querying tables, it aims to find matches in the nodes and edges of a graph. Doing so requires specific symbols and constructs for that purpose, but is still easily understandable by those who already know SQL.

Other graph query languages, such as Cypher [30], are also descriptive for this purpose but are less like SQL and have a distinct set of supported features. Still, in most cases, PGQL queries can easily be adapted to other graph query languages.

A simple example of PGQL query is as follows:

Algorithm 1: PGQL query example

```
SELECT s, d
  MATCH (s:HOST)-[e:SESSION]->(d:HOST)
  WHERE e.duration > 30
```

The `SELECT` clause specifies what values are to be returned, while the `MATCH` clause specifies the pattern to match. The parentheses are used to describe nodes, while the square brackets describe edges, with the arrow specifying the direction, if any. Inside the brackets, the colon separates the variable name to the left and the optional label, or type, to the right. The above example matches any pattern in the graph that involves two nodes, `s` and `d`, of type `HOST` connected by a directed edge, `e`, of type `SESSION`, from `s` to `d`, whose duration is greater than 30, and then returns the two nodes for each match.

In general, PGQL allows for a rich description of graph patterns; however, it has limitations which make it impossible to fully express certain attack patterns and, in particular, the information we wish to retrieve from it. For our specific use case, PGQL has the following key limitations:

1. Subquery is not supported in the FROM clause.

2. There is limited array aggregation support: In some cases, it is desirable to group matches by destination (the victim) and get an array of sources. However, the current PGQL specification supports only array aggregation of primitive types in paths (using the `ARRAY_AGG` function). Therefore, only properties like IDs can be aggregated in this way. Note that there are some cases where only the `LISTAGG` function is supported. In those cases, we use the `ARRAY_AGG` function to substitute for `LISTAGG` as if the former had similar support as the latter for simpler pattern description.

To overcome these limitations, the fingerprints contain a post-processing phase during which the query results are processed to reach a final match result.

4.1.4 Attack Fingerprint Matching

Finding matches to fingerprints in the AEN graph requires the application of an isomorphic matching algorithm. How this is accomplished depends on the graph engine used to store the AEN graph.

In engines that natively support PGQL, such as PGX and Oracle's RDBMS with the OPG extension, the fingerprints can be used directly to query the database, with only the post-processing phase requiring further implementation. In this case, the matching algorithm is implemented by the graph engine itself.

Similarly, in engines that support other graph query languages, such as neo4j, the fingerprints need first to be converted to the supported query language, but after that, only the post-processing phase requires implementation.

In contrast, when using any graph engine that does not support a graph query language, the whole fingerprint matching algorithm must be implemented. There are several general isomorphic matching algorithms, including Ullmann's algorithm [24] and its derivations (*e.g.* VF2 [25]), the Turboiso [26] algorithm and the DAF [27] algorithm. However, the specific characteristics of the AEN graph and the proposed fingerprints means that a simpler searching algorithm can be employed.

Specifically, the small diameter of the fingerprints means that recursion or any type of partial matching is unnecessary, while the types and properties of the nodes and edges allow for large swathes of the search space to be quickly pruned. In practice, the custom graph engine implemented for the AEN speeds up searching at the cost of extra memory by maintaining separate sets of nodes per type, as well as separate sets of edges per type and per source and destination pair. This can be considered analogous to the indexes employed by the general algorithms mentioned previously, such as the Turboiso and the DAF.

Consequently, finding pairs of nodes per type and edges between them is a constant-time operation. Conversely, iterating the set of edges or groups is done linearly because no index per property is maintained. However, this operation can be trivially parallelized. Aggregating values, such as summing up properties of elements in groups, must also be done linearly.

A generic fingerprint matching algorithm equivalent is presented in Algorithm 2. The algorithm starts by pairing nodes of the desired types (note that each pair is directed). Then, for each pair, it finds all edges between the source and the destination nodes. For each of those edges, the `matches` function is used to test whether the edge matches all of the `WHERE` clauses of the fingerprint and then accumulates the matching edges.

Afterwards, edges are grouped into sets according to the `GROUP BY` expression specified in the fingerprint. Subsequently, each set (group) is tested for matches to all of the `HAVING` clauses of the fingerprint. If true, the results are extracted from the elements in the set based on the `SELECT` expression. These results map to what is returned by the PGQL queries.

Algorithm 2: Generic fingerprint matching algorithm

```
pairs ← pairNodes(nodes, srcType, destType)

matched ← {}

foreach pair in pairs do
  s, d ← pair
  edges ← getEdges(s, d, edgeType)

  foreach e in edges do
    if matches(e, whereClauses) then
      matched ← matched ∪ {e}

groups ← group(matched, groupingExpr)

preResults ← {}

foreach g in groups do
  if matches(g, havingClauses) then
    gr ← extractPreResult(g, selectExpr)
    preResults ← preResults ∪ {gr}

return preResults
```

As mentioned previously, many fingerprints also require a post-processing phase, for which Algorithm 3 is the generic algorithm used. It returns a set of matches of the fingerprint as described in the respective section of each fingerprint.

Algorithm 3: Generic fingerprint post-processing phase algorithm

```
postProcGroups ← group(preResults,
    postProcGroupingExpr)

results ← {}

foreach ppg in postProcGroups do
  if matches(ppg, postProcClauses) then
    r ← extractFinalResult(ppg,
        postProcSelectExpr)
    results ← results ∪ {r}

return results
```

Finally, as explained in the following sections, some fingerprints employ the sliding window algorithm to define time windows. In those cases, Algorithms 2 and 3 are applied for each time window separately, although it would be straightforward to apply the post-processing phase to the combined results of all time windows and group them accordingly. Because the consecutive time windows share some elements, it is possible that the same results will appear on different windows. Therefore, an optional final step when the sliding window is used is the deduplication of results in different time windows, which can be applied to the results returned by Algorithm 3.

Also, to speed up searching in those cases, the sets of edges between nodes are sorted by the desired sliding property so that the start and end indexes of each window can be quickly identified through the application of a binary search. Moreover, the algorithm maintains a cursor to the initial position of the previous window so that older elements do not need to be searched.

4.2 Scanning Attacks

Scanning attacks consist of probing machines for openings that can be further explored for vulnerabilities and then exploited. They are part of the initial information gathering phase of an attack.

These attacks can target a variety of protocols and applications but are most commonly employed for scanning TCP and UDP ports [31]. They can be deployed by a single source or be distributed among several attackers. In addition, there are many different techniques used for scanning, with each focusing on different layers and using different methods to avoid detection [32, 31].

Scanning attacks can be classified based on several different properties. With regard to their footprints, they can be classified into three major types [32]:

- Vertical scan, which scans multiple ports on a single host
- Horizontal scan, which scans the same port across multiple hosts
- Block scan, which is a combination of both vertical and horizontal scans, whereby multiple ports are scanned across multiple target hosts

With regard to their timing, they can be classified as a slow scan or a fast scan, with the latter being easier to spot than the former, given its speed and short duration [33].

In the following, we propose a fingerprint for single-source fast vertical scans. Fingerprints for other types of scans can be derived by slightly modifying the fingerprint parameters as demonstrated in subsection 4.3 for the different DoS attacks.

As already mentioned, vertical scans target a specific host by sweeping across the port space, looking for open ports and running services. Unique characteristics can be summarized as follows [31]:

- The packets are sent from one source host to one destination host.
- The packets have several different destination ports.
- The amount of data/bytes exchanged is never large. For TCP scans, for instance, connections are almost never even established.
- The time frame of each single session is very short.

Taking into consideration these characteristics, we can define a typical attack as one with a short duration and a small amount of data exchanged, particularly from the victim. Otherwise the attack would be too heavy and easier to spot, but with a large number of ports involved. This definition can be described by the following fingerprint:

Algorithm 4: Fingerprint for scanning attack

```
SELECT s, d
  MATCH (s:HOST)-[e:SESSION]->(d:HOST)
  WHERE e.destSize < sizeThr
    AND e.duration < durThr
  GROUP BY s,d
  HAVING count(DISTINCT e.destPort) > portThr
```

where:

- `destSize` corresponds to the cumulative size of the packets of the session sent by the destination of the session, which in this case is the target host;
- `sizeThr` defines a threshold for a maximum expected `destSize`;
- `duration` corresponds to the total time duration of a session;
- `durThr` defines a threshold for a maximum expected `duration`;
- `destPort` corresponds to the target ports; and
- `portThr` defines a threshold for the minimum number of distinct destination ports.

When applied, the fingerprint returns all pairs of source and destination hosts where the sources and destinations correspond to the attackers and the victims, respectively, according to the aforementioned characteristics.

4.3 Denial of Service

DoS is a family of attacks that aim to disrupt the service of a target server or network resource and make it completely or partially unavailable to users. They are broadly divided into two categories [34, 35]:

- Volumetric attacks, where the target is inundated with huge amounts of traffic that overwhelm its capabilities. These include most flood attacks and amplification attacks.
- Semantic attacks, also known as resource depletion attacks, where weaknesses in applications or protocols are exploited in order to render a resource inoperable without requiring the same large volume of traffic as pure volumetric attacks. These include attacks like TCP SYN flood and slow-rate attacks like Slowloris [36].

Based on the source of attack, DoS attacks can be single-source or distributed, in which case they are commonly referred to as distributed DoS (DDoS). In this section, we use DoS to refer to both types.

Another common characteristic of many DoS attacks is that the source IP address can be spoofed in order to hide the true source of the attack and to deflect replies away from the attacker. This introduces asymmetry into the traffic load between the attacker and the victim [37, 38]. In other words, the IP addresses identified by the fingerprints as sources of attacks might be spoofed IP addresses in many cases.

In this section, we focus on selected flood attacks covering both categories of DoS attacks under different layers of the OSI model, specifically layers 3 (network layer), 4 (transport layer) and 7 (application layer).

The fingerprints follow a basic pattern of counting the number of matching sessions of a specific attack type within a short time frame. For this reason, we employed a sliding window mechanism with large overlaps between each window and applied the fingerprints separately for each window. Sliding windows were used instead of simply slicing the timeline so that any short duration attack that would otherwise be divided between two windows could be fully inside at least one window. This had no effect on long duration attacks, as they would fully cover at least one window regardless. In the fingerprints, the start and end times of a time window are represented by `twStart` and `twEnd` parameters, respectively.

4.3.1 ICMP ping flood

ICMP ping flood is an attack where a high volume of ICMP echo/ping requests are sent to a target IP address in the expectation of flooding the victim with more traffic than it is capable of handling [38].

Based on this, we identified the primary typical characteristics of an ICMP ping flood as the following:

- The attacker host sends a large number of ping requests (i.e. ICMP packets) to the target host.
- The packets correspond to echo requests and replies and thus are small.
- The time frame for any single session is very short.

These characteristics can be expressed by the following fingerprint:

Algorithm 5: Fingerprint for ICMP Flood DoS attack

```
SELECT s, d, count(e)
  MATCH (s:HOST)-[e:SESSION]->(d:HOST)
  WHERE e.protocol = 'icmp'
    AND e.destSize < sizeThr
    AND e.startTime > TIMESTAMP 'twStart'
    AND e.stopTime < TIMESTAMP 'twEnd'
  GROUP BY s,d
  HAVING count(e) > sessionThr
```

where `sessionThr` defines a threshold for the minimum number of distinct sessions to trigger the fingerprint.

The query returns the number of sessions between each pair of hosts matching the defined conditions, where the source is the attacker, or the spoofed host, and the destination is the victim. These results might be enough for single-source attacks, but to obtain a final result for distributed attacks, they need to be further processed.

This post-processing step is completed by aggregating the results for each destination host in each time window and applying a further threshold, `cntThr`, on the aggregated count (sum) of matching session per destination. The final result is then a set of attack instances, each one containing the victim host, the cumulative sum of matching sessions and a set of attacker hosts.

Since each time window is considered separately, longer attack instances can end up being reported repeatedly in multiple adjacent windows. To improve on that, the results can be deduplicated by aggregating the results of a same target that fall in contiguous windows.

4.3.2 IP Fragmentation Attack

IP packet fragmentation is a normal event whereby packets larger than the maximum transmission unit (MTU) of the route (normally 1500 bytes) are fragmented into smaller packets that are reassembled by the receiver. A problem arises when systems have trouble reassembling the packets or will expend too many resources doing so. Attackers take advantage of the siturations by crafting special fragmented packets that are impossible to reassemble, causing targets to either crash due to related bugs or to expend more and more resources trying to handle the reassembly of these degenerate packets [35, 39].

Different protocols can be used for fragmented attacks, including UDP, ICMP and TCP. Moreover, fragmented packets can be used to deceive IDSs by crafting fragmented packets that are rejected by the IDS but not by the end system, or vice versa, such that the extra or missing packets prevent the IDS from identifying an attack it otherwise would [39].

From that, we identified the general characteristics of an IP fragmentation attack as follows:

- A medium to high absolute number of fragmented packets can be observed.
- The ratio of fragmented packets to all packets is high.
- The time frame of a single session is very short.

To be able to capture the ratio of fragmented packets, we introduced two properties to the session edge: one that tracks the number of packets, `pktCnt`, comprising the session and another that tracks the number of fragmented packets among those, `fragPktCnt`.

The fingerprint can be expressed as the following query:

Algorithm 6: Fingerprint for IP Fragmentation attack

```
SELECT s, d, count(e), sum(e.fragPktCnt)
  MATCH (s:HOST)-[e:SESSION]->(d:HOST)
  WHERE e.fragPktCnt / e.pktCnt > fragRatioThr
    AND e.startTime > TIMESTAMP 'twStart'
    AND e.stopTime < TIMESTAMP 'twEnd'
  GROUP BY s, d
  HAVING count(e) > sessionThr
```

where `fragRatioThr` defines a threshold for the minimum ratio of fragmented packets to all packets of each session that is considered to be matching the fingerprint.

As before, this query returns the number of sessions matching the defined conditions between each pair of hosts, where the source is the attacker and the destination is the victim. In addition, it also returns the sum of the fragmented packet counts from all grouped sessions.

A post-processing phase is included where the results are aggregated by destination host in each time window so that distributed attacks can be identified. A further threshold, `fragPckCntThr`, was applied to the aggregated sum of fragmented packet counts to guarantee that normal absolute amounts of fragmented packets exchanged between hosts are filtered out.

The final result is then a set of attack instances, each containing the victim host, the cumulative sum of matching sessions and fragmented packet counts, and a set of attacker hosts.

Finally, a deduplication step can also be executed to combine instances from adjacent time windows.

4.3.3 TCP SYN Flood

TCP SYN flood attacks exploit the three-way TCP handshake process by sending a large volume SYN requests to a target host without ever completing the handshake process with the expected ACK requests. This causes the target server to hold multiple partially initiated connections, eventually filling its connection buffer and thus preventing subsequent real connections from being established. In some cases, this will result in crashes due to unhandled resource starvation [37].

Therefore, for this attack, we needed to keep track of the state of the TCP connection. After the initial SYN packet is sent and a session is created, we defined four possible states for the connection, with the first three mirroring the TCP states related to connection establishment [40], only with a slight change of semantics because the client and server states are combined:

- `SYN_SENT`: The initial session state when the session is created from a SYN packet sent by the source host. This means the SYN packet was sent and the source host is now waiting for the SYN-ACK packet.
- `SYN_RECEIVED`: With the session at the `SYN_SENT` state, the destination host has sent the SYN-ACK packet meaning it received the original SYN packet and is now waiting for the ACK packet that will conclude the handshake.
- `ESTABLISHED`: The source host has sent the ACK packet while the session was at the `SYN_RECEIVED` state, which concluded the three-way handshake, establishing the connection. Once established, only FIN and RST packets can change the state of the session.
- `OTHER`: A catch-all state that indicates any other scenario, such as when the first packet of the session is not a SYN packet.

Moreover, two other related properties, `synFlagCount` and `ackFlagCount`, were added to the session edge to track the number of packets added to the session that had the SYN flag and the ACK flag set, respectively.

A limitation of this technique is that it requires the packet information in the graph to be correct, which is not guaranteed in all cases. Examples include cases where the network data injected into the model is not complete, whether due to sampling or an unexpected data loss, and also cases where the system has just gone live and thus only started receiving the network data after the connections were established. Another is the case where the system is fed with NetFlow data instead of raw network data and the NetFlow application did not properly track the TCP state or the number of packets containing each flag in any given flow. In these cases, the model is not able to properly track the correct state of the connections. This makes fingerprints that rely on that information ineffective in identifying attacks.

To mitigate those issues, some correction heuristics were employed to change a session's attributes, such as the TCP state, in cases where inconsistencies between the data and the attributes are encountered. An example is when it is observed that large amounts of data are being exchanged between two hosts on a TCP session, indicating a fully established connection, but the state of the connection indicates otherwise.

In short, the characteristics of a TCP SYN flood attack can be summarized as follows:

- The attacker keeps sending SYN packets to the victim and never replies to the SYN-ACK packet, resulting in a large number of sessions in the `SYN_RECEIVED` state.
- The time frame of any single session is very short.

The above pattern can be expressed in the following query:

Algorithm 7: Fingerprint for TCP SYN flood attack

```
SELECT s, d, count(e)
  MATCH (s:HOST)-[e:SESSION]->(d:HOST)
  WHERE e.tcpState = SYN\_RECEIVED
    AND e.synFlagCount / e.ackFlagCount >
        synAckRatio
    AND e.startTime > TIMESTAMP 'twStart'
    AND e.stopTime < TIMESTAMP 'twEnd'
  GROUP BY s, d
  HAVING count(e) > sessionThr
```

where:

- `destSize` corresponds to the cumulative size of the packets in the session sent by the destination of the session, in this case, the target host.
- `sizeThr` defines a threshold for the maximum expected `destSize`.
- `duration` corresponds to the total length of a session.
- `durThr` defines a threshold for the maximum expected `duration`.
- `destPort` corresponds to the target ports.
- `portThr` defines a threshold for the minimum number of distinct destination ports.

This query mostly follows the same pattern as the preceding ones, with the distinction that it has a condition to only select a session if its TCP state is `SYN_RECEIVED`.

The post-processing phase follows the same pattern as the preceding ones as well, so distributed attacks can be identified and the `cntThr` applied.

4.3.4 Other TCP "Out-of-State" Flood Attacks

Aside from the aforementioned SYN flood attack, there are many other less common TCP-based layer 4 flood attacks variants that exploit illegal or unexpected combinations of TCP packet flags sent without first establishing a TCP connection (thus the "out-of-state" term) with the objective of causing a DoS [41]. The lack of a prior connection causes some systems to return RST packets, which can exacerbate bandwidth consumption problems related to the attack. Finally, bugs stemming from unexpected conditions can also cause issues. Examples of flag combinations used in these attacks include:

- ACK-PSH
- PSH-RST-SYN-FIN
- ACK-RST
- URG-ACK-PSH-FIN
- URG

Because these attacks involve out-of-state packets that form the initial packets of the sessions, it is possible to refine the session's TCP state property to track these cases. Specifically, a new property called `tcpFirstPktFlags` was added to the session edge to track the flags of the first packet of the session if it is a TCP packet and the TCP state is set to `OTHER`.

With that, it is possible to define a generic query following the same pattern as the SYN flood attack query, but parameterized by the first packet flags corresponding to the sought after attacks:

Algorithm 8: Fingerprint for TCP "Out-of-State" flood attacks

```
SELECT s, d, count(e)
  MATCH (s:HOST)-[e:SESSION]->(d:HOST)
  WHERE e.protocol = 'TCP'
    AND e.tcpState = OTHER
    AND e.tcpFirstPktFlags = attackFlags
    AND e.startTime > TIMESTAMP 'twStart'
    AND e.stopTime < TIMESTAMP 'twEnd'
  GROUP BY s, d
  HAVING count(e) > sessionThr
```

The query requires the same post-processing as the SYN flood attack. It is also possible to modify the fingerprint so that it matches any of the possible out-of-state attack flag combinations instead of matching each one individually by allowing `tcpFirstPktFlags` to be equal to any of the known invalid flag combinations.

4.3.5 UDP Flood

UDP flood attacks are flood attack aimed at UDP datagrams. It is considered a volumetric attack because it does not exploit any specific characteristic of the UDP protocol. Instead, it works by sending a large volumes of UDP packets to random or fixed ports on a target host, depleting its available bandwidth, which makes it unreachable by other clients. The attack can also consume a lot of the target's processing power as it tries to determine how to handle the UDP packets [42].

In summary, the key characteristics of a UDP flood attack are as follows:

- The attacker sends UDP packets to the victim at a high rate of frequency.
- The amount of data exchanged per session is relatively fixed and mostly the same.
- The time frame for any single session is very short.

These characteristics can be expressed by the following fingerprint:

Algorithm 9: Fingerprint for UDP flood attack

```
SELECT s, d, count(e)
  MATCH (s:HOST)-[e:SESSION]->(d:HOST)
  WHERE e.protocol = 'UDP'
    AND e.destSize < sizeThr
    AND e.startTime > TIMESTAMP 'twStart'
    AND e.stopTime < TIMESTAMP 'twEnd'
  GROUP BY s,d
  HAVING count(e) > sessionThr
```

Once again, this query mostly follows the same pattern as the preceding ones, with the distinction being the condition to only select UDP sessions.

The post-processing phase follows the same pattern as the preceding ones as well, so distributed attacks can be identified and the `cntThr` applied.

4.3.6 HTTP Flood

HTTP flood is a layer 7 DoS attack in which a target server is saturated with a high volume of HTTP requests. This can slow the server as it tries to handle the high volume and eventually makes the servers unable to handle legitimate traffic [43].

Because a TCP connection must be established for these attacks to be performed, the spoofing of IP addresses is not possible [35], which makes the identification of source IP addresses more reliable.

An HTTP flood attack can use different types of requests and methods (*e.g.* GET, POST), with the most damaging ones being the heaviest requests for a server to handle, such as those involving heavy processing of input or pushing large amounts of data into a database [43, 35]. Consequently, less bandwidth is required to bring down a web server using an HTTP flood attack than is required for another type of DoS attack.

Several different techniques are employed in HTTP flood attacks. Some send a large number of requests, while others send fewer, but very large or very focused, requests. In either case, the attack involves sending large amounts of IP packets to the target. Therefore, the key characteristics of an HTTP flood attack as follows:

- The attacker sends HTTP packets to the victim at a high rate of frequency.
- The amount of data exchanged per session is high.

Naturally, the fingerprint for these attacks needs to be able to identify HTTP sessions. For this reason, a `service` property was added to the session edge so that sessions can be marked as HTTP-related. Note that this property can be used for other reasons as well, such as identifying SSH or FTP sessions.

The challenge in this case is populating the field, given that HTTP is a layer 7 protocol and can, in many cases, be encrypted. We employed two techniques for this purpose. The first was performing deep packet inspection (DPI) to search for identifiers of HTTP messages, such as the version, in packet content. Once a session is identified as being "HTTP-related", it is marked as such and no DPI is required thereafter. A limitation of this technique is that it requires clear text traffic, which in most scenarios today would require the AEN to be deployed after a TLS termination proxy. DPI is also computationally expensive.

For those reasons, a second technique was employed using a service registry comprised of IP addresses and ports of services of interest, such as web services and SSH. This allows for a quick discovery of services but also for some false positives if invalid packets are sent to those servers, such as when non-HTTP packets are sent to an HTTP service.

With the capacity to identify HTTP sessions, a query can be defined as follows:

Algorithm 10: Fingerprint for HTTP flood attack

```
SELECT s, d, count(e), sum(e.pktCount)
  MATCH (s:HOST)-[e:SESSION]->(d:HOST)
  WHERE e.protocol = 'TCP'
    AND e.service = 'HTTP'
    AND e.srcSize < sizeThr
    AND e.startTime > TIMESTAMP 'twStart'
    AND e.startTime < TIMESTAMP 'twEnd'
  GROUP BY s, d
  HAVING sum(e.pktCount) > pktCntThr
```

This query is somewhat distinct from the preceding ones because it is based on the number of packets exchanged in a given time window rather than the number of sessions and also because it does not consider short-term sessions. Both differences are a consequence of the fact that HTTP flood attacks require fully established connections. The seemingly redundant clause to select only TCP sessions when there is already a clause to select only HTTP sessions is included to filter out part of the invalid packets, such as UDP packets sent to that specific service, in case the service registry was used.

Finally, the post-processing phase follows the same pattern as the preceding queries as well, with a further aggregation per destination host so that distributed attacks can be identified and the `cntThr` applied.

4.4 *Password Guessing*

Password guessing is when the attacker tries to gain access to a system by persistently attempting to guess user passwords [44, 45]. The passwords attempted are normally derived from either leaked password associated with a particular user or dictionaries of common passwords, in which case the attack is also known as a brute-force attack.

There are a few different types of password guessing attacks, but they all share the main characteristic of generating a high volume of failed login attempts, which are normally logged by the applications into which the authentications are attempted. For this reason, the AEN ingests application and system logs, like those from SSH, to extract authentication information and insert that it into the graph through nodes of type `ACCOUNT` and edges of type `AUTH_ATT` ("authentication attempt") that link an account with the target host of the authentication. To track whether the authentication attempt was successful, the edge has a Boolean property called `succ`.

Another important characteristic of password guessing attacks is that they do not necessarily happen in a short time frame. Sometimes the whole process can last for days, or even longer. That means there is no need to consider the time frame of the attempts. Incidentally, that means the AEN must keep authentication-related elements for longer than it would for many other types of elements.

In this study, we investigated three types of password guessing attacks:

- Basic: One account on one host is targeted with a brute-force attack.
- Spraying: Multiple accounts on one host are each attacked one or a few times.
- Stuffing: The same account is targeted on multiple hosts one or a few times per host.

4.4.1 *Basic password guessing*

A basic password guessing attack is one where a single account on a single host is targeted with a brute-force attack. It is the most common type of password guessing attack [44, 45]. Because it only focuses on one-to-one relations, the graph patterns should be `(:ACCOUNT)-[:AUTH_ATT]->(:HOST)`. For the sake of brevity the whole fingerprint will not be described because it is a generalization of the *spraying password guessing* fingerprint that follows.

4.4.2 *Spraying password guessing*

In a spraying password guessing attack, instead of multiple passwords being tried with a single account, the attacker tries to breach multiple accounts with a single password or a few passwords [46]. In this manner, the attacker can circumvent the most common authentication protection measures, such as account lockouts.

These attacks can be performed either from a single source, in which case tracking attempts per IP address might be a useful detection method, or from distributed sources, which makes detection harder. This is one of the strengths of the proposed fingerprint, as it focuses exclusively on authentication attempts per victim host, which makes it, by design, effective regardless of the number of source hosts involved.

In summary, spraying password guessing attacks have the following characteristics:

- One host is targeted with a high number of authentication attempts.
- The attempts are spread over several accounts such that no account has more than a few attempts.

- One or more hosts can participate in the attack.
- The time frame of an attack can be very long.

Based on the above characteristics, the query is defined as follows:

Algorithm 11: Fingerprint for spraying password guessing attack

```
SELECT h, count(DISTINCT a), ARRAY_AGG(e.id) as
    attempts
  MATCH (a:ACCOUNT)-[e:AUTH_ATT]->(h:HOST)
  WHERE count(!e.succ) > attemptThr
  GROUP BY h
  HAVING count(!e.succ) / count(e) >
      authFailRatioThr
    AND count(DISTINCT a) > accountThr
```

where:

- `attemptThr` defines a threshold for the minimum number of failed attempts per account to exclude regular login attempt failures from real users.
- `authFailRatioThr` defines a threshold for the minimum ratio of failed attempts in relation to the total number of authentication attempts.
- `accountThr` defines a threshold for the minimum number of distinct accounts that will trigger the fingerprint.

Each match returned by the query contains the victim host, the associated number of distinct target accounts on the host and, as a special output, the array of identifiers of the matching edges, called `attempts`, which is used in the post-processing step to retrieve the list of targeted accounts by fetching from the graph the source nodes of the edges in the array.

Furthermore, if retrieving the hosts responsible for the attack is desired, another query can be performed to find the source hosts of the authentication attempts in the `attempts` array based on its source properties.

4.4.3 *Credential Stuffing*

The credential stuffing attack, also known as a targeted password guessing attack, consists of trying the same credentials (*e.g.* user name and password combination) on multiple hosts [45]. The credentials used in these attack are traditionally obtained from leaks of previous attacks or are default passwords in systems that have them. The latter type is particularly common in IoT devices [47]. More advanced attacks use slight variations of the passwords for cases where the user has the same base password with small modifications per host. Ultimately, this type of attack targets password reuse by the same user on different websites and hosts or poorly designed systems. This consequently means the attacker will not try more than a few different combinations per account but will try the same combinations against multiple targets.

As with any password guessing attack, credential stuffing can be performed from either a single source or distributed sources. However, because this attack targets multiple hosts that normally do not coordinate their detection and prevention efforts, the attacker is more likely to be able to carry out the attack using a single source than with other types of password guessing attacks.

In practice, a single attack campaign can perform credential stuffing on several accounts at once. This type of attack would be detected by the fingerprint as multiple credential stuffing attacks happening together, or possibly as multiple spraying attacks, depending on the number of accounts targeted. Also note that the AEN does not have access to the password, so it cannot determine if the same passwords are being used in multiple hosts, only that multiple failed authentication attempts are being performed for a given account on multiple hosts.

In summary, credential stuffing attacks have the following characteristics:

- Multiple hosts are targeted with a high number of authentication attempts across them.
- Only one account is targeted.
- Only a few attempts are made per host.
- One or more hosts can participate in the attack.
- The time frame of an attack can be very long.

Based on the above characteristics, the query is defined as follows:

Algorithm 12: Fingerprint for credential stuffing attack

```
SELECT a, count(DISTINCT h), ARRAY_AGG(e.id) as
    attempts
  MATCH (a:ACCOUNT)-[e:AUTH_ATT]->(h:HOST)
  WHERE count(!e.succ) > attemptThr
  GROUP BY a
  HAVING count(!e.succ) / count(e) >
      authFailRatioThr
    AND count(DISTINCT h) > hostThr
```

where `hostThr` defines a threshold for the minimum number of distinct hosts that will trigger the fingerprint.

In contrast to the spraying query, this query groups by account rather than host and counts the number of matching hosts instead of the number of matching accounts. As a result, each match returned by the query contains the targeted account, the associated number of distinct hosts where authentications were attempted and the `attempts` array, which in this case is used to retrieve the list of victim hosts by fetching from the graph the destination nodes of the edges in the array in the post-processing phase.

As with the previous query, retrieving the hosts responsible for the attack is possible by performing another query to find the source hosts of the authentication attempts in the `attempts` array, based on its source properties.

5 Anomaly Detection based on the AEN Graph Model

5.1 *Measure of Anomalousness*

Anomaly detection approaches use statistical methods to help identify outliers or rare events, which are flagged as anomalous.

Anomaly is defined as something that deviates from what is standard, normal or expected [3]. When applied to intrusion detection, this involves assuming that anomalous events are more likely to be malicious.

In [48], the authors defined the anomaly score of an event as the negative log likelihood of that event, which was later adapted by Ferragut et al. [4] as the bits of rarity metric. Formally, given a random variable X with probability density or mass function f, the rarity of an event x is defined as:

$$R(x) = -\log_2 P_f(x) \tag{1}$$

The negative means that rarer events have a higher rarity value. Moreover, using the log helps with numerical stability, while the base 2 causes the rarity of the event to be measured in bits. Finally, note that the negative log of zero is defined by convention to be positive infinity.

In [4], the authors also demonstrated that the bits of rarity metric has some important limitations when used for anomaly detection because it is not *regulatable* or *comparable* between two different types of data. As a supporting example, the authors defined two uniform discrete distributions, one with 100 values and one with 2000 values. If a threshold of 10 is chosen to define what is anomalous or not, then no event of the first distribution will be considered anomalous while all events of the second distribution will be even though they are all equally likely.

Note how, in this example, a predefined threshold cannot be used to regulate the number of anomalous events identified in a sample of any distribution. Furthermore, note how it is not possible to compare the rarity of the events of two distinct distributions because the rarity metric of an event is an absolute value that does not describe the rarity of that event relative to its distribution.

For these reasons, the authors proposed a regulatable and comparable anomalousness metric called bits of meta-rarity based on the "probability of the probability" of the event rather than just the probability of an event. More formally, given a random variable X with probability density or mass function f defined on the domain $\mathcal{D}$, the bits of meta-rarity anomaly score $A : \mathcal{D} \to \mathbb{R}_{\geq 0}$ of en event x is defined as:

$$A(x) = -\log_2 P_f(f(X) \leq f(x)) \tag{2}$$

Going back to the previous example, note how for any value x of either distribution, $P_f(f(X) \leq f(x)) = 1$ and consequently $A(x) = -\log_2 1 = 0$. This implies that neither distribution has any anomalous event, regardless of the threshold used (as long as it is greater than 0), and also that the anomaly scores of the different distributions can be compared.

Moreover, for a given threshold θ, the probability that $A(x)$ exceeds that value is bounded by $2^{-\theta}$ such that the ratio of events flagged as anomalous in a sample is never more than $2^{-\theta}$ as long as f fits the sample well. This condition applies for any f which makes the anomaly regulatable through θ.

Note here the importance of a high goodness of fit of f, without that the above condition will not hold.

For a continuous variable, $P_f(f(X) \leq f(x))$ is defined as the area under f restricted to those t such that $f(t) \leq f(x)$, that is

$$P_f(f(X) \leq f(x)) = \int_{\{t | f(t) \leq f(x)\}} f(t) \mathrm{d}t \tag{3}$$

For a discrete variable, $P_f(f(X) \leq f(x))$ is defined as the sum of all probabilities less than or equal to $P_f(x)$, that is

$$P_f(f(X) \leq f(x)) = \sum_{\{t | f(t) \leq f(x)\}} f(t) \tag{4}$$

As a further example, consider the discrete variable $X = \{x_1, x_2, x_3\}$, such that $f(x_1) < f(x_2) < f(x_3)$. Thus, the anomaly scores of these events are given by

$$\begin{aligned} A(x_1) &= -\log_2(f(x_1)) \\ A(x_2) &= -\log_2(f(x_1) + f(x_2)) \\ A(x_3) &= -\log_2(f(x_1) + f(x_2) + f(x_3)) \end{aligned}$$

In this case, it is clear that $A(x_1) > A(x_2) > A(x_3)$; in other words, as the events become more common, they become less anomalous.

Bringing this to the scope of our work, the variables are the features we extract from the graph as described in subsection 5.2. Each feature is a multinomial variable with k categories, each defined by an n-tuple. For instance, the categories of feature `totalsessions` are defined by the 2-tuple ($SourceHost$, $DestinationHost$), whose values are defined by the total number of sessions between those hosts.

Now recall the importance of a suitable distribution for each variable. This is normally obtained through a training phase. However, because our model is fully unsupervised, it does not contain a training phase. Instead, we estimate the probability of each observed value online based on the frequency of that observation in the sample extracted from the graph, which collectively describe the probability mass function of the feature.

This implies that, although the values of each category of a variable might be continuous in theory, they are discrete in practice, which may cause some issues. Consider, for example, the following sample of a feature: $\{x_1 = 22,\ x_2 = 11,\ x_3 = 22,\ x_4 = 555,\ x_5 = 10,\ x_6 = 9\}$.

Intuitively, x_4 should have the higher anomaly score as its value is farther from the values of the others, but that is not the case. Instead, when considering the frequency of each value, x_1 and x_3 have the same values and thus the same higher probability (i.e. $2/6$) and the same anomaly score. The other values, including the value for x_4, each appear only once and thus result in the same lower probability (i.e. $1/6$) and the same anomaly score.

To overcome this issue, we discretize the values into bins such that neighbouring values will be mapped to the same bins and thus have a higher probability. In practice, given a bin width h, the binned value of x is defined as

$$b(x) = h \left\lfloor \frac{x}{h} \right\rfloor \tag{5}$$

Note that multiplying by h is only done to keep the binned values near to the original values but is not required in practice.

To help with understanding, Table 1 shows the binned values of a sample using different bin widths. The values with lower probabilities, meaning the most anomalous, for each bin width are bolded.

Table 1: Value binning examples

Category	Bin Width		
	1	5	25
x_1	22	20	0
x_2	**11**	10	0
x_3	22	20	0
x_4	**555**	**555**	**550**
x_5	**10**	10	0
x_6	**9**	**5**	0

It can be seen that as the bin width increases, more similar values are mapped into the same bins, which increases their probabilities. With the bin width of 25, all values except that of x_4 are mapped to the same bin, resulting in a probability of $5/6$, while x_4 continues to have a probability of $1/6$, making it the most anomalous event in the sample for this bin width.

To compute the features, we first split the time range of the data into time windows, with the windows treated independently from each other. For that, we employed the previously discussed sliding window mechanism. Then, for each time window, we extract the features from the AEN graph.

Afterwards, for each feature $X = \{x_1, \ldots, x_k\}$ where k is the size or number of categories of X, its values are binned according to (5). After this process, there will be n bins, with each bin representing a value range. The probability of each bin, $p(b_j)$, where $j = \{1, \ldots, n\}$, is defined as the ratio of the number of elements in the bin over the total number of categories of the feature:

$$p(b_j) = \frac{|b_j|}{k} \tag{6}$$

Clearly, the distribution of p approximates the distribution of f such that $P_f(f(X) \leq f(x_i))$ can be approximated through $p(b(x_i))$. Therefore, it is useful to define the anomaly score of a bin b_j following (2) and (4):

$$A(b_j) = -\log_2 \sum_{\{b_m | p(b_m) \leq p(b_j)\}} p(b_m) \tag{7}$$

From that, the anomaly score of x_i is defined as equal to the anomaly score of its binned value:

$$\begin{aligned} A(x_i) &= A(b(x_i)) \\ &= -\log_2 \sum_{\{b_m | p(b_m) \leq p(b(x_i))\}} p(b_m) \end{aligned} \tag{8}$$

The last step of the anomaly detection is to compare the anomaly scores with a predefined threshold such that if the anomaly score of an element is greater than the threshold, that element is considered anomalous. Specifically, the source element of the anomalous feature tuples are the ones actually considered anomalous. For instance, for feature `totalsessions`, it is the source host, not the destination host, that is reported as anomalous.

5.2 Feature Model

In this subsection, we describe the proposed feature model, which contains a wide range of features extracted from the AEN graph. The features are categorized into session features, which are extracted from session data, and authentication features, which are extracted from authentication data.

Note that all features are contained within a time window, meaning that each operation described below is performed only on the edges that were created in that time window. Also note that the features are directed, so any feature extracted for a pair of hosts h_1 and h_2 is different from that same feature between h_2 and h_1.

5.2.1 Session Features

The main type of edge in the AEN graph model is the session edge, which represents a communication session between two hosts. Our detection model leverages session edges to extract useful features that can support threat identification.

There are a total of nine session features:

- Total sessions: The total number of sessions between a pair of hosts.
- Unique destination ports: The number of unique ports of a destination host for which there are sessions from a source host.
- Unique destination hosts with same destination port: The number of unique destination hosts to which a source host connected with the same destination port.
- Unique destination ports for a source host: The number of unique destination ports for which a host has sessions.
- Mean time between sessions: The mean time between the start of the subsequent sessions between a pair of hosts.
- Mean session duration: The mean duration of the sessions between a pair of hosts.
- Mean session size ratio: The mean ratio of the destination size (bytes sent from the destination host of the session) over the source size (bytes sent from the source host of the session) for a pair of hosts.
- Mean session velocity: The mean velocity of the sessions between a pair of hosts. The session velocity is defined as the ratio of the total number of packets of a session to the total duration of the session, which is expressed in packets/sec.
- Mean session source size: The mean source size of the sessions sent from a host.

5.2.2 Authentication Features

The authentication data contained in the AEN graph are potential sources of useful information for the detection of anomalous authentication behaviour. There are a total of six different authentication features:

- Total authentication failures: The total number of failed authentication attempts between a pair of hosts.
- Total authentication failures per account per host: The total number of failed authentication attempts by a host using a specific account to all other hosts.

- Total authentication failures per account: The total number of failed authentication attempts between a pair of hosts using a specific account.
- Unique accounts: The number of unique accounts that were used in failed authentication attempts between a pair of hosts.
- Unique accounts per host: The number of unique accounts that were used in failed authentication attempts by a host to all other hosts.
- Unique target hosts per host per account: The total number of hosts that a host attempted, but failed, to authenticated using a specific account.

6 Experimental Evaluation

6.1 Setup and Procedures

The proposed ensemble intrusion detection mechanism was evaluated in two separate sets of experiments, one using the ISOT-CID Phase 1 dataset and one using the CIC-IDS2017 dataset. These datasets were selected because they contain benign and malicious network traffic data that can be used to build an AEN graph. Additionally, both datasets include examples of the attacks for which fingerprints have been developed, allowing their performance to be assessed.

The goal of the experiments was to evaluate the model's performance in correctly classifying hosts as malicious or benign. Specifically, each of the two detection schemes were assessed individually, and afterwards, a final ensemble classification was performed.

Separate experiments were performed for each day of each of the datasets according to the following procedure:

- An AEN graph was generated based on the available data of the specific day.
- Each of the two schemes were executed against the generated graph, and the results were collected.
- Each *host* node was given three classifications, one for each of the two detection schemes and one for the combined classification. The rules employed for each classifier are described later.
- The classification performance of each of the two individual schemes and that of the ensemble classifier were calculated based on the actual and predicted classifications.

The details for each of the two schemes are described in the following sections.

6.1.1 Fingerprint Matching

The fingerprint matching scheme classifies a host as malicious if the host is found to be part of an attack by at least one fingerprint.

Table 2 shows the parameters adopted for the experiment. Parameters with the same values used by multiple fingerprints are marked as "Multiple/Default", while parameters that are unique to a single fingerprint or values that are distinct from the default are marked according to the fingerprint.

Table 2: Attack fingerprint experiment parameters

Fingerprint	Parameter	Value
Multiple/Default	`attemptThr`	50
	`authFailRatioThr`	0.8
	`cntThr`	700
	`sessionThr`	100
	`sizeThr`	600 bytes
	`twSize`	20 seconds
	`twStep`	10 seconds
Basic Pwd Guessing	`attemptThr`	4
Credential Stuffing	`hostThr`	4
HTTP Flood	`pktCntThr`	15000
	`sizeThr`	1200 bytes
	`twSize`	2 minutes
	`twStep`	1 minute
IP Fragmentation Attack	`fragPckCntThr`	600
	`fragRatioThr`	0.8
	`sessionThr`	20
Spraying Pwd Guessing	`accountThr`	4
TCP SYN Flood	`synAckRatio`	100
UDP Flood	`sessionThr`	300
Vertical Port Scanning	`durThr`	1 second
	`portThr`	50

Finally, to measure the performance of the fingerprints, we used precision (positive predicted value – PPV) and sensitivity (true positive rate – TPR) because they describe the detection performance of the scheme without taking into consideration the true negatives, which is desirable for evaluating the performance of a signature-based intrusion detection scheme. Specifically, precision is better suited for the task because it describes the ratio of true positives among all predicted positive elements, which is expected to be high for a signature-based intrusion detection scheme. In contrast, sensitivity, indicates the ratio of true positives among all actual positive elements. This is not necessarily expected to be high given that the provided fingerprints only cover a few specific types of attacks and not all attack types that exist in the dataset.

6.1.2 Anomaly Detection

The anomaly detection scheme classifies a host as malicious if it is found to be the source of any anomalous behaviour, that is, if any of the features reports a score for the host above the experiment's threshold.

The algorithm has four parameters, bin width, time window size, time window step and threshold. To assess the performance of the scheme under different combinations of parameters, and identify the optimal threshold value, we defined the following set of values:

- Bin width: 1, 2, 4, 12 and 64.
- Time window size: 30 minutes, 1 hour, 4 hours and 12 hours.
- Time window step: Half the time window size.

- Threshold: From 0 to 20 bits at 0.5 intervals.

As a consequence, for each day experiment, the anomaly detection was executed 20 times, once for each parameter combination (excluding the threshold). Afterwards, the scores were evaluated against the 40 thresholds, resulting in a total of 800 sets of results.

Finally, to measure the performance of the anomaly detection scheme, three metrics were chosen: F1 score, bookmaker informedness (BM), and the Matthews correlation coefficient (MCC). As discussed later, both datasets are unbalanced; therefore, traditional metrics like the accuracy, precision and recall were not suitable, and as such, they were not used for the evaluation. Conversely, the three chosen metrics, particularly the latter two, were chosen because they are generally considered to be better suited for this scenario [49, 50].

Nonetheless, we provide the resulting receiver operating characteristic (ROC) curve for each of the parameter combinations, representing the classifications of the separate days combined together, to show the general performance behaviour of the scheme under different parameters and different thresholds. This serves as a basis for selecting the best parameter combinations and, accordingly, discussing the performance of the algorithm. We also present the sensitivity and the false positive rate (1 − specificity) when discussing the performance of the best parameter combination so it can be correlated to the ROC curves.

6.1.3 *Ensemble Classification*

The ensemble classification was performed by fusing the classification of the individual schemes (classifiers) in two ways: One with an *and* rule, meaning a host is only considered malicious if both classifiers agree that it is malicious, and the other with an *or* rule, meaning that a host is considered malicious if either of the classifiers consider it malicious.

Naturally, the *and* rule is expected to generate few false positives and more false negatives. In contrast, the *or* rule is expected to generate more false positives and few false negatives. In practice, the classifier with fewer positive predictions sets an upper limit on those numbers when using the *and* rule and a lower limit when the *or* rule is applied.

6.2 *ISOT-CID Phase 1*

The ISOT-CID Phase 1 dataset [5] contains systems calls, system and event logs, memory dumps and network traffic (TCPdump) data extracted from Windows and Linux virtual machines (VMs) and OpenStack Hypervisors collected from a production cloud computing environment, more specifically, Compute Canada's WestGrid. It includes both benign and malicious traces of several human-generated attacks and of unsolicited Internet traffic.

The dataset includes the time stamps and IP addresses related to each attack, as well as the IP addresses that generated benign traffic. There is also a label file that labels each packet in the dataset's network traffic data as benign or malicious, and the malicious packets are labelled by the type of attack. Unsolicited traffic is labelled as malicious but does not have an attack type label.

6.2.1 *Graph Generation*

In this study, we used only the network traffic data from which we extracted communication patterns between hosts, and system logs from which we extracted authentication information.

The graph elements are labelled based on the dataset labels, with *host* nodes labelled as malicious if they are the source of at least one packet labelled as malicious. The labels of other elements are derived from the host labels such that elements related to the host inherit its labels. For instance, a *session* edge is labelled as malicious if its source host is labelled as malicious. The malicious session edges are also labelled with the attack type when available. Note that labels are independent for each day of the data, meaning that they are not maintained from one day to the next.

The details of the generated AEN graphs for each day are shown in Table 3, and the sessions' attack type labels are shown in Table 4. As can be seen in both tables, there is a high prevalence of malicious hosts and sessions; however, most malicious sessions are not labelled with an attack type. Moreover, each day has at least a few samples of different known types of attacks, but there were no samples of any DoS attacks.

Table 3: Graph details for ISOT-CID Phase 1 dataset

Day	Nodes	Hosts (malicious)	Edges	Sessions (malicious)
Day 1	376	78 (60 – 77%)	12432	8313 (7279 – 88%)
Day 2	635	134 (116 – 87%)	45334	17544 (14276 – 81%)
Day 3	653	86 (70 – 81%)	31405	9355 (8741 – 93%)
Day 4	491	94 (78 – 83%)	8258	4637 (3882 – 84%)
Combined	2155	392 (324 – 83%)	97429	39849 (34178 – 86%)

Table 4: Malicious session attack type labels for ISOT-CID Phase 1 dataset. PG stands for password guessing, PS for post scanning and UL for unauthorized login.

Day	PG	Ping	PS	UL	Unknown
Day 1	21	1	3	13	7241
Day 2	38	–	11	4	14223
Day 3	20	–	12	2	8707
Day 4	–	–	–	2	3880
Combined	79	1	26	21	34178

6.2.2 *Fingerprint Matching Results*

The results obtained after running the fingerprints on the generated graph for each of the four days of the dataset are shown in Tables 5 and 6, with the former showing the classification performance of the proposed fingerprints combined for each day and the latter showing the individual performance of each fingerprint. Fingerprints for which no matches were found are omitted.

Table 5: Classification performance of the proposed fingerprint matching scheme for ISOT-CID Phase 1 dataset

Day	TP	TN	FP	FN	PPV	TPR
Day 1	28	17	1	32	0.97	0.47
Day 2	24	18	0	92	1.00	0.21
Day 3	38	16	0	32	1.00	0.54
Day 4	23	16	0	55	1.00	0.29
Combined	113	67	1	211	0.99	0.35

As shown in Table 5, the fingerprints had very high precision for all days of the dataset with only a single false positive match resulting in a combined precision of over 0.99, which, as discussed previously, was expected given that the scheme is signature-based and given the high prevalence of malicious hosts in the dataset. The sensitivity was medium to low, depending on the day, which was once again expected, given the small number of attack types covered by the fingerprints.

Table 6: Individual fingerprint performance for ISOT-CID Phase 1 dataset. PG stands for password guessing. Fingerprints for which no matches were found are omitted.

Fingerprint	Day 1		Day 2		Day 3		Day 4	
	TP	FP	TP	FP	TP	FP	TP	FP
Basic PG	24	0	19	0	35	0	22	0
Spraying PG	28	1	24	0	38	0	23	0

Looking at the performance of the individual fingerprints in Table 6, we can see that there were only two fingerprints for which matches were found, namely the basic password guessing fingerprint and the spraying password guessing fingerprint. To understand the reason for that, we need to refer back to Table 4, where two notable pieces of information are shown. The first is that there are no known samples of DoS attacks in the dataset, which means that none of those fingerprints were expected to be matched. The second is that, while there were a few port scanning attacks, they involved a very small number of sessions (the maximum being 26 on day 4), which maps to a small number of ports scanned in total since each session only has one destination port. Moreover, as the dataset documentation states, these attacks were horizontal scans targeting only a few ports across several hosts in the network, while the available port scanning fingerprint is designed for vertical scans. Therefore, it was expected to find no matches for that fingerprint.

Note that it would be possible for samples of those attacks to be unknowingly present in the dataset from the collected unsolicited traffic. However, no instances of those attacks were observed, except for some instances of password guessing attacks.

Also of note is the fact that the network data in the dataset were sampled and thus contain gaps that can skew some of the graph elements. This can also explain some false negatives and even cause false positives.

6.2.3 Anomaly Detection Results

After running the experiments as previously described, the results from different days were combined, and an ROC curve was plotted for each of the parameter combinations. The curves are shown in Figure 2. Marked in each plot is the point where the threshold is equal to 0.5.

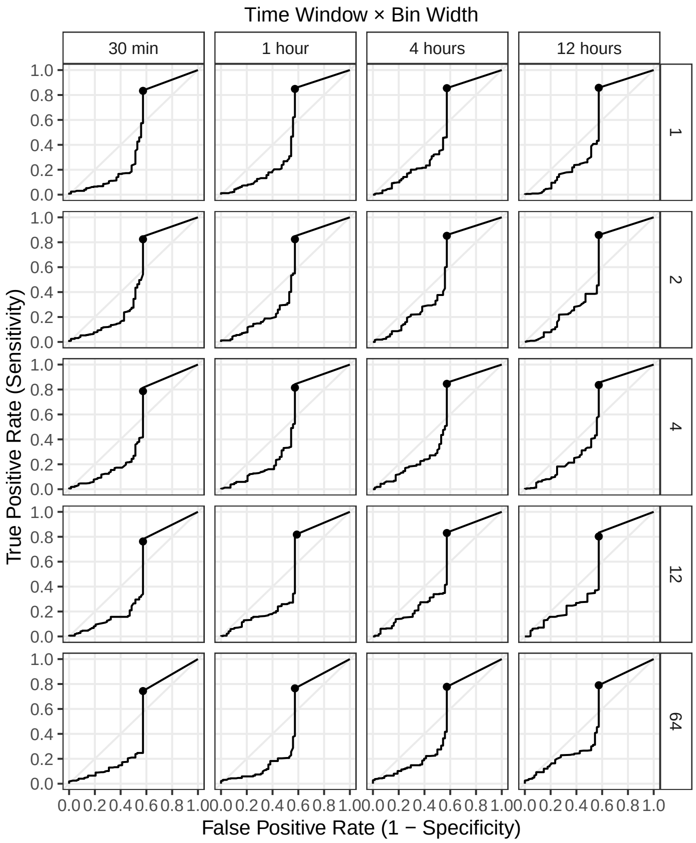

Figure 2: ROC curves of the anomaly detection scheme for the ISOT-CID Phase 1 dataset under different parameter combinations. The point in each plot marks where the threshold is equal to 0.5.

All curves show a similar pattern in which the sensitivity is poor while the threshold is high, until a point where it sharply rises until reaching its peak performance close to where the threshold is equal to 0.5. After that, it just goes straight to the top-right endpoint. Both of these characteristics can be explained by the exponential nature of the score, which means that a linear increase in the threshold will cause an exponential decrease in the true positives identified by the model. For this reason, it is common for the maximum score reported by any feature to be between 0 and 0.5, but the probability is exponentially smaller for higher scores.

When comparing the different ROC curves with regard to the other two parameters, a slightly better performance can be observed with longer time windows of 4 and 12 hours and with smaller bin widths of 1 and 2. That demonstrates that the extra information available with longer time windows allows the model to better distinguish anomalous behaviour. However, there is a limit to this, considering that too-long time windows could possibly be hiding shorter duration attacks. Also, the smaller bin widths allow for a greater variability of behaviours to be modelled. In practice, bin widths that are too large result in low resolutions of the distributions of variables that is caused by very diverse values being binned together.

These findings become even more clear when analyzing the other performance metrics, which are more suitable for the unbalanced nature of this dataset. Therefore, we selected a threshold of 0.5, bin width of 2 and time window size of 12 hours to discuss the findings further. Table 7 shows the daily and combined results of the model under that specific parameter combination.

Table 7: Performance of the proposed anomaly detection model for the ISOT-CID Phase 1 dataset

Day	TP	TN	FP	FN	TPR	FPR	F1	BM	MCC
Day 1	52	8	10	8	0.87	0.56	0.85	0.31	0.32
Day 2	94	7	11	22	0.81	0.61	0.85	0.20	0.16
Day 3	61	7	9	9	0.87	0.56	0.87	0.31	0.31
Day 4	71	7	9	7	0.91	0.56	0.90	0.35	0.37
Comb.	278	29	39	46	0.86	0.57	0.87	0.28	0.27

As can be seen, under the selected parameters, the model was able to detect the majority of the malicious hosts but also generated a relatively high number of false positives. That behaviour can be observed in the other metrics as well, with a combined F1-score of 0.87, a combined BM of 0.28 and a combined MCC of 0.27. Another notable aspect is the mostly consistent performance observed for each individual day, with only the results for day 2 having a greater deviation from the average.

In general, the observed behaviour was expected, given that the model is anomaly-based and thus prone to generating false alarms. Moreover, the high prevalence of hosts in the dataset means that the malicious behaviour is in fact not anomalous in the dataset. On the contrary, most of the traffic and hosts are labelled as malicious, which explains why the scheme generated a high number of false positives and points to a general limitation of anomaly-based detection, which can produce degraded results when the malicious behaviour is not uncommon.

6.2.4 *Ensemble Classification Results*

The ensemble classification using the *and* rule resulted in the same predictions as the fingerprint matching already shown in Table 5. This outcome means that all hosts classified as malicious by fingerprint matching were also classified as malicious with the anomaly detection. In contrast, but for the same reason, the ensemble classification using the *or* rule resulted in the same predictions as the as anomaly detection, which are summarized in Table 7.

In practice, in a real environment, where the anomaly detection threshold is not optimally chosen, the divergence between the classifiers will be greater, thus causing the performance of the ensemble classification to be distinct. Other ensemble classification rules, such as soft voting could also be used as a middle ground between the two rules evaluated in this paper.

6.3 *CIC-IDS2017*

The CIC-IDS2017 dataset [6] contains network traffic data (both pcap and NetFlow) of benign traffic, as well as several samples of attack scenarios including SSH and FTP password guessing, DoS, web attacks and instances of host infiltration. The dataset is labelled on the flow level, with each flow being labelled as either benign or with the attack performed.

6.3.1 *Graph Generation*

To build the graph, the packet data (pcap files) were used to extract the communication patterns between hosts since packets are more finely detailed than flow data. Because no system or application logs were available, we could not extract authentication information from the data. As a consequence, no authentication-related elements (*account* nodes and *authentication attempt* edges) are present in the graphs of this dataset which in turn means that no password guessing instances can be found with the fingerprints as designed.

The graph labelling followed the same rules as the previous dataset, with *host* nodes labelled as malicious if they were the source of at least one flow labelled as malicious and with the labels of other elements being derived from the host labels. One distinction was how to define the attack type labels. For that, we first combined the dataset labels into generic attack type labels. For instance, the "DoS slowloris" and "DoS GoldenEye" labels were combined into the "Denial of Service" label. Then, each flow was matched with its respective *session* edge that was labelled with the generic attack type.

In a few cases, sessions had more than one attack type. This was an artifact of how the sessions are created from packets such that one session can map to more than one flow. Moreover, some malicious sessions have no attack type labels in cases where none of their mapped flows were labelled as malicious, even though their source hosts were labelled as such.

The details of the generated AEN graphs for each day are shown in Table 8, and the sessions' attack type labels are shown in Table 9. As shown by the tables, there was a very small prevalence of malicious hosts, while the prevalence of malicious sessions varied from low (approximately 3% on day 1) to high (approximately 87% on day 4). As for the attack type labels, there was a high number of attack samples from all days. However, the types of attacks present for each day varied with most types of attacks only present for one day. Moreover, the number of sessions with unknown attack was high on days 3 and 4, which stems from the fact that those days had combined multiple attack sessions.

Table 8: Graph details for the CIC-IDS2017 dataset

Day	Nodes	Hosts (malicious)	Edges	Sessions (malicious)
Day 1	27653	8498 (1 – 0.01%)	279271	243264 (6954 – 3%)
Day 2	29216	9017 (1 – 0.01%)	298033	259938 (16571 – 6%)
Day 3	27828	8545 (2 – 0.02%)	323502	287272 (89523 – 31%)
Day 4	27035	8331 (10 – 0.12%)	460893	425649 (370297 – 87%)
Comb.	111732	34391 (14 – 0.04%)	1361699	1216123 (483345 – 40%)

Table 9: Malicious session attack type labels for CIC-IDS2017 dataset. BN stands for botnet, Inf for infiltration, PG for password guessing, PS for port scanning, WA for web attack and Unk for unknown.

Day	BN	DoS	Inf	PG	PS	WA	Unk
Day 1	–	–	–	6953	–	–	1
Day 2	–	16537	1	–	–	–	33
Day 3	–	–	6	1363	–	643	87511
Day 4	1228	45392	–	–	158678	–	165026
Comb.	1228	61929	7	8316	158678	643	252571

6.3.2 *Fingerprint Matching Results*

The results obtained after running the fingerprints on the generated graph for each of the four days of the dataset are shown in Tables 10 and 11, with the former table showing the classification performance of the proposed fingerprints combined for each day and the latter showing the individual performance of each fingerprint. Fingerprints for which no matches were found are omitted.

Table 10: Classification performance of the proposed fingerprints for the CIC-IDS2017 dataset

Day	TP	TN	FP	FN	PPV	TPR
Day 1	0	8494	3	1	0.00	0.00
Day 2	0	9011	5	1	0.00	0.00
Day 3	2	8542	1	0	0.67	1.00
Day 4	6	8320	1	4	0.86	0.60
Combined	8	34367	10	6	0.44	0.57

Table 11: Individual fingerprint performance for the CIC-IDS2017 dataset. PS stands for port scanning. Fingerprints for which no matches were found are omitted.

Fingerprint	Day 1		Day 2		Day 3		Day 4	
	TP	FP	TP	FP	TP	FP	TP	FP
HTTP Flood	0	0	0	0	0	0	1	0
TCP SYN Flood	0	0	0	0	2	0	1	0
UDP Flood	0	1	0	2	0	0	1	0
Vertical PS	0	2	0	4	2	1	5	1

As shown in Table 10, the general performance was not as high as with the previous dataset. There were no true positive matches on days 1 and 2, resulting is precision and sensitivity of 0 for those days. In contrast, days 3 and 4 had better performance, particularly day 4, with a precision of 0.86.

Having no true positives was expected for day 1 because this day only had password guessing attacks but graph had no authentication elements, which are part of the password guessing fingerprints. This was not the case for day 2, which had DoS attacks that were HTTP-based, but no matches were found for the HTTP flood fingerprint. Still, this can be explained by the types of attacks performed, such as Heartbleed and Slowloris, which are not flood attacks, making the HTTP flood fingerprint unsuitable for this case. Tuning the fingerprint parameters might allow for these attacks to be found but might also result in some false positives. Moreover, the very low prevalence of malicious hosts, with only a single one for both days 1 and 2, means that not finding that host will result in a precision and sensitivity of 0 as observed.

Continuing onto day 3, there were matches for the two malicious hosts for both the TCP SYN flood fingerprint and the vertical port scanning fingerprint. Note that according to the dataset labels, as shown in Table 9, neither type of attack was expected to be present. However, the dataset documentation states that both port scans and nmap scans were performed on that day, although not labelled, which explains the positive matches.

As for day 4, there were matches for four different fingerprints, including three DoS fingerprints and the port scanning fingerprint. The day's data are labelled as having both of those types of attacks, as well as a botnet attack. Sessions with all three labels were matched. Note that the dataset's documentation is not clear on exactly which attacks were executed as part of the botnet attack, but in any case, the attack's data were the source of some of the matches, too.

Finally, all days had false positives, which would not be expected from a signature-based scheme; however, the absolute number of false positives was low compared to the total number of hosts in the dataset. Moreover, as shown in Table 11, this was mostly from the vertical port scanning fingerprint. When analyzing the benign sessions that were matched by that fingerprint, almost 60% had port UDP/137, which is used by the NetBIOS name service. However, in these cases, it was not the destination port that was fixed at 137, but instead, the source port was 137, while the destination port varied. This behaviour is an artifact of how name queries are broadcast in NetBIOS, but the replies are directed to the host that made the query on what was originally the source port of the broadcast query. The rest of the false positives do not have such a clear explanation. Tuning the fingerprint parameters could reduce them but would also reduce the detection rate.

6.3.3 *Anomaly Detection Results*

After running the experiments as previously described, the results from different days were combined, and an ROC curve was plotted for each of the parameter combinations. The curves are shown in Figure 3. Marked in each plot is the point where the threshold is equal to 0.5.

All parameter combinations showed high levels of performance, with an area under the ROC curve (AUC) of over 0.99. However, that metric by itself is deceiving, given the highly unbalanced nature of the dataset. In reality, the model was able to detect all 14 malicious hosts with thresholds between 0.5 to 5.5 under most parameter configurations, but it reported a decreasing number of false positives as the threshold increased. Nonetheless, the relative variation was small in terms of the total number of benign hosts in the dataset.

Although not distinguishable from the ROC curves, the behaviour observed for the previous dataset with regards to the bin width can also be observed for this dataset when analyzing the other metrics, with values of 1 and 2 resulting in a better performance on average than the others. However, the benefit of a longer time window parameter is not as clear for this dataset, which shows a more mixed performance with different values for this parameter.

Based on that, we selected a threshold of 5, bin width of 1 and time window size of 12 hours for further discussion. Table 12 shows the daily and combined results of the model under that specific parameter combination.

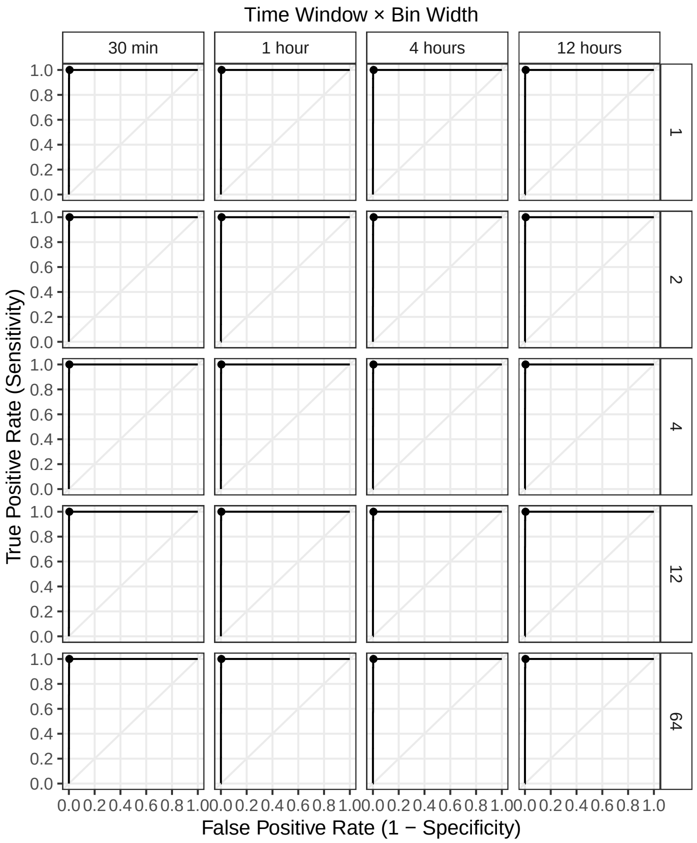

Figure 3: ROC curves of proposed scheme under different parameter combinations for the CIC-IDS2017 dataset. The point in each plot marks where the threshold is equal to 0.5.

Table 12: Performance of the proposed anomaly detection model for the CIC-IDS2017 dataset

Day	TP	TN	FP	FN	TPR	FPR	F1	BM	MCC
Day 1	1	8481	16	0	1.00	0.01	0.11	0.99	0.24
Day 2	1	9001	15	0	1.00	0.01	0.12	0.99	0.25
Day 3	2	8529	14	0	1.00	0.01	0.22	0.99	0.35
Day 4	10	8313	8	0	1.00	0.01	0.71	0.99	0.75
Comb.	14	34324	53	0	1.00	0.01	0.34	0.99	0.46

As can be seen, under the selected parameters, the model was able to detect all malicious hosts in all days with a relatively low number of false positives. As a point of comparison, using the same parameters as the previous dataset (threshold of 0.5 and bin width of 2) would not affect the number of true positives but would result in an extra 145 false positives and only slightly worse performance.

Because of the very small prevalence of malicious hosts in the dataset, the observed performance resulted in a low F1-score and a medium MCC for all days except day 4, which had a higher number of malicious hosts that can compensate for the false positives. Conversely, the BM was above 0.99 for all four days.

In summary, the scheme obtained very good results for this dataset with a varied number of parameter configurations. This shows that the scheme is suitable for detecting malicious behaviour when the prevalence of malicious hosts is low and, therefore anomalous.

6.3.4 *Ensemble Classification Results*

As with the previous dataset, the ensemble classification using the *and* rule resulted in the same predictions as the fingerprint matching shown in Table 10, while the the ensemble classification using the *or* rule resulted in the same predictions as the anomaly detection. These are summarized in Table 12.

This again shows that hosts that were classified as malicious by fingerprint matching were also classified as malicious with the anomaly detection.

7 Conclusion

This paper presented an unsupervised ensemble intrusion detection mechanism composed of two detection schemes, one signature-based that employs isomorphic subgraph matching of graphical patterns of known attacks, called attack fingerprints, and one anomaly-based, which consists of an anomaly score developed based on the work of Ferragut et al. [4].

To validate the proposed scheme we presented a collection of attack fingerprints for the AEN graph model, which were expressed using PGQL and covered common attacks, such as port scanning, DoS and password guessing, along with a subgraph matching algorithm specific for finding subgraphs isomorphic to the fingerprints. Furthermore, a total of 15 anomaly features, including nine extracted from session data and six extracted from authentication data.

The proposed schemes were evaluated individually and as an ensemble in the capacity for identifying malicious hosts using two datasets: The ISOT-CID Phase 1 dataset and the CIC-IDS2017 dataset.

The evaluation of the fingerprint matching scheme showed a combined precision of 0.99 and a combined sensitivity of 0.35 for the former dataset, while the latter dataset resulted in a combined precision of 0.44 and a combined sensitivity of 0.57. The observed results are promising, particularly considering the limited number of fingerprints available and the specific types of errors encountered. Ultimately, they demonstrate that the method is capable of identifying known attacks and is particularly suited to identifying stealth attacks, which is a weakness of traditional signature-based intrusion detection systems.

The evaluation of the anomaly detection was particularly encouraging for the CIC-IDS2017 dataset, with a BM of over 0.99 and an MCC of 0.46. This shows that the scheme has a high capacity for detecting anomalous behaviour when there was a low prevalence of malicious elements in the network.

The evaluation of the ensemble classification showed that one classifier could end up dominating the ensemble classification. This underscores the need for future exploration of possible benefits from using ensemble classification rules, such as soft voting.

As limitations, we identified the amount of effort needed to create the fingerprints, the binning of the values anomaly features that can result in suboptimal distributions and the high computational power required to build and maintain the graph. Another limitation is the high computation cost involved in searching for isomorphic subgraphs given the high complexity of the subgraph matching algorithms, although the use of indexes helps alleviate that issue with the cost of extra memory requirements.

In our future work, we aim to improve and extend the proposed fingerprint database to add other types of attacks, particularly those that are traditionally harder to detect, such as HTTP request smuggling, and to increase the feature space of the anomaly detection model by introducing more features. We believe this can help improve detection accuracy, particularly in environments that have a high prevalence of malicious hosts.

We also plan to implement more advanced classification rules as part of the anomaly detection scheme and also in the ensemble classification of the two detection schemes. In addition, we plan to employ adaptive bin width values according to the value range of each given variable to improve the fitness of the bin distributions.

Finally, we aim to conduct further evaluations using other datasets, such as the ISOT-CID Phase 2 dataset and the 2018 CIC Intrusion Detection Evaluation Dataset (CSE-CIC-IDS2018) [51].

References

[1] C. Nie, P. G. Quinan, I. Traoré, I. Woungang, "Intrusion Detection using a Graphical Fingerprint Model," in 2022 22nd IEEE International Symposium on Cluster, Cloud and Internet Computing (CCGrid), 806–813, 2022, doi:10.1109/CCGrid54584.2022.00095.

[2] R. Sommer, V. Paxson, "Outside the Closed World: On Using Machine Learning for Network Intrusion Detection," in Proceedings of the 2010 IEEE Symposium on Security and Privacy, SP '10, 305–316, IEEE Computer Society, Washington, DC, USA, 2010, doi:10.1109/SP.2010.25.

[3] A. Aldribi, I. Traoré, B. Moa, O. Nwamuo, "Hypervisor-based cloud intrusion detection through online multivariate statistical change tracking," Computers & Security, **88**, 2020, doi:10.1016/j.cose.2019.101646.

[4] E. M. Ferragut, J. A. Laska, R. A. Bridges, "A New, Principled Approach to Anomaly Detection," 2012 11th International Conference on Machine Learning and Applications, **2**, 210–215, 2012, doi:10.1109/ICMLA.2012.151.

[5] A. Aldribi, I. Traore, B. Moa, Data Sources and Datasets for Cloud Intrusion Detection Modeling and Evaluation, 333–366, Springer International Publishing, Cham, 2018, doi:10.1007/978-3-319-73676-1_13.

[6] I. Sharafaldin, A. H. Lashkari, A. A. Ghorbani, "Toward generating a new intrusion detection dataset and intrusion traffic characterization." in ICISSP, 108–116, 2018, doi:10.5220/0006639801080116.

[7] C. Phillips, L. P. Swiler, "A Graph-based System for Network-vulnerability Analysis," in Proceedings of the 1998 Workshop on New Security Paradigms, NSPW '98, 71–79, ACM, New York, NY, USA, 1998, doi:10.1145/310889.310919.

[8] O. Sheyner, S. Haines, Jand Jha, R. Lippmann, J. M. Wing, "Automated generation and analysis of attack graphs," in Proceedings of the Symposium on Security and Privacy, IEEE, 2002, doi:10.1109/SECPRI.2002.1004377.

[9] S. Jha, O. Sheyner, J. Wing, "Two formal analyses of attack graphs," in Proceedings 15th IEEE Computer Security Foundations Workshop. CSFW-15, 49–63, 2002, doi:10.1109/CSFW.2002.1021806.

[10] X. Ou, G. Sudhakar, A. A. W., "MulVAL: A Logic-based Network Security Analyzer," in Proceedings of USENIX Security Symposium, volume 8, 2005, doi:10.5555/1251398.1251406.

[11] K. Ingols, R. Lippmann, K. Piwowarski, "Practical Attack Graph Generation for Network Defense," in 2006 22nd Annual Computer Security Applications Conference (ACSAC'06), 121–130, 2006, doi:10.1109/ACSAC.2006.39.

[12] L. Akoglu, H. Tong, K. D., "Graph based Anomaly Detection and Description: A Survey," Journal Data Mining and Knowledge Discovery, **29**(3), 626–688, 2015, doi:10.1007/s10618-014-0365-y.

[13] F. Jemili, M. Zaghdoud, M. B. Ahmed, "Intrusion detection based on "Hybrid" propagation in Bayesian Networks," 2009 IEEE International Conference on Intelligence and Security Informatics, 137–142, 2009, doi:10.1109/ISI.2009.5137285.

[14] P. Xie, J. H. Li, X. Ou, P. Liu, R. Levy, "Using Bayesian networks for cyber security analysis," 2010 IEEE/IFIP International Conference on Dependable Systems & Networks (DSN), 211–220, 2010, doi:10.1109/DSN.2010.5544924.

[15] L. Xiao, Y. Chen, C. K. Chang, "Bayesian Model Averaging of Bayesian Network Classifiers for Intrusion Detection," 2014 IEEE 38th International Computer Software and Applications Conference Workshops, 128–133, 2014, doi:10.1109/COMPSACW.2014.25.

[16] K. K. Gupta, B. Nath, K. Ramamohanarao, "Conditional Random Fields for Intrusion Detection," in 21st International Conference on Advanced Information Networking and Applications Workshops (AINAW'07), volume 1, 203–208, IEEE, 2007, doi:10.1109/AINAW.2007.126.

[17] H. Ma, Y. Xie, S. Tang, J. Hu, X. Liu, "Threat-Event Detection for Distributed Networks Based on Spatiotemporal Markov Random Field," IEEE Transactions on Dependable and Secure Computing, **19**(3), 1735–1752, 2022, doi:10.1109/TDSC.2020.3036664.

[18] K. Peng, V. C. M. Leung, L. Zheng, S. Wang, C. Huang, T. Lin, "Intrusion Detection System Based on Decision Tree over Big Data in Fog Environment," Wireless Communication and Mobile Computing, **2018**, 2018, doi:10.1155/2018/4680867.

[19] C. Yin, Y. Zhu, J. long Fei, X.-Z. He, "A Deep Learning Approach for Intrusion Detection Using Recurrent Neural Networks," IEEE Access, **5**, 21954–21961, 2017, doi:10.1109/ACCESS.2017.2762418.

[20] Y. Zhang, P. Li, X. Wang, "Intrusion Detection for IoT Based on Improved Genetic Algorithm and Deep Belief Network," IEEE Access, **7**, 31711–31722, 2019, doi:10.1109/ACCESS.2019.2903723.

[21] Z. Wang, Y. Zeng, Y. Liu, D. Li, "Deep Belief Network Integrating Improved Kernel-Based Extreme Learning Machine for Network Intrusion Detection," IEEE Access, **9**, 16062–16091, 2021, doi:10.1109/ACCESS.2021.3051074.

[22] S. A. Cook, "The complexity of theorem-proving procedures," in Proceedings of the third annual ACM symposium on Theory of computing, 151–158, 1971, doi:10.1145/800157.805047.

[23] J. E. Hopcroft, J.-K. Wong, "Linear time algorithm for isomorphism of planar graphs (Preliminary Report)," in Proceedings of the sixth annual ACM symposium on Theory of computing, 172–184, 1974, doi:10.1145/800119.803896.

[24] J. R. Ullmann, "An algorithm for subgraph isomorphism," Journal of the ACM (JACM), **23**(1), 31–42, 1976, doi:10.1145/321921.321925.

[25] L. P. Cordella, P. Foggia, C. Sansone, M. Vento, "A (sub)graph isomorphism algorithm for matching large graphs," IEEE Transactions on Pattern Analysis and Machine Intelligence, **26**, 1367–1372, 2004, doi:10.1109/TPAMI.2004.75.

[26] W.-S. Han, J. Lee, J.-H. Lee, "Turboiso: towards ultrafast and robust subgraph isomorphism search in large graph databases," in SIGMOD '13, 2013, doi:10.1145/2463676.2465300.

[27] M. Han, H. Kim, G. Gu, K. Park, W.-S. Han, "Efficient Subgraph Matching: Harmonizing Dynamic Programming, Adaptive Matching Order, and Failing Set Together," Proceedings of the 2019 International Conference on Management of Data, 2019, doi:10.1145/3299869.3319880.

[28] P. G. Quinan, I. Traoré, I. Woungang, "Activity and Event Network Graph and Application to Cyberphysical Security," in I. Traoré, I. Woungang, S. Saad, editors, Artificial Intelligence for Cyber-Physical Systems Hardening, chapter 10, 217–233, Springer, 2022, doi:10.1007/978-3-031-16237-4_10.

[29] O. van Rest, S. Hong, J. Kim, X. Meng, H. Chafi, "PGQL: a property graph query language," in GRADES '16, 2016, doi:10.1145/2960414.2960421.

[30] N. Francis, A. Green, P. Guagliardo, L. Libkin, T. Lindaaker, V. Marsault, S. Plantikow, M. Rydberg, P. Selmer, A. Taylor, "Cypher: An Evolving Query Language for Property Graphs," Proceedings of the 2018 International Conference on Management of Data, 2018, doi:10.1145/3183713.3190657.

[31] M. H. Bhuyan, D. K. Bhattacharyya, J. K. Kalita, "Surveying Port Scans and Their Detection Methodologies," The Computer Journal, **54**, 1565–1581, 2011, doi:10.1093/comjnl/bxr035.

[32] S. Staniford, J. A. Hoagland, J. M. McAlerney, "Practical Automated Detection of Stealthy Portscans," Journal of Computer Security, **10**, 105–136, 2002, doi:10.3233/JCS-2002-101-205.

[33] M. De Vivo, E. Carrasco, G. Isern, G. O. de Vivo, "A review of port scanning techniques," ACM SIGCOMM Computer Communication Review, **29**(2), 41–48, 1999, doi:10.1145/505733.505737.

[34] J. Mirkovic, P. L. Reiher, "A taxonomy of DDoS attack and DDoS defense mechanisms," Comput. Commun. Rev., **34**, 39–53, 2004, doi:10.1145/997150.997156.

[35] R. Tandon, "A Survey of Distributed Denial of Service Attacks and Defenses," ArXiv, **abs/2008.01345**, 2020, doi:10.48550/arXiv.2008.01345.

[36] E. Cambiaso, G. Papaleo, G. Chiola, M. Aiello, "Slow DoS attacks: definition and categorisation," International Journal Trust Management in Computing and Communications, **1**, 300–319, 2013, doi:10.1504/IJTMCC.2013.056440.

[37] M. Bogdanoski, T. Suminoski, A. Risteski, "Analysis of the SYN flood DoS attack," International Journal of Computer Network and Information Security (IJCNIS), **5**(8), 1–11, 2013, doi:10.5815/IJCNIS.2013.08.01.

[38] V. K. Yadav, M. C. Trivedi, B. Mehtre, "DDA: an approach to handle DDoS (Ping flood) attack," in Proceedings of International Conference on ICT for Sustainable Development, 11–23, Springer, 2016, doi:10.1007/978-981-10-0129-1_2.

[39] T. H. Ptacek, T. N. Newsham, "Insertion, Evasion, and Denial of Service: Eluding Network Intrusion Detection," Technical report, Secure Networks inc Calgary Alberta, 1998.

[40] "Transmission Control Protocol," RFC 793, 1981, doi:10.17487/RFC0793.

[41] MazeBolt, "Layer 4 — MazeBolt Knowledge Base," .

[42] A. Bijalwan, M. Wazid, E. S. Pilli, R. C. Joshi, "Forensics of random-UDP flooding attacks," Journal of Networks, **10**(5), 287, 2015, doi:10.4304/jnw.10.5.287-293.

[43] I. Sreeram, V. P. K. Vuppala, "HTTP flood attack detection in application layer using machine learning metrics and bio inspired bat algorithm," Applied Computing and Informatics, 2019, doi:10.1016/j.aci.2017.10.003.

[44] C. Paar, J. Pelzl, B. Preneel, "Understanding Cryptography: A Textbook for Students and Practitioners," 2010, doi:10.1007/978-3-642-04101-3.

[45] D. Wang, Z. Zhang, P. Wang, J. Yan, X. Huang, "Targeted online password guessing: An underestimated threat," in Proceedings of the 2016 ACM SIGSAC conference on computer and communications security, 1242–1254, 2016, doi:10.1145/2976749.2978339.

[46] Mitre, "Brute Force: Password Spraying," .

[47] M. Patton, E. Gross, R. Chinn, S. Forbis, L. Walker, H. Chen, "Uninvited connections: a study of vulnerable devices on the internet of things (IoT)," in 2014 IEEE joint intelligence and security informatics conference, 232–235, IEEE, 2014, doi:10.1109/JISIC.2014.43.

[48] G. Tandon, P. K. Chan, "Tracking user mobility to detect suspicious behavior," in Proceedings of the 2009 SIAM International Conference on Data Mining, 871–882, SIAM, 2009, doi:10.1137/1.9781611972795.75.

[49] A. Luque, A. Carrasco, A. Martín, A. de las Heras, "The impact of class imbalance in classification performance metrics based on the binary confusion matrix," Pattern Recognit., **91**, 216–231, 2019, doi:10.1016/j.patcog.2019.02.023.

[50] D. Chicco, G. Jurman, "The advantages of the Matthews correlation coefficient (MCC) over F1 score and accuracy in binary classification evaluation," BMC Genomics, **21**, 2020, doi:10.1186/s12864-019-6413-7.

[51] Canadian Institute for Cybersecurity, "CSE-CIC-IDS2018 on AWS: A collaborative project between the Communications Security Establishment (CSE) & the Canadian Institute for Cybersecurity (CIC)," .

Advances in Science, Technology and Engineering Systems Journal Vol. 8, No. 2, 64-70 (2023)

www.astesj.com

Special Issue on Computing, Engineering and Multidisciplinary Sciences

ASTESJ

ISSN: 2415-6698

Omni-directional Multi-view Image Measurement System in the Co-sphere Framework

Yung-Hsiang Chen[1,2], Jin H. Huang[*,3]

[1]*Ph.D. Program of Mechanical and Aeronautical Engineering, Feng Chia University, Taichung, 407102, Taiwan*

[2]*Aeronautical Systems Research Division, National Chung-Shan Institute of Science and Technology, Taichung, 407102, Taiwan*

[3]*Department of Mechanical Engineering, Feng Chia University, Taichung, 407102, Taiwan*

ARTICLE INFO

Article history:
Received: 26 December, 2022
Accepted: 22 February, 2023
Online: 11 March, 2023

Keywords:
3D Reconstruction
Camera Calibration
Multi-view Image
Stereo camera

ABSTRACT

This study presents an "Omnidirectional multi-view image measurement system", which can be used to provide multi-camera 3D reconstruction and multi-view image information. Its characteristic is that four cameras take images from multiple perspectives in the co-sphere framework. The C_0 is the middle camera fixed as the geometric center point of measurement, and provides a front image. The other three cameras C_1~C_3 provide side images, and the co-circular spheres are separated by 120 degrees to extend the circle. The arc rod adjusts the multi-angle imaging. Place the multi-view camera in the arc track and move to the specified position in the sphere to position and capture images. By changing the angle between the cameras, the range of images captured by the cameras can be changed. If the multi-view images of four cameras C_0, C_1, C_2 and C_3 are captured at the same time, a stereo camera pair can be formed by any two cameras. The stereo camera pair C_0-C_1, C_0-C_2 and C_0-C_3 can be compiled by using the parallax principle of left and right images matching. Finally, through the demonstration and verification of camera calibration and 3D reconstruction, it can be used for all-round multi-view image measurement.

1. Introduction

The optical measurement method has the characteristics of global, non-contact, non-destructive, high measurement accuracy and real-time measurement, and is a very important part in the field of experimental mechanics. Among them, the advantage of non-contact is that it will not cause damage to the object to be measured, and high precision and real-time measurement are very important measurement characteristics for the industry that pursues light, thin and small for research and development. Therefore, combining these advantages, Optical metrology has gradually become one of the current research focuses. The advantage of non-contact is that it will not cause damage to the object to be measured, and high precision and real-time measurement are very important. Combined these advantages, the optical quantity Measurement has gradually become one of the current research focuses. There are many optical measurement methods, such as Electronic Speckle Pattern Interferometry (ESPI), Photoelastic Method, Shadow Moiré Method and Digital Image Correlation (DIC).

When using these optical measurement methods, different cameras are usually used together with image processing technology for research and analysis. There are many stereo vision systems for 3D reconstruction applications [2-6]. For example, in [7], the author presented the 3D-DIC method with stereo vision. The combination of DIC method and 3D stereo vision, that can be applied to 3D deformation measurement and becomes the basic framework of 3D-DIC method. The 3D-DIC method is applied to the surface profile measurement research. Whether it is applied to 3D-DIC measurement or other non-contact image measurement systems, the camera structure is mostly composed of two cameras connected by a horizontal bracket. The distance and angle between them make the images overlap within a certain range. When the measurement range exceeds the visible range of the two image capture devices, only partial images of the object can be captured. The occlusion area is the camera cannot directly observe the measurement object. The camera posture must be adjusted according to the different shapes of the object, and the image capture device must be re-installed. In camera calibration

---

[*] Corresponding Author: Jin H. Huang, Department of Mechanical Engineering, Feng Chia University, Taichung, Taiwan, email: jhhuang@fcu.edu.tw

“ This paper is an extension of work originally presented in 2022 IEEE International Conference on Consumer Electronics - Taiwan [1]”

https://dx.doi.org/10.25046/aj080207

procedure, the range of camera angle of view and the need for continuous calibration of the adjusted camera are application constraints. It is necessary to simplify and repeat the definition of the relationship between the coordinates of the calibration measurement system and the object to be measured.

In order to solve the visible range of the two image problems, some scholars proposed a dual-axis parallel motion mechanism with two degrees of freedom of vertical motion and horizontal motion [8]. The device uses a servo motor as a positioning control, and is mounted on a camera device, which can precisely control the camera's imaging angle. Each servo motor of the X and Y axes operates independently, and will not become the load of another servo motor for image capture and analysis. Those three cameras to build a co-circular geometric multi-camera imaging platform system [9], connect the three cameras in series with a semi-circular measuring rod, make the optical axes of the multi-cameras co-intersect at a point in space, and the distance between the cameras. The mechanism can be used to adjust the spacing along the semi-circular measuring rod. With the superimposition feature of multiple cameras, the system can increase the range of overlapping areas of 3D reconstruction feature points and the correction parameters established inside, and simplify the complex correction procedures required for on-site measurement and reconstruction of 3D information, expanding the original 3D-DIC observation. The scope of field of view, and simplify the procedure of repeatedly defining and determining the relationship between the coordinates of the calibration measurement system and the object to be measured. According to the application of displacement and strain measurement, when observing objects of different sizes, as long as the camera distance is adjusted, it can be applied to reconstruct the three-dimensional space information of the object, and explore and increase the image data of the three-dimensional scene object in the overlapping area.

2. Research methods

The development of image measurement is bound to develop towards global, large-scale and rapid measurement. In order to meet practical purposes, multi-view images cannot be measured by only one or two cameras. It is necessary to develop an all-round multi-view image measurement system. The development of a multi-view large-scale measurement system is a very important topic. Based on this, this study proposes omnidirectional multi-camera 3D reconstruction and provide multi-view images.

In the application of 3D vision, two images taken at different positions are generally used, and the relative depth of the entire scene can be reconstructed from the 2D images. Developed 3D reconstruction products for non-contact image measurement of structural deformation. It is a system that uses two cameras to form a stereo vision measurement entity structure that can be used to measure the 3D global surface of an object. This technology uses the characteristics of the object surface as a surface comparison target to obtain 3D reconstruction measurements. When the measurement range exceeds the visible range of the two cameras, only partial images can be observed, and the area covered by the object cannot be measured.

In order to overcome the limitation of image occlusion, the "Omni-directional Multi-view Image Measurement System" with the co-sphere to solve the problem of object occlusion. The intersecting area can be increased by multiple cameras for 3D reconstruction. Provides a camera imaging device, which is convenient for shooting multiple sets of images. This device includes three arc measuring rods, so that the multi-camera circular motion can be captured by changing the movement of the multi-camera. That adjust the angle of the camera through the rotating seat. It is characterized in that multiple cameras are fixed on the arc frame, and the observation angle of the cameras is adjusted so that it has the characteristic of a co-sphere.

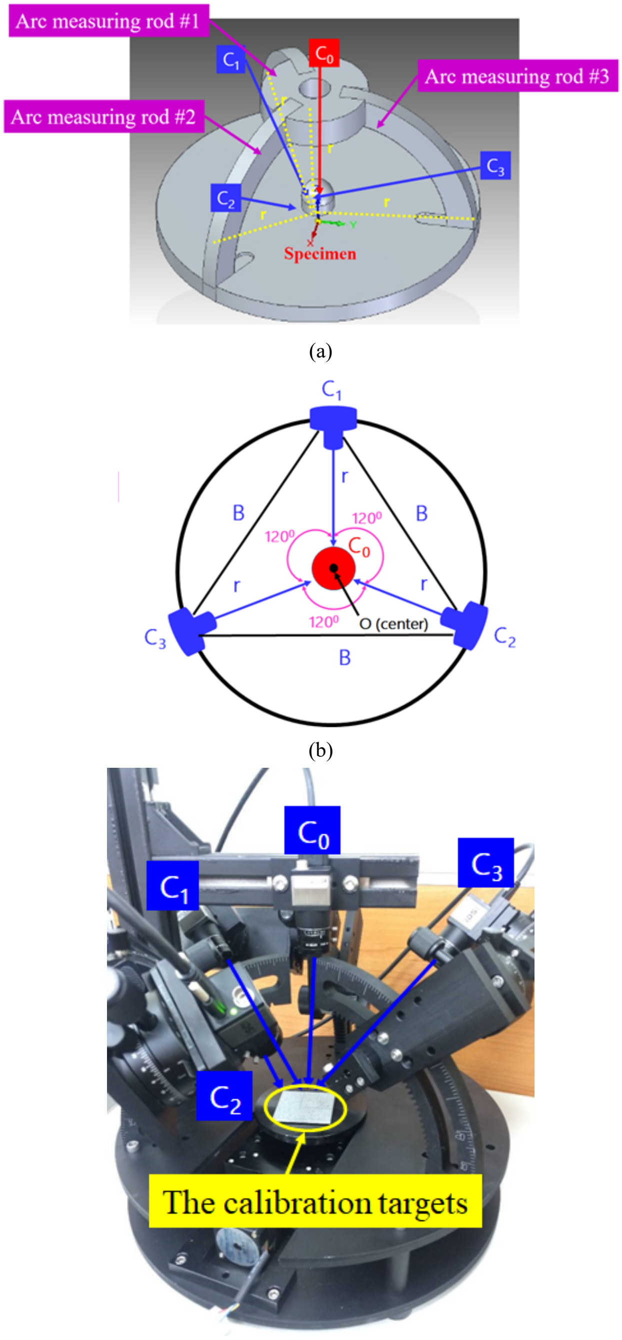

(a)

(b)

(c)

Figure 1: Omni-directional multi-view image measurement system

Figure 1 is the proposed omni-directional multi-view image measurement system. The C_0 is the middle camera fixed as the geometric center point of measurement, and provides a front image. The other three cameras C_1~C_3 provide side images, and the co-circular spheres are separated by 120 degrees to extend the circle. The arc rod adjusts the multi-angle imaging. Place the multi-view camera in the arc track and move to the specified position in the sphere to position and capture images. By changing the angle between the cameras, the range of images captured by the cameras can be changed. If the multi-view images of four cameras C_0, C_1, C_2 and C_3 are captured at the same time, a stereo camera pair can be formed by any two cameras. The stereo camera pair C_0-C_1, C_0-C_2 and C_0-C_3 can be compiled by using the parallax principle of left and right images matching. Table 1 is omni-directional multi-view image measurement system specifications. Fig. 2 is four cameras captured the multi-angle images.

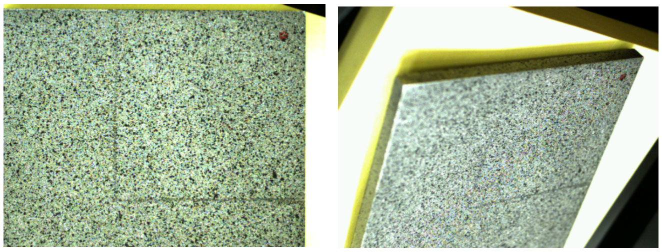

(a) C_0 image (b) C_1 image

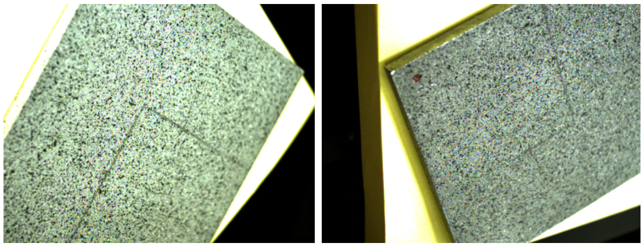

(c) C_2 image (d) C_3 image

Figure 2: Four cameras captured the multi-angle images.

The internal camera calibration parameter is the camera mapping relationship between the 3D calibration target point and the 2D image point in the camera coordinate system. The external camera calibration parameter is the camera refer to the rotation and translation relationship between the world coordinate system, where the target point is located and the camera coordinate system. Camera calibration is the process of obtaining the internal and external parameters of the camera, that are defined the corresponding relationship between the three-dimensional coordinates and the image pixels through the calibration points marked on the calibration target.

Table 1: Omni-directional multi-view image measurement system specifications

Specifications	**Characteristic**
Number of cameras	Four-camera multi-view image. The C_0 is the middle camera fixed as the geometric center point of measurement, and provides a front image. The other three cameras C_1~C_3 provide side images, and the co-circular spheres are separated by 120 degrees to extend the circle.
Camera	UI-3130CP Rev. 2 - IDS Imaging Development Systems GmbH, USB 3.0, CMOS, 575.0 fps, 800 × 600, 0.48 MPix, 1/3.6", ON Semiconductor, Global Shutter.
Lens	UH1220-10M, Focal Length: 12 mm, Aperture: f/2.0~C,Min. Working Distance: 10 cm, Distortion: <0.1%
Arc measuring rod	Three arc rods have a radius of 15 cm.
Measurable range	Measurable range: 3 cm × 3 cm × 3 cm (L×W×H), Minimum measurable resolution: 0.375 mm.
Dimension size	40 cm × 40 cm × 40 cm (L×W×H).
Power	110 V / 60 Hz.

In [10], the author presented a two-step correction method, using radially consistent constraints, so that the correction of camera internal parameters is not affected by radial distortion. The method requires a high-cost three-dimensional high-precision calibration target. In [11], the author proposed the plane calibration method, which is uses image coordinate estimation to obtain a two-dimensional homography matrix. The internal and external parameters of the camera calibration and the radial distortion coefficient can be linearly solved. In [12], the author proposed a camera calibration method based on one-dimensional camera calibration points. This study in order to collect 360° omni-directional image information, the polar coordinate system is used. The advantage of polar coordinates is that it can describe the system directivity of the azimuth angle position of single/multiple cameras relative to the calibration target on an image plane. In the polar coordinate system are represented by radius and angle, which are included cylindrical coordinate system and spherical coordinate system. Fig. 3 shows the spherical coordinate system and the hemispherical calibration model. A point P in the spherical coordinate system is defined by two angles φ, θ and radius r. The corresponding relationship between spherical coordinates $(\mathrm{r},\theta,\varphi)$ and rectangular coordinates (x,y,z) is as follows:

$$\begin{aligned} \mathrm{x} &= r\sin\theta\cos\varphi & \mathrm{r} &= \sqrt{x^2+y^2+z^2} \\ \mathrm{y} &= r\sin\theta\sin\varphi \ , & \theta &= \cos^{-1} z/r \\ \mathrm{z} &= r\cos\theta & \varphi &= \tan^{-1} y/x \end{aligned} \tag{1}$$

where, O is the origin point. r is the radius length coordinate value, that is the distance from point P to the coordinate center. φ is the coordinate value of the azimuth angle (0≤φ≤2π), that is the counterclockwise rotation angle from the X axis. θ is the elevation angle coordinate value (0≤θ≤π), that is the upward rotation angle from the XY plane.

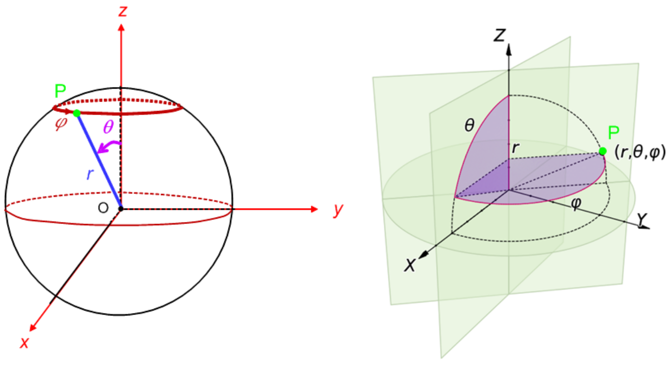

(a) spherical coordinate system

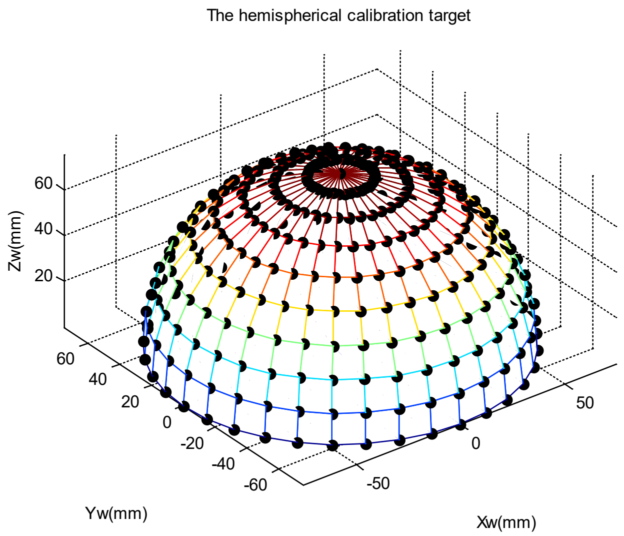

(c) hemispherical calibration model

Figure 3: The spherical coordinate system and the hemispherical calibration model

3. Experimental result

Fig. 4 is the calibration targets. Fig. 4(a) is a 30mm×30mm chess plane calibration target, which is composed of 9×9 square grids intersecting micro-dots with an equidistant distance of 5mm. Figure 4(b) is a hemispherical calibration target with a radius of 15mm and a height of 15mm, which is used to verify the feasibility of 3D reconstruction of the omnidirectional multi-view measurement system. Place the calibration piece in the middle of the measurement system, move the multi-camera in the arc track to the designated position in the sphere to position and take images, and change the range of images captured by the multi-camera by changing the angle between any two cameras .

(a) Chess-board (b) Hemispherical

Figure 4: The calibration targets

3.1. Omni-directional multi-camera calibration results

Calibrate each stereo pair separately using the checkerboard pattern of calibration target. To calibrated multi-camera system for stereo camera pair C_0-C_1, C_0-C_2 and C_0-C_3. The internal and external of multi-camera calibration parameters are showed as Table 2 and Table 3. That are respectively to find out the three-dimensional correspondence in space. Fig. 5 is the experimental result of omni-directional multi-camera calibration.

Fig. 5 (a) is the C_0-C_1 stereo camera as an example. The calibration parameters of the C_0 and C_1 single cameras are obtained respectively, and the C_0-C_1 stereo calibration parameters are obtained by binocular vision to find out the stereo correspondence in space. Similarly, another two sets of stereo cameras can be arranged to perform local three-dimensional reconstruction on C_0-C_2 and C_0-C_3. Finally, the multi-view cameras calibration and pose estimation are shown in Fig. 5(b).

Table 2: The internal camera calibration parameters

(a) C_0-C_1

Parameter	C_0	C_1
Principal point (u_0, v_0)	415.2, 277.1	403.7, 288
Focal length (fx, fy)	2593, 2593.2	2561.4, 2562.7
Skew	0.234	6.753
kappa 1	-0.038	0

(b) C_0-C_2

Parameter	C_0	C_2
Principal point (u_0, v_0)	416.5 , 271	410.3, 292.3
Focal length (fx, fy)	2619.5, 2619.9	2611.7, 2612.6
Skew	-0.012	-0.012
kappa 1	-0.043	-0.043

(c) C_0-C_3

Parameter	C_0	C_3
Principal point (u_0, v_0)	415.4, 265.1	364.2, 270.4
Focal length (fx, fy)	2618.3, 2618.5	2584.9 , 2585.2
Skew	0.006	-2.413
kappa 1	-0.041	-0.034

Table 3: The external of camera calibration parameters

(a) C_0-C_1

Parameter	Rotation [°]	Translation [mm]
X axis	41.38 ± 0.0031	94.36 ± 0.64
Y axis	-34.19 ± 0.0021	110.3 ± 0.76
Z axis	-7.591 ± 0.00014	87.28 ± 7.5
Baseline	169.405 mm	

(b) C_0-C_2

Parameter	Rotation [°]	Translation [mm]
X axis	-40.67 ± 0.0026	107 ± 0.35
Y axis	2.595 ± 0.00042	60.76 ± 0.15
Z axis	118.1 ± 0.00048	57.3 ± 3.2

Baseline	135.734 mm

(c) C_0-C_3

Parameter	Rotation [°]	Translation [mm]
X axis	18.32 ± 0.0048	93.07 ± 0.53
Y axis	38.01 ± 0.0064	83.63 ± 0.4
Z axis	-108.4 ± 0.0019	66.92 ± 7.8
Baseline	141.901 mm	

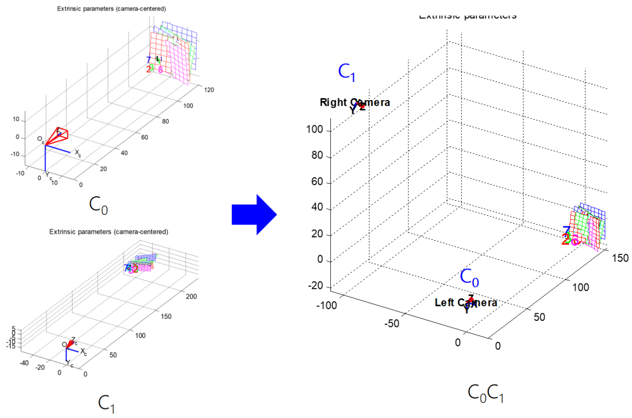

(a) Stereo camera C_0-C_1

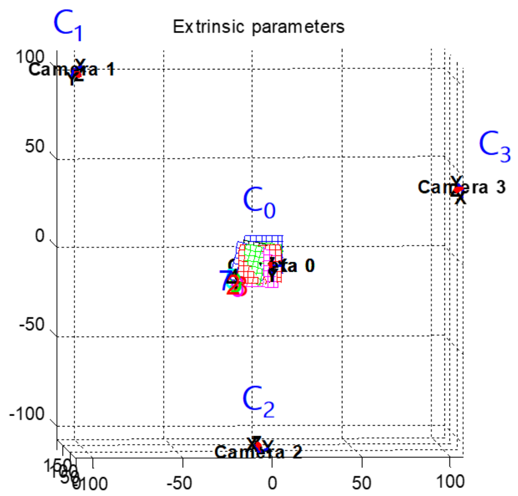

(b) Multi-view cameras

Figure 5: The experimental result of omni-directional multi-camera calibration.

3.2. Simulated omni-directional multi-camera image results

This study used the IDS UI-3130CP color camera as an example to discuss the calibration and 3D reconstruction of an omni-directional multi-view image measurement system. The omni-directional multi-camera image system is used to analyze the simulated omni-directional multi-camera image. Fig. 6 is IDS UI-3130CP color camera. Table 4 is IDS UI-3130CP color camera specifications. According to the optical design parameters of the measurement system: The image resolution is 800×600 pixels. The chip size of the image sensor is 4.8 μm×4.8 μm with a 12mm 1:2.0 1/1.8” lens. The best working distance is 15cm, and the simulation results can be measured within the working range of 3cm×3cm×3cm (L×W×H).

Figure 6: IDS UI-3130CP color camera

Table 4. IDS UI-3130CP color camera specifications

Name	**UI-3130CP Rev. 2**
Family	CP
Interface	USB 3.0
Sensor type	CMOS
Manufacturer	ON Semiconductor
Frame rate	396 fps
Resolution (h×v)	800×600 pixels
Optical Area	3.84 mm×2.88 mm
Shutter	Global Shutter
Optical class	1/3.6"
Resolution	0.48 MPix
Pixel size	4.8 μm×4.8 μm

Figure 7 is the simulated the setup of omni-directional multi-view measurement with four cameras. Fig. 8 is the simulated four cameras captured multi-view image. Four-camera multi-view image. The C_0 is the middle camera fixed as the geometric center point of measurement and provides a front image, is showed as Fig. 8(a). The other three cameras C_1~C_3 provide side images and the co-circular spheres are separated by 120 degrees to extend the circle, is showed as Fig. 8(b)-(d).

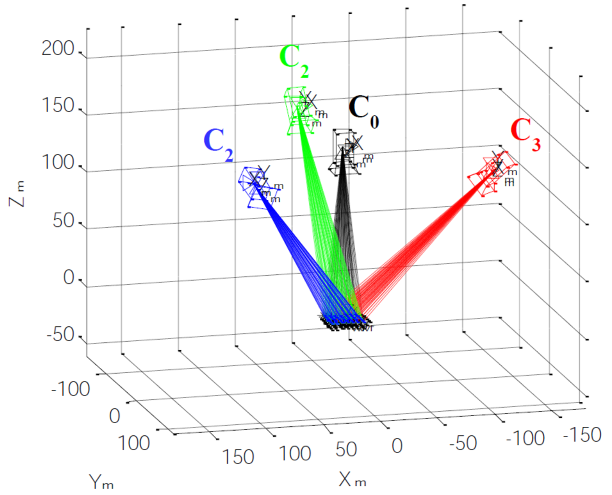

Figure 7: Simulated the setup of omni-directional multi-view measurement with four cameras

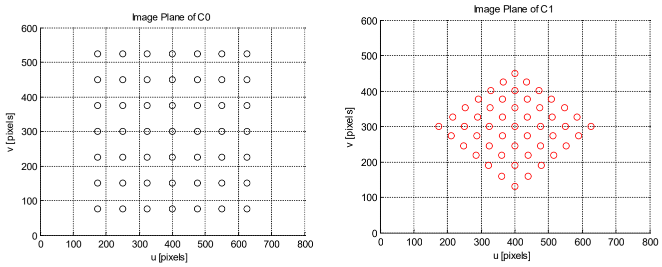

(a) C_0 simulated image (b) C_1 simulated image

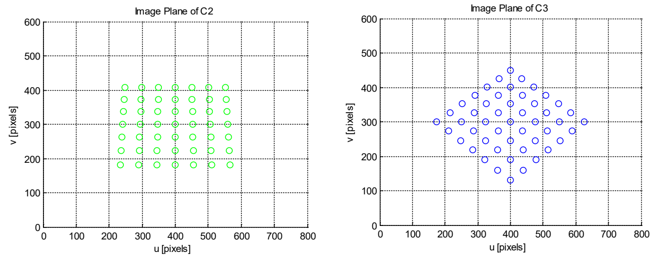

(c) C_2 simulated image (d) C_3 simulated image

Figure 8: Simulated four cameras captured multi-view image

3.3. Omni-directional multi-view 3D reconstruction results

The hemispherical calibration target is a radius of 15mm and a height of 15mm in the middle of the omnidirectional multi-view camera. The multi-view images of four cameras C_0, C_1, C_2, and C_3 through any two cameras to form a stereo camera pair. Using the principle of parallax matching of the left and right images, the stereo camera pair C_0-C_1, C_0-C_2, and C_0-C_3 can be compiled performs three-dimensional reconstruction of each part. We used the hemispherical calibration target for the omnidirectional 3D reconstruction. Fig. 9 is the omni-directional original multi-view images. Fig. 10 is the omni-directional multi-view of 3D reconstruction for hemispherical calibration target.

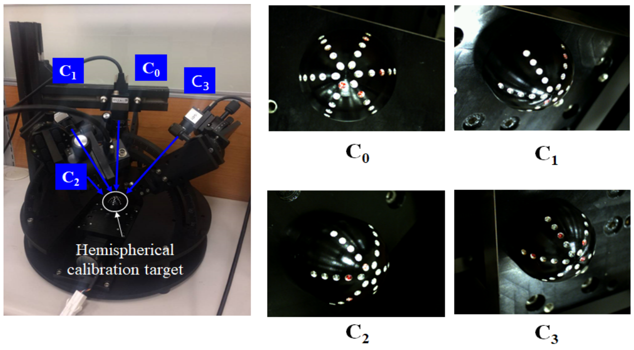

(a) Experimental setup (b) Original image

Figure 9: The omni-directional original multi-view images

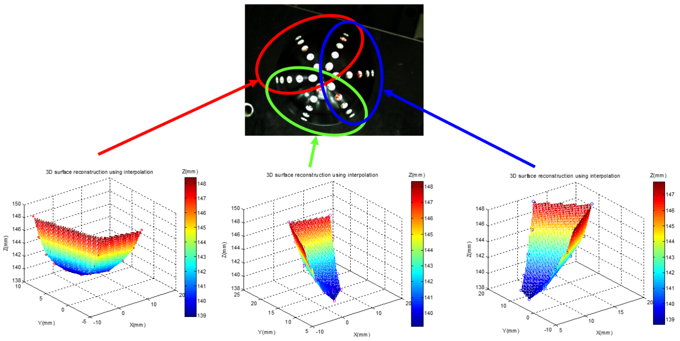

(a) C_0-C_1 (b) C_0-C_2 (c) C_0-C_3

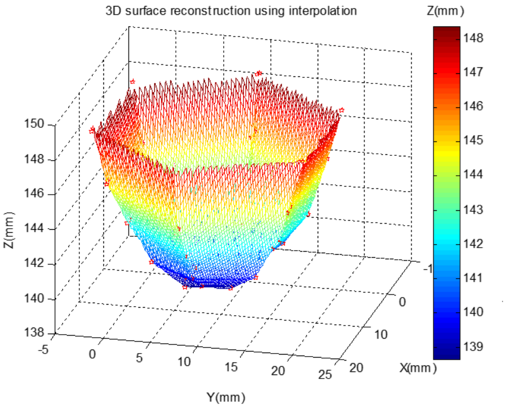

(d) Right-view of 3D

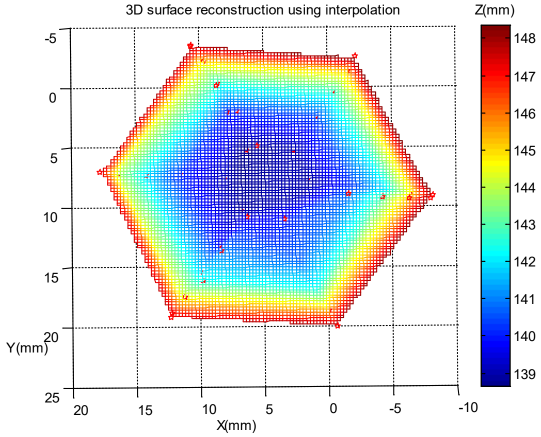

(e)Top-view of 3D

Figure 10: The omni-directional multi-view of 3D reconstruction for hemispherical calibration target

4. Conclusion

This research successfully developed an "omnidirectional multi-angle image measurement system". Any camera can move along the arc measuring rod to a designated position within the sphere to position and capture images. The three local 3D reconstructions of C_0-C_1, C_0-C_2, and C_0-C_3 are performed through the arrangement of stereo cameras, and the same position superposition calculation is performed, and the optimal 3D reconstruction calculation is performed using the ICP (Iterative Closest Point) iterative closest point algorithm. Finally, the 3D reconstruction experiment results of the 14.8 mm-high semicircular sphere calibration piece were obtained, and the measurement error was 1.3%. With the current best measurement working distance is 15 cm, the multi-angle imaging optical imaging analysis has been completed the measurement range of 3cm×3cm×3cm to 0.375 mm resolution.

Conflict of Interest

The authors declare no conflict of interest.

References

[1] Y.H. Chen, J.H. Huang, "Calibration and 3D reconstruction of omni-directional multi-view image measurement system," 2022 IEEE International Conference on Consumer Electronics - Taiwan, 591-592, 2022. DOI: 10.1109/ICCE-Taiwan55306.2022.9869096

[2] D. Murray, J.J. Little, “Using real-time stereo vision for mobile robot navigation,” Autonomous Robots, **8**(2), 161-171, 2000. DOI: 10.1023/A:1008987612352

[3] N.G. Oh, J.I. Cho, K. Park, “On performance enhancement of a following tracker using stereo vision,” ICCAS 2010, 1259-1262, 2010. DOI: 10.1109/ICCAS.2010.5669716

[4] E. Dandil, K.K. ÇEVİK, “Computer vision based distance meaurement system using stereo camera view,” 3rd International Symposium on Multidisciplinary Studies and Innovative Technologies (ISMSIT), 1-4, 2019. DOI: 10.1109/ISMSIT.2019.8932817

[5] J. Liu, J. Pan, N. Bansal, C. Cai, Q. Yan, X. Huang, Y. Xu., “PlaneMVS: 3D plane reconstruction from multi-view stereo,” In IEEE Conference on Computer Vision and Pattern Recognition (CVPR), 2022.

[6] Z. Yang, Z. Ren, Q. Shan, Q. Huang, “MVS2D: Efficient multiview stereo via attention-driven 2D convolutions,” Computer Vision and Pattern Recognition (or CVPR) 2022.

[7] P.F. Luo, Y.J. Chao, M.A. Sutton, W. H. Peters, “Accurate measurement of three-dimensional deformations in deformable and rigid bodies using computer vision”, Experimental Mechanics, **33**, 123-132, 1993. DOI: 10.1007/BF02322488

[8] Y.H. Chen, Y.S. Shiao, “Two axis independent parallel manipulators of control and stereo vision matching”, Journal of Industrial Education and Technology, **33**, 137-148, 2008.

[9] C.H. Hwang, W.C. Wang, Y.H. Chen, “Camera calibration and 3D surface reconstruction for multi-camera semi-circular DIC system”, International Conference on Optics in Precision Engineering and Nanotechnology (icOPEN2013), 8769, 123-132, 2013. DOI: 10.1117/12.2021044

[10] R. Y. Tsai, “A versatile camera calibration technique for high-accuracy 3D machine vision metrology using off-the-shelf TV cameras and lenses,” IEEE Journal of Robotics and Automation, **3**(4), 323-344, 1987. DOI: DOI: 10.1109/JRA.1987.1087109

[11] Z. Zhang, “A flexible new technique for camera calibration,” IEEE Transactions on Pattern Analysis and Machine Intelligence, **22**(11), 1330-1334, 2000.

[12] Z. Zhang, “Camera calibration with one-dimensional objects,” IEEE Transactions on Pattern Analysis and Machine Intelligence, **26**(7), 892- 899, 2004.

Advances in Science, Technology and Engineering Systems Journal Vol. 8, No. 2, 71-77 (2023)

www.astesj.com

Special Issue on Computing, Engineering and Multidisciplinary Sciences

ASTESJ

ISSN: 2415-6698

Detecting the Movement of the Pilot's Body During Flight Operations

Yung-Hsiang Chen[1,2], Chen-Chi Fan[1], Jin H. Huang[*,3]

[1]*Ph.D. Program of Mechanical and Aeronautical Engineering, Feng Chia University, Taichung, 407102, Taiwan*

[2]*Aeronautical Systems Research Division, National Chung-Shan Institute of Science and Technology, Taichung, 407102, Taiwan*

[3]*Department of Mechanical Engineering, Feng Chia University, Taichung, 407102, Taiwan*

ARTICLE INFO

Article history:
Received: 03 January, 2023
Accepted: 22 February, 2023
Online: 11 March, 2023

Keywords:
3D Space Trajectory
Aircraft Cockpit Design
Markerless Motion
Multi-view Image

ABSTRACT

This research presents a "Multi-camera for pilot's cockpit measurement system", which uses four multi-view images to eliminate the instrument and human body shielding and record the touched area. That could record the body reaction time (velocity and acceleration) and trajectory of the tested personnel. Real-time conversion of multi-view images corresponding to the 3D skeletal joint coordinate information of the human body, which measure the human-computer interaction human factors engineering integration of limb reaction time and trajectory measurement system. Finally, make prototypes, test and optimize, and achieve the research on the optimal cockpit touch area by conducting multi-view image simulation feasibility experiment framework and measurement process method. Using multiple depth-sensing cameras to perform low-cost, standardized automatic labeling of human skeleton joint dynamic capture.

1. Introduction

Considering human factors engineering design is the foundation of workplace planning and the basis for product design development. Its anthropometric data is very important for work and daily life, and the correct anthropometric data is of great help to workplace design, work planning and human-machine interface safety considerations. Due to the rapid development of camera technology in recent years, the image resolution has also been greatly improved. It can achieve a certain accuracy in experimental measurement applications. It can also be used for non-contact optical measurement with image analysis software. The human motion tracking technologies are included marker/markerless. Markerless motion applications are such as sports science. For example, in [2], the author presented captured of an athlete for sport research. The basic concept of digital photogrammetry is to locate the specific punctuation point of the measurement position in the image, compare the measurement punctuation position at different times, and then obtain the displacement of the measurement point. Camera measurement can get good measurement results as long as the punctuation points in the image are clearly visible. The image analysis method has the advantages of non-contact measurement method, and the influence of the local environment on the measurement is also very small. Therefore, this research chooses to apply the camera to develop the metrology technology.

In [3], the author presented the DIC (Digital Image Correlation) method with 3D stereo vision. The DIC method is applied to 3D deformation measurement. The 3D-DIC method is applied to the surface profile measurement research. Whether 3D-DIC or other non-contact image measurement systems is composed of stereo cameras. The distance and angle between two cameras overlap within a certain range. When the measurement range exceeds the visible range of the two image capture devices, only partial images of the object can be captured. The camera must be adjusted according to the different shapes of the object, and the image capture device must be re-installed. The range of camera angle of view and the need for continuous calibration of the adjusted camera are application constraints. It is necessary to simplify and repeat the definition of the relationship between the coordinates of the calibration measurement system and the object to be measured.

In order to solve the aforementioned problems, in [4], the author presented a two-axis parallel motion mechanism for

---

[*] Corresponding Author: Jin H. Huang, Department of Mechanical Engineering, Feng Chia University, Taichung, Taiwan, email: jhhuang@fcu.edu.tw

" This paper is an extension of work originally presented in 2022 IEEE International Conference on Consumer Electronics - Taiwan [1]"

https://dx.doi.org/10.25046/aj080208

vertical and horizontal motion. The device uses a servo motor as a positioning control, and is mounted on a camera device. That can precisely control the camera's imaging angle. Both X and Y axes operates are independently, and will not become the load of another servo motor for image capture and analysis. Using three cameras to build a semi-circular geometric multi-camera imaging platform system [5]. Those multi-camera are set with a semi-circular measuring rod and the optical axes of the multi-cameras co-intersect at a point in space. The mechanism can be used to adjust the spacing with the semi-circular measuring rod. With the superimposition feature of multiple cameras, the system can increase the range of overlapping areas of 3D reconstruction feature points and the correction parameters established inside. It's required for on-site measurement and reconstruction of 3D information. The field of view and simplify the procedure of repeatedly defining and determining the relationship between the coordinates of the calibration measurement system and the object to be measured.

The image analysis techniques and photogrammetric image acquisition are precisely and quickly measure. The 3D-based machine vision in metrology is popular. The aircraft pilot's cockpit design needs to meet pilots' feasibility in 5~95% of body figuration. MIL-STD-1333 [6] is defined the pilot's reach zone and MIL-STD-1472 [7] is defined schematic diagram of the pilot's cockpit reach zone area. The analysis of actions related for the pilot's reach zone. That is necessary to detect the human head and movement of the upper and lower limbs.

The conventional technology can only measure the static human body of a single person, and it is necessary to manually adjust the human body measurement data multiple times, manually select the measurement mark points, and manually edit and superimpose the 3D human body model. This innovative technology provides dynamic human trajectory calculation reaction time, and can automatically mark human bone joints and superimpose standardized 3D human joint coordinates.

Most studies discuss pilots' eye gaze strategies, is lack of pilot's movement monitoring with optical tracking in the aircraft cockpit [8-12]. The aim of this research evaluate human-computer interaction and human factors engineering on multi-camera for pilot's cockpit measurement system. Using multiple depth-sensing cameras to perform dynamic capture and record the reaction time and trajectory of the subject's limbs, including real-time conversion of multi-view images corresponding to the 3D skeletal joint coordinate information of the human body.

2. Research methods

Fig. 1 is the aircraft pilot's cockpit design for pilots' feasibility in 5~95% of body figuration. When pilot wear a flight suit, comfort, easy operation and visual display, are the requirement to be concerned. And the maneuverability of control and display of information have to be effectively functioned under the constant high G (gravity) force condition. At present, the evaluation of pilots' human factors engineering, is used the research of physical model and interview as the basis for the adjustment of the aircraft cockpit design. The information presents from the research is difficultly analyzed and takes lots of time and manpower. The common improper design of human factors engineering are showed as: over-sized helmet, close instrument panel, the pilot body touches the control lever, the hand is too short to reach the control lever, and the pilot's long foot touches the instrument panel.

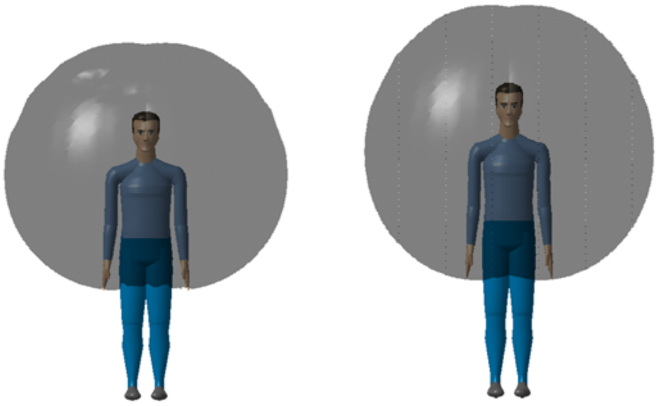

(a)5% (b)95%

Figure 1: The aircraft pilot's cockpit design for pilots' feasibility in 5~95% of body figuration

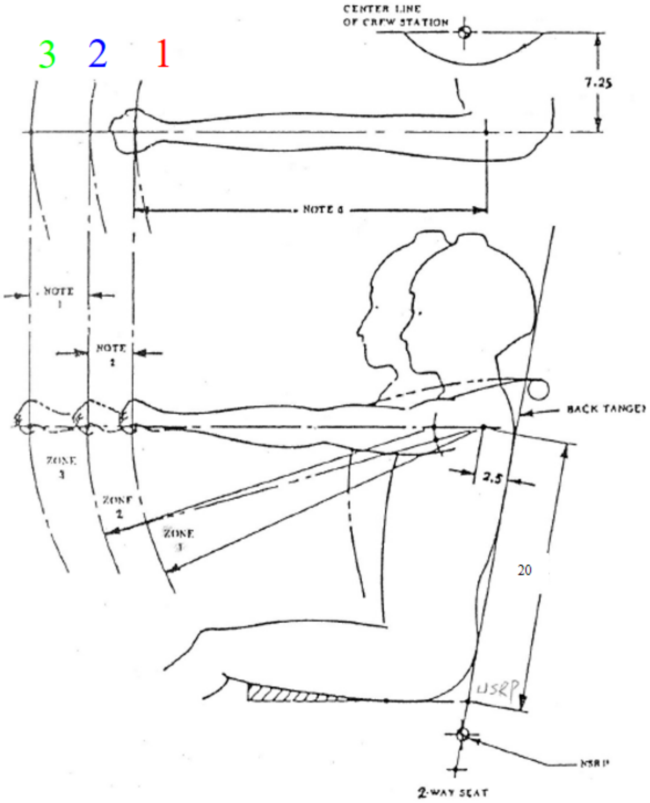

Figure 2: MIL-STD-1333 [6] is defined the pilot's reach zone.

Fig. 2 is MIL-STD-1333 [6], that defined pilot's reach zone. The pilot reach zones are divided into three areas. (1) ZONE 1 [Natural arm-reach mechanism zone (shoulder strap locked)]: Both hands can operate naturally to reach in ZONE 1, while shoulders are attached to the back of the seat, and arm and shoulder muscles do not need to be stretched forcefully. (2)ZONE 2[Maximum arm-reach mechanism zone (shoulder strap locked)]: The maximum arm-reach mechanism zone is defined while arm and shoulder muscles are stretched to the maximum. All the critical control devices in flight are included within ZONE 2.

(3)ZONE 3 [Maximum arm-reach mechanism zone (shoulder strap unlocked)]: The maximum mechanism arm-reach zone is defined while shoulders are as far forward as possible and arms fully reach. All the none-critical and none-essential control devices in flight are included within ZONE 3.

Fig 3 is MIL-STD-1472 [7] defined the touched area of aircraft cockpit. The motion of pilot's head and upper limbs are needed to detect in accord with the analysis of pilot's motion around touched area. To record and analyze the posture the pilot's upper body muscles touching the cockpit reach zone and motions around area, we proposed to use four cameras to build up a multi-view image. The pilot executes the instrument operation according to the instructions of different subjects. The system analyzes where each instrument should be located in tested pilot's touching area by image processing and motion detection of human upper limb.

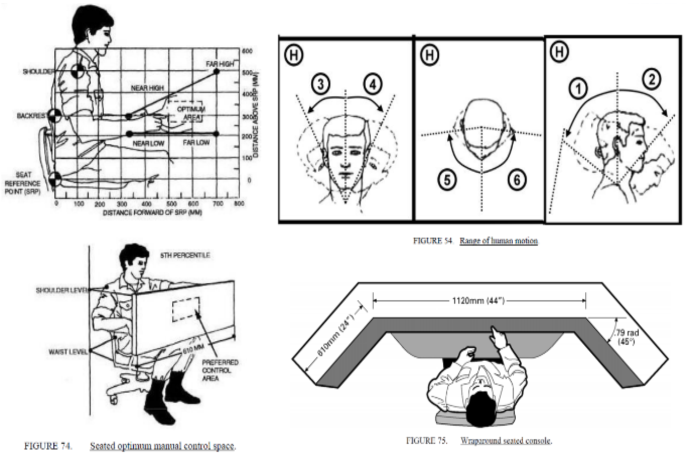

Figure 3: MIL-STD-1472 [7] defined the touched area of aircraft cockpit

Fig. 4 is the schematic diagram of multi-view image measurement system setup with human factors engineering. First, simulate the pilot operation in different positions and height of instrument panel. Then, utilize the concept of human skeleton detection to measure the position which the pilot reads or touches the instrument. Subsequently, develop an automatic measure evaluation system in pilot's reachable areas, with the utilization of multi-view imaging by four cameras and 3D machine vision method.

Fig. 5 is the multi-camera for pilot's cockpit measurement system. Using multiple depth image sensors to measure and track the operation of cockpit personnel with optical measurement technology, that measure pilot's reaction time and trajectory. Where, C_0 is placed in front of the pilot for pilot's head and eyes. C_1 is above the pilot's seat. The head is defined as the origin of the measurement. The reachable area of the upper limb in the X-Y plane is recorded in different conditions. Both C_2 and C_3 are arranged on the left and right sides of the pilot respectively. That is exclude the shielding of instruments and the human body and record the contact area of the X-Z plane. This technology proposes multi-view images to correspond to human body 3D skeletal joint coordinate information and explores human-computer interaction human factors engineering integration of limb reaction time and trajectory measurement system.

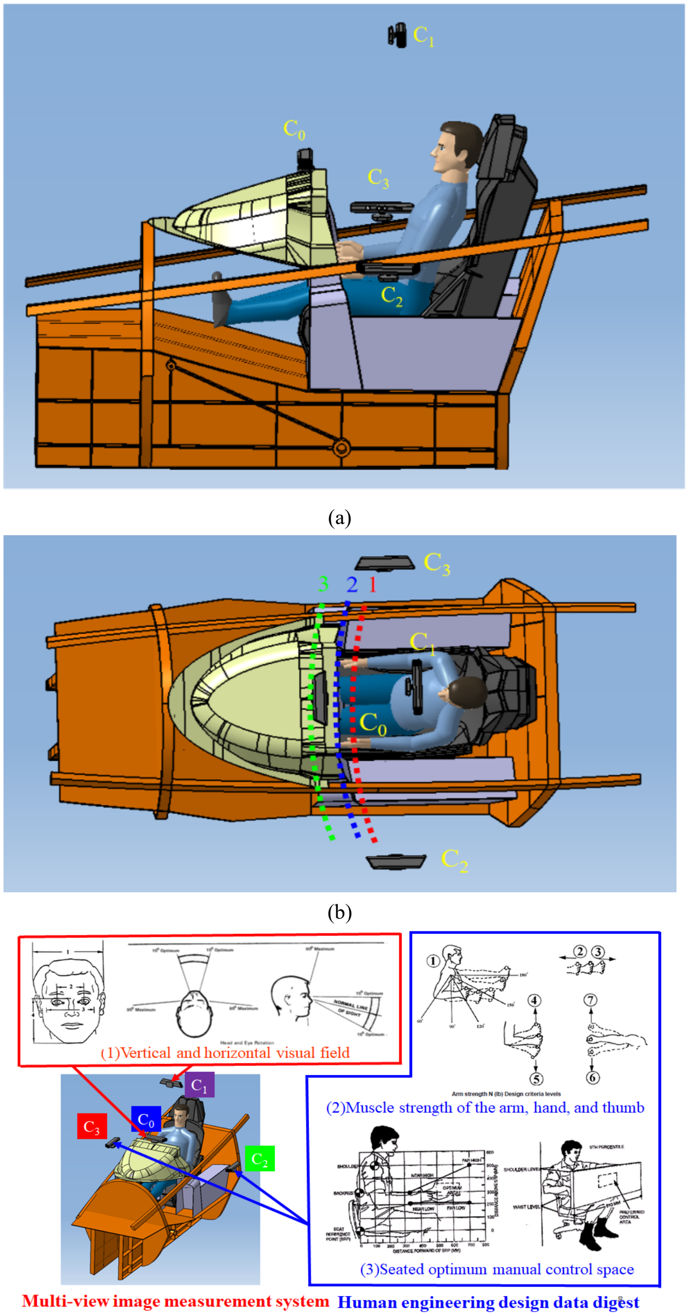

(a)

(b)

(c)

Figure 4: Schematic diagram of multi-view image measurement system setup with human factors engineering

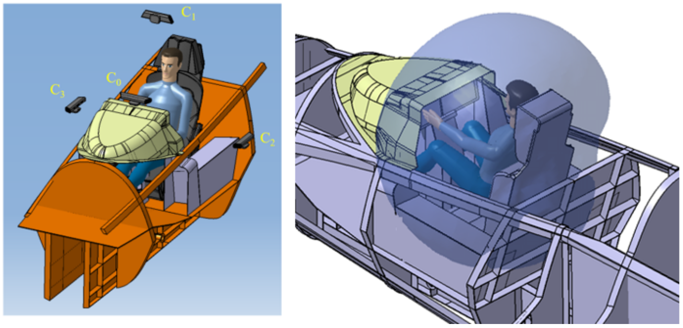

(a) Multi-camera for measured pilot's reaction time and trajectory

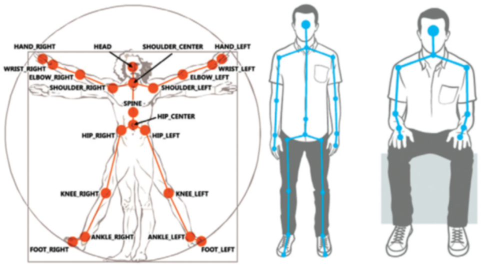

(b) human body 3D skeletal joint coordinate information

Figure 5: The multi-camera for pilot’s cockpit measurement system.

3. Experimental result

In order to verify the feasibility of a multi-view measurement system, the schematic diagram of simulated multi-view image setup is showed as Fig. 6. Where, fig 6(a) is a top view, Fig. 6(b) is a right view and Fig. 6(c) is a front view. Fig. 7 is the simulated multi-view image, in which Fig. 7(a) uses a hemispherical calibration target for 3D analysis, and the simulation result is shown in Fig. 7(b). The C_0 image is placed in front of the pilot to measure the head and eyes.

Fig. 7(c) is the C_1 image is on the top of the seat. The pilot’s head is defined as the measurement reference point. The upper limbs in the X-Y plane can be touched under different constraints with MIL-STD-1333 definition. Figs. 7(d) and (e) are C_2 and C_3 image respectively, which are installed on the left and right sides of the pilot. Those exclude the cockpit instruments and human body shielding and record the touched area on the X-Z plane.

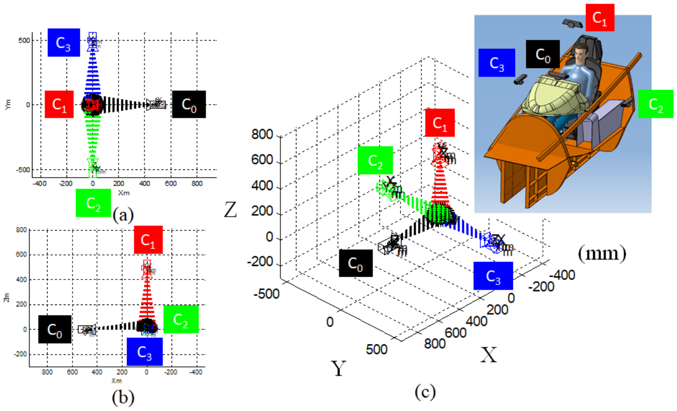

(a) (b) (c)

Figure 6: Schematic diagram of simulated multi-view image setup

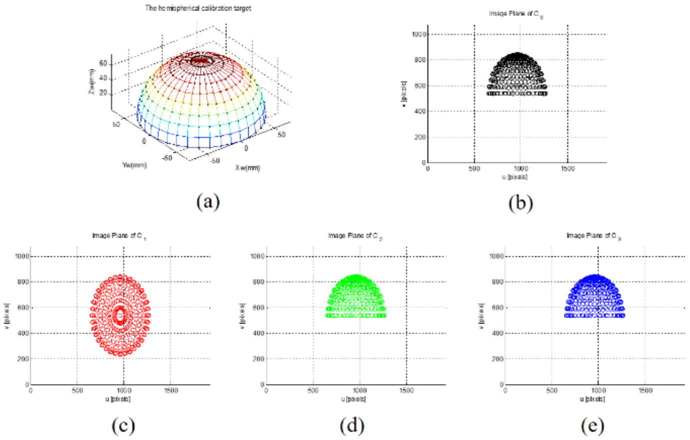

(a) (b) (c) (d) (e)

Figure 7: Simulated multi-view image

Fig. 8 shows that the Kinect camera includes a motor and color image (RGB camera in the middle). Those are include a 3D depth image (two lenses on the left and right), an infrared emitter, an infrared CMOS camera and sound (array microphone). 3D machine vision human skeleton detection results, as shown in Fig. 9. The Kinect camera defines the human skeleton joint coordinate map. This research selected Kinect camera to cost reduction. The Kinect v2 depth camera is cheap than high speed camera, and the measurement accuracy is mostly under 2 mm at 1.5 m [14]. Those condition would be meet our measurement system demonstration. The system utilizes four multi-view cameras to perform dynamic capture and record the reaction time and trajectory of the subject's limbs, including real-time conversion of multi-view images corresponding to the 3D skeletal joint coordinate information of the human body based on references. The proposed method have been practically tested in Figure 11. In Fig. 11 is captured 3D skeletal joint of the human body with Kinect.

(a) Physical diagram

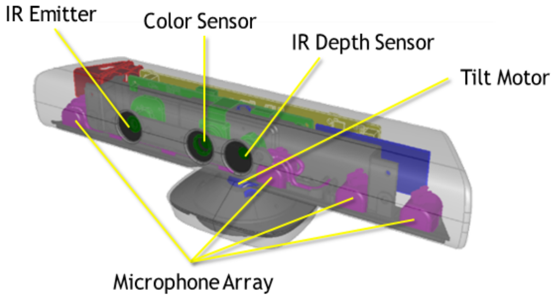

(b) System architecture diagram

Figure 8: Kinect camera [13]

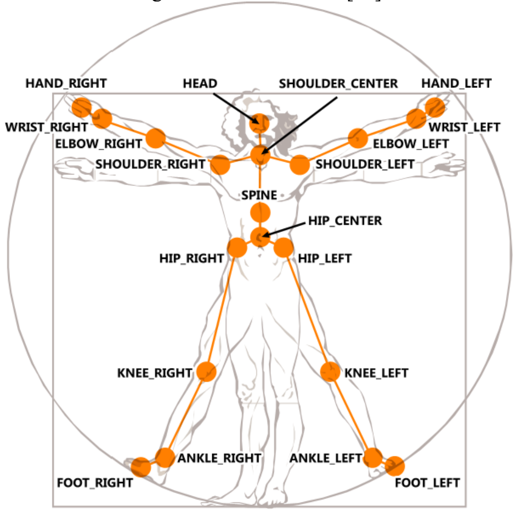

Figure 9: The Kinect camera defines the human skeleton joint coordinate map [13]

Pilot will isn't wear any equipment in our system, which is direct collection the joints information of the human skeleton. Use Kinect to obtain the coordinates of each joint point of the human body in space. The distance formula and vector inner product formula to calculate the distance and bending angle of the human joint points. Kinect is cheap, easy to carry, and used to evaluate the reaction time of the body of the test personnel. Due to the complex movements of the subject or the influence of environmental factors, occlusion may occur. Multi-angle shooting through multiple Kinects can successfully solve such problems. The integration of information collected by multiple Kinects can reduce occlusion. Real-time measurement and on-site operation testing analysis the cockpit instruments and human body.

Fig. 10 is the "Reach to Grasp" action sequence diagram. The six human skeleton joint coordinates verify the feasibility of the human reaction time and trajectory calculation of the cockpit personnel operating the measurement tracking system. Fig. 11 illustrates captured 3D skeletal joint coordinate information of the human body with Kinect

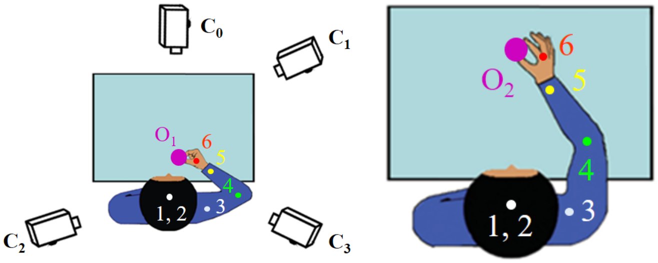

(a) Start (b) End

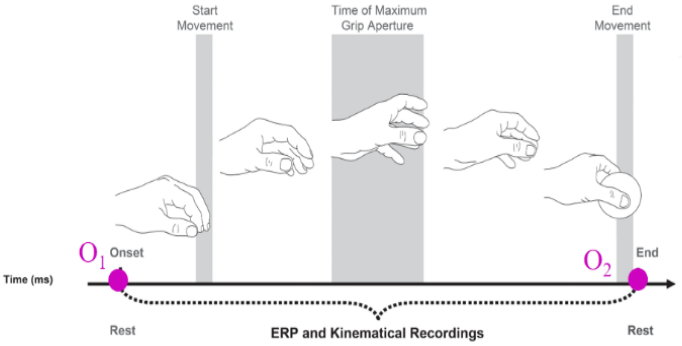

(c) "Reach to Grasp" action sequence

Figure 10: "Reach to Grasp" action sequence diagram

(a) Experimental setup

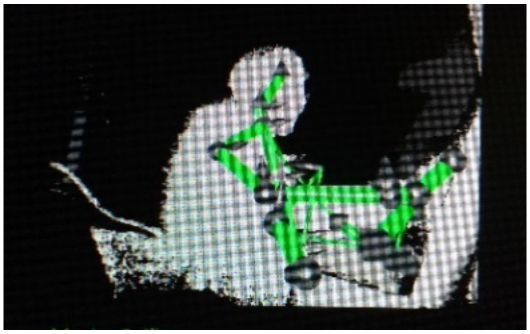

(b) C_2 image

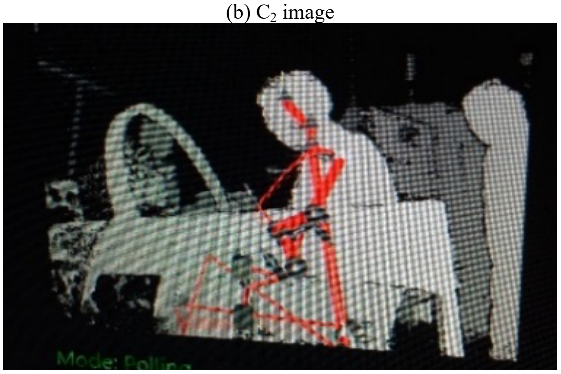

(c) C_3 image

Figure 11: Captured 3D skeletal joint coordinate information of the human body with Kinect

Fig. 12 is the 3D space trajectory of pilot's skeleton joints. Fig. 13 is the reaction time of the right arm of the pilot's body. Among them, the action of "Reach to Grasp" moves from point O_1 to point O_2 at 485 ms. The starting action is within 0.4-1.4 seconds, the maximum grasping action starts, the elapsed moving time MT1: 790 ms and the highest moving speed APV1: 1165 mm/s. Finally, the moving speed of the right arm feature points #4~#6 exceeds 800 mm/s, and the rest of the head and shoulder feature points #1~#3 are almost still.

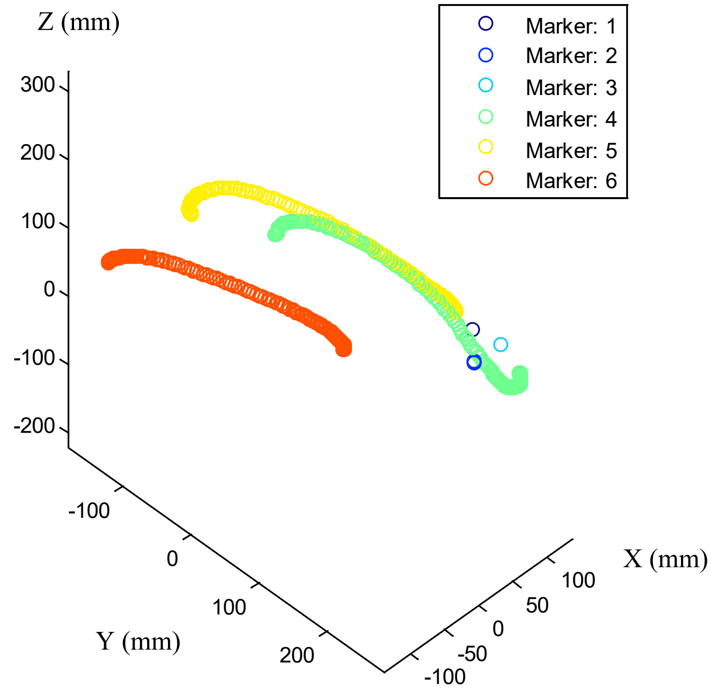

(a) 3D space trajectory

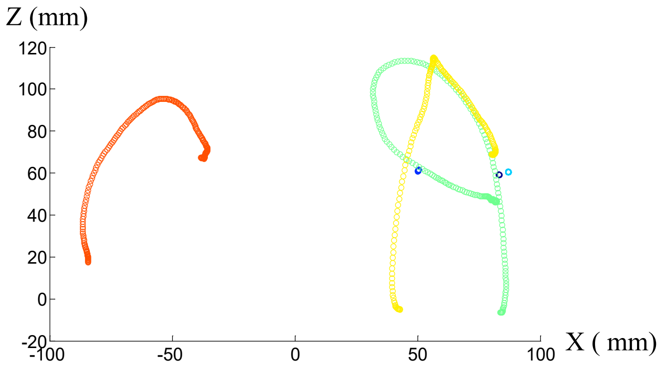

(b)C_0 image trajectory (front view)

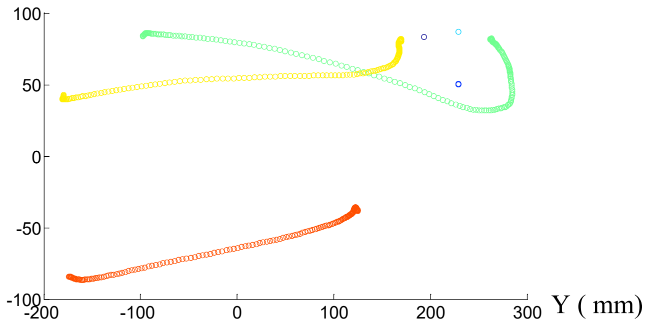

(c)C_1 image trajectory (top view)

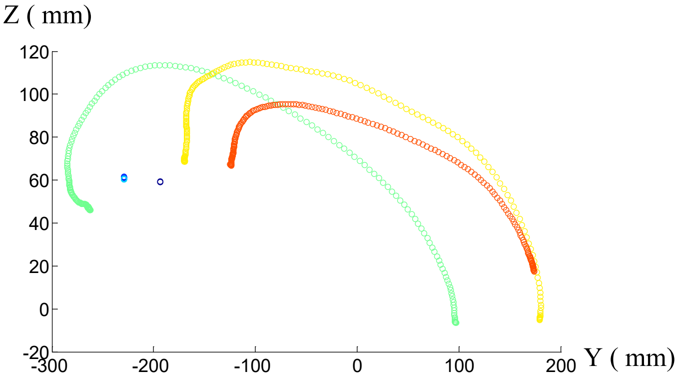

(d)C_2 image trajectory (left view)

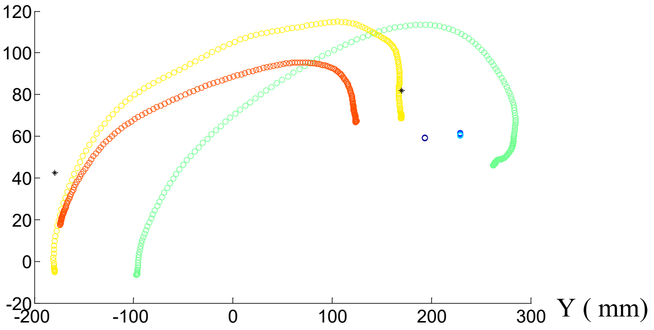

(e)C_3 image trajectory (right view)

Figure 12: The 3D space trajectory of pilot's skeleton joints

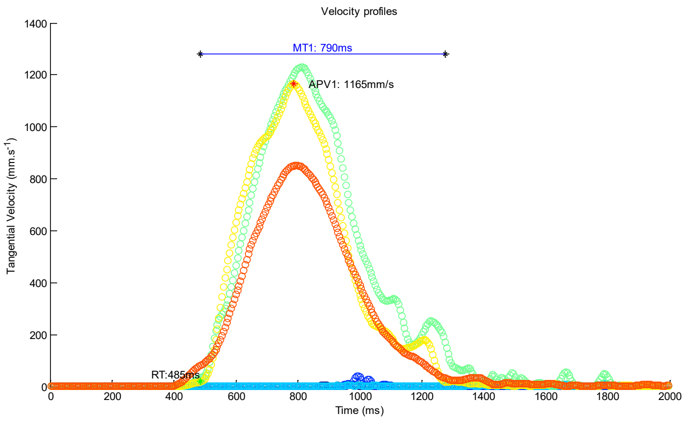

Figure 13: The reaction time of the right arm of the pilot's body.

4. Conclusion

The study successfully proposes a measurement and tracking system for movements of the pilot's body during flight operations. In order to overcome the limitation of image occlusion, the "Omni-directional Multi-view Image Measurement System" is used. The intersecting area can be increased by multiple cameras for 3D reconstruction. Measurement system flowchart is record skeleton detection of posture and touch area trajectory data, and then 3d data fitting with four multi-Kinect analysis. This system uses four multi-view images to eliminate the instrument and human body shielding and record the touched area. That could record the body reaction time (velocity and acceleration) and trajectory of the tested personnel. Real-time conversion of multi-view images corresponding to the 3D skeletal joint coordinate information of the human body, which measure the human-computer interaction human factors engineering integration of limb reaction time and trajectory measurement system. Finally, make prototypes, test and optimize, and achieve the research on the optimal cockpit touch area by conducting multi-view image simulation feasibility experiment framework and measurement process method. Using multiple depth-sensing cameras to perform low-cost, standardized automatic labeling of human skeleton joint dynamic capture.

Conflict of Interest

The authors declare no conflict of interest.

Reference

[1] Y.H. Chen, J. H. Huang, "Measurement and tracking system for movement of the pilot's body during flight operations," 2022 IEEE International Conference on Consumer Electronics - Taiwan, 539-540, 2022. DOI: 10.1109/ICCE-Taiwan55306.2022.9868976

[2] E. Kruk, M.M. Reijne, “Accuracy of human motion capture systems for sport applications; state-of-the-art review”, European Journal of Sport Science, **18**(6), 806-819, 2018. DOI: 10.1080/17461391.2018.1463397

[3] P.F. Luo, Y.J. Chao, M.A. Sutton, W. H. Peters, “Accurate measurement of three-dimensional deformations in deformable and rigid bodies using computer vision”, Experimental Mechanics, **33**, 123-132, 1993.

[4] Y.H. Chen, Y.S. Shiao, “Control simulation and experiment of two-axis parallel kinematic mechanism”, 2016 Taiwan Power Electronics Symposium, 2006.

[5] C.H. Hwang, W.C. Wang, Y.H. Chen, “Camera calibration and 3D surface reconstruction for multi-camera semi-circular DIC system”, Proc. SPIE 8769, International Conference on Optics in Precision Engineering and Nanotechnology (icOPEN2013), 2013.

[6] MIL-STD-1333B, “Aircrew station geometry for military aircraft”, 09 JAN, 1987.

[7] MIL-STD-1472H, “Human Engineering”, 15 SEP, 2020.

[8] O. Lefrançois, N. Matton, M. Causse, "Improving airline pilots' visual scanning and manual flight performance through training on skilled eye gaze strategies, Safety, **7**(4), 2021. DOI: 10.3390/safety7040070

[9] R. Li, B. Jumet, H. Ren, W. Song, ZTH Tse, "An inertial measurement unit tracking system for body movement in comparison with optical tracking", Proceedings of the Institution of Mechanical Engineers, Part H: Journal of Engineering in Medicine, **234**(7), 728-737, 2020. DOI: 10.1177/0954411920921695

[10] P. Biswas, "Using eye gaze controlled interfaces in automotive environments", Springer, 2016.

[11] M.G. Glaholt, "Eye tracking in the cockpit: a review of the relationships between eye movements and the aviators cognitive state", Defence Research and Development Canada Scientific Report DRDC-RDDC-2014-R153, 2014.

[12] E. Machida, M. Cao, T. Murao, H. Hashimoto, "Human motion tracking of mobile robot with Kinect 3D sensor", 2012 Proceedings of SICE Annual Conference (SICE), 2207-2211, 2012.

[13] www.developer/microsft.com/windows/kinect/.

[14] G. Kurillo, E. Hemingway, M.L. Cheng, L. Cheng, "Evaluating the accuracy of the azure kinect and kinect v2," Sensors (Basel). **22**(7), 2469, 2022. DOI: 10.3390/s22072469

Advances in Science, Technology and Engineering Systems Journal Vol. 8, No. 2, 78-86 (2023)

www.astesj.com

Special Issue on Computing, Engineering and Multidisciplinary Sciences

ASTESJ

ISSN: 2415-6698

Day-Ahead Power Loss Minimization Based on Solar Irradiation Forecasting of Extreme Learning Machine

Adelhard Beni Rehiara*,[1], Sabar Setiawidayat[2], Frederik Haryanto Sumbung[3]

[1]*Electrical Engineering Department, University of Papua, Manokwari, Indonesia*

[2]*Electrical Engineering Department, University of Widyagama, Malang, Indonesia*

[3]*Electrical Engineering Department, University of Musamus, Merauke, Indonesia*

ARTICLE INFO

Article history:
Received: 27 December, 2022
Accepted: 28 February, 2023
Online: 11 March, 2023

Keywords:
ELM
Forecasting
NASA
Solar irradiation
Power loss

ABSTRACT

Power losses exist naturally and have to be cared for in the operation of electrical power systems. Many researchers have worked on various methods and approaches to reduce losses by incorporating distributed generators (DG), particularly from renewable sources. These studies are based on the maximum unit penetration of the DGs, which is rarely achieved, resulting in inaccurate calculations. This paper proposes an advanced solution for calculating power losses by incorporating an Extreme Learning Machine (ELM) method for forecasting the solar irradiation. The ELM algorithm was used to create a model for forecasting solar radiation in the Manokwari region and its surroundings. Daily solar radiation in the region has been predicted using the model. NASA's 8016 data on temperature and solar irradiation were used to train the ELM model. With an MAE value of around 0.6392 and a training time of 4.4375 seconds, the test results demonstrate that the built model has good accuracy. The operation of a 1000 kWp solar power plant based on the ELM data forecasting can reduce the power loss of the existing distribution network around the location from 1.5095 kW/hour to 0.9068 kW/hour. Furthermore, the power plant operation can minimize the power loss by 39.9249 percent, from 36.2280 kW to 21.7640 kW.

1. Introduction

Solar energy is the bedrock of alternative energy sources since it may be used to develop other renewable energies [1]. In addition, photochemical power operations and other physical processes both heavily rely on solar energy. The earth's surface will receive solar energy via a radiation mechanism. The radiation will be filtered into the atmospheric layer, which contains gaseous substances as well as other solid forms including water vapour, dust, and aerosols, before it reaches the surface of the planet [2]. This filtration procedure has lowered the solar radiation's intensity to the point where it will not damage earthly life. The geographic position of a region on the earth's surface affects the amount of solar energy that reaches that region [3]. As a result, there are three ways to gather information about the intensity of solar radiation in a given area: directly using pyranometers, pyrheliometers, and Campbell Stokest measuring instruments; using satellite image data; and numerical simulation through computer modeling to determine the potential for future radiation. However, due to a lack of measuring tools, there is still extremely little and difficult-to-access sun irradiation data available in Indonesia. Since satellite image data is internationally available, it is widely used [4].

The escalation of world energy demand and the need for environmentally sustainable development have attracted human attention to renewable energy sources [5]. Among the renewable energy sources, solar power has become increasingly prevalent as a utility-scale renewable energy supply due to its simplicity of installation and maintenance. Furthermore, solar technology has matured, and mass manufacturing of PV panels as the core component of a solar power plant has reduced the cost. Thus, solar power integration into the grid is on the rise, and facilities might be present in the coming years [6].

Power losses in an electric power grid are caused by the current flowing in the conductor lines, where long conductor

---

*Corresponding Author: Adelhard B. Rehiara, Email: a.rehiara@unipa.ac.id

https://dx.doi.org/10.25046/aj080209

lines with large loads will result in significant power losses. However, this power loss cannot be avoided, so the only thing that can be done is to minimize the loss. Some of the methods that have been offered in previous research to minimize the losses include power injection through flexible alternating current transmission systems (FACTS) [7,8], distributed generators (DGs) [9–13], and optimal sizing and placement of capacitors [14–16], so that the voltage profile can be corrected, which results in minimal power losses.

In this paper, a model for forecasting solar irradiation was created for use in the Manokwari region and its surrounds, which are located at latitude -0.8457 and longitude 134.0504. The model was created using an extreme learning machine (ELM) algorithm that is modified from a neural network to improve learning speed. The model is used to forecast the local daily solar irradiation intensity. The data is then used to calculate the potency for minimizing power losses through the interconnection of a 1 MWp solar power plant to an existing power grid around the location. Then the objectives of this paper are given as: 1) designing a suitable model for the specific area based on the ELM algorithm, 2) forecasting the day-ahead solar irradiance for that location, and 3) investigating the possibility of power loss minimization in a power grid based on the forecasting data. This paper is an extension of work originally presented at the CyberneticsCom conference [1].

The frame of the paper is structured as follows: Section II provides problem statement. Section III describes the research approach and the methods used. The data source, results, and explanations of the findings are presented in Section IV. The paper's primary research findings are summarized in Section V.

2. Problem Statement

Previous research on power losses has been argued in [17], who have developed the Power Voltage Sensitivity Constant (PVSC), which has been developed to determine the location and size of multiple DG units so that active power losses in a distribution system can be reduced. The method was tested on an IEEE 69 reconfigured bus system under three different total loads and heavy conditions. It can be concluded from the results that the proposed methodology gives maximum loss reduction while considering DG size. Authors in [18] presented the use of the multiobjective cuckoo search (MOCS) algorithm to strategically place the unified power flower controller (UPFC) in order to reduce transmission losses. For the multiobjective issue under consideration, the pareto-optimal technique is used to extract the pareto-optimal solution. The best compromise option is extracted from the set of pareto-optimal solutions using the fuzzy logic method. A typical IEEE 30 bus test setup is used to evaluate the suggested method. The results show that the MOCS algorithm is relatively more effective in optimizing the multiobjective problem. Authors in [19] presented a multiobjective optimization methodology to optimally place a STATCOM in electric power distribution networks. Total cost and power loss are the objectives to be met so that the STATCOM placement can minimize these issues. The combination of multiobjective ant colony optimization (MACO) and the bacterial foraging optimization algorithm (BFOA) successfully solved the problems of minimization by testing the method's effectiveness in a 5-bus system. Authors in [20] proposed a method to control droop optimization strategically for inverter control of the islanded microgrid operation, which includes PV penetration and battery energy systems. Two-level controls are used to achieve maximum power loss minimization. A perturbation and observation (P&O) method is used to make the droop functions more adaptable. Load and inverter capacity are changed in three cases to check the effectiveness of the proposed method. Under various loading scenarios and system topologies, simulation studies have shown that it is capable of minimizing microgrid power loss while maintaining frequency and voltage stability. The fundamental disadvantage of this approach is that it only relies on the blind exploration of unknown functions, which degrades performance as the complexity of the grid increases and makes it possible that complex power systems will not achieve the lowest global power loss.

An extreme learning machine (ELM) is a single-layer feed-forward neural network (FFNN), which is a family of artificial neural networks (ANN). Implementing a single hidden layer minimizes the computation while minimizing the FFNN structure. This simplification can shorten calculation time by thousands of times while overcoming the FFNN's primary learning speed drawback. ELM is one of the most well-liked model-based systems because of the continued high accuracy of the system. The use of ELM algorithms is widespread in control [21,22], diagnosis [23,24] and forecasting [4,25]. When it comes to particular forecasting, ELM excels at predicting the solar irradiation of the Lamongan and Muara Karang regions [4], and the stock performance of PT. Telkom [25].

The existing methods have provided outstanding solutions for power loss minimization in the power grid through the penetration of solar power. However, the methods are based on maximizing the penetration of solar PV. This condition is not fully true, since solar irradiation is very dependent on weather conditions. Therefore, this disadvantage can be addressed by incorporating solar irradiation forecasting into the calculation of optimal power flow. The proposed method is capable of achieving detailed power loss minimization, which improves system reliability.

3. Methods

3.1. Extreme Learning Machine

A single hidden layer feed-forward neural network (SLFN), which has an effective training method, is the basis of an Extreme Learning Machine (ELM) [21]. This brilliance results from the absence of iteration in ELM. However, the hidden layer requires more neurons to provide effective prediction. The right number of neurons in the hidden layer of the ELM must also be determined using the trial-and-error method [4].

The ELM algorithm allows for the weightings to be selected at random without necessarily adjusting the input weights and hidden layer biases. The hidden layer output matrices can then be used to perform a generalized inverse operation to determine the SLFNs' output weight. The time for both training and performance has been shortened by this approach [21].

For a given n training set samples (x_j, t_j) where $x_j=[x_{j1}, x_{j2},..., x_{jn}]^T$ and $t_j=[t_{j1}, t_{j2},..., t_{jn}]^T$, an SLFN with N hidden neurons and an activation function $g(x)$ is expressed as [1,21,26]:

$$o_j = \sum_{j=1}^{n} \beta_i\, g\left(w_i x_j + b_i\right), \quad i = 1,2,\ldots,N \tag{1}$$

where $w_i=[w_{i1}, w_{i2},..., w_{in}]^T$, $\beta_i=[\beta_{i1}, \beta_{i2},..., \beta_{in}]^T$, b_i, and o_j are the connecting weight of the i-th hidden neuron to the input neuron, the connecting weights of the i-th hidden neuron to the output neurons, the bias of the i-th hidden node, and the actual network output with respect to input x_j respectively.

The standard SLFN can minimize the deviation between t_j and o_j, so that (1) can be rewritten as follows.

$$t_j = \sum_{i=1}^{N} \beta_i\, g\left(w_i x_j + b_i\right), \quad j = 1,2,\ldots,n \tag{2}$$

The simplification of (2) is $T=H\beta$ and the output weight matrix β can be solved using the least squares method as specified in (3).

$$\beta=H^{\dagger}T \tag{3}$$

The completed forms of the network output matrix T and hidden layer output matrix H are given as follows.

$$H = \begin{bmatrix} g(w_1 x_1 + b_1) & \cdots & g(w_N x_1 + b_N) \\ \vdots & \ddots & \vdots \\ g(w_1 x_n + b_1) & \cdots & g(w_N x_n + b_N) \end{bmatrix} \tag{4}$$

$$T = \left[t_1^T,\ldots,t_n^T\right]^T \tag{5}$$

3.2. Solar Power Plant

The sun emmits electromagnetics radiation with an effective temperature of 5777 K. Radiant energy, the ammount of energy within the radiation, is spread over the time and measured as radiant power also known as irradiance. The radiant power that reach the Earth surface is normaly measured in square meter through a pyranometer. Extraterrestrial irradiance (EXT) is very observable due to the absence of interference when the radiance traveling thru the space. The amount of irradiance reaching the earth's surface is approximately 1361.1 W/m^2, which is also known as global horizon irradiance (GHI) expressed in terms of clear-sky irradiance and is one of the most useful variables to calculate when working with solar data. This variable represents the best scenario for a photovoltaic system since it represents the maximum that could be received on the day, resulting in uninterrupted generation [2].

A solar power plant has at least one solar panel to convert energy directly from the sun. An inverter is also required to meet the output needs, and some accessories are involved to protect the process. The energy from a solar power plant depends on solar irradiation, while the constant parameters in calculating output power are the covered area and efficiency of the solar PV modules. Therefore, the output power of a solar power plant is formulated as follows [27].

$$P_{PV} = A_c N_{PV} S_{ir} \eta \tag{6}$$

where P_{PV}, A_c, Sir, and η are output power (W) dimension of solar PV modules (m^2), number of PV modules, solar irradiance (W/m^2) and efficiency of the solar PV modules.

3.3. Forward Backward Method

The voltage, power, and power loss in a radial distribution network are calculated in this research using the forward backward approach. This approach was created by reference [29] as it is described in their paper. By figuring out three fundamental computations, this method expands on the Distflow method to finish the analysis of power flow in distribution networks. The computations are used to determine the voltage magnitude, active power, and reactive power.

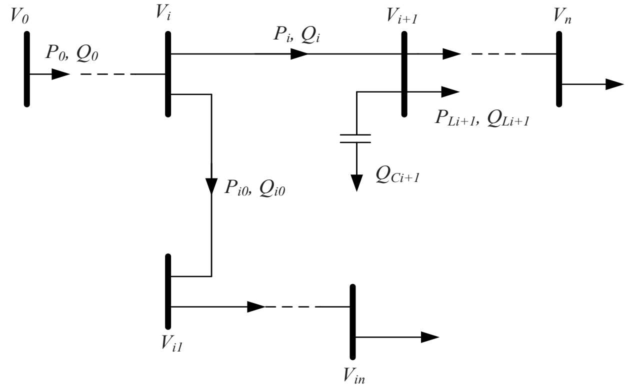

Figure 1: Single line diagram of a general distribution system

Consider the balanced three-phase, radial distribution feeder in Figure 1 with n branches/nodes and nc shunt capacitors. Without a branch from V_k to V_{kn} on the figure, the power and voltage at each node from V_0 to V_n can be calculated by the following equations [28–30].

$$P_{i+1} = P_i - \left(r_{i+1} \frac{P_i^2 + Q_i^2}{V_i^2} \right) - P_{Li+1} \tag{7}$$

$$Q_{i+1} = Q_i - \left(x_{i+1} \frac{P_i^2 + Q_i^2}{V_i^2} \right) - Q_{Li+1} + Q_{Ci+1} \tag{8}$$

$$V_{i+1}^2 = V_i^2 - 2\left(r_{i+1}P_i + x_{i+1}Q_i\right) + \left(r_{i+1}^2 + x_{i+1}^2\right)\frac{P_i^2 + Q_i^2}{V_i^2} \tag{9}$$

where P_{Li+1} and Q_{Li+1} are loads connected at node $i+1$; P_{i+1} and Q_{i+1} are the effective real and reactive power flows from node $i+1$; r_{i+1} and x_{i+1} are resistance and capacitance of the line leading to bus $i+1$; P_i and Q_i are real and reactive power flowing from bus i; V_i and V_{i+1} are the voltage magnitudes on bus i and bus $i+1$; and Q_{Ci+1} is an additional reactive power of the capacitor on the bus $i+1$.

The aforementioned equations are referred to as the forward equation, and each procedure is referred to as a forward update. Other calculating techniques and sequences in the Distflow are known as "backward updates" and "backward equations." The initial values of P_0 and Q_0 in this approximation method are determined by summing the active and reactive power of loads. V_0 is the initial voltage, which is also utilized as the system's base voltage in the approach method's calculation procedure [29]. The parameters in the bracket of equations (7) and (8) denote active and reactive power losses. At the end of each branch, the active and reactive power should be equal to zero [28–30].

3.4. Optimal Power Flow

An important method for improving a system's performance and lowering operational costs is optimization. A power system subject to dispersing loads amongst power plants is called optimal power flow (OPF). It is possible to decrease the overall fuel cost of all committed plants while still adhering to network limits. The OPF problem was generally expressed as follows [31–33]:

$$\text{Min}\, f(x, u) \tag{10}$$

subjected to

$$g(x, u) = 0 \tag{11}$$

$$h(x, u) \leq 0 \tag{12}$$

Where f, g and h are the objective functions, the equality constraints represent power flow equations and the system operating constraints, respectively.

The vector x is the dependent variable and consists of the voltage magnitude of load buses, the phase angle of all buses except that of the slack bus, the active power of the slack generator, and generators' reactive power. The vector of x is also called a state variable, and it is formulated in the following equation:

$$x^{\mathrm{T}} = [\mathrm{P}_{\mathrm{G1}}, \mathrm{V}_{\mathrm{L1}}, \ldots, \mathrm{V}_{\mathrm{LNL}}, Q_{\mathrm{G1}}, \ldots, Q_{\mathrm{GNC}}, \mathrm{S}_{\mathrm{l1}}, \ldots, \mathrm{S}_{\mathrm{lTL}}] \tag{13}$$

The vector u is a control variable that includes the active output power of generators at generator buses P_G, the terminal voltage magnitude at generation bus bars V_G, the output of shunt VAR compensators Q_C, and the tap setting of the tap regulating transformers T. Therefore, the vector u can be modeled as follows:

$$u^{\mathrm{T}} = [\mathrm{P}_{\mathrm{G1}}, \ldots, \mathrm{P}_{\mathrm{GNG}}, \mathrm{V}_{\mathrm{G1}}, \ldots, \mathrm{V}_{\mathrm{GNG}}, \mathrm{Q}_{\mathrm{C1}}, \ldots, \mathrm{Q}_{\mathrm{CNC}}, \mathrm{T}_1, \ldots, \mathrm{T}_{\mathrm{NT}}] \tag{14}$$

where S_l is transmission line loading and the subscripts *NL, TL, NG, NC*, and *NT* denote the number of load buses, transmission lines, generators, shunt VAR compensators, and regulating transformers, respectively.

The objective function in an OPF problem is to minimize the generators' costs in the operations. The cost function represents the relationship between operating costs and output power as expressed in equation (15), where a_i, b_i, and c_i are the coefficients of the fuel cost model.

$$F = \sum_{i=1}^{\mathrm{NG}} a_i P_{Gi}^2 + b_i P_{Gi} + c_i \tag{15}$$

There are certain equality and inequality restrictions in the problem of optimal power flow. The power flow equations are represented by the equality constraints g, as computed as follows:

$$\mathrm{P}_{\mathrm{Gi}} - \mathrm{P}_{\mathrm{Di}} = \sum_{j=1}^{NB} \left(\mathrm{V_i V_j Y_{ij}} \cos\left(\theta_{\mathrm{ij}} + \delta_{\mathrm{j}} - \delta_{\mathrm{i}}\right)\right) \tag{16}$$

$$\mathrm{Q}_{\mathrm{Gi}} - \mathrm{Q}_{\mathrm{Di}} = -\sum_{j=1}^{NB} \left(\mathrm{V_i V_j Y_{ij}} \sin\left(\theta_{\mathrm{ij}} + \delta_{\mathrm{j}} - \delta_{\mathrm{i}}\right)\right) \tag{17}$$

Where P_{Gi} and Q_{Gi} are the i-th generator's active and reactive power; P_{Di} and Q_{Di} are the i-th bus's active and reactive demand. V_i and V_j are the voltage magnitudes at buses i and j; Y_{ij} models the element of the admittance bus matrix at row i and column j; *NB* is the number of buses; δ_i, δ_j, and θ_{ij} are the angels of V_i, V_j, and Y_{ij}, respectively.

The inequality constraint h limits the physical devices as well as system security. The inequality constraints consist of generator constraints in equations (18) to (20), transformer constraints in equation (21), and shunt capacitor constraints in equation (22). System security constraints, on the other hand, are given in equations (23) and (24).

$$P_{Gi}^{\min} \leq P_{Gi} \leq P_{Gi}^{\max} \quad i = 1, \ldots, NG \tag{18}$$

$$Q_{Gi}^{\min} \leq Q_{Gi} \leq Q_{Gi}^{\max} \quad i = 1, \ldots, NG \tag{19}$$

$$V_{Gi}^{\min} \leq V_{Gi} \leq V_{Gi}^{\max} \quad i = 1, \ldots, NG \tag{20}$$

$$T_i^{\min} \leq T_i \leq T_i^{\max} \quad i = 1, \ldots, NT \tag{21}$$

$$Q_{Ci}^{\min} \leq Q_{Ci} \leq Q_{Ci}^{\max} \quad i = 1, \ldots, NG \tag{22}$$

$$V_i^{\min} \leq V_i \leq V_i^{\max} \quad i = 1, \ldots, NL \tag{23}$$

$$S_{ij} \leq S_{ij}^{\max} \quad i = 1, \ldots, TL \tag{24}$$

where P_{Gi}^{min} and P_{Gi}^{max} are the minimum and maximum active power of i-th generator and Q_{Gi}^{min} and Q_{Gi}^{max} denote the minimum and maximum reactive power of i-th generator; S_{ij} and S_{ij}^{max} are line flow and maximum line flow between bus i and j.

3.5. Model Validation

The developed model needs to be evaluated in order to detect and prevent any potential problems that might appear after running the ELM model. The mistakes will be eliminated through the validation process, making the model sufficiently precise for the simulation to match reality as predicted. The model is verified using the mean absolute error (MAE). It can be expressed as follows [4]:

$$MAE = \frac{\sum_{i=1}^{Y} \left| \hat{y}_i - y_i \right|}{Y} \tag{25}$$

where $\hat{y}_i$, y_i and Y are forecasting data, real data and number of samples, respectively.

4. Result and Discussion

4.1. Datasets

NASA [34] provided the datasets used to train the ELM model, which are located at latitude -0.8457 and longitude 134.0504. The data is based on Modern-Era Retrospective analysis for Research and Applications, Version 2 (MERRA-2) that starts to provide data from 1980. The elevation from MERRA-2 is average for a 0.5 x 0.625 degree latitude/longitude region about 944.25 meters. For the entire year 2021, there are 8016 data items in the dataset for both solar irradiance and ambient temperatures. The solar irradiance data ranges from 0 to 1033.38 Wh/m^2, which is clear-sky surface shortwave downward irradiance combined with the all-sky insolation clearness index. In same way the ambient temperature ranges from 18.47 to 26.5 ˚C, which is the MERRA-2 temperature at 2 meters. The model can be used in the research area based on location-specific data. In fact, the model can be used in any other field that has the necessary data for the defined domains and is available to be trained.

4.2. Training and Validation

The training is carried out using the Windows X-compatible MatLab 2021b program. The PC's hardware includes a Core i7-2600 CPU running at 3.40 GHz with 4 GB of RAM.

The datasets of 8016 from NASA are used to train the ELM model. The training time of 4.4375 seconds demonstrates the ELM's superiority, and its precision is sufficient, as indicated by a little modest MAE value. The test data is made up of data for 24 hours, which is the average amount of time for the entire year 2021. Training and testing with 5000 neurons take approximately 4.4375 seconds and 0.0625 seconds, respectively. The validation of the model was done using mean absolute error (MAE), with an error of about 0.6392 for the developed model.

4.3. Simulations

The simulations are performed to forecast the Manokwari region's daily solar irradiation and ambient temperatures. Then the results are presented in Figures 2 to 5.

The distribution of solar irradiation data is depicted in Figure 2 as fluctuating between 0 and a maximum of 1022.9 Wh/m^2. On the other side, hourly fluctuations occur at 14:00, when the difference between the minimum and maximum is rather large, measuring about 142.45 Wh/m^2. The graph also demonstrates that the forecasted results were located within these gaps [1].

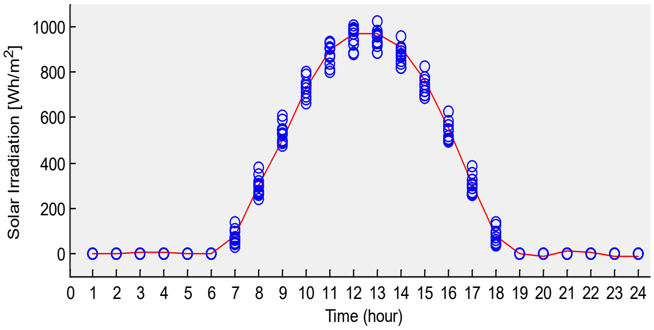

Figure 2: Solar irradiation distribution

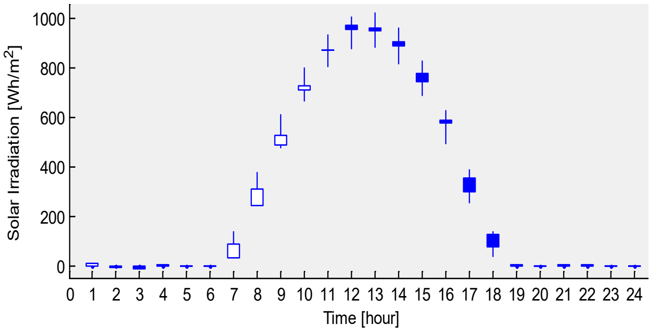

Figure 3: Forecasting of solar irradiation

As shown in Figure 3, a candlestick diagram is used to present the data between the minimum and maximum as well as factual and forecasted data. A thin line in this graph joins the minimum and maximum data points. On the other side, a thick line connects the error rate, which is the discrepancy between the actual and forecasted data. According to the simulation results in Figure 3, the highest error rate occurs at 8:00, around 55.75 Wh/m^2. The thick line is currently white, implying that the difference is negative in size as a result of the projected result being greater than the actual data [1].

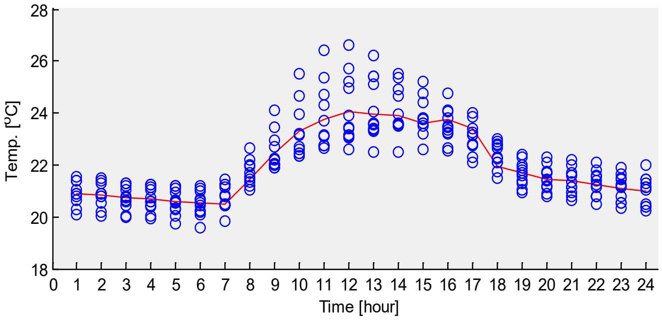

Figure 4: Ambient temperature distribution

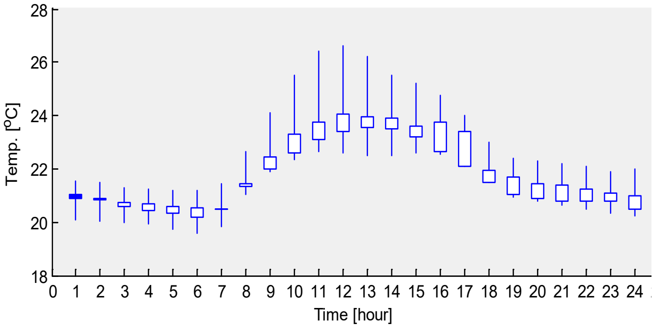

Figure 5: Forecasting of ambient temperature

The ELM model also outputs ambient temperature in accordance with solar irradiation forecasts. The forecasted environmental temperatures are given in Figures 4 and 5 [1]. As seen in Figure 4, the data distribution simultaneously displays a relatively significant variation in the Manokwari region, in contrast to the distribution of data from solar irradiation. This region is close to the equator and directly adjacent to the Pacific Ocean, which indicates a considerable change in environmental circumstances.

The candlestick diagram in Figure 5 depicts data changes between maximum and minimum data for the remainder of the year, with the highest data difference occurring at noon and being 4.02 ˚C. The figure also shows the discrepancy between the actual and anticipated data, with the largest variance of approximately 1.10 ˚C occurring around 16:00 [1].

4.4. Model Performances

Using the same ELM data for both training and testing, a straightforward feedforward neural network (FFNN) is used to assess the model's performance. The results of the performance test indicate that more than 1000 neurons cannot be operated on the same machine, while the FFNN requires 203.3281 seconds for training and 0.1250 seconds for testing. The average deviations for both approaches are 0.03 ˚C and 0.28 Wh/m^2, respectively [1]. The comparisons revealed that the ELM model has the same accuracy as the FFNN in extremely fast computing.

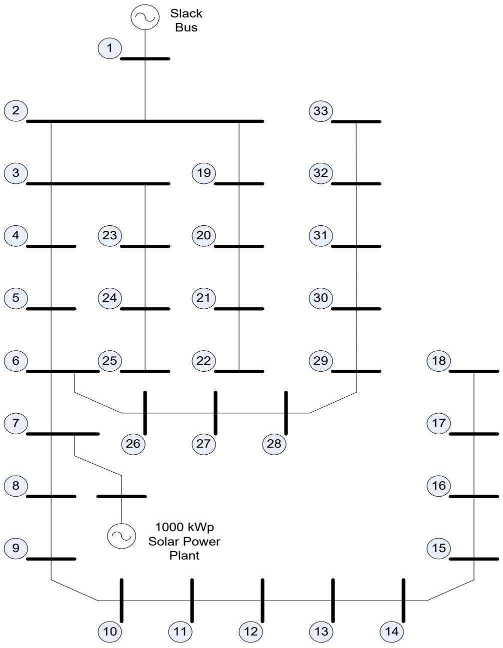

Figure 6: Single line diagram

4.5. Power Losses Minimization

Surrounding the research location, a distribution line, namely the Rajawali feeder, is operated. The feeder consists of 33 load buses connected to 32 lines, as figured in Figure 6, with data attached in Tables 1 and 2 [29].

Based on Figure 6, it can be seen that the distribution lines are connected in a radial connection. The longest line is from bus 1 to bus 18, where some tabs are taken from bus 6 to connect buses 26 and 33 and a tab is added for the solar power plant penetration. The other branches of the feeder are taken from bus 2 to connect buses 19 and 22 and from bus 3 to connect buses 23 and 25.

Table 1: Bus data

No	Bus Type*	Voltage (pu)	Angle (deg)	Load		Generation	
				P (kW)	Q (kVar)	P (kW)	Q (kVar)
1	1	1.00	0.00	0.00	0.00	0.00	0.00
2	2	1.00	0.00	100.00	60.00	0.00	0.00
3	2	1.00	0.00	90.00	40.00	0.00	0.00
4	2	1.00	0.00	120.00	80.00	0.00	0.00
5	2	1.00	0.00	60.00	30.00	0.00	0.00
6	2	1.00	0.00	60.00	20.00	0.00	0.00
7	3	1.00	0.00	200.00	100.00	1000.00	0.00
8	2	1.00	0.00	200.00	100.00	0.00	0.00
9	2	1.00	0.00	60.00	20.00	0.00	0.00
10	2	1.00	0.00	60.00	20.00	0.00	0.00
11	2	1.00	0.00	45.00	30.00	0.00	0.00
12	2	1.00	0.00	60.00	35.00	0.00	0.00
13	2	1.00	0.00	60.00	35.00	0.00	0.00
14	2	1.00	0.00	120.00	80.00	0.00	0.00
15	2	1.00	0.00	60.00	10.00	0.00	0.00
16	2	1.00	0.00	60.00	20.00	0.00	0.00
17	2	1.00	0.00	60.00	20.00	0.00	0.00
18	2	1.00	0.00	90.00	40.00	0.00	0.00
19	2	1.00	0.00	90.00	40.00	0.00	0.00
20	2	1.00	0.00	90.00	40.00	0.00	0.00
21	2	1.00	0.00	90.00	40.00	0.00	0.00
22	2	1.00	0.00	90.00	40.00	0.00	0.00
23	2	1.00	0.00	90.00	50.00	0.00	0.00
24	2	1.00	0.00	420.00	200.00	0.00	0.00
25	2	1.00	0.00	420.00	200.00	0.00	0.00
26	2	1.00	0.00	60.00	25.00	0.00	0.00
27	2	1.00	0.00	60.00	25.00	0.00	0.00
28	2	1.00	0.00	60.00	20.00	0.00	0.00
29	2	1.00	0.00	120.00	70.00	0.00	0.00
30	2	1.00	0.00	200.00	600.00	0.00	0.00
31	2	1.00	0.00	150.00	70.00	0.00	0.00
32	2	1.00	0.00	210.00	100.00	0.00	0.00
33	2	1.00	0.00	60.00	40.00	0.00	0.00

*Type of bus: 1:slack; 2:load; 3:generator

Table 2: Line data

No	Line (From - To)	Impedance (Ohm)		No	Line (From - To)	Impedance (Ohm)	
		R	jX			R	jX
1	1 - 2	0.0922	0.0470	17	14 - 15	0.5910	0.5260
2	2 - 3	0.4930	0.2511	18	15 - 16	0.7463	0.5450
3	2 - 19	0.1640	0.1565	19	16 - 17	1.2890	1.7210
4	3 - 4	0.3660	0.1864	20	17 - 18	0.7320	0.5740
5	3 - 23	0.4512	0.3083	21	19 - 20	1.5042	1.3554
6	4 - 5	0.3811	0.1941	22	20 - 21	0.4095	0.4784
7	5 - 6	0.8190	0.7070	23	21 - 22	0.7089	0.9373
8	6 - 7	0.1872	0.6188	24	23 - 24	0.8980	0.7091
9	6 - 26	0.2030	0.1034	25	24 - 25	0.8960	0.7011
10	7 - 8	0.7114	0.2351	26	26 - 27	0.2842	0.1447
11	8 - 9	1.0300	0.7400	27	27 - 28	1.0590	0.9337
12	9 - 10	1.0440	0.7400	28	28 - 29	0.8042	0.7006
13	10 - 11	0.1966	0.0650	29	29 - 30	0.5075	0.2585
14	11 - 12	0.3744	0.1238	30	30 - 31	0.9744	0.9630
15	12 - 13	1.4680	1.1550	31	31 - 32	0.3105	0.3619
16	13 - 14	0.5416	0.7129	32	32 - 33	0.3410	0.5302

A solar power plant has been prepared to be installed on the Rajawali feeder, which is planned to be integrated into the grid through the feeder. The power plant has an output power of 1000 kW, and the plant consists of 3498 PV panels with an output power of 260 Wp. The PV panel data is provided as follows.

Optimum operating voltage (Vmp) : 30.60 V
Optimum operating current (Imp) : 8.50 A
Open–circuit voltage (Voc) :37.70 V
Short–circuit current (Isc) : 9.15 A
Maximum power (Pmax) : 260 W
Efficiency :16 %
Operating module temperature : -40 to 85 ˚C
Maximum system voltage :1000 VDC
Maximum series fuse rating :15 A
Power tolerance : 0–3%
Solar cell type : Monocrystalline
Number of cells : 60
Dimensions (mm) : 1636x992x45

The solar power plant will be used as a model to investigate the use of ELM forecasting results to investigate the penetration effect of the solar power plant in increasing the voltage profile and thus improving power losses. The results will be compared with the existing operating conditions, which probably have high power losses in operation.

The simulation is carried out using forecasting data from both NN and ELM methods. The forecasting results will then be converted into electrical energy, which will be integrated into the grid according to the specifications of the solar panels used and calculated using equation (6). The results of hourly load forecasting will also be influenced by the pattern of changes in load on each bus, which varies according to peak load times. The simulation results show an improvement in the voltage profile and power loss, as shown in Tables 3 and 4, and also illustrated in Figure 7.

Table 3: Average voltage magnitude (p.u.) and load profile (kW)

Bus	Existing	NN	ELM	Load	Bus	Existing	NN	ELM	Load
1	1.000	1.000	1.000	135.06	18	0.928	0.941	0.941	59.64
2	0.997	0.998	0.998	85.47	19	0.995	0.996	0.996	74.16
3	0.986	0.987	0.987	120.79	20	0.992	0.991	0.991	84.24
4	0.983	0.985	0.985	66.00	21	0.990	0.990	0.990	93.02
5	0.976	0.981	0.981	96.91	22	0.989	0.989	0.989	80.38
6	0.968	0.978	0.978	80.29	23	0.985	0.984	0.984	73.44
7	0.963	0.984	0.984	99.46	24	0.983	0.978	0.978	133.77
8	0.955	0.976	0.976	113.71	25	0.983	0.975	0.975	63.01
9	0.954	0.970	0.970	73.32	26	0.962	0.974	0.974	88.08
10	0.953	0.965	0.965	94.15	27	0.961	0.971	0.971	67.16
11	0.948	0.962	0.962	73.55	28	0.956	0.960	0.960	65.13
12	0.941	0.958	0.958	69.21	29	0.953	0.952	0.952	62.47
13	0.936	0.951	0.951	85.46	30	0.951	0.948	0.948	65.37
14	0.935	0.949	0.949	69.00	31	0.949	0.944	0.944	77.83
15	0.933	0.947	0.947	82.24	32	0.948	0.943	0.943	78.92
16	0.929	0.944	0.944	140.82	33	0.948	0.942	0.942	99.92
17	0.928	0.942	0.942	98.08	Avg	0.962	0.968	0.968	86.37

The outer buses on the feeder are those of 18, 22, 25, and 33, which have the lowest average voltage on the lines. After the penetration of the solar power plant, the average voltages are increasing on the buses, except for bus number 22, which is highly influenced by the slack bus voltage, as shown in Table 3. Overall, the average voltage of the feeder is increased by the solar power plant from 0.962 to 0.968 for both NN and ELM forecasting. The voltage profile improvement also occurs in many cases of power plant injection into a grid, which acts as a distributed generator, as reported in references [9–11,14,17].

Table 4: Power Loss Minimization (kW)

Time	Existing	NN	ELM	Time	Existing	NN	ELM
1	1.4050	1.4050	1.4050	14	1.6290	1.0760	0.4550
2	1.4270	1.4270	1.4270	15	1.6020	1.0760	0.4660
3	1.4110	1.4110	1.4110	16	1.5960	1.0760	0.4560
4	1.4810	1.4810	1.4810	17	1.5510	1.0760	0.4560
5	1.4840	1.4840	1.4840	18	1.5460	1.0760	0.4480
6	1.4960	1.0760	0.4270	19	1.5640	1.5640	1.5640
7	1.5020	1.0760	0.4320	20	1.5060	1.5060	1.5060
8	1.5210	1.0760	0.4320	21	1.4780	1.4780	1.4780
9	1.5060	1.0760	0.4380	22	1.4020	1.4020	1.4020
10	1.5270	1.0760	0.4350	23	1.4050	1.4050	1.4050
11	1.5960	1.0760	0.4420	24	1.4020	1.4020	1.4020
12	1.5980	1.0750	0.4580	Σ	36.2280	29.9520	21.7640
13	1.5930	1.0760	0.4540	%	100.0000	17.3236	39.9249

The data in Table 4 shows that at night, the power loss forecast for the line will be the same as the existing condition. Therefore, the power loss simulation is carried out using the forward backward sweep (FBS) method. Furthermore, when the sun starts to shine, the power loss is analyzed by the Optimal Power Flow (OPF) method. This is a fact of the system because it is a pure radial distribution system without solar power penetration. Then the power loss problem needs to be solved with the FBS method because it will cause simulation calculation errors with the OPF method that is used for a complex power system. In a different way, during the day, there is energy penetration on the system's bus 7, transforming the system into a multi-machine system connected to a radial distribution system, where power loss problems should be counted using the OPF method.

When the solar power starts to penetrate at 6 a.m., the ELM simulation shows a decrease in power loss until it reaches a maximum at around 12 p.m., and after noon, the power loss slowly increases as the solar radiation reaching the PV panel is reduced. The ELM method is smaller than the NN method because the ELM prediction gives more accurate results compared to the NN forecast, which yields a high percentage of power loss minimization. Data on the table shows that average power loss without solar power penetration is about 1.5095 kW/hour, which is reduced in average by the penetration of about 1.2480 kW/hour and 0.9068 kW/hour of NN and ELM forecasting, respectively.

On the other hand, the simulation results show that the power loss simulated through NN forecasting tends to be constant throughout the solar power plant's operation. This resulted in less solar power penetration, and its contribution to the power loss is also less, as indicated by the small percentage of power loss, which is only 17.3236 % compared to the ELM forecasting percentage that reached 39.9249 %.

The standard deviations of power losses have decreased from 6.9441 in the existing condition to 5.7440 and 4.2015 for both NN and ELM, respectively. This indicates that the performance of the system has improved with the penetration of solar power plants. However, the smallest standard deviation values indicate that power loss minimization represents a more accurate result of the ELM algorithm.

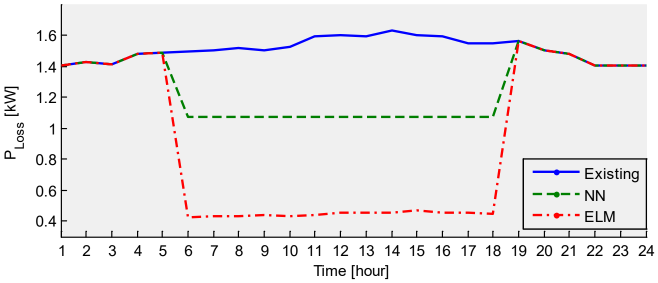

Figure 7: Power losses improvement

Figure 7 depicts the difference in power loss for the following day of the normal calculation versus the improved results due to the penetration of the 1000 kWp solar power plant on bus 7. The figure shows that there is a high power loss improvement predicted with ELM compared to the NN prediction, which tends to be stable throughout the operating time of the solar power plant. The prediction results show the accumulated power loss through NN predictions of 29.9520 kW and ELM predictions of 21.7640 kW, which is slightly lower than the normal calculation of about 36.2280 kW. This prediction result is not high for predictions in the day ahead, but it will change significantly for long-term forecasting.

Overall, the proposed method is done in the sequence of forecasting solar irradiation a day ahead in [1], injecting the solar irradiation into a power grid, calculating power flow in the grid, and investigating the power losses by comparing the results with another method. It is found that by applying the proposed method in a microgrid system, the average voltage is raised to 0.968 p.u. and further power losses in day-ahead operation can be minimized to 0.79% of the total load of 2763.84 kW. The proposed method is also valid in terms of accuracy as measured by standard deviation.

5. Conclusions

In this study, an ELM model has been developed to forecast solar data for the following day as well as data on the ambient temperature. The ELM model includes 5000 neurons in the hidden layer and was trained using annual datasets of about 8016 items. The forecasting process takes 0.0625 seconds, while training takes 4.4375 seconds of CPU time. The model has been verified using the MAE approach and has a relatively low error rate of 0.6392, making it considered accurate enough to be used to forecast solar irradiation and the surrounding air temperature at the sampling sites. The ELM model's performances have also been compared with those of a straightforward feed-forward neural network (FFNN), which has the same accuracy but requires less time to train and evaluate.

Power loss minimization for the day-ahead operation of a 1000 kWp solar panel based on the ELM data forecasting can reach 21.7640 kW, or about 39.9249 percent, compared to the existing operation without solar penetration of about 36.2280 kW. The power loss is reduced by the penetration of the solar power plant from 1.5095 kW/hour to 0.9068 kW/hour.

Acknowledgment

The first author would like to thank his colleagues from Electrical Engineering Department, Engineering Faculty of Papua University, Manokwari, who provided insight and expertise that greatly assisted this research.

References

[1] A.B. Rehiara, S. Setiawidayat, "Day Ahead Solar Irradiation Forecasting Based on Extreme Learning Machine," in 2022 IEEE International Conference on Cybernetics and Computational Intelligence (CyberneticsCom), 63–66, 2022, doi:10.1109/CyberneticsCom55287.2022.9865532.

[2] J.M. Bright, Introduction To Synthetic Solar Irradiance, 1-1-1–32, doi:10.1063/9780735421820_001.

[3] B. Brahma, R. Wadhvani, "Solar Irradiance Forecasting Based on Deep Learning Methodologies and Multi-Site Data," Symmetry, **12**(11), 2020, doi:10.3390/sym12111830.

[4] M. Abdillah, W.A. Pramudito, T.A. Nugroho, D.N. Fitria, "Solar irradiance forecasting using kernel extreme learning machine: case study at Lamongan and Muara Karang regions, Indonesia," 17, 2022.

[5] V.V.V.S.N. Murty, A. Kumar, "Optimal Energy Management and Techno-economic Analysis in Microgrid with Hybrid Renewable Energy Sources," Journal of Modern Power Systems and Clean Energy, **8**(5), 929–940, 2020, doi:10.35833/MPCE.2020.000273.

[6] D. Sampath Kumar, O. Gandhi, C.D. Rodríguez-Gallegos, D. Srinivasan, "Review of power system impacts at high PV penetration Part II: Potential solutions and the way forward," Special Issue on Grid Integration, 210, 202–221, 2020, doi:10.1016/j.solener.2020.08.047.

[7] S. Monshizadeh, "Comparison of Intelligent Algorithms with FACTS Devices for Minimization of Total Power Losses," Advances in Intelligent Systems and Computing, 926(Query date: 2022-12-02 17:21:04), 120–131, 2020, doi:10.1007/978-3-030-15032-7_10.

[8] S.P. Dash, "Optimal location and parametric settings of FACTS devices based on JAYA blended moth flame optimization for transmission loss minimization in power systems," Microsystem Technologies, **26**(5), 1543–1552, 2020, doi:10.1007/s00542-019-04692-w.

[9] A. Alam, "Optimal placement of DG in distribution system for power loss minimization and voltage profile improvement," 2018 International Conference on Computing, Power and Communication Technologies, GUCON 2018, (Query date: 2022-12-02 17:21:04), 837–842, 2019, doi:10.1109/GUCON.2018.8674930.

[10] S. Essallah, "Optimal Multi-Type DG Integration and Distribution System Reconfiguration for Active Power Loss Minimization using CPSO Algorithm," 2019 International Conference on Control, Automation and Diagnosis, ICCAD 2019 - Proceedings, (Query date: 2022-12-02 17:21:04), 2019, doi:10.1109/ICCAD46983.2019.9037947.

[11] G.A.S. Gandhi, "Optimal allocation of DG for minimization of power loss and total investment cost using an analytical approach," 2020 21st National Power Systems Conference, NPSC 2020, (Query date: 2022-12-02 17:21:04), 2020, doi:10.1109/NPSC49263.2020.9331891.

[12] S. Ansari, J. Zhang, R.E. Singh, "A review of stabilization methods for DCMG with CPL, the role of bandwidth limits and droop control," Protection and Control of Modern Power Systems, **7**(1), 2, 2022, doi:10.1186/s41601-021-00222-x.

[13] N. Pragallapati, S.J. Ranade, O. Lavrova, "Cyber Physical Implementation of Improved Distributed Secondary Control of DC Microgrid," 2021 1st International Conference on Power Electronics and Energy (ICPEE), doi:10.1109/icpee50452.2021.9358705.

[14] M. Kang, "Optimal placement and sizing of DG and shunt capacitor for power loss minimization in an islanded distribution system," Lecture Notes of the Institute for Computer Sciences, Social-Informatics and Telecommunications Engineering, LNICST, 245(Query date: 2022-12-02 17:21:04), 43–52, 2018, doi:10.1007/978-3-319-94965-9_5.

[15] M.B. Essa, "Distribution power loss minimization via optimal sizing and placement of shunt capacitor and distributed generator with network

reconfiguration," Telkomnika (Telecommunication Computing Electronics and Control), **19**(3), 1039–1049, 2021, doi:10.12928/TELKOMNIKA.v19i3.15223.

[16] D. Bhowmik, "Optimal placement of capacitor banks for power loss minimization in transmission systems using fuzzy logic," Journal of Engineering Science and Technology, **13**(10), 3190–3203, 2018.

[17] S. Nawaz, "A new technique to solve DG allocation problem for distribution power loss minimization," ICIC Express Letters, Part B: Applications, **9**(7), 701–706, 2018, doi:10.24507/icicelb.09.07.701.

[18] N.T. Rao, "Comparative study of Pareto optimal multi objective cuckoo search algorithm and multi objective particle swarm optimization for power loss minimization incorporating UPFC," Journal of Ambient Intelligence and Humanized Computing, **12**(1), 1069–1080, 2021, doi:10.1007/s12652-020-02142-4.

[19] M. Sankaramoorthy, "A hybrid MACO and BFOA algorithm for power loss minimization and total cost reduction in distribution systems," Turkish Journal of Electrical Engineering and Computer Sciences, **25**(1), 337–351, 2017, doi:10.3906/elk-1410-191.

[20] N. Vazquez, "A Fully Decentralized Adaptive Droop Optimization Strategy for Power Loss Minimization in Microgrids with PV-BESS," IEEE Transactions on Energy Conversion, **34**(1), 385–395, 2019, doi:10.1109/TEC.2018.2878246.

[21] R. Adelhard Beni, C. He, S. Yutaka, Y. Naoto, Z. Yoshifumi, "An Adaptive Internal Model for Load Frequency Control Using Extreme Learning Machine," TELKOMNIKA, **16**(6), 2879–2887, 2018, doi:http://dx.doi.org/10.12928/telkomnika.v16i6.11553.

[22] Y. Lu, W. Yu, J. Wang, D. Jiang, R. Li, "Design of PID Controller Based on ELM and Its Implementation for Buck Converters," International Journal of Control, Automation and Systems, **19**(7), 2479–2490, 2021, doi:10.1007/s12555-019-0989-1.

[23] P. Winangun, I.M. Widyantara, R. Hartati, "Extreme Learning Machine Based Diagnostic Approach with Linear Kernel for Classifying Lung Disorders," Majalah Ilmiah Teknologi Elektro, **19**(1), 83–88, 2020, doi:10.24843/MITE.2020.v19i01.P12.

[24] C. Jia, H. Zhang, "ELM Neural Network-based Fault Diagnosis Method for Mechanical Equipment," in 2019 Chinese Automation Congress (CAC), 5257–5261, 2019, doi:10.1109/CAC48633.2019.8996333.

[25] M.N. dan I.C. dan I. Indriati, "Stock Price Earning Ratio Prediction Using the Kernel Extreme Learning Machine Algorithm (Case Study: PT TELKOM)," Jurnal Pengembangan Teknologi Informasi Dan Ilmu Komputer, **4**(10), 3455–3462, 2020.

[26] G. Huang, S. Song, J.N.D. Gupta, C. Wu, "Semi-Supervised and Unsupervised Extreme Learning Machines," IEEE Transactions on Cybernetics, 44(12), 2405–2417, 2014, doi:10.1109/TCYB.2014.2307349.

[27] F. Odoi-Yorke, A. Woenagnon, "Techno-economic assessment of solar PV/fuel cell hybrid power system for telecom base stations in Ghana," Cogent Engineering, **8**(1), 1911285, 2021, doi:10.1080/23311916.2021.1911285.

[28] S.F. Mekhamer, S.A. Soliman, M.A. Mostafa, M.E. El-Hawary, "Load flow solution of radial distribution feeders: a new approach," in 2001 IEEE Porto Power Tech Proceedings (Cat. No.01EX502), **3**, 5, 2001, doi:10.1109/PTC.2001.964918.

[29] B.R. Wihyawari, "Radial Power Flow Analysis of Rajawali Feeder in Manokwari Power Grid," in ICTVT 2021, State University of Yogyakarta, 2021.

[30] J.A.M. Rupa, S. Ganesh, "Power Flow Analysis for Radial Distribution System Using Backward/Forward Sweep Method," International Journal of Electrical and Computer Engineering, **8**(10), 1628–1632, 2014.

[31] A.B. Rehiara, "Optimal Power Flow of the Manokwari Power Grid Regarding Penetration of 20 MW Combined Cycle Power Plant," in 2019 International Conference on Advanced Mechatronics, Intelligent Manufacture and Industrial Automation (ICAMIMIA), 53–57, 2019, doi:10.1109/ICAMIMIA47173.2019.9223393.

[32] L.T. Al-Bahran, A.Q. Abdulrasool, "Multi objective functions of constraint optimal power flow based on modified ant colony system optimization technique," IOP Conference Series: Materials Science and Engineering, **1105**(1), 012015, 2021, doi:10.1088/1757-899X/1105/1/012015.

[33] H. Bouchekara, "Solution of the optimal power flow problem considering security constraints using an improved chaotic electromagnetic field optimization algorithm," Neural Computing and Applications, **32**(7), 2683–2703, 2020, doi:10.1007/s00521-019-04298-3.

[34] NASA, NASA/POWER CERES/MERRA2 Native Resolution Hourly Data, 2021.

Advances in Science, Technology and Engineering Systems Journal Vol. 8, No. 2, 87-96 (2023)

www.astesj.com

Special Issue on Computing, Engineering and Multidisciplinary Sciences

ASTESJ

ISSN: 2415-6698

Development and Analysis of Models for Detection of Olive Trees

Ivana Marin[1], Sven Gotovac[2], Vladan Papić[*,2]

[1]*Faculty of Science, University of Split, Split, 21000, Croatia*

[2]*Faculty of Electrical Engineering, Mechanical Engineering and Naval Architecture, University of Split, Split, 21000, Croatia*

ARTICLE INFO

Article history:
Received: 26 January, 2023
Accepted: 04 March, 2023
Online: 11 March, 2023

Keywords:
Tree detection
Olive tree
Remote sensing
Deep learning

ABSTRACT

In this paper, an automatic method for detection of olive trees in RGB images acquired by an unmanned aerial vehicle (UAV) is developed. Presented approach is based on the implementation of RetinaNet model and DeepForest Phyton package. Due to fact that original (pretrained) model used in DeepForest package has been built on images of various types of trees but without images of olive trees, original model detection was unsatisfactory. Therefore, a new image dataset of olive trees was created using sets of images chosen from five olive groves. For neural network training, individual olive trees were manually labeled, and new models were generated. Each model has been trained on different set of images from selected olive groves. Pretrained model and new models were compared and evaluated for various test scenarios. Obtained results showed high precision and recall values of proposed approach and great improvement in performance compared to the pretrained model.

1. Introduction

It is predicted that close to 10 billion people will live on Earth by 2050 [1]. At the moment, about 37% of the total land surface is used for food production [2], and it is estimated that the necessary increase in food production between 2010 and 2050 will be between 35% to 56% [3]. Needed increase in production can be achieved by increasing the share of agricultural land and/or increasing productivity on existing agricultural land by applying the so-called precision or smart agriculture [4]. Olive (*Olea Europea*) is one of the most widespread plants and plantations in the world. Olive oil is a basic ingredient in Mediterranean cuisine, and it is popular all over the world. Worldwide, consumption of olive oil has been constantly increasing [5]. According to the latest reports of the International Olive Council (https://www.internationaloliveoil.org), worldwide olive oil production for 2020/2021 crop year was just above 3.000.000 tons. Spain is the largest producer of olives and olive oil in the world (close to 50% of world production) and EU countries in total produce around 70% of world production. In 2019, the global olive oil market size was above 13 billion US dollars, and it is projected to reach 16.64 billion US dollars by 2027, with annual growth of 3.2% during the forecast period (2020-2027) [6].

Therefore, olive trees and olive oil are economically very important for the producing countries. On the demand side, world consumption of olive oil has also witnessed a substantial growth in the course of the three past decades [7]. This makes olive growing and oil production a good choice for research and implementation of new approaches aiming to respond to the challenges in food production. Complex systems such as those in agriculture should be continuously monitored, measured, and analyzed. The above implies the use of new information and communication technologies [8]. Remote sensing is the process of detecting and monitoring physical characteristics of larger areas [9] using satellites, aircraft, and drones. Therefore, farmers don't need to physically visit all parts of the land to gather data that can be used to analyze different aspects of the crop and yield. The application of artificial intelligence and machine learning in agriculture is increasingly intensive due to its ability to understand, learn and react to different situations (based on learning) in order to increase the efficiency and quality of production.

Images collected for agricultural applications can be obtained from satellites such as ESA Sentinel-2A. However, these types of images depend on weather conditions (cloudiness) and have a low spatial resolution (Sentinel up to 10 m), which is not satisfactory for certain treatments [10]. It is to be expected that the temporal and spatial resolution will improve over time, but problems with clouds will certainly remain. The use of drones for data collection

---

[*] Corresponding Author: Vladan Papić, FESB, Ruđera Boškovića 32, Split, Croatia, vpapic@fesb.hr

https://dx.doi.org/10.25046/aj080210

enables higher spatial resolution, the time of recording images is determined by the user, and data can be collected even in cloudy weather. A greater number of camera types are available (RGB, multispectral, hyperspectral, thermal). The collected data are of significantly higher quality than those collected by satellite [11]. Also, UAV-based imaging implies lower operational costs compared to imaging systems on manned aircraft or satellites, so it can be considered a preferred solution for monitoring smaller regions. The collected images can be used after applying different computer vision algorithms for different types of applications, such as counting and estimating the size of trees [12,13], assessing fruit maturity [14], assessing crops [15], plant diseases [16], etc.

Importance of counting and identification of olive trees in aerial images can be explained by multiple reasons. Perhaps the most obvious reason is that the number of trees is a fundamental criterion for the access to public grants by olive tree farmers. Another reason is the fact that crop yield estimation is based on the number of trees in the orchard (along with other parameters such as number and volume of fruits). Furthermore, irrigation plans and water management are based on inventory and arrangement of the trees in the orchard [17][18]. Also, detection and localization of individual tree is prerequisite for more advanced analysis of plant health and fruit status using remote sensing technology.

Counting of trees by humans is prone to errors but, first of all, it is tiresome and time-consuming. Therefore, automatization of this process is lately in focus of research community [19]. Availability of various sources of aerial images such as high-resolution satellite images, images acquired by unmanned aerial vehicles (UAVs) combined with advanced image processing algorithms, makes this task solvable.

The availability of different sensors has enabled different approaches in the detection of individual trees during the last decade. For example, some authors use hyperspectral and airborne laser scanning (ALS) for tree detection and classification [20]. In contrast to hyperspectral sensors that can use several hundreds of narrow frequency bands (10-20 nm) for detection, multispectral sensors usually use 3 to 15 frequency bands. The width of these bands is usually slightly larger. For example, the multispectral camera used by the popular UAV DJI Phantom 4 has, in addition to the RGB sensor (visible spectrum), 5 more monochrome sensors with a width of 32 or 52 nm. Captured wavelengths are: blue (450 nm ± 16 nm), green (560 nm ± 16 nm), red (650 nm ± 16 nm), red edge (730 nm ± 16 nm), near-infrared (840 nm ± 26 nm). Images obtained from hyperspectral sensors contain much more data than images from multispectral sensors and have a greater potential to detect differences among land and water features. However, multispectral sensors are very popular for precision agriculture because they are much cheaper than hyperspectral sensors. Also, from available multispectral information, various vegetation indexes can be calculated [21]. Vegetation indexes calculated for each image pixel can be used to enhance the presence of green, vegetation features and thus may distinguish plants from the other objects present in the image [22-24]. One of the most frequently used and implemented vegetation indexes calculated from multispectral information as normalized ratio between the red and near infrared bands is the Normalized Difference Vegetation Index (NDVI). NDVI correlates with chlorophyll, which in turn correlates with plant health (Figure 1). Based on calculated NDVI and utilization of red band thresholding, the algorithm for detection of olive trees, resulted in an overall estimation error of 1.3% [22]. Jan Peters et al. proposed an object-based classification method for detection of olive trees from multi-spectral images [23]. This approach was comprised of a four-step model: image segmentation, feature extraction, classification, and result mapping. Obtained overall accuracy was 84.3%.

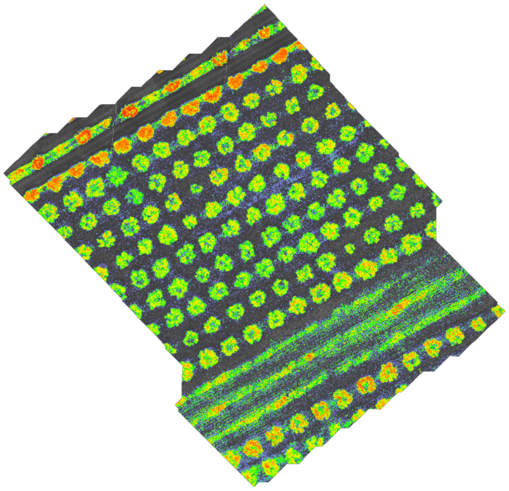

Figure 1: Example of a NDVI olive orchard image obtained with multispectral camera.

Sensor data can be used for more advanced image processing and analysis. The most popular classical methods of image analysis include machine learning (K-means, support vector machines - SVM), wavelet-based filtering, vegetation indices and regression analysis [25, 26]. In the image processing procedure, a preprocessing step is common (image segmentation, contrast enhancement and edge detection, color model selection, noise removal by filtering, feature extraction by various transformations, dimensionality reduction), after which object-based image analysis (OBIA) is performed [27].

An approach that uses classical image methods for the automatic detection and recognition of a single tree and labelling is presented in [28]. Authors pre-processed the images with the unsharp masking followed by improved multi-level thresholding-based segmentation. The circular Hough transform was applied for the identification of the circular blobs that presented single trees. Another study presented an algorithm that used RGB satellite images for a classification system. The system consists of several steps: it includes image pre-processing, image segmentation, feature extraction and classification [29]. All images were preprocessed to suppress the additive noise. Next, the region of interest was segmented from the pre-processed images using K-Means segmentation, through which statistical features were extracted and classified. The best classification results reported in that paper were achieved with Random Forest that outperformed other tested algorithms by an overall accuracy of 97.5%.

As in many other areas, deep learning has played an increasingly important role in the field of image processing in agriculture in recent years [30]. Changes in lighting, camera position and camera distance (height) to the ground significantly affect the performance of classical methods compared to methods that use deep learning. Compared to classical methods, the approach using deep learning requires larger computing resources and larger databases of labeled images for learning. The aforementioned limitations have been overcome or largely removed in recent years due to the availability of advanced graphics processors and tools for easy labeling of learning images. Also, publicly available image databases such as PASCAL Visual Object Classes (PASCAL VOC), Microsoft Common Objects in COntext (COCO) and ImageNet, which contain thousands of object classes and millions of images and are available to researchers for model training, are also useful in this area. Deep learning models can be tuned and trained to detect fruits on these bases using transfer learning. However, it can be noted that the mentioned bases do not contain images of orchards [31].

One recent example of implementation of deep learning for identification and mapping of trees can be found in [32]. In the presented approach, the UAV RGB photograph of the forest was automatically segmented into several tree crown objects using color and 3D information and the slope model. After that, an object-based CNN classification was applied for each crown image. Classification results of the presented system showed good results in classifying seven tree classes, including several tree species with more than 90% accuracy. Another recent paper presents deep learning-based approach for estimating the biovolume of individual trees [33]. In this paper, authors used Mask R-CNN and UAV images for olive tree crown and shadow segmentation.

DeepForest is an open-source (MIT license) Python package that uses deep learning object detection networks to predict bounding boxes corresponding to individual trees in RGB imagery [34]. In order to make training models for tree detection simpler, DeepForest use the RetinaNet model [35, 36] from the TorchVision package [37]. More precisely, the model was trained on images from 40m x 40m windows obtained from 1km x 1km maps downloaded from National networks of ecological observatories (NEON) using a semi-supervised LiDAR-based algorithm to generate millions of moderate-quality annotations for model pretraining. In the next step, the pretrained model was retrained on over 10,000 hand annotations of RGB imagery from six NEON sites which further improved generalization abilities. Obtained model can be used directly to make predictions for new data or used as a foundation for retraining the model using labelled data from a new application.

Individual tree detection may not seem particularly difficult computer vision task at first, but it can be a demanding task for various reasons. Perhaps the biggest problem are closely planted trees forming joint crowns. In olive growing, this type of problems is related to extensive types of orchards (orchards with lower productivity per hectare, low mechanization level, small amount of labor relative to the area under cultivation) which is not usual for larger plantations with larger production of olive fruits and oil. Other challenges are related to varying sizes of trees in an orchard, misaligned plantation of trees, different types of soil and vegetation under trees, etc. As a result, there is quite vivid research activity in this field.

Although the use of other types of sensors, such as multispectral ones, could make the detection and labeling of individual trees simpler (as could be assumed by analyzing Figure 1), in this work we are focused on the use of RGB sensors as the most widespread and cheapest. In order to simplify and speed-up the process, only 2D information from the obtained terrain maps was used. Our approach is based on the implementation of deep neural networks for detection, more precisely on adaptation of the DeepForest package. Due to fact that original (prebuilt) model used in DeepForest package has been built on images from various types of trees but without images of olive trees, it was expected that results obtained on that model would not be good enough for implementation on olive groves. Therefore, a new image dataset of olive trees was created, individual olive trees were labeled, and new models were created. New models were built using different sets of images chosen from five olive groves. Since those olive groves had different characteristics, choice of olive groves used for model creation was important for detection results. This paper is an extension of work originally presented in conference 2022 International Conference on Software, Telecommunications and Computer Networks [38]. In this work, comparing to conference paper, a more detailed explanation of multiple models creation will be given. Also, in addition to detailed comparison of various models, analysis of the detection results for one olive orchard monitored in different seasons of year will be done.

Contributions of this paper are following: we propose a methodology for automatic olive trees detection based on adaptation of publicly available open source DeepForest package. Image dataset of five olive orchards were annotated and used for further research. Also, we present analysis on the variability of the olive trees detection results with the same neural network model in the case of olive grove surveillance at different times of year.

The remainder of the paper is organized as follows: in Section 2 the proposed methodology is described, along with the test sites description and used software tools. In Section 3, a detailed description of used procedure is given. Section 4 presents the results of the tree detection based on implementation of our models. The discussion and conclusion are then presented in Section 5.

2. Materials and Methods

2.1. Study Sites

For this study, five olive orchards were surveyed (Figure 2). Two orchards were in Mravinci, north of Split, Croatia (Mravinci01: 43°31’40.7” N, 16°30’57.8” E and Mravinci02: 43°31’37.4” N, 16°30’57.8” E). Both olive orchards at this location can be classified as extensive. They are characterized with irregular pruning and non-uniform shaping of trees. Most of the trees are free vise shaped while smaller number of trees have monoconical and globe shaped plants. Other three orchards were located in Tinj, south-west of city of Benkovac in Zadar County, Croatia (Tinj01: 44°00’49” N, 15°28’13.2” E, Tinj02: 44°01’10.6” N, 15°28’19.5” E and Tinj03: 44°00’26” N, 15°29’31.0” E). All olive trees at this location were vise shaped and rather heavy pruned. Since olive orchard at Tinj03 location is quite large (12.000 olive trees), surveillance with UAV did not cover all plants. In four separate flights (Flight01, Flight02, Flight03, Flight04), around 5% of total area was covered (around 600 olive plants detected and annotated). Each flight for this olive grove was used for generating separate map and, in this paper, each is treated individually for the analysis.

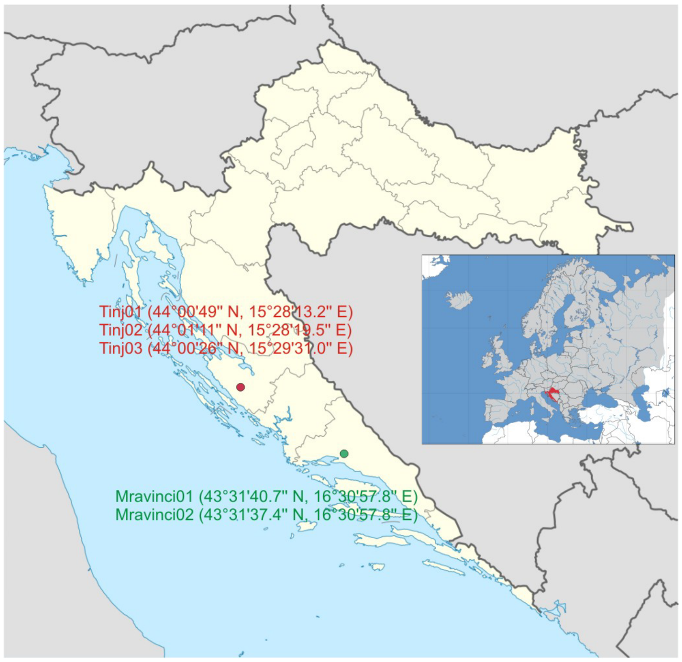

Figure 2: Locations of surveyed olive groves (Dalmatia region, Croatia). Three olive orchards in Tinj and two in Mravinci.

Also, one of the orchards (Tinj02) has been mapped in two different seasons of year (May and December) in order to analyze differences in detection performance not only for different orchards but also for the same orchard surveilled at different seasons and times of day.

Both observed regions have a Mediterranean climate characterized by dry summers and mild, wet winters. The UAV flights were performed on five dates: 10 May 2021 (Mravinci01), 11 May 2021 (Tinj01 and Tinj02), 20 December 2021 (Tinj02), 18 January 2022 (Mravinci02) and 5 April 2022 (Tinj03).

2.2. UAV for Images Acquisition

Nine image datasets were acquired using high resolution sensors onboard UAV platform to monitor the olive groves. RGB and multispectral images were collected using the camera on DJI Phantom 4 Multispectral drone. DJI Phantom 4 Multispectral drone is equipped with camera with six 1/2.9” CMOS (Complementary metal–oxide–semiconductor) image sensors. One CMOS sensor is RGB sensor for visible light imaging while other five sensors are used for multispectral imaging. Each sensor has 2.08 megapixels (MP).

For this research, we used only information from RGB sensor. In order to collect images needed for making the map of an olive orchard, UAV was programmed to fly at 35 m above ground altitude (AGL) with airspeed of 5 m/s. The forward and sideway image overlaps were 75%. Ground sampling distance (GSD) was 2 cm.

2.3. Software Tools

DJI Terra (https://www.dji.com/hr/dji-terra) was used as a flight planner software. Also, this software was used for stitching of the collected multispectral and RGB images and production of 2D terrain maps of monitored olive orchards (Figure 3). Since maps generation is a compute-intensive process, minimum hardware configuration for map reconstruction using DJI Terra is 16GB RAM and a NVIDIA graphics card with at least 4GB VRAM. For this purpose, one NVIDIA GForce RTX 3060 GPU with 12 Gb VRAM was used.

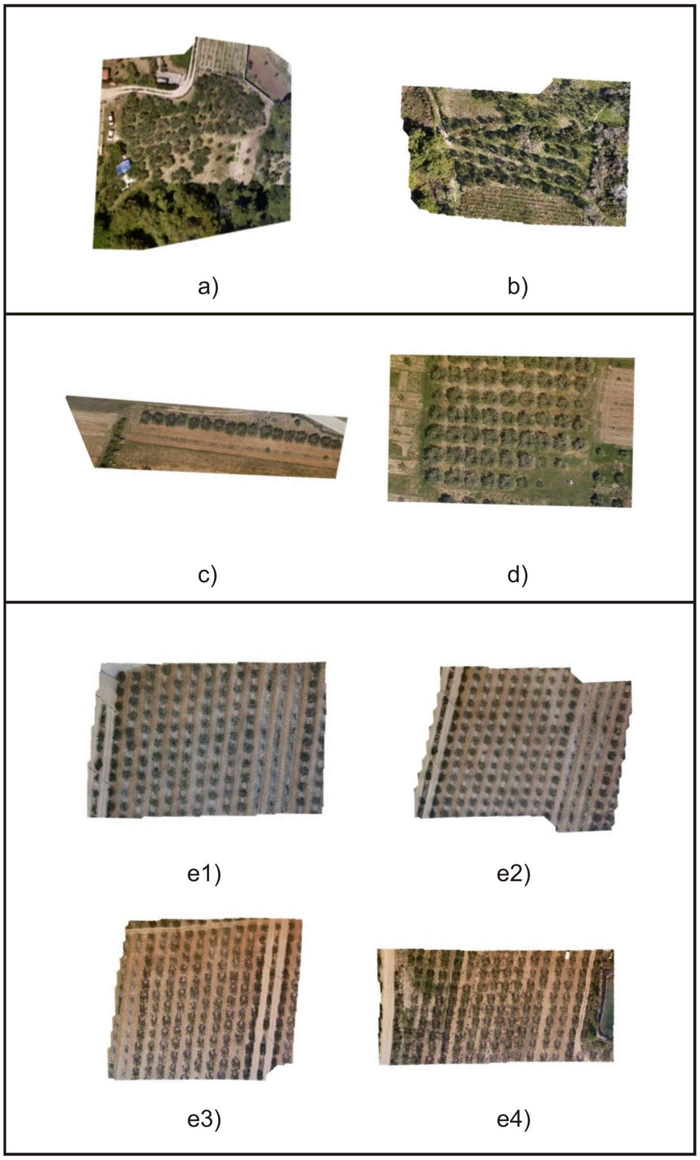

Figure 3: Maps of olive groves. a) Mravinci01, b) Mravinci02, c) Tinj01, d) Tinj02, e1) Tinj03 – Flight01, e2) Tinj03 – Flight02, e3) Tinj03 – Flight03, e4) Tinj03 – Flight04.

Labeling of individual olive trees on generated olive orchard maps was done using Computer Vision Annotation Tool (https://www.cvat.ai/). It is a free (for individual data scientists and small teams) web-based image and video annotation tool used for labeling data for computer vision algorithms. Labeled annotations for object detections was done in Pascal VOC format [39]. Each label is defined with four values (x_{min}, y_{min}, x_{max}, y_{max}): where x_{min} and y_{min} are coordinates of the upper left corner of the rectangle label and x_{max} and y_{max} are coordinates of the lower right corner of the rectangle label.

Implementation and evaluation of object (olive tree) detectors and image processing was done using Python 3.10.4. programming language with the DeepForest package that comes with the prebuilt RetinaNet model from the torchvision package. Proposed implementation has been done on Windows operating system although the package has been tested also on MacOS, and Linux.

2.4. RetinaNet Detector

Popular object detection models can be broadly classified into two categories: two-stage and single-stage detectors. Two-stage detectors are using one model to extract regions of objects (first stage), and a second model is used to classify and further refine the localization of the object (second stage). Single-stage detectors have only one model which skip the region proposal stage of two-stage models and run detection directly over a dense sampling of locations. Comparing to two-stage detectors, these types of models usually have faster inference (possibly at the cost of performance) [40]. RetinaNet is a single-stage detector which is fast and has accuracy comparable to two-stage detectors. RetinaNet uses a feature pyramid network (FPN) [41] which enables the detection of objects at multiple scales and introduces a new loss, the Focal loss function [35], to alleviate the problem of the extreme foreground-background class imbalance. Focal Loss function approach addresses this problem that occurs in single-stage detectors by assigning less weight to easily classified examples and focusing on correcting misclassified ones. RetinaNet's network architecture FPN backbone is on top of a feedforward ResNet architecture [42] with the goal of generating rich, multi-scale convolutional feature pyramid. RetinaNet attaches two subnetworks to this backbone, one for classifying anchor boxes and one for regressing from anchor boxes to ground-truth object boxes (Figure 4).

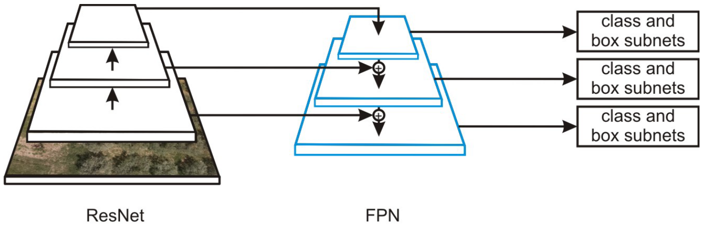

Figure 4: ResNet network architecture.

3. Procedure

After collecting sets of images for five olive orchards (parameters described in Section 2.2.), maps of olive groves for each flight were obtained with DJI Terra software. Each map was annotated using CVAT i.e. individual olive trees were labeled as a ground truth. However, generated maps have higher resolution than the images used for training the prebuilt RetinaNet model from the DeepForest package. Furthermore, their resolution may, generally, vary depending on the flight parameters and used sensor.

In order to get better predictions, it is necessary to divide each map into smaller windows that are more similar to the data on which the DeepForest model was trained. When forecasting, the input map is divided into smaller overlapping windows and then the model in each window tries to detect trees. Detections from all windows are then collapsed into detections (predictions) on the entire map, while redundant filtering is carried out frame by the non-max suppression method. This method keeps only the highest reliability frame from all detections whose predicted limit frames match more than the default intersection over union (IoU) threshold (Figure 5).

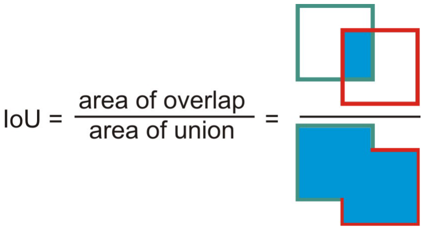

Figure 5: IoU illustration.

First detection results were obtained using the pretrained DeepForest model. Different window sizes (ranging from 600 x 600 to 1000 x 1000 pixels with a step of 50) with different "overlaps" (10-40% with a step of 5%) were tested and evaluated on maps Tinj1 and Tinj2 (Figure 3). During inference, the model tries to detect olive trees on each window, and afterwards, detections from all windows are compressed into detections on the whole map.

Finally, the windows size of 750 x 750 pixels was chosen with an overlap of 20%. For the pretrained model, the best predictions were obtained using confidence limit (τ) of 0.3.

Table 1: Models trained, N – total number of trees in maps (ground truth objects)

Model	Trained on maps	N
M1	Tinj02	69
M2	Tinj03 – Flight01	133
M3	Tinj02, Tinj03 – Flight01	202
M4	Tinj02, Tinj03 – Flight01, Tinj03 – Flight04	356
M5	Tinj03 – Flight01, Tinj03 – Flight04	287
M6	Tinj02, Tinj03 – Flight01, Mravinci02	277
M7	Tinj02, Tinj03 – Flight01, Tinj03 – Flight04, Mravinci02	431
M8	Tinj01, Tinj03 – Flight01, Tinj03 – Flight04, Mravinci02	381

Since the prebuilt model had been trained on various types of trees and not olives, further steps were needed in order to improve predictions and reduce the number of other trees being detected as olive trees. Therefore, an adaptation of the pretrained RetinaNet model to the local data using transfer learning was done. During this step, eight new models were trained. For each model, different labeled maps were used for training (Table 1).

Again, for new models, various windows sizes with different "overlaps" were tested. After tests, an image size of 1000 × 1000 pixels with 40% overlap was chosen.

Each network was trained for five epochs with stochastic gradient descent with a momentum of 0.9, a learning rate equal to 0.001 and a confidence threshold of 0.7. All trained models used a confidence threshold of 0.5 at inference time. As already written, a confidence threshold of 0.3 was chosen for the pretrained model because, in this case, all predicted bounding boxes had low confidence scores.

4. Results

4.1. Performance Evaluation

In order to evaluate the proposed methodology, exact number of olive trees in the evaluation areas was determined by a human observer (ground truth). The performance assessment of the methodology was approached by comparing the actual number of plants, and their distribution with the results of detection of a deep neural network for eight created models (and pretrained model).

A number of metrics defined below are proposed for quantitative assessment.

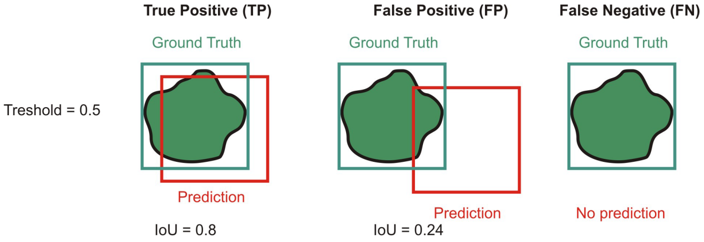

Figure 6: Examples of TP, FP and FN bounding boxes when default IoU = 0.5.

Using the calculated IoU value each predicted bounding box is classified into one of the following categories (illustrated in Figure 6):

- True Positive (TP): detection is correct (predicted frame matches with correct) if valid IoU >= threshold,
- False Positive (FP): the detection is wrong (a frame is provided for the object which is not in the picture, or the intended frame does not match the correct one) if IoU < threshold,
- False Negative (FN): the object in the image is not detected.

Precision: presents the hit ratio for the trees found by the algorithm.

$$Precision = \frac{TP}{TP+FP} = \frac{TP}{all\ detections} \tag{1}$$

where TP (true positives) is the number of olive trees correctly identified by the algorithm, and FP (false positives) is the number of instances wrongly proposed by the algorithm as potential olive trees.

Recall: presents the proportion of the trees correctly found by the algorithm.

$$Recall = \frac{TP}{TP+FN} = \frac{TP}{all\ ground\ truth\ boxes} \tag{2}$$

where FN (false negatives) is the number of olive trees that were not identified.

F1 score: the harmonic mean of precision and recall,

$$F1\ score = \frac{1}{\frac{1}{Precision}+\frac{1}{Recall}} = 2x\frac{Precision\ x\ Recall}{Precision+Recall} \tag{3}$$

For the calculation of previous metrics, IoU value of 0.5 was used (the most commonly used values for IoU are 0.5 and 0.75 [43]).

Average precision (AP): summarizes the precision recall curve into one number, it can be interpreted as the area under the precision-recall (PR) curve.

$$AP = \int_0^1 p(r)dr \tag{4}$$

where p(r) is Precision for particular Recall value.

Precision – Recall (PR) curve is obtained by plotting points (r(τ), p(τ)) where r(τ) and p(τ) denote precision and recall at confidence threshold τ. In practice, the area is calculated under interpolated monotone curve instead of the actual ”zig-zag” PR curve. Average precision is calculated according to MS COCO [44]. For AP calculation, 101 recall points on the PR curve are used (0 to 1 with a step size of 0.01). More precisely, AP@0.5 calculated with a fixed IoU threshold of 0.5 is used, while AP is obtained by averaging AP@α for IoU thresholds α from 0.5 to 0.95 with a step size of 0.05.

4.2. Evaluation Results

In this section, the evaluation results for the trained olive tree detectors will be presented. Tables 2 and 3 show evaluation results of all 9 models on maps Tinj03 - Flight02 and Tinj03 - Flight03. As it can be seen from Table 1, these maps weren’t used for any model’s training.

Combined results for both maps (Tinj03 - Flight02 and Tinj03 - Flight03) are presented in Table 4.

This maps present parts of a large orchard (each map corresponds to one drone flight). Since the implementation of computer-based tree counting and labeling is particularly interesting for large orchards (small orchards are economically less significant), results for that type of orchards are the focus of our interest and basis for a future applications.

As expected, model (M5) for which training phase used only other parts (maps) of the same orchard (Tinj03), showed slightly better results than others but differences were not significant, moreover, two models have higher precision (M2 and M8) and one (M8) has higher AP. Recall and F1 measure, as can be seen, of the pretrained model lags significantly behind models trained on images of olive groves obtained by drone.

Table 2: Results for map Tinj03 – Flight02

Model	Precision	Recall	F1	AP@0.5	AP
pretrained	0.1212	0.0258	0.0426	0.0069	0.0044
M1	0.3333	0.1935	0.2449	0.1034	0.0354
M2	0.9434	0.9677	0.9554	0.9585	0.6484
M3	0.9212	0.9806	0.9500	**0.9754**	**0.6652**
M4	0.9375	0.9677	0.9524	0.9567	0.6037
M5	**0.9500**	**0.9806**	**0.9651**	0.9750	0.6441
M6	0.9379	0.9742	0.9557	0.9632	0.6408
M7	0.9157	0.9806	0.9470	0.9645	0.6367
M8	0.9487	0.9548	0.9518	0.9479	0.6512

Table 3: Results for map Tinj03 – Flight03

Model	Precision	Recall	F1	AP@0.5	AP
pretrained	0.2667	0.0500	0.0842	0.0194	0.0092
M1	0.4545	0.2188	0.2954	0.1565	0.0352
M2	**1.0000**	0.8875	0.9404	0.8812	0.5256
M3	0.9605	0.9125	0.9359	0.9094	0.5650
M4	0.9813	**0.9813**	**0.9813**	0.9787	0.6016
M5	0.9691	**0.9813**	0.9752	**0.9799**	**0.6514**
M6	0.9419	0.9125	0.9270	0.8968	0.5034

M7	0.9398	0.9750	0.9571	0.9604	0.5981
M8	0.9810	0.9688	0.9748	0.9601	0.6474

Table 4: Mean metrics value on maps Tinj03 – Flight02 and Tinj03 – Flight03

Model	Precision	Recall	F1	AP@0.5	AP
pretrained	0.1939	0.0379	0.0634	0.0131	0.0068
M1	0.3939	0.2061	0.2701	0.1300	0.0353
M2	**0.9717**	0.9276	0.9479	0.9199	0.5870
M3	0.9409	0.9466	0.9429	0.9424	0.6151
M4	0.9594	0.9745	0.9668	0.9677	0.6026
M5	0.9596	**0.9809**	**0.9701**	**0.9774**	0.6478
M6	0.9399	0.9433	0.9413	0.9300	0.5721
M7	0.9277	0.9778	0.9520	0.9625	0.6174
M8	0.9649	0.9618	0.9633	0.9540	**0.6493**

According to the results from table 4, it can be commented that models M5 and M8 stand out as the best possible options in this case.

Since majority of models used some maps from Tinj03 orchard (7 out of 9), more objective detection results may be the ones obtained for Tinj02 orchard (5 out of 9). Results for Tinj02 are presented in Table 5.

Again, the best model (M4) in this case, used map of the orchard in the training phase. The best model for previous case (M5) showed rather low precision result (0.7941) while one of the best models for detections on Tinj03 maps – M8 showed rather high precision (0.9552) and recall (0.9275) values on this map, also. Both models, M5 and M8 have not used Tinj02 maps in training phase. Detections obtained by applying these two models to two evaluation maps and the Tinj02 map (neither of these models used Tinj02 map for the training) compared to detections of the pretrained model are presented in Figure 7.

Table 5: Results for map Tinj02 (flight from May 2021).

Model	Precision	Recall	F1	AP@0.5	AP
pretrained	0.6585	0.7826	0.7152	0.669	0.2795
M1	0.9296	0.9565	0.9429	0.9465	0.5526
M2	0.873	0.7971	0.8333	0.7472	0.2496
M3	0.8481	**0.971**	0.9054	**0.9669**	0.5378
M4	**0.9571**	**0.971**	**0.964**	0.9661	**0.5688**
M5	0.7941	0.7826	0.7883	0.7358	0.1567
M6	0.9286	0.942	0.9353	0.9374	0.5684
M7	0.9167	0.9565	0.9362	0.9291	0.512
M8	0.9552	0.9275	0.9412	0.9146	0.4582

Corresponding to this, Table 6 presents the exact number of detected olive trees, ground-truth labels, TP, FP, and FN. It can be noted that, on map Tinj03 - Flight 02 (Figure 7), in both models (M5 and M8), some of the fig trees planted between olives were mistaken for olive trees.

Next evaluation was done on the detection results for an extensive orchard that has not been used for training of any model (Mravinci01 – Figure 3.a.). Mravinci01 can be seen as a special case of the olive grove because it is characterized by irregular pruning, overlapping tree crowns, and the non-uniform shaping of trees. Moreover, in this aerial image, various types of trees are also present, apart from olives. In the case of the map Mravinci01, even human annotators have a hard time labeling olive trees. Precision and recall values are significantly lower than in previous cases.

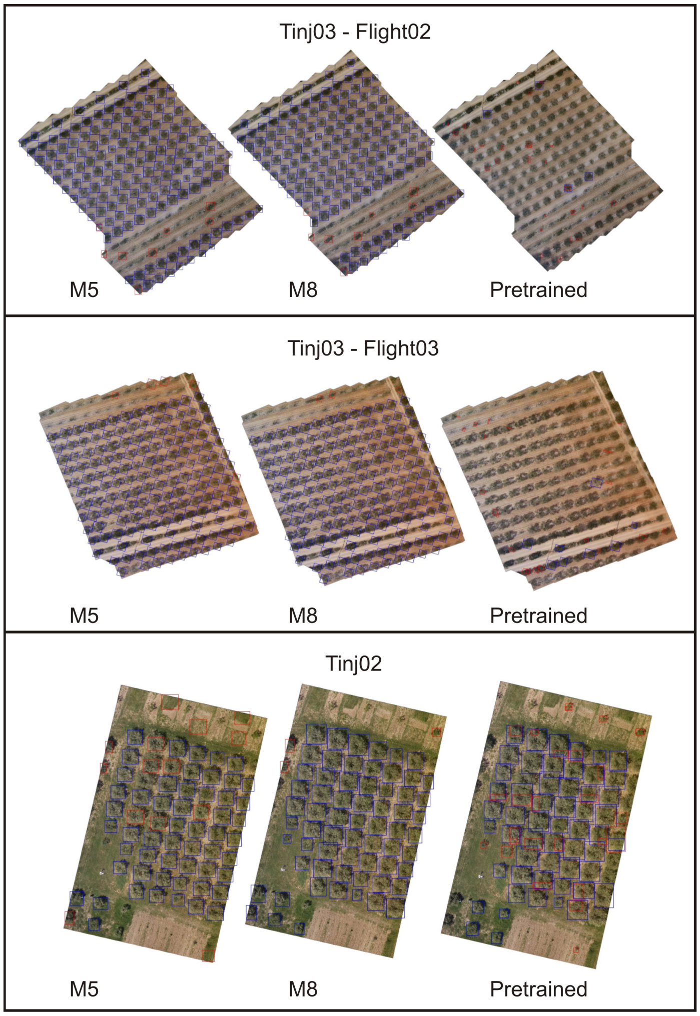

Figure 7: Detections made by model M5, model M8 and pretrained models. True positive (TP) detections are shown in blue, false positive (FP) detections are shown in red.

Table 6: Model M5, model M8 and pretrained model detections on maps Tinj03 – Flight02, Tinj03 – Flight03 and Tinj02

map	true boxes	model	detections	TP	FP	FN
Tinj03 – Flight02	155	M5	160	152	8	3
		M8	156	148	8	7
		pretrained	33	4	29	151
Tinj03 – Flight03	160	M5	162	157	5	3
		M8	158	155	3	5
		pretrained	30	8	22	152
Tinj02	69	M5	68	54	14	15
		M8	67	64	3	5
		pretrained	82	54	28	15

Best precision was achieved with model M6 (0.5068) and highest recall was achieved with model M3 (0.6138). This is expected due to aforementioned reasons, as well as lack of proper training examples for model generation (only Mravinci02 map can be considered as extensive orchard but with larger distances between trees). However, even here, significant improvement of generated models over pretrained model can be confirmed - precision for pretrained model was 0.1205 and recall 0.0516. The pretrained model produced drastically more false positives, especially on the part of the map with the pine trees (Figure 8).

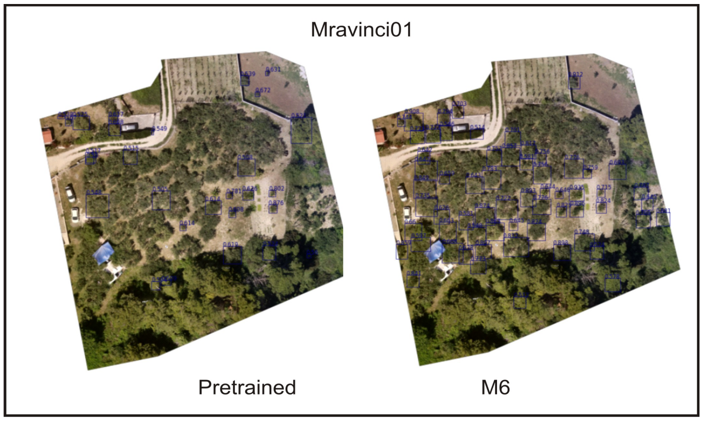

Figure 8: Special case: M6 vs Pretrained model comparison for olive grove Mravinci01.

Finally, we present analysis results of differences in detection performance for the same orchard surveilled at different seasons and times of day. One of the test orchards (Tinj02) has been mapped in May (and used for generating some of models presented in Table 1) and later in December of the same year (2021). Detection results for second flight (map) are given in Table 7.

Table 7: Results for map Tinj02 (flight from December 2021).

Model	Precision	Recall	F1	AP@0.5	AP
pretrained	0.6706	0.7215	0.6951	0.5425	0.1995
M1	0.8462	0.8354	0.8408	0.8217	0.367
M2	0.75	0.6456	0.6939	0.4926	0.1676
M3	0.8222	**0.9367**	0.8757	0.9039	0.4976
M4	0.9605	0.9241	0.9419	0.92	0.5043
M5	0.9016	0.6962	0.7857	0.6863	0.2983
M6	**0.9737**	**0.9367**	**0.9548**	**0.9302**	**0.5083**
M7	0.9012	0.9241	0.9125	0.9124	0.4457
M8	0.9733	0.9241	0.9481	0.9196	0.4576

As opposite to results presented in Table 5, for the second flight, the best performance has been achieved with model M6. Interesting, performance of some models was better for December flight than for May flight (M6, M8). Precision and recall comparison for all models is presented in Figures 9 and 10.

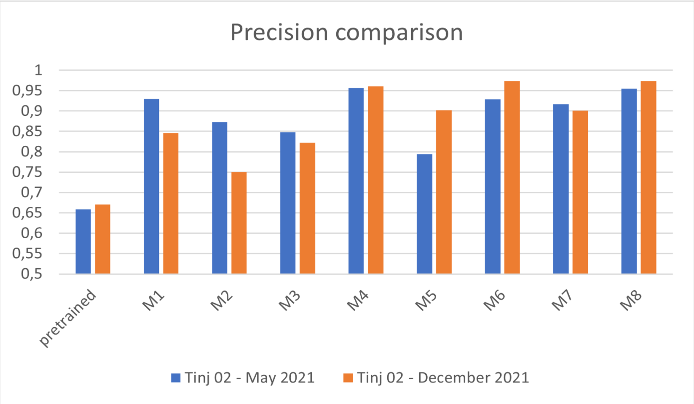

Figure 9: Precision comparison for Tinj02 maps.

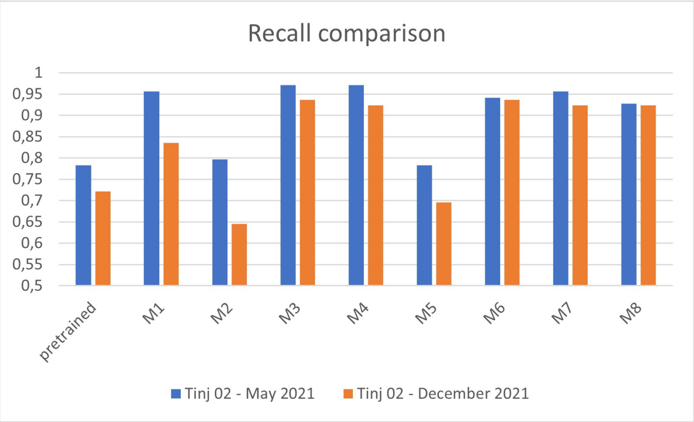

Figure 10: Recall comparison for Tinj02 maps.

When compared to variations (absolute differences) in results for all models between two similar maps taken the same day in the same large orchard, absolute differences were similar. For instance, average absolute difference for precision results between maps generated for Tinj02 flights is 0.048 while the average absolute difference for precision results between maps generated for Tinj03-Flight02 and Tinj03-Flight03 is 0.054. This implies that detection results for the same olive orchard are not to be significantly degraded during period of several months. However, this should be confirmed on a larger number of test cases.

5. Discussion and conclusion

Automatic olive tree detection is a task with many challenges. Acquired images of the olive groves can vary significantly due to different types of soil and vegetation in orchards, changes in vegetation during seasons, the age of the orchard and tree sizes, irregular pruning and pruning types, the non-uniform shaping of trees, changes in weather conditions and illumination. Also, trees in the orchard can be planted very closely, forming joint crowns, and making it very difficult, even for human annotator, to label individual tree. In this paper, we presented a procedure for development of a deep learning object detector for detecting individual olive trees from aerial RGB images by fine-tuning the prebuilt RetinaNet model on local data.

During development of the olive trees object detector, several models were trained using a different training set of images - different olive grove maps. Maps of five diverse olive groves (small and large) were generated but the focus was on automatization of monitoring a large olive grove such as Tinj03. Comparison of model performance for the olive tree detection in different times of the year was presented. As it can be seen from the obtained results, there was generally no degradation in detection. For some particular tests such as evaluation of detections from diverse parts of the orchard in Tinj03, the best performing models were the model M5 which uses only other parts of the same orchard as the training data, and model M8, which expands that data with images from two other olive groves (Tinj01 and Mravinci02). As already said, even though the olive groves such as Tinj03 will be the focus of future research, a trained detector should be generalizable to orchards with diverse vegetations and various-sized olive trees. In this context, for further use, we propose the model M4 and, alternatively, M8. Although there is no clear winner between tested models, perhaps M4 could be considered as the most reliable. Proposed model (M4) has been trained on 356 ground truth olive trees while the runner-up (M8) has been trained on 381 ground truth olive trees which classifies them in top 3 models according to the number of trees used for training. This indicates that further improvements can be expected with additional training examples.

Comparing to the prebuilt model that showed very poor performance in olive trees detection, experimental results have shown the dominance in performance of fine-tuned models. Achieved precision and recall even with the relatively small training dataset (generally > 95% for heavy pruned orchards) makes this approach useful for the implementation.

Findings related to the fairly stable detection results of the same olive orchard taken several months apart are certainly interesting because, to the best of our knowledge, there has been no such analysis in the literature so far.

There are several directions for future research. The most imminent one should be utilizing the olive-tree detector for olive groves analysis, such as crop yield estimation and monitoring plant health and fruit status using vegetation indices. Automated collection of images of individual olive trees will greatly speed up and facilitate the analysis process. Image processing procedures aimed at obtaining information about plant health (e.g. from NDVI index values) or plant water status (e.g. from thermal camera data) will be able to be automated, because in this way only the part of the image related to an individual tree (output from the detector) will be brought to the input.

Moreover, as noted, there is still room for further improvement of the obtained detection model(s) by expanding the existing training datasets with more aerial images of olive trees from different localities, types of pruning and in different seasons to obtain more robust olive detectors.

Conflict of Interest

The authors declare no conflict of interest.

References

[1] National Research Council, Division on Earth and Life Studies, Board on Earth Sciences and Resources, Committee on Strategic Directions for the Geographical Sciences in the Next Decade, Understanding the Changing Planet: Strategic Directions for the Geographical Sciences, National Academies Press, 2010.

[2] C.I. Gan, R. Soukoutou, D.M. Conroy, Sustainability Framing of Controlled Environment Agriculture and Consumer Perceptions: A Review. Sustainability 2023, **15**(1), 304. https://doi.org/10.3390/su15010304.

[3] M. Dijk, T. Morley, M.L. Rau, S. Yashar, A meta-analysis of projected global food demand and population at risk of hunger for the period 2010–2050, Nature Food, **2**, 2021, 494–501, https://doi.org/10.1038/s43016-021-00322-9.

[4] M. Elferink, F. Schierhorn, Global Demand for Food is Rising. Harvard Business Review April 07, 2016.

[5] D. Niklis, G. Baourakis, B. Thabet, G. Manthoulis, "Trade and logistics: the case of the olive oil sector," in MediTERRA 2014. Presses de Sciences Po, 203 – 226, 2014, doi : 10.3917/scpo.cihea.2014.02.0203.

[6] F. B. Insights, "Olive oil market size, share & covid-19 impact analysis, by type (refined olive oil, virgin olive oil, olive pomace oil, and others), end-user (household/retail, food service/horeca, food manufacturing, and others), and regional forecast, 2020–2027", 2021.

[7] S. Mili, M. Bouhaddane, "Forecasting Global Developments and Challenges in Olive Oil Supply and Demand: A Delphi Survey from Spain". Agriculture, 2021, **11**(3), 191. https://doi.org/10.3390/agriculture11030191.

[8] A. Kamilaris, A., Gao, F., Prenafeta-Boldú, F.X., Ali, M.I., "Agri-IoT: A Semantic Framework for Internet of Things-Enabled Smart Farming Applications". 3rd World Forum on Internet of Things (WF-IoT) IEEE, Reston, VA, USA, 442–447, 2016, doi: 10.1109/WF-IoT.2016.7845467.

[9] W. Bastiaanssen, D. Molden, I. Makin, "Remote sensing for irrigated agriculture: examples from research and possible applications". Agric. Water Manag. **46** (2), 137–155, 2000, doi: 10.1016/S0378-3774(00)00080-9.

[10] P. Nevavuori, N. Narra, T. Lipping, "Crop yield prediction with deep convolutional neural networks", Computers and Electronics in Agriculture, vol. **163**, 2019, https://doi.org/10.1016/j.compag.2019.104859.

[11] A. Matese, P. Toscano, S. F. Di Gennaro, L. Genesio, F. P. Vaccari, J. Primicerio, C. Belli, A. Zaldei, R. Bianconi, B. Gioli, "Intercomparison of UAV, aircraft and satellite remote sensing platforms for precision viticulture". Remote Sensing, **7**(3):2971-2990, 2015, https://doi.org/10.3390/rs70302971.

[12] M. Waleed, T. -W. Um, A. Khan and Z. Ahmad, "An Automated Method for Detection and Enumeration of Olive Trees Through Remote Sensing," in IEEE Access, vol. **8**, 108592-108601, 2020, doi: 10.1109/ACCESS.2020.2999078.

[13] J. M. Ponce, A. Aquino, B. Millan, J. M. Andújar, "Automatic Counting and Individual Size and Mass Estimation of Olive-Fruits Through Computer Vision Techniques," in IEEE Access, vol. **7**, pp. 59451-59465, 2019, doi: 10.1109/ACCESS.2019.2915169.

[14] S. Benalia, B. Bernardi, J. Blasco, A. Fazari, G. Zimbalatti, "Assessment of the Ripening of Olives Using Computer Vision", Chemical Engineering Transactions. **58**, 355-360, 2017, https://doi.org/10.3303/CET1758060.

[15] Petteri Nevavuori, Nathaniel Narra, Tarmo Lipping, "Crop yield prediction with deep convolutional neural networks", Computers and Electronics in Agriculture, **163**, 2019, https://doi.org/10.1016/j.compag.2019.104859.

[16] X. Liu, W. Min, S. Mei, L. Wang, S. Jiang, "Plant Disease Recognition: A Large-Scale Benchmark Dataset and a Visual Region and Loss Reweighting Approach", IEEE Transactions on Image Processing, **30**, 2003-2015, 2021, doi: 10.1109/TIP.2021.3049334.

[17] N. T. Waskitho, "Unmanned aerial vehicle technology in irrigation monitoring", Advances in Environmental Biology, **9**(23), 7–10, 2015.

[18] C. Albornoz, L. F. Giraldo, "Trajectory design for efficient crop irrigation with a UAV," 2017 IEEE 3rd Colombian Conference on Automatic Control (CCAC), 2017, 1-6, doi: 10.1109/CCAC.2017.8276401.

[19] Z. Zhen, L. J. Quackenbush, and L. Zhang, "Trends in automatic individual tree crown detection and delineation—evolution of lidar data," Remote Sensing, **8**(4): 333. https://doi.org/10.3390/rs8040333.

[20] M. Dalponte, H. O. Orka, L. T. Ene, T. Gobakken, and E. Nasset, "Tree crown delineation and tree species classification in boreal forests using hyperspectral and als data", Remote Sensing of Environment, **140**, 306–317, 2014. https:// doi.org/10.1016/j.rse.2013.09.006.

[21] G. Avola, S.F. Di Gennaro, C. Cantini, E. Riggi, F. Muratore, C. Tornambè, and A. Matese, "Remotely Sensed Vegetation Indices to Discriminate Field-Grown Olive Cultivars", Remote Sensing, **11**, 1242, 2019, https://doi.org/10.3390/rs11101242.

[22] I. N. Daliakopoulos, E. G. Grillakis, A. G. Koutroulis, I. K. Tsanis, "Tree crown detection on multispectral vhr satellite imagery", Photogrammetric Engineering & Remote Sensing, **75**(10), 1201–1211, 2009, DOI: 10.14358/PERS.75.10.1201.

[23] J. Peters, F. Van Coillie, T. Westra, R. De Wulf, "Synergy of very high resolution optical and radar data for object-based olive grove mapping", International Journal of Geographical Information Science, **25**(6), 971–989, 2011, https://doi.org/10.1080/13658816.2010.515946.

[24] R. Sarabia, A. Aquino, J. M. Ponce, G. Lopez, J. M. Andújar, "Automated identification of crop tree crowns from uav multispectral imagery by means of morphological image analysis", Remote Sensing, **12**(5), 748, 2020, https://doi.org/10.3390/rs12050748.

[25] L. Saxena, L. Armstrong, "A survey of image processing techniques for agriculture". Proceedings of Asian Federation for Information Technology in Agriculture, Australian Society of Information and Communication Technologies in Agriculture. Perth, Australia, 401-413, 2014.

[26] E. Hamuda, M. Glavin, E. Jones, "A survey of image processing techniques for plant extraction and segmentation in the field", Computers and Electronics in Agriculture, **125**, 184–199, 2016, doi:10.1016/j.compag.2016.04.024.

[27] A. Singh, B. Ganapathysubramanian, A.K. Singh, S. Sarkar, "Machine learning for high-throughput stress phenotyping in plants", Trends Plant Sci. **21** (2), 110–124, 2016, DOI:https://doi.org/10.1016/j.tplants.2015.10.015.

[28] A. Khan, U. Khan, M. Waleed, A. Khan, T. Kamal, S. N. K. Marwat, M.

Maqsood, F. Aadil, “Remote sensing: An automated methodology for olive tree detection and counting in satellite images,” IEEE Access, **6**, 77 816–77 828, 2018, doi: 10.1109/ACCESS.2018.2884199.

[29] M. Waleed, T.-W. Um, A. Khan, and U. Khan, “Automatic detection system of olive trees using improved k-means algorithm”, Remote Sensing, **12**(5), 2020, https://doi.org/10.3390/rs12050760.

[30] A. Kamilaris, F.X. Prenafeta-Boldú, “Deep learning in agriculture: a survey”, Computers and Electronics in Agriculture, **147**, 70–90, 2018, https://doi.org/10.1016/j.compag.2018.02.016.

[31] I. Sa, Z. Ge, F. Dayoub, B. Upcroft, T. Perez, T., C. McCool, “Deepfruits: a fruit detection system using deep neural networks”. Sensors, **16**(8) , 2016, https://doi.org/10.3390/s16081222.

[32] M. Onishi, T. Ise, “Explainable identification and mapping of trees using UAV RGB image and deep learning”, Scientific reports, **11**(1), 903, 2021, https://doi.org/10.1038/s41598-020-79653-9.

[33] A. Safonova, E. Guirado, Y. Maglinets, D. Alcaraz-Segura, S. Tabik, “Olive tree biovolume from uav multi-resolution image segmentation with mask r-cnn”, Sensors, **21**(5), 2021, https://doi.org/10.3390/s21051617.

[34] B. G. Weinstein, S. Marconi, M. Aubry-Kientz, G. Vincent, H. Senyondo, E. P. White, “Deepforest: A python package for RGB deep learning tree crown delineation”, Methods in Ecology and Evolution, **11**(12), 1743 – 1751, 2020, https://doi.org/10.1111/2041-210X.13472.

[35] T.-Y. Lin, P. Goyal, R. Girshick, K. He, P. Dollar, “Focal loss for dense object detection”, 2017 IEEE International Conference on Computer Vision (ICCV), 2999 – 3007, 2017, doi: 10.1109/ICCV.2017.324.

[36] T. -Y. Lin, P. Goyal, R. Girshick, K. He and P. Dollár, "Focal Loss for Dense Object Detection," in IEEE Transactions on Pattern Analysis and Machine Intelligence, **42**(2), 318-327, 1 Feb. 2020, doi: 10.1109/TPAMI.2018.2858826.

[37] S. Marcel, Y. Rodriguez, „Torchvision the machine-vision package of torch“, Proceedings of the 18th International Conference on Multimedea 2010, Firenze, Italy, October 25-29, 2010, DOI: 10.1145/1873951.1874254.

[38] I. Marin, S. Gotovac, V. Papić, "Individual Olive Tree Detection in RGB Images," 2022 International Conference on Software, Telecommunications and Computer Networks (SoftCOM), 2022, 1-6, doi: 10.23919/SoftCOM55329.2022.9911397.

[39] M. Everingham, L. Van Gool, C. K. Williams, J. Winn, and A. Zisserman, “The pascal visual object classes (VOC) challenge”, International Journal of Computer Vision, **88** (2), 303-338 2010, https://doi.org/10.1007/s11263-009-0275-4.

[40] C. Coelho, M. F. P. Costa, L. L. Ferras, A. J. Soares, “Object detection with retinanet on aerial imagery: The algarve landscape”, International Conference on Computational Science and Its Applications. Springer, 2021, 501 – 516, DOI: 10.1007/978-3-030-86960-1_35.

[41] T.-Y. Lin, P. Doll´ ar, R. Girshick, K. He, B. Hariharan, S. Belongie, “Feature pyramid networks for object detection”, 2017 IEEE Conference on Computer Vision and Pattern Recognition (CVPR) 936-944, 2017, DOI: 10.1109/CVPR.2017.106.

[42] K. He, X. Zhang, S. Ren, J. Sun, “Deep residual learning for image recognition”, 2016 IEEE Conference on Computer Vision and Pattern Recognition (CVPR), Las Vegas, NV, USA, 2016, 770-778, doi: 10.1109/CVPR.2016.90.

[43] R. Padilla, W. L. Passos, T. L. B. Dias, S. L. Netto, E. A. B. da Silva, “A comparative analysis of object detection metrics with a companion open-source toolkit”, Electronics,, 2021, **10**(3), 279, https://doi.org/10.3390/electronics10030279.

[44] T.-Y. Lin, M. Maire, S. Belongie, L. Bourdev, R. Girshick, J. Hays, P. Perona, D. Ramanan, C. L. Zitnick, P. Dollar, „Microsoft COCO: Common objects in context,”, Computer Vision – ECCV 2014. ECCV 2014, Lecture Notes in Computer Science, **8693**. Springer, Cham, https://doi.org/10.1007/978-3-319-10602-1_48.

Advances in Science, Technology and Engineering Systems Journal Vol. 8, No. 2, 97-107 (2023)

www.astesj.com

Special Issue on Computing, Engineering and Multidisciplinary Sciences

ASTESJ

ISSN: 2415-6698

The First Application of the Multistage One-Shot Decision-Making Approach to Reevaluate a Technology Project Decision Problem

Mohammed Al-Shanfari*

Graduate School of International Social Sciences, Yokohama National University, Yokohama, Hodogayaku, 79-4 Tokiwadai, 240-8501, Japan

ARTICLE INFO

Article history:
Received: 26 October, 2022
Accepted: 02 March, 2023
Online: 24 March, 2023

Keywords:
Multistage decision-making
One-shot decision theory
Scenario-based decision theory
Decision tree
IT project

ABSTRACT

Decision-makers must make a suitable sequence of decisions under uncertainty in a relatively long period for particular projects and situations. Conventional decision-making approaches under uncertainty are based on expected utility theory and do not sufficiently reflect the one-time nature of decisions. Similarly, the conventional approaches do not adequately incorporate the decision-maker's intuitions in the decision-analysis process. Numerous studies have demonstrated that salience information (attention-grabbing) is crucial in human decision-making exercises. However, there is limited information on the decision-making approaches incorporating the salience information and the applications of such approaches in actual practice. This study applies an approach called the multistage one-shot decision-making approach (MOSDMA) to reevaluate a previous decision problem related to a department technology project from the sultanate of Oman. Unlike traditional lottery-based approaches, MOSDMA is scenario-based, introducing an essential alternative for multistage decision-making under uncertainty. The paper is the first contribution to using the passive focus point introduced in MOSDMA in actual applications. The aim is to verify the explicability and effectiveness of the suggested method for solving decision-making under uncertainty problems in actual practice. The paper exhibits positive findings and promising potential of the approach advocating further future studies in theory and application aspects.

1. The Introduction

The case presented in this paper is the first application of the new multistage one-shot decision-making approach (MOSDMA) in reevaluating a former decision problem. The paper is an extension of work originally presented at the 2021 IEEE International Conference on Industrial Engineering and Engineering Management (IEEM)[1]. In decision-making, decisions are typically made with a certain level of uncertainty. Uncertainty is principally deemed inherent in decision-making and significantly influences the decision alternatives. Uncertainty can be generally defined as the lack of knowledge about the probabilities of the future state of events that cannot be entirely eliminated [2]. Numerous theories have been suggested to cope with decision-making under uncertainty (e.g., [3–14]). Most existing theories adhere to the Bernoullian framework of the weighted average. Nevertheless, some decisions under uncertainty are irreversible and can be made only once, where the probability distribution is partial or insufficient. These types of decision problems are known as one-shot decision problems that could lead to significant gains or losses. In such problems, a decision-maker has only one chance to make a decision under uncertainty. Typical examples are private real-estate investments, new technology innovations, product developments, and emergency management for abnormal events. The accelerated industry clock speed environment makes one-shot decision problems extremely applicable in the technology project management fields.

Psychological experimentations studies have demonstrated that individuals systematically disregard the axioms for the expected utility and for the subjective expected utility (e.g.,[15,16]) and do not perform a summing process and weighting process (e.g.,[17–19]). Empirical studies have revealed that salience (attention-grabbing) information is crucial in human decision-making (e.g.,[20,21]). Accordingly, in [22,23] the author discusses that a decision-maker assesses alternatives based on some associated event or scenario called (the focus of a decision), which is most salient to the decision-maker because of its consequent payoff and probability, thus offering a one-shot decision theory (OSDT) [22]. In place of conventional (lottery-

---

[*] Corresponding Author: Mohammed Al-Shanfari, Yokohama, Hodogayaku, 79-4 Tokiwadai, 240-8501, Japan, mohammedshanfari@gmail.com

https://dx.doi.org/10.25046/aj080211

based) methods, the author reasons that the OSDT is needed to solve one-shot decision problems because it is scenario-based, appealing to common phenomena and intuition. When making such a one-shot decision with little or partial information, it is most common to take on one scenario, which is crucial to the decision-maker and the decision-maker's basis for reaching the desired conclusion. The OSDT presents twelve focus points that describe the decision-maker's attitude towards the possibility, satisfaction, and optimality criteria. The OSDT is generalized to the focus theory of choice (FTC) in [24–26], employing (positive and negative) evaluation systems and relative likelihood. Relative likelihood is used to measure probabilities by the highest probability event in a subset of events. Hence, as the FTC is event-based, it offers a model for practical rationality.

Detailed comparisons are offered in [23,27], to explain the advantages of OSDT and to address the differences between other decision theories based on optimistic and pessimistic utilities such as SEU. In SEU, for example, if the optimal alternative reappears many times, the total payoff gained almost confidently attains the maximum. In contrast, OSDT provides a clear answer to why an alternative is optimal when only one decision chance is left to a decision-maker. In brief, as OSDT is close to the human way of thinking, the OSDT appeals to intuition, ease of application, and explicability. A decision with OSDT results directly from human-centric decision-making, involving the decision-maker rather than just the decision analyst. This is because the decision analyst usually develops decision models based on non-human-centric methods such as the SEU. The OSDT has been successfully applied to production planning problems [28], auction problems [29], newsvendor problems for innovative products [30–32], duopoly markets of innovative products [27,33], and private real estate investment [34].

Founded on the OSDT success, the multistage one-shot decision-making approach (MOSDMA) is proposed in [35] as an extension of OSDT to cope with multistage decision-making under uncertainty problems, where decision-making can be performed only once for each stage. Extending the advantages of OSDT, MOSDMA is an essential option for multistage decision-making under uncertainty because it is scenario-based and different from other lottery-based approaches. In multistage problems, decisions are made only once at each stage to reach a final result in a series of interdependent decisions. In [36], the authors have proposed a decision model for individual multi-period consumption–investment problems utilizing the MOSDMA. In MOSDMA, according to the decision-maker's attitude towards satisfaction and likelihood, one state (focus point) is chosen at each stage. The indicated backward induction determines the sequence of optimal decisions. In such problems, the obtained sequence of optimal decisions is suitable for making a final decision. However, studies on MOSDMA are still at an early stage, particularly from the applied aspects.

Uncertainty oversight and risk management fields have evolved as essential to decision-making and project management science [37–39]. Nonetheless, studies need to gain a mutual comprehension of the portrayal of risk and uncertainty in various fields and sufficient ways to handle it [40]. For example, managerial decision-making research discussed the significance of practical and applicable models to assist decision-making under uncertainty [41], as decision-makers will be compelled to make critical decisions based on appropriate assessments. Correspondingly, recent research [41–43] established difficulties in employing mathematical models and scientific approaches in practice. For example, some challenges include limited evidence on the approaches' efficiencies, not reflecting past experiences, practicality, and lack of capabilities to apply them.

In this paper, the MOSDMA is applied to reevaluate a former information technology (IT) project decision problem. This is the first time utilizing the MOSDMA to solve a decision-making problem in actual practice. The aim is to verify the explicability and effectiveness of the proposed approach to solving decision-making under uncertainty problems in actual practice. The MOSDMA is relatively newer than OSDT; the research can contribute to closing the gap between the theory and application aspects. In the theoretical contribution, this paper extends MOSDMA for a multiple-criteria evaluation problem concerning qualitative and quantitative data [44]. Consequently, research can offer real-life applications for further improvement in the approach, alternatives evaluation stage, and decision-making process in similar fields such as IT project decision-making, decision governance, and activities related to former decision evaluation. For example, evaluations of the former decisions can be relevant to lesson-learned activities, assurance, consulting, and governance-related activities.

The remainder of the research is arranged in the following structure. Section 2 presents the case study decision problem. Then, in section 3, the problem is solved by applying the approach. Finally, sections 4 and 5 present the discussion and conclusion of this research.

2. The case study

The case study is a former Information Technology (IT) project which went through a sequence of decisions in an IT system lifecycle within a financial institution in Oman. The institution is developing and incorporating best practices in corporate governance and decision-making. The non-routine decision problems related to such projects are normally raised to a dedicated project committee for group consensus. The institution is committed to employing and improving decision-making governance practices.

An assurance function (AF) decided to implement a Department Management System (DMS) to improve and automate the department workflow, which could have been inspired by the department's needs and the country's encouragement to enhance efficiency through technology in all sectors around 2008. The DMS is a technology solution that streamline and automates the department's operations and assignments, such as planning, reporting, monitoring, and follow-up . Consequently, a vendor was chosen to deliver one of the best systems in the international market.

Although the first implementation of DMS was concluded, users could only partially utilize the system because of flows in the implementation, such as process compatibility, system reliability, and user adoption. In addition, users found that the implemented version could have been more user-friendly and sufficiently aligned with the practiced workflow. Various efforts were made to solve the identified challenges through a series of patches and customization—still, some issues needed to be fixed satisfactorily. After an extensive debate with the solution provider, the DMS was decided to be upgraded to a newer version. Considerable person-hours were spent in revising and implementing the new version from both sides.

A time came to review the entire project as a part of the department review and the system lifecycle. Though the system may have introduced new benefits, the absence of DMS was not causing a significant hindrance to their workflow and not yielding the best-desired outcome. Therefore, a view was to present this experience and information before the decision-makers and seek a decision to abandon the project. However, the previous decision-makers felt abandoning the system would be a waste after spending a considerable amount of the contract, the experience gained with this competitive product, and the remaining retention fees. Given this rationale, the directives were to evaluate other alternatives or make an additional effort to utilize the DMS for fair use of investment.

In reconsidering the circumstances, the most recent version from the existing DMS provider could be more reliable and user-friendly. Nevertheless, the latest version will add an additional cost to the contract. In a separate endeavor for other alternatives, it was determined by an organization functioning in a similar sector that they had developed a customized in-house system for their Department. The expense was less than the current DMS, and the experience with their vendor was satisfactory. However, their locally customized system has limited features and scope compared to the international DMS product upgrade in the discussion. Moreover, details about implementation feasibility, additional costs, and future capacity are not accessible yet at the time of making the decision.

Until this point of system lifecycle, the decision-making process was mainly based on similar discussions and intuitions with limited use of scientific decision analysis tools and related mathematical decision-making approaches in the alternatives evaluation stage. However, not using these approaches may not hinder making an informed decision but can provide more context and improvements to the decision-making process for better judgment and justification. Next, the above-introduced case will be defined and reevaluated using the MOSDMA.

3. The solution

3.1. Problem description

The study employed a decision-making simulation with a focus group of mainly three participants involved in the project and aware of the decision made. The participants assist in supplying, designing, and harvesting qualitative and quantitative data sources, including interviews, discussions, documents, and workshops.

The data-gathering methodology is arranged in three main steps, as summarized in Figure 1. In step 1, an initial case review was performed to understand the case and collect foundational information for the subsequent steps. The foundational information is collected through a short questionnaire, discussions, and examination of relevant project documents. The goal is to construct the case decision story by determining the system's objective, the decision-making process, the previous alternatives, risk appetite, the type of decision-makers, and the satisfaction of the decisions made in the case. Step 1 main result is manifested in the summarized case study in section 2. Building on step 1, the research can proceed by tailoring a decision-making tool kit to harvest data related to solving this case study in step 2. The decision-making tool kit consists of a decision tree, a probability scale card, and a weighted sum scorecard. Through collaboration, three inputs of the participants are captured using the consented decision-making tool kit. The probabilities and the weight of each considered objective are donated following the decision tree in Figure 2. After the final values are placed in the finalized decision tree, the described problem can be solved. All data are detailed in the following sections.

The alternatives, in this case, are evaluated by considering three objectives: payoff as cost and benefit (CB), social impact (SI), and user satisfaction (US). First, to find the payoff (CB), the savings are obtained, as shown in Table 1. Then the CB of the three potential options is computed, as displayed in Table 2. Next, a tailored weighted sum scorecard and probability scale card are developed, as shown in Tables 3 and 4. The main weight assigned for CB, SI, and US objectives are 0.4,0.3, and 0.3, respectively. The objectives and weight are subjective to the participants' experience and agreement. Then using this kit, appropriate values are selected for each scenario. Therefore, the decision tree and the final values are visualized in Figure 2.

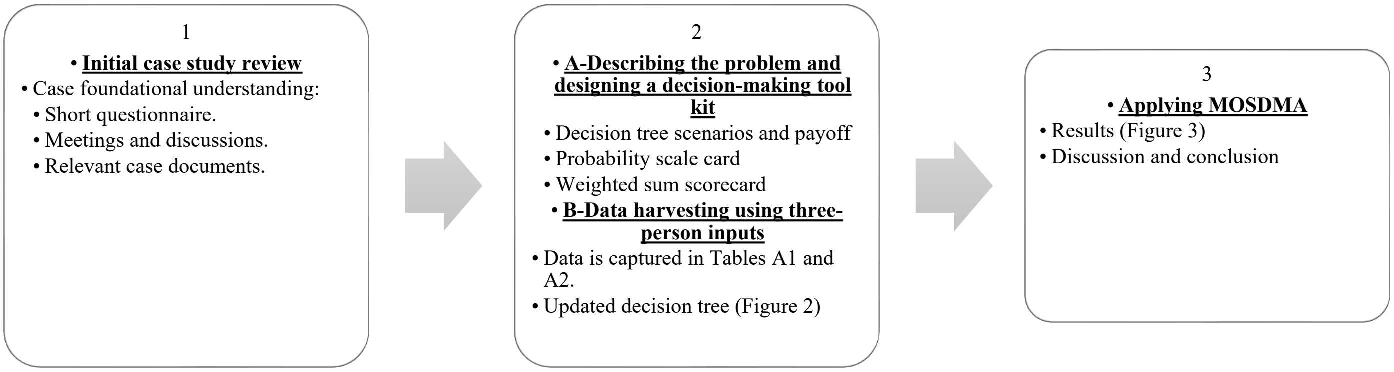

Figure 1:The data-gathering methodology steps

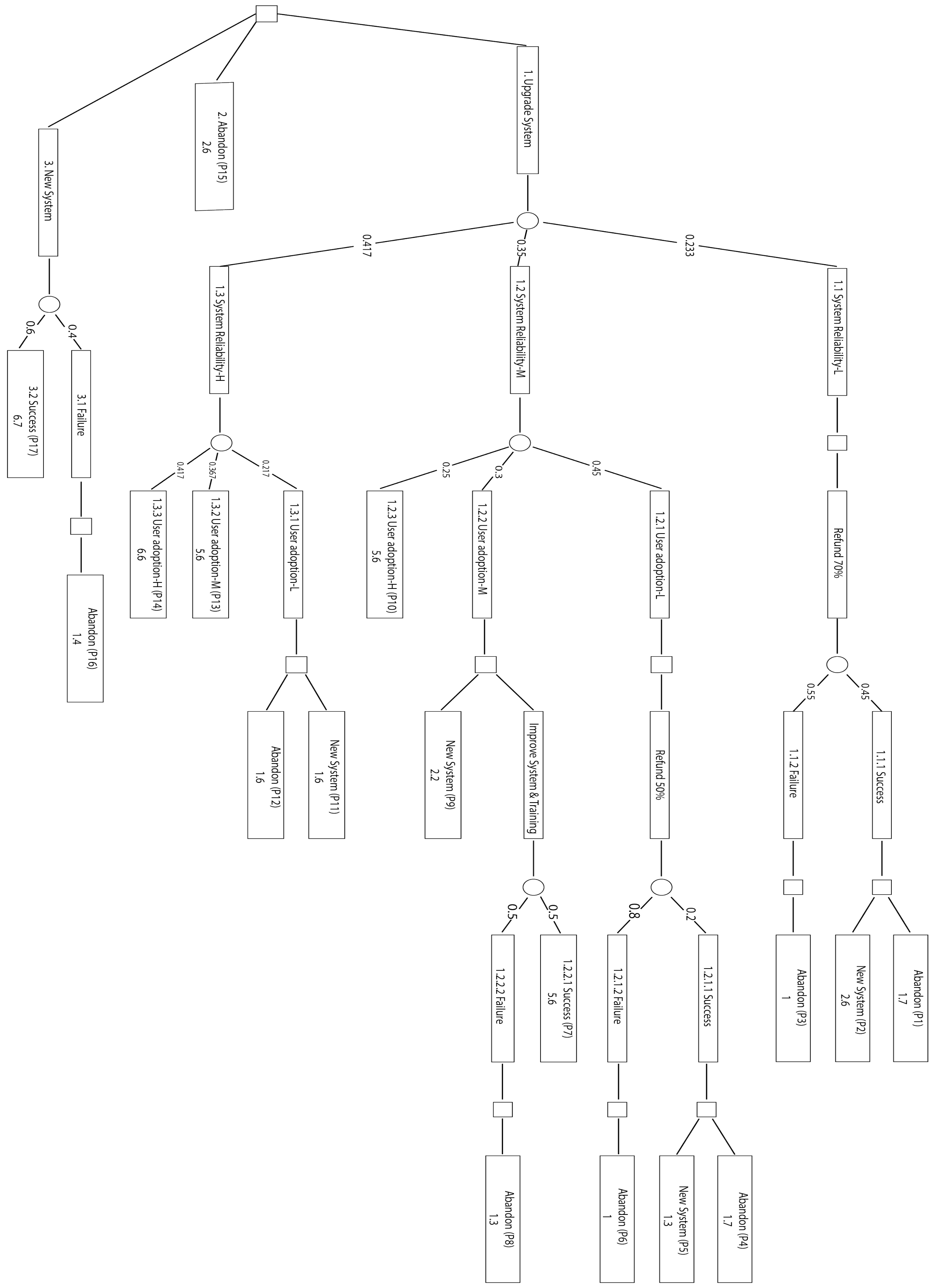

Figure 2: The decision tree showing final values.

Table 1: Estimated savings

Hours Before Automation (HBA)	Hours After Automation (HAA)	Hours Savings per assignments [a] (HS)	Total Hours Saved per year [b] (THS)	Total saved cost per year [c]	Total saved cost in 5 years
200 Hours	113 Hours	87 Hours	4350 Hours	121,800 USD[d]	609,000 USD

The above data is based on the solution forecasted benefit analysis provided by the vendor and applied to AF's annual average functions.

[a] (HS = HBA – HAA)

[b] (Average 50 assignments per year) × HS

[c] (Average hour costs 28 USD) × THS

[d] USD (United States dollars).

Table 2: Cost and Benefits (CB) estimations

Alternatives	Annual total savings cost [a]	5 years of total savings cost [a]	Previous payments (PP)	1st Year Cost (YC)	Total Setup Cost 1st Year (TYC)	4 years total annual maintenance cost (TAMC)	5 years Cumulative Cost (CC)	5 Years Net Benefits (NB)
Upgrade Current System	121,800	609,000	PP1	YC1	TYC1	TAMC1	CC1	NB1 (Highest Value)
New System	121,800	609,000	PP2	YC2	TYC2	TAMC2	CC2	NB2
Abandon	0	0	PP3	0	0	0	0	0 (Lowest Value)

[a] Values are estimated in table 1.

Values are shown in USD (United States dollars).

Table 3: The weighted sum method

Objectives	Aim	1	2	3	4	5	6	7
Cost/Benefits (CB) in USD	Max.	-300,000 or less	-299, 000 to -200,000	-199, 000 to -1	0 to 49,000	50,000 to 149,000	150,000 to 249,000	250, 000 or more
User satisfaction (US)	Max.	VL	L		M		H	VH
Social impact (SI)	Min.	VH	H		M		L	VL

(1) indicates the least favorite outcome, while (7) indicates the most favorable outcome.

VL = (Very High) , L= (Low), M = (Medium), H = (High) , VH = (Very High)

USD = United States dollars

Table 4: Probability scale card tool.

Levels	Impossible	Nearly Impossible	Very Low	Low	Moderate Low	Moderate	Moderate high	High	Very High	Extremely High	Certain
Probabilities	0	10%	20%	30%	40%	50%	60%	70%	80%	90%	100%

The CB objective is achieved for all the outcomes based on a simple premise: Payoff is equal to potential benefits after subtracting applicable costs or losses. After finalizing the payoff details, the team decides on the values for each path's objective. Then, the values are normalized based on the weighted sum scorecard described in Table 3. Finally, the values are normalized by multiplying them by the corresponding main weight of the objective. For example, in path 1, the CB, SI, and US values are normalized to the scores 2, 2, and 1 and then to the scores multiplied by the weights of the objectives 0.4, 0.3, and 0.3, which yield a final outcome of 1.7. This process of collecting and normalizing the outcome with weight scores is detailed in Table A2 in the appendix.

Based on the case study review and previous undesired outcomes, two major uncertainties were identified: system reliability and user adoption. Subsequently, the event branches low (L), medium (M), and high (H) are assigned to the parent uncertainties. The alternative (Upgrade System) has 14 possible scenario paths (numbered from P1 to P14), and the alternative (New system) has two. While the alternative (Abandon) has one certain value (P15), as expressed in the decision tree in Figure 1 and Table A2 in the appendix.

To find the probability of each scenario, the average of the three responses is taken using a customized probability scale card with 11 scales corresponding to a level and a probability, as shown in Table 4. The lowest level, "impossible," denotes a probability of 0 for the event. Comparably, the highest level, "Certain," denotes a probability of 1. Subsequently, the final outcomes and the final probabilities are positioned in the decision tree presented in Figure 2 to solve the decision problem using the MOSDMA.

3.2. Applying the approach

The multistage one-shot decision-making approach (MOSDMA) offers in which twelve types of focus points to harmonize with different types of decision-makers [36]. Out of twelve focus points, four examples of focus points characteristics are described in Table 5 by considering combinations of likelihood and satisfaction. In type (I), both likelihood and satisfaction are higher, which appears appropriate for an active decision-maker. In contrast, in type (III), it appears appropriate for an apprehensive decision-maker as although some scenario has a lower likelihood, it is still considered can induce more significant losses (as shown by the lower satisfaction level). Purchasing insurance can exemplify a type (III) focus point behavior. Type (II) looks appropriate for passive decision-makers with lower satisfaction levels and higher likelihood. Whereas in type (IV), the focus point appears proper for daring personalities. Because though the likelihood of some scenarios is lower, higher gains (higher satisfaction level) could tempt individuals to contemplate such a scenario (for example, purchasing a lottery).

Based on the focus point characteristics, the types (I), (II), (III), and (IV) are named active focus point, passive focus point, apprehensive focus point, and daring focus point, respectively.

Table 5: Characteristics of four focus points (types I-IV)

Four types of focus points	Satisfaction	Likelihood
(I) Active Focus Point (AFP)	higher	higher
(II) Passive Focus Point (PFP)	lower	higher
(III) Apprehensive Focus Point (APFP)	lower	lower
IV. Daring Focus Point (DFP)	higher	lower

Taking into account the stakeholders in this study case, only the Passive Focus Point (PFP) is considered to incorporate the overall intuition and feelings at this point of the project. First, consider a decision $a \in A$ on a decision node A at the initial stage (stage 1). Then, the outcomes and probabilities are normalized using the satisfaction function $u(x,a)$ and the relative likelihood function $\pi(x)$, as per (1) and (2) below.

$$u(x,a) = r(x,a)/\max_{x\in X} r(x,a) \quad , \tag{1}$$

where $x \in X$ stands for a state.

$$\pi(x) = p(x)/\max_{x\in X} p(x). \tag{2}$$

Then the passive focus point (PFP) of $a \in A$ is given as

$$x(a) = \underset{x\in X}{\operatorname{argmaxmin}}\{\pi(x), 1 - u(x,a)\} \tag{3}$$

which means that for $a \in A$ $x(a)$ is a state that can obtain a relatively low outcome with a relatively high probability (an unfavorite scenario of a). This state mirrors the pessimistic mentality of decision-makers. Following computing all the PFPs of $a \in A$, the final optimal alternative on the decision node A denoted as $a(A)$ is chosen by

$$a(A) = \underset{a\in A}{\operatorname{argmax}} u(x(a),a) \quad , \tag{4}$$

indicates that decision-makers select the alternative with the highest outcome among the unfavorite scenarios.

In MOSDMA, the PFP of each alternative is found from the last stage (stage 4 in Figure 2), compared by their outcomes fitting to the focus point, and rolled back until the initial stage (stage 1) is reached to make the final selection. Rather than computing the expected utility of each alternative, comparing each other on a decision node and then rolling back in stochastic dynamic programming. Figure 3 has been designed to resemble the decision tree in Figure 2 to translate the results computed by applying (1), (2), (3), and (4). In this case, there are four stages: stage 4 is the last, and stage 1 is the initial stage. Stages 4, 3, and 2 are condensed to the chance nodes, and stage 1 is the primary decision node. First, (1) and (2) are employed to normalize the outcomes and probabilities to find satisfaction and likelihood values. Then, (3) is used to get PFP between siblings' branches in each stage, starting from the last stage (stage 4) to stage 2. The PFPs are highlighted in gray in Figure 3. Finally, following the migration of the outcome values corresponding to the highlighted PFPs in stage 2 to stage 1, the final decision can be selected using (4) in stage 1.

For example, starting from stage 4, to acquire the PFP between the sibling branches 1.2.2.1 and 1.2.2.2, first by applying (3), the minimum value of {π(x) , 1-u(x,a) } at each branch is found. The minimums for branches 1.2.2.1 and 1.2.2.2 are 0 and 0.768, respectively. From these two minimums, the maximum value is 0.768, which indicates that the focus point between these two siblings is branch 1.2.2.2. Subsequently, the outcome and probability values of branch 1.2.2.2 are migrated to parent branch 1.2.2. The outcome r(x, a) migrates with the same value 1.3; however, probability p(x) is multiplied by the parent's branch 1.2.2 probability (0.5´0.30 = 0.15). The same rolling-back process employed in stage 4 is replicated in stage 3. Similarly, by applying (3), the minimum values for the branches 1.2.1, 1.2.2, and 1.2.3 are 0.821, 0.424, and 0, respectively. As a result, branch 1.2.1 is the focus point with the maximum value among its sibling. Likewise, the rest of the PFPs in stage 3 are found, and their outcomes and probabilities are migrated to the parent's branches in stage 2 as in the previous stage. The outcome and probability values for parent 1.2 after migration from the child branch 1.2.1 are 1 and 0.126 (0.35 ´ 0.36), respectively. Duplicating the same process in previous stages, the PFP in stage 2 are the branches 1.1 and 3.1. For the initial stage (stage 1), only the outcomes of branches 1.1 and 3.1 are migrated to stage 1. In stage 1, as shown in Figure 3, the final outcomes 1, 2.6, and 1.4 are compared using (4) to make the final decision. Accordingly, alternative number 2 (Abandon the system) is the highest outcome among the unfavorite scenarios, which resembles a pessimistic mentality as per the PFP type.

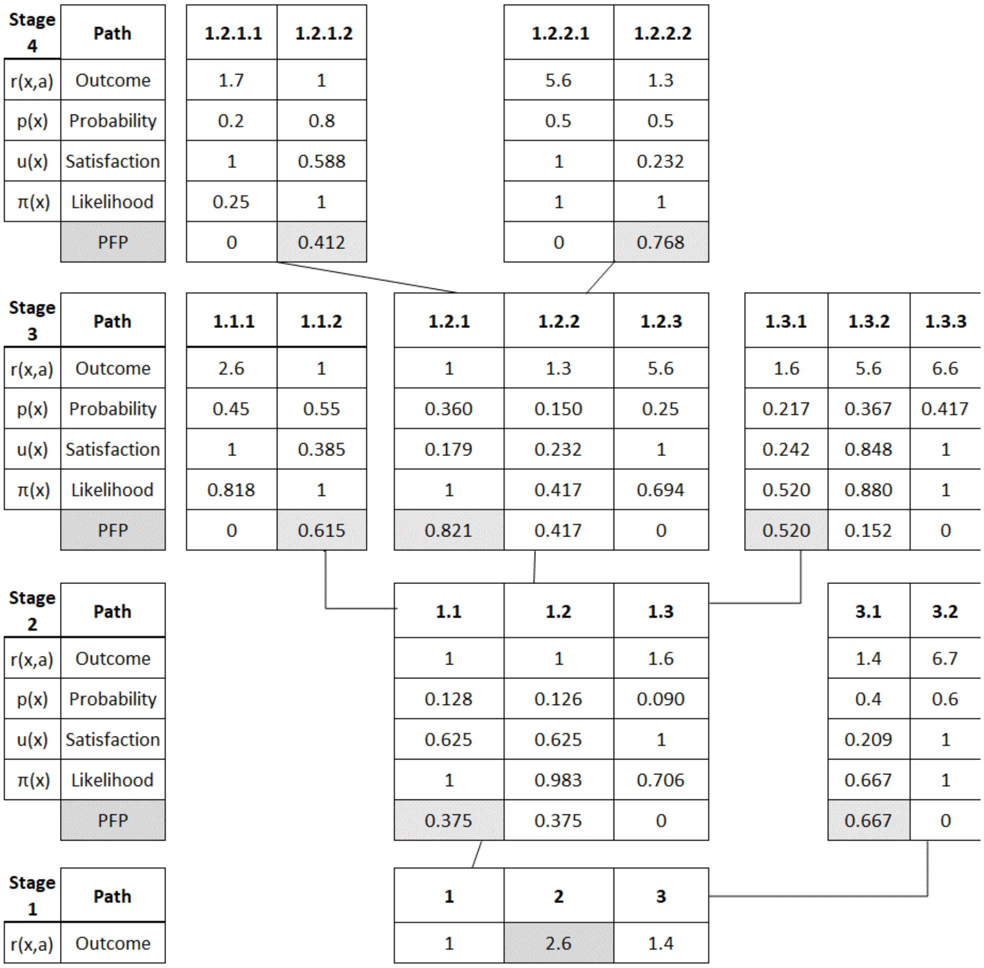

Stage 4	Path	1.2.1.1	1.2.1.2	1.2.2.1	1.2.2.2
r(x,a)	Outcome	1.7	1	5.6	1.3
p(x)	Probability	0.2	0.8	0.5	0.5
u(x)	Satisfaction	1	0.588	1	0.232
π(x)	Likelihood	0.25	1	1	1
	PFP	0	0.412	0	0.768

Stage 3	Path	1.1.1	1.1.2	1.2.1	1.2.2	1.2.3	1.3.1	1.3.2	1.3.3
r(x,a)	Outcome	2.6	1	1	1.3	5.6	1.6	5.6	6.6
p(x)	Probability	0.45	0.55	0.360	0.150	0.25	0.217	0.367	0.417
u(x)	Satisfaction	1	0.385	0.179	0.232	1	0.242	0.848	1
π(x)	Likelihood	0.818	1	1	0.417	0.694	0.520	0.880	1
	PFP	0	0.615	0.821	0.417	0	0.520	0.152	0

Stage 2	Path	1.1	1.2	1.3	3.1	3.2
r(x,a)	Outcome	1	1	1.6	1.4	6.7
p(x)	Probability	0.128	0.126	0.090	0.4	0.6
u(x)	Satisfaction	0.625	0.625	1	0.209	1
π(x)	Likelihood	1	0.983	0.706	0.667	1
	PFP	0.375	0.375	0	0.667	0

Stage 1	Path	1	2	3
r(x,a)	Outcome	1	2.6	1.4

Figure 3: Applying the Passive Focus Point (PFP).

4. Discussion

In this paper, the pessimistic mentality was considered to apply the passive focus point (PFP) following the MOSDMA. The PFP brings a relatively low outcome with a relatively high probability. In the PFP type of the MOSDMA approach, the decision-maker chooses one decision that can get the highest outcome amongst the unfavorite scenarios from the decision alternatives in the initial decision stage (stage 1 in Figure 3). This paper considered the pessimistic mentality to apply the passive focus point (PFP), one of the twelve focus points introduced by the MOSDMA. The PFP obtains a moderately low outcome with a relatively high probability. The decision-makers select one conclusion to obtain the highest outcome among the unfavorite scenarios proposed in the initial decision stage, as represented by stage 1 findings in Figure 3. The endorsed alternative is the alternative (Abandon the system) with the outcome of 2.6. This decision-making mirrors the pessimistic mental set in using the PFP. The acquired empirical reevaluation of alternatives is intuitively acceptable and comparable to the actual feelings of the individuals concerned. No major difficulties were noticed in applying and understanding the approach. Participants found it uncomplicated and valuable for future use.

Eventually, despite the pessimistic feelings when deciding back around 2014, the chosen alternative was “upgrade the system,” while other alternatives were discounted. The motivation was founded on the discussion of not demolishing the consumed resources; the experience gained, and the time devoured in this solution and the initiative implementation. More in-depth evaluations could give more systematic explanations and justification for the decisions made. In this case, the decision-makers did not include comparable decision analysis approaches in the alternative evaluation stage and leaned mainly on deliberating the available information and intuition. They may have believed that other alternatives may bring the lowest outcomes and satisfaction levels if unsuccessful, which could be supported using such a scenario-based method. This reveals opportunities for improvements in the alternatives evaluation stage and fills the gaps in acknowledging the value of such decision-making approaches in actual practice.

If the case is solved assuming the decision-maker is optimistic using the same approach but with an active focus point (AFP) type, the result would be “3. New System”. Later, it was found that the project did not produce the best-desired outcomes. The new management is reviewing alternative 3, “discard the current product and implement a new system.” However, there is a high degree of attention to reviewing the problem and improving the decision-making process. The new direction could be based on the undesired project outcomes and immaculate corporate governance improvements.

5. Conclusion

This study employs the multistage one-shot decision-making approach (MOSDMA) to revisit an actual decision problem for the first time. More studies are required from both theoretical and applied aspects, as MOSDMA is considered a new approach at an early stage. Nevertheless, this research is the first contribution involving the passive focus point (PFP) suggested by MOSDMA to reexamine a real multistage decision-making-under-uncertainty problem.

The obtained empirical reevaluation of alternatives is intuitively acceptable to the contributors. The study showed that MOSDMA could assist in reevaluating previous decisions and its capability to make an informed one with proper analysis and justifications aligned to stakeholders' satisfaction levels and intuition. This establishes the effectiveness of the MOSDMA and the promising capability of the introduced workflow to reevaluate such decision problems in similar environments. Furthermore, the approach was found reasonably explicable, practical, and systematically considering the decision-makers' intuitions.

The quality of the assessed scenarios and the gathered data is restricted to the experience and commitment of the participants in this decision-making analysis exercise. The knowledge of the future outcome and collaborating in a group setup or open disclosed style may have influenced the participant's inputs since this is a reevaluation of a past problem with currently known outcomes compared to the pressure confronted in real-time decision-making or undisclosed inputs of each participant. Since 2014, considerable restructuring has occurred in the financial institution. Accordingly, a number of applicable people involved in this case were unreachable to participate and to add more inputs to this study. Nevertheless, this limitation could be mediated since this is a decision review of a recently known outcome and a well-documented project.

Further future research is needed to improve MOSDMA theoretically and for more practical applications. For instance, forthcoming approach applications may consider more contemporary decision problems, complex stages, more data and comparisons with other approaches, other focus groups and organizations, and various details in capturing the participant inputs and reactions. Nevertheless, this study demonstrates that the approach could be employed to reexamine a former decision problem which can contribute to analyzing lessons learned and areas for improvement. Likewise, MOSDMA has the prospect of being utilized in the areas of crucial new unresolved problems, auditing, governance practices, and consulting assignments.

Conflict of Interest

The author declares no conflict of interest.

Acknowledgment

Appreciation is extended to the immense support of the participants. The views and opinions expressed in this paper do not necessarily reflect the official policy or position of the Omani institutions.

References

[1] M. Aishanfari, P. Guo, “Application of the Multistage One-shot Decision-making Approach to an IT Project in the Central Bank of Oman,” in 2021 IEEE International Conference on Industrial Engineering and Engineering Management (IEEM), 552–557, 2021, doi:10.1109/IEEM50564.2021.9672939.

[2] F.H. Knight, Risk, uncertainty and profit, Houghton Mifflin, 1921.

[3] S. Cerreia-Vioglio, D. Dillenberger, P. Ortoleva, “Cautious Expected Utility and the Certainty Effect,” Econometrica, **83**(2), 693–728, 2015, doi:https://doi.org/10.3982/ECTA11733.

[4] D. Dubois, H. Prade, R. Sabbadin, “Decision-theoretic foundations of qualitative possibility theory,” European Journal of Operational Research, **128**(3), 459–478, 2001, doi:10.1016/S0377-2217(99)00473-7.

[5] T. Galaabaatar, E. Karni, “Subjective Expected Utility With Incomplete Preferences,” Econometrica, **81**(1), 255–284, 2013, doi:https://doi.org/10.3982/ECTA9621.

[6] I. Gilboa, “Expected utility with purely subjective non-additive probabilities,” Journal of Mathematical Economics, **16**(1), 65–88, 1987, doi:10.1016/0304-4068(87)90022-X.

[7] P. Guo, Y. Wang, “Eliciting dual interval probabilities from interval comparison matrices,” Information Sciences, **190**, 17–26, 2012, doi:10.1016/j.ins.2011.12.014.

[8] D. Kahneman, A. Tversky, “Prospect Theory: An Analysis of Decision under Risk,” Econometrica, **47**(2), 263–291, 1979, doi:10.2307/1914185.

[9] J. von Neumann, O. Morgenstern, A. Rubinstein, Theory of Games and Economic Behavior (60th Anniversary Commemorative Edition), Princeton University Press, 1944.

[10] J. Quiggin, “A theory of anticipated utility,” Journal of Economic Behavior & Organization, **3**(4), 323–343, 1982, doi:10.1016/0167-2681(82)90008-7.

[11] L.J. Savage, “The foundations of statistics.,” Naval Research Logistics Quarterly, **1**(3), 236–236, 1954, doi:https://doi.org/10.1002/nav.3800010316.

[12] D. Schmeidler, “Subjective Probability and Expected Utility without Additivity,” Econometrica, **57**(3), 571–587, 1989, doi:10.2307/1911053.

[13] F. Gul, W. Pesendorfer, “Expected Uncertain Utility Theory,” Econometrica, **82**(1), 1–39, 2014, doi:https://doi.org/10.3982/ECTA9188.

[14] P. Guo, H. Tanaka, “Decision making with interval probabilities,” European Journal of Operational Research, **203**(2), 444–454, 2010, doi:10.1016/j.ejor.2009.07.020.

[15] M. Allais, “Le comportement de l’homme rationnel devant le risque: critique des postulats et axiomes de l’école américaine,” Econometrica: Journal of the Econometric Society, 503–546, 1953.

[16] D. Ellsberg, “Risk, ambiguity, and the Savage axioms,” The Quarterly Journal of Economics, 643–669, 1961.

[17] Z. Zhou, W. Zhao, X. Chen, H. Zeng, “MFCA extension from a circular economy perspective: Model modifications and case study,” Journal of Cleaner Production, **149**, 110–125, 2017, doi:10.1016/j.jclepro.2017.02.049.

[18] N. Stewart, F. Hermens, W.J. Matthews, “Eye Movements in Risky Choice,” Journal of Behavioral Decision Making, **29**(2–3), 116–136, 2016, doi:https://doi.org/10.1002/bdm.1854.

[19] L. Zhou, Y.-Y. Zhang, Z.-J. Wang, L.-L. Rao, W. Wang, S. Li, X. Li, Z.-Y. Liang, “A Scanpath Analysis of the Risky Decision-Making Process,” Journal of Behavioral Decision Making, **29**(2–3), 169–182, 2016, doi:https://doi.org/10.1002/bdm.1943.

[20] N. Lacetera, D.G. Pope, J.R. Sydnor, “Heuristic Thinking and Limited Attention in the Car Market,” American Economic Review, **102**(5), 2206–2236, 2012, doi:10.1257/aer.102.5.2206.

[21] M.R. Busse, N. Lacetera, D.G. Pope, J. Silva-Risso, J.R. Sydnor, “Estimating the Effect of Salience in Wholesale and Retail Car Markets,” American Economic Review, **103**(3), 575–579, 2013, doi:10.1257/aer.103.3.575.

[22] P. Guo, “One-Shot Decision Theory,” IEEE Transactions on Systems, Man, and Cybernetics - Part A: Systems and Humans, **41**(5), 917–926, 2011, doi:10.1109/TSMCA.2010.2093891.

[23] P. Guo, One-Shot Decision Theory: A Fundamental Alternative for Decision Under Uncertainty, Springer, Berlin, Heidelberg: 33–55, 2014, doi:10.1007/978-3-642-39307-5_2.

[24] X. Zhu, K.W. Li, P. Guo, “A bilevel optimization model for the newsvendor problem with the focus theory of choice,” 4OR, 2022, doi:10.1007/s10288-022-00520-6.

[25] P. Guo, “Focus theory of choice and its application to resolving the St. Petersburg, Allais, and Ellsberg paradoxes and other anomalies,” European Journal of Operational Research, **276**(3), 1034–1043, 2019, doi:10.1016/j.ejor.2019.01.019.

[26] P. Guo, “Dynamic focus programming: A new approach to sequential decision problems under uncertainty,” European Journal of Operational Research, 2022, doi:10.1016/j.ejor.2022.02.044.

[27] P. Guo, “One-shot decision approach and its application to duopoly market,” International Journal of Information and Decision Sciences, **2**(3), 213, 2010, doi:10.1504/IJIDS.2010.033449.

[28] X. Zhu, P. Guo, “Bilevel programming approaches to production planning for multiple products with short life cycles,” 4OR, **18**(2), 151–175, 2020, doi:10.1007/s10288-019-00407-z.

[29] C. Wang, P. Guo, “Behavioral models for first-price sealed-bid auctions with the one-shot decision theory,” European Journal of Operational Research, **261**(3), 994–1000, 2017, doi:10.1016/j.ejor.2017.03.024.

[30] P. Guo, X. Ma, “Newsvendor models for innovative products with one-shot decision theory,” European Journal of Operational Research, **239**(2), 523–536, 2014, doi:10.1016/j.ejor.2014.05.028.

[31] X. Zhu, P. Guo, “Single-level reformulations of a specific non-smooth bilevel programming problem and their applications,” Optimization Letters, **14**(6), 1393–1406, 2020, doi:10.1007/s11590-019-01444-7.

[32] X. Zhu, P. Guo, “Approaches to four types of bilevel programming problems with nonconvex nonsmooth lower level programs and their applications to newsvendor problems,” Mathematical Methods of Operations Research, **86**(2), 255–275, 2017, doi:10.1007/s00186-017-0592-2.

[33] P. Guo, R. Yan, J. Wang, “Duopoly Market Analysis within One-Shot Decision Framework with Asymmetric Possibilistic Information,” International Journal of Computational Intelligence Systems, **3**(6), 786–796, 2010, doi:10.2991/ijcis.2010.3.6.9.

[34] P. Guo, “Private Real Estate Investment Analysis within a One-Shot Decision Framework,” International Real Estate Review, **13**(3), 238-260., 2010.

[35] Y. Li, P. Guo, “Possibilistic individual multi-period consumption–investment models,” Fuzzy Sets and Systems, **274**, 47–61, 2015, doi:10.1016/j.fss.2015.01.005.

[36] P. Guo, Y. Li, “Approaches to multistage one-shot decision making,” European Journal of Operational Research, **236**(2), 612–623, 2014, doi:10.1016/j.ejor.2013.12.038.

[37] S. Ward, C. Chapman, “Transforming project risk management into project uncertainty management,” International Journal of Project Management, **21**(2), 97–105, 2003, doi:10.1016/S0263-7863(01)00080-1.

[38] A. Jaafari, “Management of risks, uncertainties and opportunities on projects: time for a fundamental shift,” International Journal of Project Management, **19**(2), 89–101, 2001, doi:10.1016/S0263-7863(99)00047-2.

[39] S.D. Green, “Towards an integrated script for risk and value management,” Project Management, **7**(1), 52–58, 2001.

[40] O. Perminova, M. Gustafsson, K. Wikström, “Defining uncertainty in projects – a new perspective,” International Journal of Project Management, **26**(1), 73–79, 2008, doi:10.1016/j.ijproman.2007.08.005.

[41] B.J. Galli, “The Future of Economic Decision Making in Project Management,” IEEE Transactions on Engineering Management, **67**(2), 396–413, 2020, doi:10.1109/TEM.2018.2875931.

[42] W.G. Meyer, “The Effect of Optimism Bias on the Decision to Terminate Failing Projects,” Project Management Journal, **45**(4), 7–20, 2014, doi:10.1002/pmj.21435.

[43] B.J. Galli, “Effective Decision-Making in Project Based Environments: A Reflection of Best Practices,” International Journal of Applied Industrial Engineering (IJAIE), **5**(1), 50–62, 2018, doi:10.4018/IJAIE.2018010103.

[44] M. Aruldoss, T.M. Lakshmi, V.P. Venkatesan, “A Survey on Multi Criteria Decision Making Methods and Its Applications,” American Journal of Information Systems, **1**(1), 31–43, 2013, doi:10.12691/ajis-1-1-5.

Appendix

Table A1: Probabilities inputs following Table 4 and the decision tree in Figure 2

Alternatives	**Event ID**	**Probabilities**			
		Participant 1	**Participant 2**	**Participant 3**	**Final (Average)**
1	1.1	0.25	0.25	0.2	0.233
	1.2	0.35	0.4	0.3	0.350
	1.3	Residual Probability			0.417
	1.1.1	0.35	0.4	0.6	0.450
	1.1.2	Residual Probability			0.550
	1.2.1	0.45	0.5	0.4	0.450
	1.2.2	0.25	0.35	0.3	0.300
	1.2.3	Residual Probability			0.250
	1.2.1.1	0.15	0.25	0.2	0.200
	1.2.1.2	Residual Probability			0.800
	1.2.2.1	0.45	0.55	0.5	0.500
	1.2.2.2	Residual Probability			0.500
	1.3.1	0.2	0.15	0.3	0.217
	1.3.2	0.35	0.35	0.4	0.367
	1.3.3	Residual Probability			0.417
2					1.000
3	3.1	0.45	0.45	0.3	0.400
	3.2	Residual Probability			0.600

Table A2. Collecting and normalizing the outcome with weight scores.

Final Outcomes Results				**Final Outcomes Scores**				**Scores with Weight**			
Path ID[a]	**CB[b]**	**SI**	**US**	**CB**	**SI**	**US**	**Total**	**CB (0.4)**	**SI (0.3)**	**US (0.3)**	**Total**
P1	******	H	VL	2	2	1	**5**	0.8	0.6	0.3	**1.7**
P2	******	H	M	2	2	4	**8**	0.8	0.6	1.2	**2.6**
P3	******	VH	VL	1	1	1	**3**	0.4	0.3	0.3	**1**
P4	******	H	VL	2	2	1	**5**	0.8	0.6	0.3	**1.7**
P5	******	H	VL	1	2	1	**4**	0.4	0.6	0.3	**1.3**
P6	******	VH	VL	1	1	1	**3**	0.4	0.3	0.3	**1**
P7	******	L	H	5	6	6	**17**	2	1.8	1.8	**5.6**
P8	******	H	VL	1	2	1	**4**	0.4	0.6	0.3	**1.3**

P9	******	M	L	1	4	2	**7**	0.4	1.2	0.6	**2.2**
P10	******	L	H	5	6	6	**17**	2	1.8	1.8	**5.6**
P11	******	H	L	1	2	2	**5**	0.4	0.6	0.6	**1.6**
P12	******	H	L	1	2	2	**5**	0.4	0.6	0.6	**1.6**
P13	******	L	H	5	6	6	**17**	2	1.8	1.8	**5.6**
P14	******	VL	VH	6	7	7	**20**	2.4	2.1	2.1	**6.6**
P15	******	H	M	2	2	4	**8**	0.8	0.6	1.2	**2.6**
P16	******	VH	VL	2	1	1	**4**	0.8	0.3	0.3	**1.4**
P17	******	VL	H	7	7	6	**20**	2.8	2.1	1.8	**6.7**

[a] Each Path ID (P1 to P17) corresponds to a path in Figure 2 with the same naming convention.

[b] The CB values are masked for the easiness, readability, and privacy reasons.

Advances in Science, Technology and Engineering Systems Journal Vol. 8, No. 2, 108-115 (2023)

www.astesj.com

Special Issue on Computing, Engineering and Multidisciplinary Sciences

ASTESJ

ISSN: 2415-6698

Hybrid Machine Learning Model Performance in IT Project Cost and Duration Prediction

Der-Jiun Pang*

International University of Malaya-Wales (IUMW), Faculty of Arts and Science, Kuala Lumpur, 50480, Malaysia

ARTICLE INFO

Article history:
Received: 26 October, 2022
Accepted: 02 March, 2023
Online: 24 March, 2023

Keywords:
Machine Learning
Project Cost and Time Estimation
Budget and Duration Prediction
Hybridization

ABSTRACT

Traditional project planning in effort and duration estimation techniques remain low to medium accurate. This study seeks to develop a highly reliable and efficient hybrid Machine Learning model that can improve cost and duration prediction accuracy. This experiment compared the performance of five machine learning models across three different datasets and six performance indicators. Then the best model was verified with three other types of live project data. The results indicated that the MLR-DNN is a highly reliable, effective, consistent, and accurate machine learning model with a significant increase in accuracy over conventional predictive project management tools. The finding pointed out a potential gap in the relationship between dataset quality and the Machine Learning model's performance.

1. Introduction

This paper is an extension of work initially presented at the 2022 IEEE Symposium on Computer Applications & Industrial Electronics (ISCAIE2022) [1]. Planning and estimation are imperative for any Information Technology (IT) project. Estimation aids in tracking progress and delivery velocity. However, due to the close relationship between cost and time factors, any project delay might result in cost overruns.

The investigators [2], [3] revealed that the top-ranked IT project risk is "*Underestimated Costs and Time*". According to the authors [4], 60% of IT projects have cost and time problems. Budget and timeline underestimation seems to occur at various stages of the project lifecycle. The most undesirable scenario happens when the budget and duration are underestimated at the beginning of the project lifecycle.

Artificial intelligence (AI) can improve decision-making in complex environments with clear objectives. A study concluded that, in terms of accuracy, artificial intelligence tools outperform traditional tools [5]. The value of AI can only be activated as humans and machines function complementarily integrated.

Hybridizing Machine Learning (ML) models are getting their popularity recently. According to researchers [6], hybridization effectively advances prediction models. This article focuses on the performance of various hybrid ML models in prediction accuracy enhancement to improve cost and duration estimation to address the critical IT failure problem.

2. Methodology

2.1. The Machine Learning Model Evaluation

This study was designed to demonstrate to the research community that the evaluations are comprehensive and can explain their significance. Five hybrid ML models were developed using Python and evaluated using three different datasets, including two public datasets. These models were trained and tested on three different datasets to reduce bias caused by data quality. The best-performing ML model was selected based on the performance measured by six different metrics. It was then put forward for live project verification to determine its performance in predicting project cost and duration.

These five hybrid ML models were: Hybrid Multiple Linear Regression Deep Neural Network (MLR-DNN), Particle Swarm Optimised DNN (PSO-DNN), Hybrid Gradient Boosting Regression DNN (GBR-DNN), Hybrid Random Forest Regression DNN (RFR-DNN), and Hybrid eXtreme Gradient Boosting DNN (XGB-DNN).

Controlled experiments play a vital role in applied machine learning, and the behaviour of algorithms on specific problems must be learned empirically. A machine learning experiment procedure involves a series of steps, 1. Data collection. 2. Data pre-processing: cleaning and manipulating acquired data to prepare it for modelling. 3. Model training: the model is trained on a training dataset, usually a subset of the data collected. 4. Model tuning: change in hyperparameters to optimize the model's performance. ML performance is measured by the defined performance metrics indicated in section 2.2. 5. Model evaluation: determine the

---

[*] Corresponding Author: Der-Jiun Pang, Email: djpang@gmail.com

https://dx.doi.org/10.25046/aj080212

model's performance on a testing dataset or another subset of the data collected. 6. Model deployment: the best model is then used to make predictions on live project data.

2.2. Performance Metrics

Evaluating the performance of ML models is essential to ensure their effectiveness. The choice of the performance metric is an important factor in this evaluation process. It depends on the specific ML problem being solved and the project's goals. The performance parameter used in this study is accuracy, which evaluates the number of correct predictions made as a percentage of all predictions made. The associated "accuracy" performance metrics used were $RMSE$, MAE, $RMSLE$, $MMRE$, $MdMRE$ and $Pred(m)$.

The **Root Mean Square Error ($RMSE$)** acts as a heuristic model for testing and training measures differences between predicted values and actual values from 0 to ∞. The smaller the $RMSE$, the better the model [7]. $\hat{y}_i$ is predicted output or forecasted values and y_i is the actual or observational values.

$$RMSE = \sqrt{\sum_{i=1}^{n} \frac{(\hat{y}_i - y_i)^2}{n}} \tag{1}$$

The **Root Mean Squared Log Error ($RMSLE$)** is a logarithmically calculated $RMSE$ commonly used metric or loss function in the regression-based machine learning model. The lesser error, the better the model is.

$$RMSLE = \sqrt{\frac{1}{n}\sum_{i=1}^{n}[log(y_i + 1) - log(\hat{y}_i + 1)]^2} \tag{2}$$

The **Mean Absolute Error (MAE)** measures the magnitude of errors regardless of their direction in a series of estimates. MAE is superior to $RMSE$ in terms of explanation-ability. $RMSE$ has a distinct advantage over MAE using absolute values, which is undesirable in many mathematical calculations. The smaller value, the better the model is.

$$MAE = \frac{1}{n}\sum_{i=1}^{n} |y_i - \hat{y}_i| \tag{3}$$

The **Mean Magnitude of Relative Error ($MMRE$)** and **Median Magnitude of Relative Error ($MdMRE$)** are two important performance metrics derived from the overall mean and median errors. The primary function of $MMRE$ is to serve as an indicator for differentiating between prediction models. The model with the lowest $MMRE$ typically being chosen typically implies low uncertainty or inaccuracy. The better the model, the smaller the values are.

$$MMRE = \frac{1}{n}\sum_{i=1}^{n} MRE_i \tag{4}$$

$$MdMRE = \frac{1}{n}\sum_{i=1}^{n} MdMRE_i \tag{5}$$

Percentage of Estimate, $\boldsymbol{Pred(m)}$, is an alternative to the $MMRE$ that is a commonly used prediction quality metric. It simply measures the proportion of forecasts within $m\%$ the actual value. The bigger the m, the less information and confidence in a prediction's accuracy [8].

$$Pred(m) = \frac{1}{n}\sum_{i=1}^{n} \begin{cases} 1, & if\ MRE_i \le \frac{m}{100} \\ 0, & otherwise \end{cases} \tag{6}$$

2.3. Degree of Augmentation

The degree of augmentation (DOA), χ, is a prediction enhancement measurement in error reduction to measure a hybrid model. A dual-layer hybrid cascaded ML model comprises two ML models represented as layers one and two (Figure 1). In stage one, the layer one ML model makes a prediction value $\hat{y}_{t-1}$ as inputs to stage two (y_t) to be processed by the layer two ML model with prediction output $\hat{y}_t$. The difference (or error) in the predicted result versus the actual result at stage one is denoted as Δ_{t-1}.

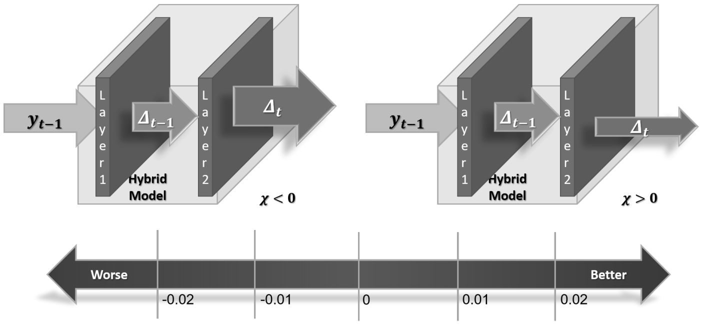

Figure 1: The Degree of Augmentation Scale

$$y_t = \hat{y}_{t-1} \tag{7}$$

$$\Delta_{t-1} = |y_{t-1} - \hat{y}_{t-1}| = |y_{t-1} - y_t| \tag{8}$$

Similarly, the difference in stage 2 is represented as Δ_t.

$$\Delta_t = |y_t - \hat{y}_t| = |\hat{y}_{t-1} - \hat{y}_t| \tag{9}$$

The assumption of difference in stage two is more diminutive than in stage one. The effect of convergence resulted in MAE reduction; therefore, augmentation occurred.

$$\Delta_t < \Delta_{t-1} \tag{10}$$

$$\hat{y}_{t-1} < \frac{y_{t-1} + \hat{y}_t}{2} \tag{11}$$

$$\chi = \Delta_{t-1} - \Delta_t = y_{t-1} - 2y_t + \hat{y}_t \tag{12}$$

By using equation (12), the $MMRE$ for stage one (Δ_{t-1}) and stage two (Δ_t) enables to calculate of the degree of augmentation, χ, for each of the hybrid models. The degree of augmentation, χ is bi-directional. A negative value indicates $MMRE$ increases or diverging, whereas a positive value specifies $MMRE$ decrease or converges. The positive magnitude of χ shows the strength of augmentation. The higher the χ means the better the hybrid model. The more significant negative value of χ means the hybrid model is ineffective. $\chi > .01$ is considered effective, $\chi \leq 0$ is ineffective. For $0 < \chi \leq .01$ is marginally effective, which means its augmentation is not significant enough to remain effective.

In an optimistic augmentation scenario, the Interquartile Range (IQR) becomes narrower, whereas the range becomes wider in an adverse augmentation scenario. This convergent phenomenon indicates the $MMRE$ decreases in positive augmentation. Contrary, in a divergent case, $MMRE$ increases in negative boost.

2.4. Data Collection

Figure 2 illustrates the data collection procedure. Each dataset was randomly split into two groups in a 70:30 ratio, 70% for training and 30% for testing. The relevant dataset was acquired online or gathered from previous project material. The collected data was then converted (if necessary) and pre-processed using scaling (for example, the *scikit-learn* scaling package) to prepare for ML assessment.

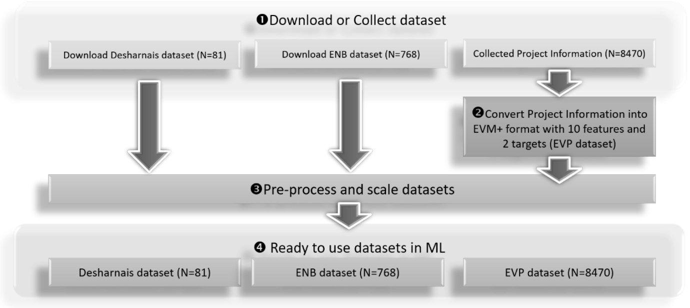

Figure 2: The data collection procedure

2.5. ML Evaluation

These ML models were evaluated in three steps depending on their algorithm settings. First, the respective models were trained using historical data in the learning or training step. Later in the testing step, these ML models were tested based on a peer comparison of their performance indicators. Each ML model was optimized through hyperparameter tuning until the best results were obtained (Figure 3).

2.6. Dataset Descriptions

A study concurs that the model may poorly correlate with a dataset that makes learning "incomplete" [9]. This evaluation used three dataset sources to minimize potential bias due to the dataset's influences. Two are publicly available, and the third dataset is a collection of actual historical project data named EVP. Both Desharnais and ENB datasets were selected in this study because of their multi-target attributes.

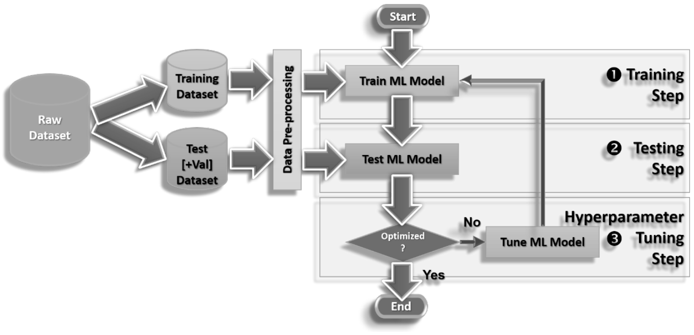

Figure 3: The ML evaluation workflow

It is challenging to ensure the quality of an ML dataset, mainly because the relationship between the qualities of the data and their effect on the ML system's compliance with its requirements is infamously complex and hard to establish [10]. In this study, dataset quality was defined as its appropriateness in terms of accuracy and value.

1) **Desharnais Dataset**

Jean-Marc Desharnais gathered the Desharnais dataset from ten organizations in Canada between 1983 and 1988. There are 81 projects (records) and 12 attributes [11], a relatively small public dataset of which four nominal fields are considered redundant in ML model evaluation. Table 1 provides statistical information about this dataset. Four entries have missing data. Most studies that use this dataset use 77 of the 81 records [12]. This study backfilled the missing fields with a "-1" value. Small dataset size issues could be compensated by adopting data-efficient learning or data augmentation strategies [13]. Desharnais datasets were used in many research. Therefore, it can benchmark the investigation against other published results.

2) **ENB Dataset**

The Energy Building Dataset [14] contains 768 instances of eight measured building parameters as feature variables. The dataset includes the two corresponding target heating load and cooling load attributes. A nominal field is considered redundant in this dataset.

Table *2* provides statistical information about this public dataset. The data comes from real-world applications and reflects real-world events with a multi-target. ENB is another popular dataset being used by many studies. The data size is deemed appropriate with more than 300 samples [15]. The ENB dataset is interesting, with only two targets closely associated, while the features have no interdependency, making prediction more complicated.

Table 1: Descriptive Statistics for Desharnais Dataset

Descriptive Statistics	id	Proj	Team Exp	Mgr Exp	Year End	LEN	Effort	TRXN	Entities	Points Non Adjust	Adjust	Points Adjust	LANG
Valid	81	81	81	81	81	81	81	81	81	81	81	81	81
Missing	0	0	0	0	0	0	0	0	0	0	0	0	0
Mean	41.00	41.00	2.19	2.53	85.74	11.67	5046.31	182.12	122.33	304.46	27.63	289.23	1.56
Std. Deviation	23.53	23.53	1.42	1.64	1.22	7.43	4418.77	144.04	84.88	180.21	10.59	185.76	.71
IQR	40.00	40.00	3.00	3.00	2.00	8.00	3570.00	136.00	112.00	208.00	15.00	199.00	1.00
Minimum	1.00	1.00	-1.00	-1.00	82.00	1.00	546.00	9.00	7.00	73.00	5.00	62.00	1.00

Descriptive Statistics	id	Proj	Team Exp	Mgr Exp	Year End	LEN	Effort	TRXN	Entities	Points Non Adjust	Adjust	Points Adjust	LANG
Maximum	81.00	81.00	4.00	7.00	88.00	39.00	23940.00	886.00	387.00	1127.00	52.00	1116.00	3.00

Table 2: Descriptive Statistics for ENB Dataset

Descriptive Statistics	id	Relative compactness	X1	X3	X4	X5	X6	X7	X8	Y1	Y2
Valid	768	768	768	768	768	768	768	768	768	768	768
Missing	0	0	0	0	0	0	0	0	0	0	0
Mean	384.500	.764	671.708	318.500	176.604	5.250	3.500	.234	2.813	22.307	24.588
Std. Deviation	221.847	.106	88.086	43.626	45.166	1.751	1.119	.133	1.551	10.090	9.513
IQR	383.500	.147	134.750	49.000	79.625	3.500	1.500	.300	2.250	18.675	17.513
Minimum	1.000	.620	514.500	245.000	110.250	3.500	2.000	.000	.000	6.010	10.900
Maximum	768.000	.980	808.500	416.500	220.500	7.000	5.000	.400	5.000	43.100	48.030

Table 3: Descriptive Statistics for EVP Dataset

Descriptive Statistics	X1	X2	X3	X4	X5	X6	X7	X8	X9	X10	Y1	Y2
Valid	8470	8470	8470	8470	8470	8470	8470	8470	8470	8470	8470	8470
Missing	0	0	0	0	0	0	0	0	0	0	0	0
Mean	.500	.053	.642	.633	.804	.791	3.057	1.162	.170	.013	1.002	.838
Std. Deviation	.006	.139	.276	.318	.272	.318	18.152	2.354	.316	.203	.205	.251
IQR	.000	.035	.446	.554	.297	.314	.926	.079	.375	.059	.042	.245
Minimum (x10^{-3})	.500	141.9	3.000	34.55	8.000	7.000	460.0	99.00	-1524	-3953	.000	35.15
Maximum	1.000	1.000	1.611	3.976	3.774	4.757	1461.738	136.935	2.864	1.068	4.700	2.656

3) EVP Dataset

Earned Value Management (EVM) is widely acknowledged as the most reliable contemporary project management instrument or cost and timeline forecasting technique. EVM calculates the amount of work performed to measure project performance and progress. The Earned Value Plus dataset is based on the conventional EVM attributes and added two new attributes related to the project management and size indexes. It contains 8,470 (more than 8000 records) instances from more than 600 historical project data in EVM format was deemed sufficient to train the ML model effectively (Table 3).

3. Experimental Results

Each optimized model was tested in four cycles. Evaluation results were obtained through each testing cycle and tabulated for each performance indicator. Each performance metric was calculated based on the average performance. The following subsections describe how the ML model performed, illustrated by graphical presentation in two graphs. The first graph shows performance results in $RMSE$, MAE and $RMSLE$. The second graph shows the performance results in $MMRE$, $MdMRE$ and $Pred(0.25)$.

3.1. Desharnais Dataset

MLR-DNN was the most optimal model for predicting the probability of a given experiment, while PSO-DNN appeared as the worst. MLR-NNN had the highest $Pred(0.25)$ value and the best $RMSLE$ and MAE values among all models tested in this study (Figure 4 and Figure 5). MLR-DNN is a hybrid cascaded ML model comprising MLR (Multiple Linear Regressor) and cascading with DNN (Deep Neural Network) embedded with four hidden layers and 64 neurons in each hidden layer.

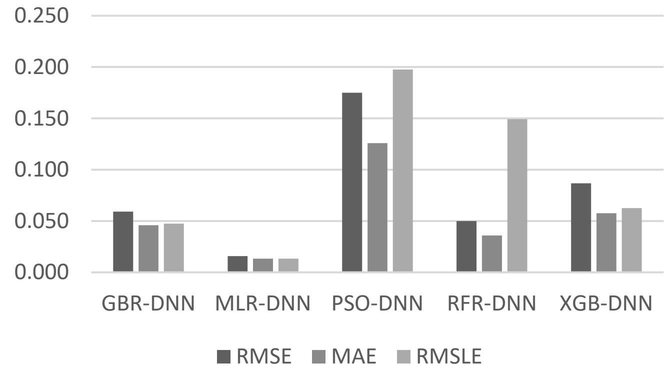

Figure 4: The $RMSE$, MAE, and $RMSLE$ results in the Desharnais dataset

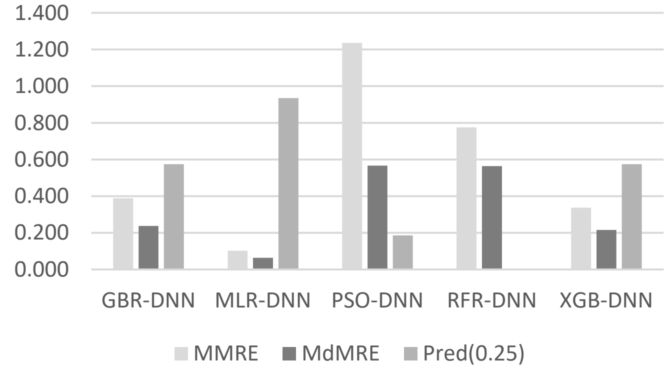

Figure 5: The $MMRE$, $MdMRE$, $Pred(25)$ results in the Desharnais dataset

3.2. ENB Dataset

MLR-DNN outplayed all other performance metrics, with the lowest $MMRE$ value being the least desirable model. The optimum $MdMRE$ value was .011, and the highest $Pred(0.25)$

value was .492, according to the most favourable $RMSE$ value. The most accurate MAE value was .004 (Figure 6 and Figure 7).

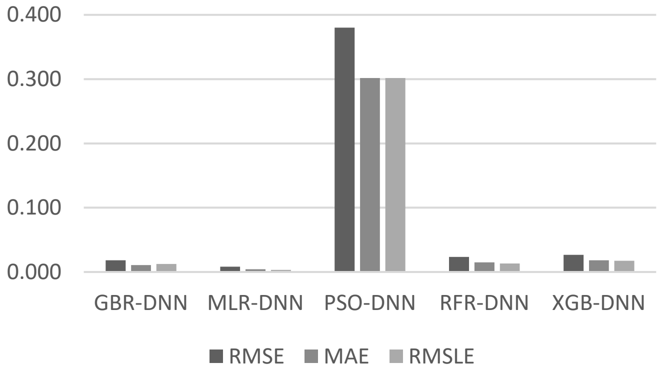

Figure 6: The $RMSE$, MAE, and $RMSLE$ results in the ENB dataset

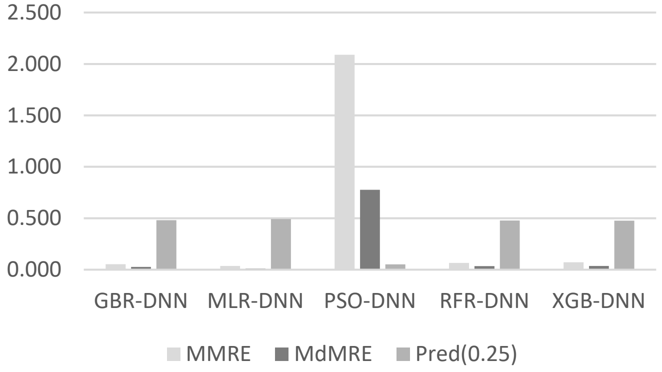

Figure 7: The $MMRE$, $MdMRE$, $Pred(25)$ results in the ENB dataset

3.3. EVP Dataset

MLR-DNN ranked as the top-performing ML model, with the lowest $MdMRE$ value and highest $Pred(0.25)$ value. The most favourable $RMSE$ value was .003, the best $RMSLE$ value was .003 and the most accurate MAE value of <.001 (Figure 8 and Figure 9).

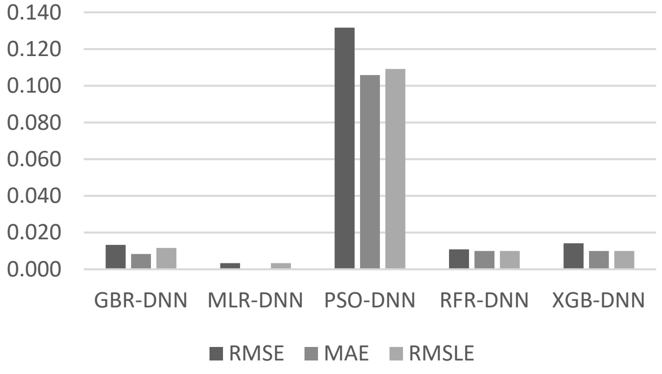

Figure 8: The $RMSE$, MAE, and $RMSLE$ results in the EVP dataset

3.4. Degree of Augmentation

The degree of augmentation, χ, is used as an error reduction indicator in a cascaded hybrid ML model using equation (12). The $MMRE$ for stage one (Δ_{t-1}) and stage two (Δ_t) enables us to calculate the degree of augmentation, χ , for each of the hybrids cascaded ML models (Figure 1). The hybrid model MLR-DNN demonstrated an average error reduction of .026 compared to the MLR model alone. PSO-DNN was excluded from the DOA comparison because PSD-DNN is not a cascaded standalone ML model but part of DNN with Particle Swarm Optimization (PSO) backpropagation. Overall results revealed that MLR-DNN outperformed all three other hybrids cascading DNN models, suggesting that cascading two different ML models may not produce positive results. Both GBR-DNN and XGB-DNN did not improve prediction accuracy, whereas the RFR-DNN model performed worse than RFR or DNN alone.

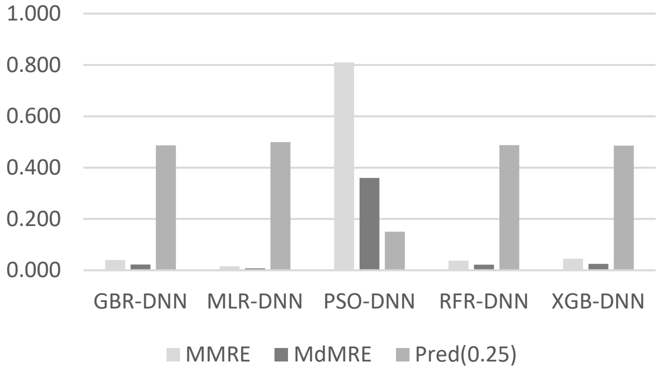

Figure 9: The $MMRE$, $MdMRE$, $Pred(25)$ results in the EVP dataset

Based on the performance results, the MLR-DNN model performed exceptionally well on all three datasets. The dependency on the quality of the dataset remains significant. This finding indicated that the PSO-DNN model was the most underwhelming performer in ENB and EVP datasets. However, for all three datasets, the least compelling performer was PSO-DNN. The runner-up position for both ENB and EVP datasets was GBR-DNN. However, the runner-up for the Dasharnais dataset was XGB-DNN.

The results also indicated that hybrid cascaded ML models such as GBR-DNN & XGB-DNN do not guarantee a positive gain and may sometimes have detrimental effects, for example, the RFR-DNN model. GBR-DNN performed relatively well in Desharnais and ENB datasets. However, it performed poorly in the EVP dataset. The result indicated that the quality of the dataset remains significant. This finding opens the door for future research.

The interquartile range (IQR) is a reliable measure of variability representing the dispersion of the middle 50% of the data [16]. The IQR is calculated as IQR = Q3 − Q1 statistically; the smaller IQR indicates the error range is relatively small. MLR-DNN showed the narrowest IQR and largest Mann-Whitney U effect size to strengthen its position as the most accurate ML model among the other models in this study. MLR-DNN enhanced the overall prediction accuracy compared to other models with a significant magnitude of error reduction.

From observation of the statistical value in

Table 4 for the degree of augmentation χ and Mann-Whitney U test effect size r, it seems like there is some form of proportion.

The investigators [17] explained that effect size is the difference between the variable's value in the control and test groups. The magnitude of χ increases and r increases, $|\chi| \propto r$. The significant difference between χ and r is that the effect size does not cater to attributes of positive or negative augmentation. This finding reflects that the degree of augmentation is a more appropriate performance indicator for measuring cascaded hybrid ML models.

Table 4: Degree of Augmentation Statistical Data

	GBR-DNN		**MLR-DNN**		**RFR-DNN**		**XGB-DNN**	
Descriptive statistics	$\boldsymbol{\Delta_{t-1}}$	$\boldsymbol{\Delta_t}$	$\boldsymbol{\Delta_{t-1}}$	$\boldsymbol{\Delta_t}$	$\boldsymbol{\Delta_{t-1}}$	$\boldsymbol{\Delta_t}$	$\boldsymbol{\Delta_{t-1}}$	$\boldsymbol{\Delta_t}$
Valid	11857	1779	11857	1779	11857	1779	11857	1779
Missing	0	0	0	0	0	0	0	0
Mean	.007	.006	.028	.002	.006	.009	.006	.006
Std. Deviation	.019	.018	.035	.003	.018	.011	.018	.014
IQR	.006	.006	.024	.001	.005	.007	.005	.005
Minimum (x10-6)	.105	8.492	12.13	1.059	.001	51.88	.002	.083
Maximum	.615	.115	.578	.061	.648	.188	.659	.397
p-value of Shapiro-Wilk		<.001		<.001		<.001		<.001
Degree of Augmentation χ		.001		.026		-.003		.000
Mann-Whitney U		9205868		809668		6171934.5		8978979
Wilcoxon W		79517879		2394758		76472087.5		79290990
(z) score		-8.701		-62.910		-28.286		-10.166
p-value		.000		.000		.000		.000
Effect Size r		.074		.538		.239		.061

4. Verification Results

Three types of live project data (Waterfall, Hybrid, and Agile) were used to verify MLR-DNN performance. The live performance results explained how effective MLR-DNN could be used practically in project management.

4.1. Waterfall Project

XYZ is one of the largest telecommunications operators in South East Asia. Due to exponential growth in customer demand, XYZ decided to enhance its operations support capability. MLR-DNN was used during the live project verification stage to forecast the budget and duration. Two EVM data samples were collected at 43% and 53% completion points. Table 5 displays the results.

MLR-DNN outperformed traditional EVM by 8.4% and 54.1% in average cost at Estimate At Completion (EAC) and average schedule prediction at Estimate Duration At Completion (EDAC), respectively. These findings align with a study which indicates CPI (cost) accuracy is relatively better than SPI (time) accuracy in EVM calculation [18].

Table 5: Waterfall Project Verification

% Complete	**Actual**		**ML Prediction**		$\boldsymbol{MRE}$	
	EAC	EDAC	EAC	EDAC	EAC	EDAC
43%	.70	.67	.80	.65	.1	.02
53%	.70	.67	.74	.65	.04	.02
				$MMRE$	.07	.02

The MLR-DNN model improved and significantly enhanced the performance of project effort and duration estimation. Work Breakdown Structure (WBS) and EVM remain moderately accurate despite being less dependent on humans. The result indicated that the dataset's quality continues to have a significant impact, opening future research opportunities.

4.2. Hybrid Waterfall-Agile Project

Hybrid Agile-Waterfall projects combine agile approaches with waterfall methodologies to deliver projects. The waterfall method to record specific requirements and the agile methodology to deliver gradually in sprints are examples of hybrid projects. Another hybrid agile-waterfall model is software development teams adopting the agile methodology, while hardware implementation teams stick to the waterfall approach. The amount of agile versus waterfall project technique adoption in scope coverage determines the blending ratio.

STU is a major telecommunications operator in South East Asia with millions of customers. It would like to optimize and enhance its operations support and telemarketing capability. The project cost is moderately high: hardware, commercial out-of-shelf products, software customization, system integration, consulting, and professional services.

Table 6: Hybrid Waterfall-Agile Project Verification

% Complete	**Actual**		**ML Prediction**		$\boldsymbol{MRE}$	
	EAC	EDAC	EAC	EDAC	EAC	EDAC
31%	.86	.96	1.23	.82	.37	.14
38%	.86	.96	.88	.73	.02	.23
54%	.86	.96	.84	.81	.02	.15
70%	.86	.96	.88	.74	.02	.22
92%	.86	.96	.75	.92	.11	.04
				$MMRE$	.11	.16

Five samples were collected from the same project at different stages and times (Table 6). One noticeable phenomenon is that prediction accuracy depends on the percentage of completion points. The closer the project's end, the more accurate the forecast is. At 31% completion, it was a less accurate prediction than the 54% completion point. The characteristic of EVM is inherited and aligned with findings in [10].

The predicted EDAC was accurate enough, with an average variance of 16% compared to any existing PM techniques and tools with 35-60%. There were insufficient details as to why there was a higher variance of EDAC than compared to EAC. Nevertheless, the project details revealed many change requests initiated that might impact prediction accuracy.

4.3. Agile Project

The MLR-DNN was fed with live agile project-scaled EVP data to predict project duration and cost in this verification test. Agile projects are typically shorter in duration and use fixed-length iterations. These projects usually have a low to medium budget, fixed period, and flexible scope.

ABC is a popular online banking software offering various electronic payment services to customers and financial institutions. A backlog of enhancements was prioritized in a different sprint by adopting a 100% agile methodology for the whole software development life cycle. Project resources were relatively small, usually less than ten people.

Project size was determined by the amount of project value in USD. Project is considered "small" < 500k; 1 million > "medium" ⩾ 500k, and "large" > 1 million. The percentage of completion was defined as the average project delivery progress

Table 7: Agile Project Verification

% Complete	**Actual**		**ML Prediction**		***MRE***	
	EAC	EDAC	EAC	EDAC	EAC	EDAC
100% (Sprint 1)	1	1	.99	1.00	.01	0
100% (Sprint 2)	1	1	.99	.99	.01	.01
50% (Sprint 3)	1	1	.77	.59	.23	.41
70% (Sprint 4)	.85	1	.93	.77	.08	.23
80% (Sprint 5)	.92	1	.94	.86	.02	.14
				MMRE	.07	.16

Three project-type live data samples were collected at different stages, iterations, sprints, and releases comprised of Agile, Hybrid, and Waterfall projects (Table 7). The overall prediction accuracy comparison between traditional EVM vs MLR-DNN in three project types is illustrated in Figure 10.

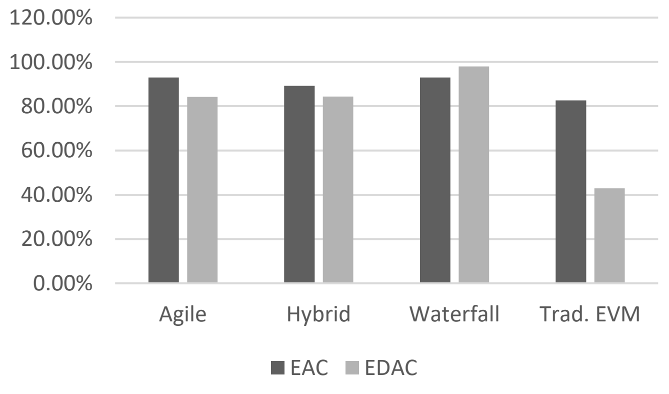

Figure 10: Performance Comparison between MLR-DNN and Traditional EVM in both Schedule and Cost Prediction

MLR-DNN model performed well in agile projects. It accurately predicted cost and schedule dimensions for many waterfall projects. Cost forecast accuracy is relatively better than duration forecast accuracy.

5. Machine Learning Biases

Machine learning (ML) algorithms are becoming more used in various industries. These algorithms, however, are not immune to bias, which can have detrimental repercussions. Therefore, it is critical to understand and address potential ML biases in order to ensure that these algorithms are fair and equal.

Type I - Algorithmic bias refers to systematic errors or unfairness resulting from employing algorithms inherited from the ML model, including how the model was constructed or trained, leading to biased outcomes [19]. Type II – Dataset bias is another type of bias that relates to the tendency of ML models to deliver inaccurate or unreliable predictions due to flaws or inconsistencies in the data used to train them [20]. It can result from various factors, including data collection methods and pre-processing techniques. To reduce ML biases, practitioners should evaluate models and datasets for performance and choose the least biased models.

6. Conclusion and Further Research

Traditional project planning in effort and duration estimation techniques remain low to medium accurate. This study seeks to develop a highly reliable and efficient Hybrid ML model that can improve cost and duration prediction accuracy. The results of the experiments indicated that MLR-DNN was the superior, effective, and reliable machine learning model.

The verification results in Agile, Hybrid and Waterfall projects indicated that the MLR-DNN model improved and significantly enhanced project effort performance and duration estimation. Despite WBS and EVM (conventional project management tools) being less dependent on humans, they are moderately accurate.

The results indicated that hybrid cascaded ML models such as GBR-DNN & XBG-DNN do not guarantee a positive gain and may sometimes have detrimental effects, for example, the RFR-DNN model. MLR-DNN inherits other neural network flaws being computationally costly and operating in black boxes with little explanation.

The accuracy of neural networks (including MLR-DNN) depends on the volume and the quality of training data [21]. Therefore, the dataset's quality significantly impacts the ML model's performance. This finding opens the door for future research.

References

[1] D.-J. Pang, K. Shavarebi, S. Ng, "Development of Machine Learning Models for Prediction of IT project Cost and Duration," in 2022 IEEE 12th Symposium on Computer Applications & Industrial Electronics (ISCAIE), IEEE: 228–232, 2022, doi:10.1109/ISCAIE54458.2022.9794529.

[2] D.-J. Pang, K. Shavarebi, S. Ng, "Project practitioner experience in risk ranking analysis-an empirical study in Malaysia and Singapore," Operations Research and Decisions, **32**(2), 2022, doi:10.37190/ord220208.

[3] D.-J. Pang, K. Shavarebi, S. Ng, "Project Risk Ranking Based on Principal Component Analysis - An Empirical Study in Malaysia-Singapore Context," International Journal of Innovative Computing, Information and Control, **18**(06), 1857–1870, 2022, doi:10.24507/IJICIC.18.06.1857.

[4] TD. Nguyen, T.M. Nguyen, T.H. Cao, "A conceptual framework for is project success," in Lecture Notes of the Institute for Computer Sciences, Social-Informatics and Telecommunications Engineering, LNICST, 142–154, 2017, doi:10.1007/978-3-319-56357-2_15.

[5] D. Magaña Martínez, J.C. Fernandez-Rodriguez, "Artificial Intelligence Applied to Project Success: A Literature Review," International Journal of

Interactive Multimedia and Artificial Intelligence, **3**(5), 77, 2015, doi:10.9781/ijimai.2015.3510.

[6] A. Mosavi, M. Salimi, S.F. Ardabili, T. Rabczuk, S. Shamshirband, A.R. Varkonyi-Koczy, “State of the art of machine learning models in energy systems, a systematic review,” Mdpi.Com, **12**(7), 2019, doi:10.3390/en12071301.

[7] S. Bayram, S. Al-Jibouri, “Efficacy of Estimation Methods in Forecasting Building Projects’ Costs,” Journal of Construction Engineering and Management, **142**(11), 05016012, 2016, doi:10.1061/(ASCE)CO.1943-7862.0001183.

[8] D. Port, M. Korte, “Comparative studies of the model evaluation criterions MMRE and PRED in software cost estimation research,” in ESEM’08: Proceedings of the 2008 ACM-IEEE International Symposium on Empirical Software Engineering and Measurement, ACM Press, New York, New York, USA: 51–60, 2008, doi:10.1145/1414004.1414015.

[9] E. Korneva, H. Blockeel, “Towards Better Evaluation of Multi-target Regression Models,” in Communications in Computer and Information Science, Springer Science and Business Media Deutschland GmbH: 353–362, 2020, doi:10.1007/978-3-030-65965-3_23.

[10] S. Picard, C. Chapdelaine, C. Cappi, L. Gardes, E. Jenn, B. Lefevre, T. Soumarmon, “Ensuring Dataset Quality for Machine Learning Certification,” in Proceedings - 2020 IEEE 31st International Symposium on Software Reliability Engineering Workshops, ISSREW 2020, 275–282, 2020, doi:10.1109/ISSREW51248.2020.00085.

[11] A.K. Bardsiri, “An intelligent model to predict the development time and budget of software projects,” International Journal of Nonlinear Analysis and Applications, **11**(2), 85–102, 2020, doi:10.22075/ijnaa.2020.4384.

[12] MF Bosu, SG Macdonell, “Experience: Quality benchmarking of datasets used in software effort estimation,” Journal of Data and Information Quality, **11**(4), 1–26, 2019, doi:10.1145/3328746.

[13] R.M. Thomas, W. Bruin, P. Zhutovsky, G. Van Wingen, “Dealing with missing data, small sample sizes, and heterogeneity in machine learning studies of brain disorders,” Machine Learning, 249–266, 2019, doi:10.1016/B978-0-12-815739-8.00014-6.

[14] OpenML enb, May 2021.

[15] M.A. Bujang, N. Sa’at, T.M. Ikhwan, T.A.B. Sidik, “Determination of Minimum Sample Size Requirement for Multiple Linear Regression and Analysis of Covariance Based on Experimental and Non-experimental Studies,” Epidemiology Biostatistics and Public Health, **14**(3), e12117-1 to e12117-9, 2017, doi:10.2427/12117.

[16] D.T. Larose, Discovering Knowledge in Data: An Introduction to Data Mining, 2005, doi:10.1002/0471687545.

[17] P. Kadam, S. Bhalerao, “Sample size calculation,” International Journal of Ayurveda Research, **1**(1), 55, 2010, doi:10.4103/0974-7788.59946.

[18] M. Fasanghari, S.H. Iranmanesh, M.S. Amalnick, “Predicting the success of projects using evolutionary hybrid fuzzy neural network method in early stages,” Journal of Multiple-Valued Logic and Soft Computing, **25**(2–3), 291–321, 2015.

[19] S.S. Gervasi, I.Y. Chen, A. Smith-Mclallen, D. Sontag, Z. Obermeyer, M. Vennera, R. Chawla, “The Potential For Bias In Machine Learning And Opportunities For Health Insurers To Address It,” Https://Doi.Org/10.1377/Hlthaff.2021.01287, **41**(2), 212–218, 2022, doi:10.1377/HLTHAFF.2021.01287.

[20] A. Paullada, I.D. Raji, E.M. Bender, E. Denton, A. Hanna, “Data and its (dis)contents: A survey of dataset development and use in machine learning research,” Patterns, **2**(11), 100336, 2021, doi:10.1016/J.PATTER.2021.100336.

[21] J. Zhou, X. Li, H.S. Mitri, “Classification of rockburst in underground projects: Comparison of ten supervised learning methods,” Journal of Computing in Civil Engineering, **30**(5), 04016003, 2016, doi:10.1061/(ASCE)CP.1943-5487.0000553.

Advances in Science, Technology and Engineering Systems Journal
Vol. 8, No. 2, 116-122 (2023)
www.astesj.com
Special Issue on Computing, Engineering and Multidisciplinary Sciences

ASTES Journal
ISSN: 2415-6698

Hybrid Discriminant Neural Networks for Performance Job Prediction

Temsamani Khallouk Yassine *,[1], Achchab Said [1], Laouami Lamia[2] , Faridi Mohammed[2]

[1] *University Mohammed V, ENSIAS, Rabat, Morocco*

[2] *University Hassan 1, ENCG, Settat, Morocco*

ARTICLE INFO

Article history:
Received: 28 September, 2022
Accepted: 16 March, 2023
Online: 11 April, 2023

Keywords:
Artificial Neural Network
Performance job prediction
Particle swarm optimization
Human talent
Variable selection

ABSTRACT

Determining the best candidates for a certain job rapidly has been one of the most interesting subjects for recruiters and companies due to high costs and times that takes the process. The accuracy of the models, particularly, is heavily influenced by the discriminant variables that are chosen for predicting the candidates scores. This study aims to develop an performance job prediction systems based on hybrid neural network and particle swarm optimisation which can improve recruitment screening by analyzing historical performances and conditions of employees. The system is built in four stages: data collection, data preprocessing, model building and optimisation and finally model evaluation. Additionally, we highlight the significance of Particle Swarm Optimization (PSO) in enhancing the performance of the models created by presenting a training algorithm that uses PSO. We conduct a study to compare the performance of each hybrid model and summarize the results.

1 Introduction

The field of human resources (HR) has undergone significant changes over the past few decades, and the rise of artificial intelligence (AI) has had a major impact on how HR functions are performed. From recruitment and employee evaluation to training and career development, the introduction of AI has led to a transformation in the way HR professionals perform their duties. This article will delve into the literature on the impact of AI in HR, analyzing the advantages and drawbacks of utilizing AI in this field, and examining the potential implications for HR professionals and organizations.

Another area where AI is having an impact is in employee evaluation and performance management. AI algorithms can analyze an employee's work history, skills, and achievements to predict their potential for growth and future success within the company. This can help HR professionals make informed decisions about employee development and career advancement. For example, in a study by Deloitte, 92% of HR professionals reported that AI has improved the accuracy of performance evaluations (Deloitte, 2019). Performance job prediction has become increasingly popular with the advent of machine learning algorithms such as decision trees, random forests, and support vector machines, which can handle vast quantities of data and discern intricate connections between various variables. These algorithms can be trained on historical performance data to make predictions about the future performance of new hires or current employees. In this study, we will focus on the application of the ANN on the candidates performance prediction [1].

Designing an ANN with the appropriate parameters can result in a powerful tool. In fact, the process of choosing selecting the architecture that will works well includes the number of input, hidden neurons and weight values, for a complex situations can pose an optimization task challenge. The training process plays a crucial role in determining the ANN topology. Firstly, the most suitable architecture needs to be chosen by assessing the problem at hand, which entails identifying the number of input, hidden, and output neurons. Secondly, the ideal weight values that enable the ANN model to perform at its best must be identified. While the ANN architecture is typically determined by experience, some researchers have started using meta-heuristic algorithms such as Particle Swarm Optimization to explore various possible architectures and select the optimal one based on a fitness criterion.

The primary objective of this study is to create a job performance prediction model that utilizes ANN, PSO, and appropriately selected variables based on the availability of data. The first step involves examining the effectiveness of variable selection models by comparing discriminant analysis and logistic regression techniques. The second step entails identifying the optimal ANN topology by proposing a training process that employs the PSO algorithm to determine the ideal neural network topology.

---

*Corresponding Author: TEMSAMANI Khallouk Yassine, Rabat, Temsamani.khallouk.yassine@gmail.com

https://dx.doi.org/10.25046/aj080213

2 Literature review

2.1 *Performance job prediction*

Performance job prediction is the process of using various data points, such as an employee's job performance, education and skill sets, personality traits, and even social media activity, to make predictions about an individual's potential for growth and success within a company [2]. This information can be used by organizations to make informed decisions about employee evaluation, promotion, and training. The goal of performance job prediction is to create a more productive and efficient workforce by identifying high-potential employees and providing them with the resources and support they need to succeed [3].

One of the key advantages of performance job prediction is its ability to provide actionable insights into employee performance. For example, organizations can use these predictions to identify high-performing employees and provide them with the resources and training they need to excel in their roles. In addition, predictions can help managers make informed decisions about promotions, pay increases, and other compensation-related matters.

The accuracy of performance job prediction models is dependent on the quality and quantity of data used in the model. Data sources may include things like past performance evaluations, training data, and demographic information. The use of multiple data sources allows organizations to build a more complete picture of an employee's potential, providing a more accurate prediction.

One of the most commonly used approaches for performance job prediction is regression analysis. This method uses statistical methods to model the relationship between predictor variables (e.g., past performance, training data) and the dependent variable (future performance). Regression analysis can provide valuable insights into the impact of different factors on an employee's performance, allowing organizations to make informed decisions about staffing, development, and compensation.

An alternative method involves utilizing machine learning algorithms, such as decision trees, random forests, and gradient boosting, to construct models that predict employee performance by analyzing data [4]–[7].

2.2 *Classification for Prediction*

Smart choices can be made by utilizing techniques such as classification and prediction. Scholars in the domain of machine learning have suggested numerous methods for classification and prediction assignments. This research, in particular, focuses on the classification methods employed in the machine learning procedure. These approaches to analyzing data are used to derive models that define significant data categories or anticipate forthcoming trends in the data [8].

The classification process is composed of two main phases: during the learning phase, the classification algorithm scrutinizes the training data to generate a classifier, which is essentially a set of guidelines for classification. In the classification phase, the accuracy of the classifier is evaluated by testing it on the test data. If the accuracy is satisfactory, the model can be utilized to make predictions on new data. There are several techniques for classification, such as Bayesian approaches, decision trees, neural networks, and numerous others.

This study will focus on the application of the artificial neural network and its parameter optimization [9].

2.3 *Artificial Neural Network*

Artificial neural networks, a subcategory of artificial intelligence, draw inspiration from neurobiology and entail designing machines capable of learning and accomplishing specific assignments, such as classification, prediction, or grouping. These networks comprise interlinked neurons that learn from the data they encounter to detect linear and nonlinear patterns in intricate data, resulting in dependable forecasts for new scenarios. The inaugural neuron model, which was grounded on biological neurons, was introduced in 1943 by McCulloch and Pitts.

In 1943, McCulloch and Pitts introduced the first neuron model, which proved that formal neurons are capable of performing logical functions. Later, in 1949, psychologist Donald Hebb introduced parallel and connected neural network models and proposed many rules for updating weights, including the well-known Hebbian rule [10]. Frank Rosenblatt, a psychologist, created the perceptron model in 1958. This model was able to identify simple shapes and carry out logical functions [11]. Nevertheless, in 1969, Minsky and Papert revealed the limitations of the perceptron, specifically in addressing nonlinear problems [11]. In the 1980s, interest in artificial neural networks was renewed by the introduction of Rumelhart's Back-Propagation algorithm, which enhances parameters for multilayered neural networks by transmitting errors to the hidden layers [12].

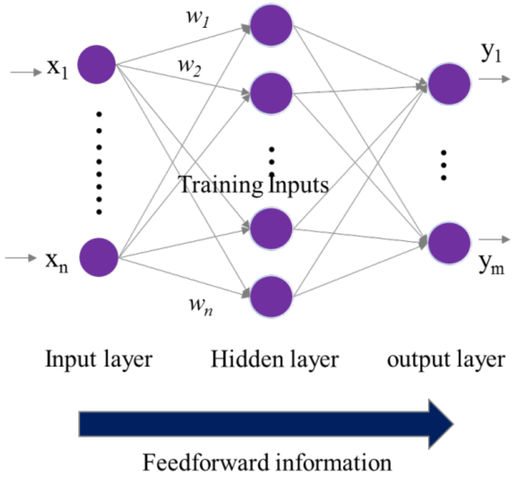

Figure 1: Artificial Neural Network

Since then, the use and application of neural networks have expanded into various fields. In fact, studies have demonstrated that a Multilayer Perceptron network with a single hidden layer has the capability to estimate any function of Rn in Rm with high accuracy [13]. The structure and settings of a neural network are crucial factors that determine its effectiveness and efficiency.The multilayer network is a commonly used structure in neural networks, consisting of an input layer, one or more hidden layers, and an output layer. The hidden layer functions as a mediator between the input and output neurons, and the connections among the layers are represented by the weights of the connecting links. Generally, the layers in a neural network are linked together in a manner that allows data to flow solely in one direction - this is known as a feed-forward approach. There are no loops or cycles in the network. The data originates from the input layer, traverses through the hidden layers, and finally arrives at the output layer. An example of a neural network with a single hidden layer is shown in Figure 1 to provide a better understanding of its functioning. In addition, previous research has demonstrated that this architecture is optimal for solving classification problems, which is the focus of this article [13].

For a neural network with one hidden layer, we can observe that each hidden neuron (indexed $j = 1, ..., n$) takes in an input that is the result of a weighted sum of the inputs to the entire network. The transfer function f is used to process the input and convert it into an output signal.

$$\mathrm{z_j} = f\left(\mathrm{w_{j0}} + \sum_{\mathrm{i=1}}^{\mathrm{n}} \mathrm{w_{ji} x_i}\right) \tag{1}$$

The variable n and and the variable m are the number of input neurons and the hidden ones, respectively and w_{ij} is the weight from the i_{th} input neuron to the j_{th} hidden neuron, x_i is input variable i and w_{j0} is a bias term. The hidden neuron signals are subsequently transmitted to the output neurons through weighted connections, similar to the transmission between the input and hidden layers. Consequently, the output neurons obtain the sum of all weighted hidden neurons, which is then passed through a transfer function g, based on the required output range. The output y_o of the network's output neuron o is formulated as:

$$\mathrm{y_o} = g\left(\mathrm{b_{z0}} + \sum_{\mathrm{i=1}}^{\mathrm{m}} \beta_{\mathrm{zj}}\left(f\left(\mathrm{w_{j0}} + \sum_{\mathrm{i=1}}^{\mathrm{n}} \mathrm{w_{ji} x_i}\right)\right)\right) \tag{2}$$

With b_{zj} represent the weight from the J_{TH} hidden neuron to the O_{th} output neuron and b_{z0} is the bias. As mentioned earlier, the reason why neural networks are popular in different areas is due to their capacity to approximate linear or nonlinear functions. However, the challenge is to determine the optimal topology and weight values of the network that can closely approximate the target function. This task can be thought of as an optimization problem, where the objective is usually to minimize a cost function based on the total sum of squared errors.

2.4 Optimizing parameters for ANN

2.4.1 Input variables

Once the artificial neural network is established, the next step is to identify the necessary information required to build the network. This information is provided in the form of input variables that are used to assess the potential job performance of candidates. To permit to the ANN to accurately classify new observations, the input variables must be carefully selected to ensure the classification model performs well. Therefore, it is crucial to identify the most relevant variables for classification purposes.

2.4.2 Architecture

Tthe structure of an ANN is an input layer, output layer, and one or more hidden layers. Hence, there are other crucial factors that have an impact on the performance of the artificial neural network, and they need to be considered while designing it. These factors comprise the number of neurons present in each layer and the number of hidden layers that are incorporated into the network. These parameters determine the behavior of the neural network and vary depending on the problem to be solved.

The study employs the neural network architecture with one hidden layer for classification purposes [13] , which is widely acknowledged as the optimal structure for such problems according to existing literature.

Selecting the appropriate number of neurons for the hidden layers of an artificial neural network can be a difficult task. Having too many neurons can lead to an increase in the number of computations required by the algorithm. Conversely, selecting too few neurons in the hidden layer can result in a reduction in the model's capacity to learn [14]. So, it is crucial to choose the optimal number of neurons to achieve the highest possible performance of the neural network.

2.4.3 Learning algorithm

The process of finding the optimal weights and biases that maximize the performance of a neural network is known as learning algorithms, which consist of a set of rules. Various techniques have been used in literature to determine the best architectures and topology of weights and biases for the neural network, depending on the learning type.

Supervised learning refers to the scenario where the dataset used for training is labeled, while unsupervised learning train on unlabeled datasets. In unsupervised learning, the weights of the neural network are adjusted based on specific criteria to identify patterns or regularities in the observations.

The principal goal of this research is to improve the performance of an artificial neural network (ANN) in predicting job performance of a candidate. This is done using a supervised learning approach where the labels for the classes are already known and provided during the training stage. The learning algorithm adjusts the connection weights between inputs layers and the target ones to estimate their dependencies and minimize the error function, such as mean squared error.

The optimisation techniques can be classified into two groups:

- The first set of techniques is based on the steepest descent method and includes methods like gradient descent, Levenberg Marquardt, Backpropagation, and their variations. However, some of these algorithms require a significant amount of computational resources in terms of time and memory. Out of these, the Backpropagation algorithm is the most widely utilized, as it is a highly effective tool for determining the gradient in neural networks. However, it has its limitations, particularly with regards to the issue of getting stuck in local minima.
- The second group encompasses techniques that are inspired by the evolution of living species, such as genetic algorithms and swarm algorithms among others.

2.4.4 Transfer Function

Before training a neural network, one of the parameters that needs to be determined is the transfer function. The selection of an activation function is dependent on the specific use case. For instance, binary functions are well-suited for organization and distribution problems, whereas continuous and differentiable functions like sigmoid function are utilized to approach continuous functions. Notably, the sigmoid transfer function is commonly used because it combines nearly linear, curvilinear, and nearly constant behavior based on the input value [14]. The sigmoid transfer function's adaptability enables the artificial neural network to manage both linear and non-linear issues. It's possible to represent the sigmoid function as:

$$f(x) = \frac{1}{(1 + \exp(-x))} \qquad (3)$$

The function being used as the transfer function in this study is bounded between zero and one, and it takes a real-valued input and produces an output within that range.

2.5 Particle Swarm Optimization (PSO)

PSO is an evolutionary computation method that was created by J. Kennedy, a social psychologist, and R. Eberhart, an electrical engineer, in 1995 [15]. It is a type of swarm intelligence algorithm that draws inspiration from the natural behavior of social organisms, such as birds flocking, and is employed as an optimization technique in a variety of research domains.

Social animals that live in groups, like swarms, often need to travel long distances to migrate or search for food. To do so efficiently, they optimize their movements in terms of time and energy expenditure and cooperate with one another to achieve their objective. The PSO algorithm is rooted in this behavior and is utilized to discover solutions to problems by optimizing a continuous function in a data space. Each member of the group, similar to the animals in a swarm, decides their movement based on their own experience and that of their peers, resulting in a complicated and effective process [15].

The PSO algorithm is designed around a group of individuals known as particles. At the first time, these particles are placed randomly in the solution space and move around in search of the optimal remedy to the challenge. Each particle's position represents a potential solution to the challenge. The movement of each piece is governed by specific rules. Each particle has a memory that allows it to remember the best point it has encountered so far and tends to return to that point. Additionally, each particle is informed of the best point found by its neighbors and tends to move towards that point.

The initial step for utilizing the PSO algorithm involves establishing a search area comprising of particles and a fitness function for optimization. Afterward, we commence by initializing the system with a set of haphazard solutions (particles). Each particle is allotted a positional value signifying a plausible solution data, a velocity value that denotes the extent to which the data can be modified, and a personal best value (pBest) that represents the particle's most optimal solution reached thus far.

Algorithm 1: PSO algorithm[16]

```
for Particle i in swarm S do
    Set up the particle i ;
end
while stopping condition is false do
    for Individual i of the swarm do
        Calculate the fitness f(xi(t));
        if the fitness value>p_best then
            Assign the current value as the updated personal
              best (p_best);
        end
    end
    Select the optimal fitness value among all particles and
      denote it as (g_best);
    for Individual i of the swarm do
        Adjust the velocity of the particle in accordance
          with the Eq (1);
        Adjust the velocity of the particle in accordance
          with the Eq (2);
    end
end
```

3 Research Framework

In order to define the solutions, a research framework must first be developed. The research includes four major processes that are included in this research: data collection, preprocessing of data, variable selection, model building and the evaluation of the model.

The proposed framework is shown in the Figure 2 below.

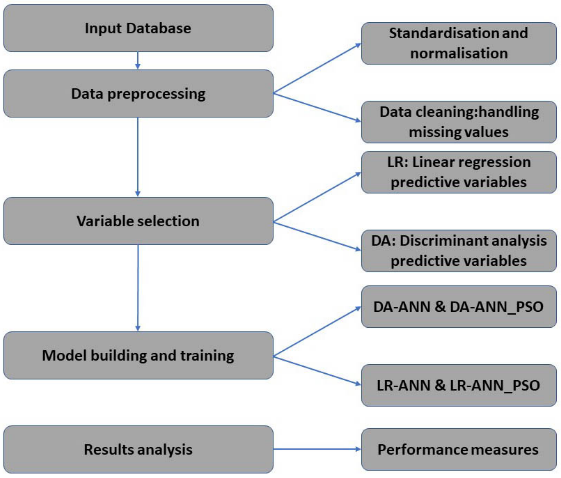

Figure 2: The proposed methodology

3.1 Discriminant variables

To determine the optimal architecture for an ANN, the first step is to identify the input variables. These variables will be used to construct mathematical models that predict job performance. However, selecting the appropriate variables can be a challenge and is crucial for the model's accuracy. In this study, 15 variables listed in Table 2 were used, based on the availability of data.

3.2 Data preprocessing

Studies and research have demonstrated that several AI algorithms may exhibit poor performance due to the inferior quality of data and variables. Therefore, two critical steps are required to enhance the feasibility of the variables for constructing a predictive model: variable selection modeling for reducing dimensionality and data preprocessing. This process involves data preparation and normalization to accomplish reduction or classification tasks. The Table 1 below shows the variables used in this study.

Table 1: Dataset description

Variables	Description	Value
ID	Employee's id	integer
Age	Employee's Age	Integer
Gender	Employee's gender	M or F
Marital status	Employee's status	S or M
Diploma	Employee Education Degree	Bachelor High Diploma Master, Phd
Experience years	Employee year of experience	Integer
Salary	Employee salary	Integer
Communication Level	Employee level in communication	1 to 5
Motivation enthusiasm	Employee motivation for work	Yes or No
Language score	Employee language level	1 to 5
Specialisation	Employee general Specialisation	IT, Economics HR, Network business
Effectiveness in a remote environment	Employee ability in remote	Yes or no
Seniority	Employee seniority in the company	Junior Senior Manager
Physical abilities	Employee ability to work	Yes or no
Additional Certificate	Employee additional certificate	Yes or no
Employee performance	Employee performance	BA Good

3.3 Variables selection models

In classification studies, it is crucial to determine which variables hold the most importance in distinguishing between different categories. Moreover, it is often challenging to obtain trustworthy and meaningful data. Therefore, it is essential to identify the most significant variables that can offer insights to forecast candidate performance to reduce the effort required to gather and verify data.

When creating a prediction model, it can be helpful to reduce the number of variables in order to improve computational efficiency and increase the accuracy of classification algorithms, like neural networks. To achieve this, we'll use two types of classification techniques statistical methods and artificial intelligence in order to identify the most important variables that distinguish between candidates' performance. Then, we'll choose the best variable selection model to optimize the performance of the neural network.

In this study, we are more focused on the statistical method Statistical method used in this study is chosen for its popularity in variable selection is discriminant analysis (DA) and logistic regression. Discriminant analysis is commonly utilized to identify a linear combination of features that can effectively distinguish between two or more groups, in order to reduce the number of dimensions prior to classification.

3.4 Artificial Neural Network Architecture

This study utilizes an ANN model for predicting the job performance of candidates chosen at random. As previously stated, the architecture of the ANN is critical to its functionality and effectiveness. Therefore, this section focuses on determining the optimal topology that can differentiate between a good candidate and a poor one based on the selected variables.

To define the architecture of an ANN, certain parameters must be determined such as the number of input neurons, hidden layers, and hidden neurons. According to the literature, ANNs with one hidden layer are considered the optimal structure for classification problems[13].

4 Cross validation

Any bias or bad quality due to dataset could potentially have a huge impact on determining the artificial neural network and its parameters. In this sense, the cross validation technique is made to minimize this genre of problem.

In our experiment we will use a 3 fold-cross validation technique to train and test our model to avoid over fitting.

To be precise, we divided our dataset into three equal subsets, which implies that our model will undergo training and testing procedures three times. The mean value of the accuracy measures obtained from each of the three iterations is used to evaluate the overall accuracy of the model.

5 Performance evaluation

To evaluate the performance of our model, we use this list of evaluation metrics:

Overall accuracy: In general, accuracy refers to the percentage of correctly classified records by the model. The formula for calculating accuracy can be derived from the confusion matrix presented in Table 2.

$$\text{Accuracy} = \frac{TP + TN}{TP + TN + FP + FN} \tag{4}$$

Precision: It can be described as the proportion of the correctly predicted cases (True Positive) to the combined number of True Positive and False Positive.

Recall: It can be expressed as the proportion of the correctly predicted cases (True Positive) to the combined number of True Positive and False Negative.

Specificity: The True Negative Rate is calculated as the number of True Negatives divided by the sum of True Negatives and False Positives.

Predicted		
Actual	**BA**	**Good**
BA	True Negative	False Positive
Good	False Negative	True Positive

F-Measure: F-measures take the harmonic mean of the Precision and Recall Performance measures [17].

$$F\_\text{Measure} = \frac{\text{Precision} \times \text{Recall}}{\text{Precision} + \text{Recall}} \tag{5}$$

6 Empirical study

As mentioned earlier, the main aim of this study is to employ a combination of neural network and Particle Swarm Optimization to forecast the job performance of a random applicant. The initial stage in this approach, as described in the research methodology, involves choosing the suitable variables that can be utilized to create a the optimal method.

6.1 Data and variables

The dataset used in this study issued from a Moroccan firm contains the most variables used on the manual recruitment process based on the survey made inside each department of this firm. Data collected contains more than 1000 individuals. A variable class is created with two values (BA if the candidate is below the average, Good is the candidate have a good qualification). The individuals was selected randomly from a different department: IT department, finance department, HR department, Data department...

Before using our Data as input for our model, a normalizing function Eq.6 was applied to bound data values to -1 and +1 with X is the input matrix, Y is the normalized matrix, x_{min} and x_{max} are respectively the maximal and the minimum values of a variable [18].

$$Y = \frac{0.9 - 0.1}{\text{xmax} - \text{xmin}}X + \left(0.9 - \frac{0.9 - 0.1}{\text{xmax} - \text{xmin}}\text{xmax}\right) \tag{6}$$

6.2 Results

The initial step of processing and managing data involves dealing with missing values, decreasing the number of variables, and examining the most significant ones, which is crucial. So, we begin our process of building a performance job prediction model by handling the missing values. Our dataset contains many missing values so to fix this problem, we refer to KNN imputation. In fact, a new observation is imputed by finding the samples in the training set closest to it and averages these nearby points to fill in the value.[4]

Secondly, we need to determine the influence of each variables on a candidate's job performance by using variable selection techniques. We will compare common models such as Discriminant Analysis and Logistic Regression, and summarize the variables selected by each model in a table below.

Table 2: Variables selection results

Variables selection Techniques	**Number variables**	**Selected Variables**
DA	8	Gender, Marital status, Seniority , Salary Communication level Employee ethics Specialisation, Physical abilities
Logistic Regression	12	Age, Gender, Marital status, Seniority , Salary, Diploma Experience years Language score Communication score Specialisation, Additional Certificate, Effectiveness in a remote environment

The presented table displays how each model has selected a distinct set of variables based on their discriminatory power. The feature sets have been divided into two categories: the first group contains eight variables chosen by DA, and the second group includes twelve variables chosen by LR.

The ANN model's input layer will rely on the set of variables selected by the variable selection models. As a result, two hybrid neural network models, MDA-ANN and LR-ANN, are constructed accordingly.

After defining the best variables that will have a big impact on our target variable, it's time now to define the best architecture for our model, for this reason we compare the following learning algorithm based on PSO, and the hybrid artificial neural network trained separately.

Now, we have reached the step of designing the topology of our hybrid neural network. for this step, we used the following parameters:

The architecture that produced the highest performance accuracy applied to our model was determined to be 12-18-1 (12 input neurons, 18 hidden neurons, and one output neuron). The 12 input neurons in this case correspond to the number of variables selected by the logistic regression algorithm, indicating that these variables have strong discriminatory power when it comes to predicting candidate performance.

Table 3: PSO parameters

Parameters	**Architecture optimization**	**Weights optimization**
Swarm Size	20	20
Stop criteria & iteration	100	100
Search area range	[3, 20]	[-2.0, 2.0]
Inertia factors	$(w_n = 0.9 * w_{n-1})$ $w_0 = 0.8$	$(w_n = 0.9 * w_{n-1})$ $w_0 = 0.8$

We can see also that the application of our Hybrid artificial neural network separately decrease the performance of the two models DA-ANN and LR-ANN compared to its application with the PSO. The results will be presented and analyzed in the table 5.

Note that the evaluation of the evaluation metrics alone does not give a good judgment on the quality of the prediction and the classification. In this performance comparison, we will also focus on the performance attribute to each class which gives important information about a model especially to select the variables which discriminate the performance of the candidates.

This appears clearly in the application of the hybrid algorithm: DA-ANN and DA-ANN_PSO. In fact, even with its big accuracy, they present the less rate of good classification of good candidates (47.5%, 48.3%) contrary to below average candidates (between 83.3% and 83.4%). The LR-ANN_PSO model gives the best classification rate. These findings suggest that the variables identified by the LR statistical models provide more insights into a candidate's job performance.

Table 4: Results

Model	**LR-ANN**	**LR-ANN _PSO**	**DA-ANN**	**DA-ANN**
Accuracy	72.5%	75.0%	65.0%	65.4%
Precision	70.1%	72.9%	47.5%	48.3%
Sensitivity	73.1%	75.6%	74.9%	75.1%
Specificity	72.0%	74.5%	60.3%	60.6%
F-measure	71.6%	74.2%	58.1%	58.8%
BA	74.9%	77.0%	83.4%	83,3%
Good	70.1%	72.9%	47.5%	48.3%

7 Conclusion

In this research, we have implemented a hybrid discriminant neural network relying on particle swarm optimisation and statistical variables selection techniques. The models developed takes into account the variables mostly used in the manuel performance job prediction, otherwise, the constraints of missing values was fixed by the K-nearest neighbor algorithm.

The proposed methodology of variables selection evaluated the impact of different variables selection models by comparing Multivariate Discriminant Analysis and Logistic Regression. The findings demonstrate that logistic regression perform exceptionally well as a variables selection model for Artificial Neural Networks (ANN) to distinguish between candidates job performance. Moreover, the application of the variables chosen by this technique gives the best performance for the task of prediction the candidate job performance prediction.

The hybrid neural network applied with the learning algorithm PSO gives the best results in term of optimisation and finding the local minima and then in the prediction of the job performance. This model will be very useful for recruiter to assess and predict the performance of future candidates.

References

[1] S. S. A. Mohan, Support Vector Machines for Job Performance Prediction: A Comparative Study, Ph.D. thesis, 2021.

[2] J. Zhang, Y. Liu, The Use of Big Data Analytics in Job Performance Prediction: A Literature Review, Ph.D. thesis, 2020.

[3] S. Kaur, M. Singh., "A Review of Machine Learning Algorithms for Job Performance Prediction," 2019.

[4] J. Delaney, The rise of predictive employee analytics, Ph.D. thesis, 2019.

[5] S. Krishnan, Predictive employee analytics: A new frontier in HR. Forbes., Ph.D. thesis, 2020.

[6] D. L. . C. J.Russell, Employee analytics: How to improve business performance by measuring and managing your workforce., Ph.D. thesis, 2015.

[7] H. . Y.Zhang, A review of predictive analytics in human resources management., Ph.D. thesis, 2018.

[8] J. Han, M. Kamber, Data Mining: Concepts and Techniques, Ph.D. thesis, 2006.

[9] K. K. Y. Geoffrey K.F. Tso, "Predicting electricity energy consumption: A comparison of regression analysis, decision tree and neural networks," Energy, **32**, 1761–1768, 2007, doi:doi.org/10.1016/j.energy.2006.11.010.

[10] E. D. et P. Naïm, Des réseaux de Neurones, EYROLLES, 1992.

[11] F. Rosenblatt, "The perceptron: a probabilistic model for information storage and organization in the brain." Journal of Applied Mathematics and Physics, **5**, 1958, doi:doi.org/10.1037/h0042519.

[12] J. L. M. David E. Rumelhart, "Parallel distributed processing: explorations in the microstructure of cognition, vol. 1 : foundations," The MIT Press, **9**, 386–408, 1987.

[13] Y.-C. L. Jae H. Min a, "Bankruptcy prediction using support vector machine with optimal choice of kernel function parameters," Expert Systems with Applications, **28**, 603–614, 2005, doi:doi.org/10.1016/j.eswa.2004.12.008.

[14] D. T. L. et C. D. Laros, Discovering Knowledge in Data: An Introduction to Data Mining, Second Edition, WILEY, 2014.

[15] J. K. R. Eberhart, "A new optimizer using particle swarm theory," MHS'95. Proceedings of the Sixth International Symposium on Micro Machine and Human Science, doi:10.1109/MHS.1995.494215.

[16] S. A. Fatima Zahra Azayite, "Topology design of bankruptcy prediction neural networks using Particle swarm optimization and backpropagation," 1–6, 2018, doi:https://doi.org/10.1145/3230905.3230951.

[17] "Archives ourvertes," 2018.

[18] "cyberleninka," 2018.

Advances in Science, Technology and Engineering Systems Journal Vol. 8, No. 2, 123-129 (2023)

www.astesj.com

Special Issue on Computing, Engineering and Multidisciplinary Sciences

ASTESJ

ISSN: 2415-6698

Assessment of Scattered-Bend Loss in Polymer Optical Fiber (POF) Displacement Sensor

Latifah Sarah Supian*[,1], Danial Haikal Mohd Razali[1], Chew Sue Ping[1], Nurul Sheeda Suhaimi[1], Sharifah Aishah Syed Ali[2], Nani Fadzlina Naim[3], Harry Ramza[4]

[1]*Department of Electrical and Electronics Engineering, Faculty of Engineering, National Defence University of Malaysia, Kuala Lumpur, 57000, Malaysia*

[2]*Faculty of Defense Science and Technology, National Defence University of Malaysia, Kuala Lumpur, 57000, Malaysia*

[3]*School of Engineering, College of Engineering, UiTM, Shah Alam, 40450, Malaysia*

[4]*Department of Electrical Engineering, Faculty of Industrial Technology and Informatics, Universitas Muhammadiyah Prof. Dr. HAMKA, Jakarta, 13420, Indonesia*

ARTICLE INFO

Article history:
Received: 09 January, 2023
Accepted: 30 March, 2023
Online: 28 April, 2023

Keywords:
Bending loss
Coupling effect
Displacement
Optical sensor
Polymer optical fiber
Scattering loss

ABSTRACT

This work investigated the coupling behavior of the scattered-bend loss in displacement sensor during the bending of the fiber by using a multimode polymer optical fiber (POF). To utilize the scattered-bend effect for displacement measurement, a side coupling technique can be used by twisting a pair of POF fibers and bent the structure into a loop. The working principle of the sensor is quite simple. The bent radius grows smaller as the fiber draughts which simulate a change of displacement. The scattered-bend loss increases as the illuminating fiber is bent in decreasing angle and the light being coupled to the receiving fiber. The fabricated sensor is tested based on static measurement analysis and the sensor is characterized by its sensitivity, resolution, linearity, and repeatability error. From the experiment, the fabricated sensor has a range of roughly 160 mm with a sensitivity of 0.817 nW/mm, a resolution of 1.228 mm, and a repeatability error of 1.856 %. The sensor exhibits high linearity from 0 mm to 80 mm. The sensor's design structure and analysis are simple, comprehensive, and cost-effective, with potential benefits in industrial applications.

1. Introduction

An optical fiber is a data transmission medium that uses lightwave propagation in conjunction with a fiber that is often constructed of glass or plastic. Optical fiber is mostly used in the application of high-speed and long communication. Various features of light behavior in optical fiber have been researched through time, including bend-loss studies which this work is based on and this paper is an extension of work originally presented in 2022 IEEE 9th International Conference of Photonics[1] among others [2], light propagation [3], coupled-mode theory [4] and scattering [5]. Until now, researchers have been attempting to explain many occurrences and properties in various types of optical fiber.

In sensing applications, most of the sensors can sense a variety of parameters such as temperature [6], pressure [7], displacement [8], biomedical [9], food quality [10,11] and chemical [12]. Many fibers have been used in the application of sensors such as glass optical fiber [13], polymer optical fiber, Fiber Bragg Grating [14], etc. In comparison to other fibers, POF is inexpensive, flexible [15] and is well known for its high reliability in short-distance communication and sensing applications. POF is widely recognized for its physical toughness, which can withstand the huge physical strain, as well as its low weight when compared to silica-based fiber, which is much more delicate and fragile due to the incredibly thin glass fiber it contains [16]. POFs are also immune to electromagnetic interference and have multiplexing capabilities [17].

---

*Corresponding Author: L.S. Supian, Faculty of Engineering, NDUM, +60129266933, cawa711@gmail.com/ sarah@upnm.edu.my

https://dx.doi.org/10.25046/aj080214

1.1. Common Techniques

Researchers had offered many techniques to obtain a high-performance sensor with a simple structure and low-cost manufacture in Polymer Optical Fiber (POF) sensor applications [18]. Among the techniques proposed by researchers are long-period gratings [19], nonlinear effects [20], surface plasmon resonance [21] and fiber bragg gratings [22]. An intensity-based technique has addressed a high-performance, simple, and a low-cost sensor for various detections based on the approaches indicated above since it does not require specific equipment [23]. A sensor that uses light intensity as the measurement detecting technique is known as an intensity-based sensor [24]. The common sensor that uses an intensity-based sensor is a pressure sensor, temperature sensor, turbidity sensor, and displacement sensor. In terms of displacement measurement sensors, various methods have been proposed. Most of the methods are able to detect static, dynamic, and plane-in-out measurement analysis.

Diffraction grating technique [25] has achieved a 4 mm to 14 mm range of the best linearity for displacement range, however, it has a complicated design setup and complicated analysis, and the range is very small. The technique is found to be complicated because it requires a specific angle cut or called a diffraction angle at the end of the illuminating fiber which can cause a loss if the cut not clean enough. The analysis of this method is also difficult to determine the diffraction order its need to obtain the LED light wavelength, light cone angle, the period of the diffraction grating, and diffraction angle of the illuminating fiber.

This works integrated the principle of macro-bend loss and scattering loss to realize the fabricated sensor. The works studied and investigated the right tapered depth, bending angle and turns in order to optimize the results.

1.2. Macro-bend and Scattering Loss

The displacement sensor described in this research is based on the coupling of scattered-bend loss where to determine the scattering loss in POF, two fibers were twisted together. The first fiber is acting as illuminating fiber, while the second fiber couples scattered-bend radiation loss using the side coupling approach [26]. Fiber loss increases as a result of bending, as does coupling power. Based on this technique, the power coupling structure is employed for the displacement measurement sensor. The power coupling was visualized by measuring the outputs and calculate the coupling ratio at each bend diameter.

In optical application, there are a few detected types of losses in light transmission which are bend loss, dispersion loss, scattering and attenuation loss [27]. A bending loss is a loss that occurred due to the physical pressure where bending is applied to the optical fiber strand. There are two types of bending losses which are macroscopic bending and microscopic bending [28]. When the light source propagates, the power gets transferred into other modes, so the changing of the mode due to different refraction index due to bending makes the power leaked where the power will not continue to propagate in the fiber core, which the radiated light is known as scattering loss. This loss is caused by the material compositional fluctuation, density of the material, and manufacturing defects of the fiber [29]. Due to the bending of the fiber and density fluctuation in the core of the fiber, the loss is called scattered-bend loss.

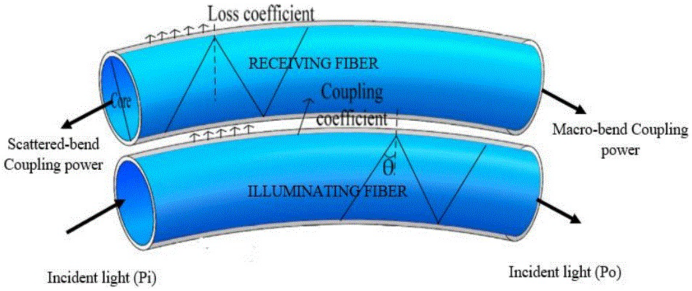

Figure 1: Coupled macro-bend and scattered-bend illustration.

In this method, the coupled scattered-bend loss has generated a polynomial to exponential-like curve while the macro-bend is producing an exponential curve [30]. This is caused by the power of the macro-bend being reflected at back-end of the receiving fiber. In general, due to the bending of fiber, consequently, there are two losses increase which are the macro-bend loss and scattered-bend loss. The macro-bend loss is propagating in the same direction as the light while a scattered-bend loss propagates in opposite direction toward the back-end of the receiving fiber. This can be illustrated in Figure 1.

To utilize the scattered-bend loss in the sensor application in this research, a polymer optical fiber, POF from ESKA Mitsubishi SK-40 bare multimode is used due to its durability and flexibility to the tightest bend and has a larger core which is 0.98 mm. To observe the relationship of the scattered-bend and macro-bend based on the changing of the bend radius, the coupling power received at both ends of the receiving fiber is measured and the ratio with respect to the LED input power can be calculated as:

$$C_s = \frac{P_2}{P_i}\% \quad (1)$$

$$C_m = \frac{P_1}{P_i}\% \quad (2)$$

Where C_s is the coupling ratio of scattered-bend, P_2 is the received power at the back-end of the fiber, C_m is the coupling ratio of macro-bend, P_1 is the received power at forward-end of the fiber and P_i is the input power of the light source.

2. Experimental Design and Setup

Based on the coupling ratio of both macro-bend and scattered-bend equations, it can be observed that with the increases of bend-diameter, the power received at both back-end and forward-end is increasing. In this research, variation of the received power and bending diameter testing parameters are applied in displacement detection. The design of the sensor structure is shown in Figure 2 setup.

In the proposed structure, only a single light source as input is required for the illuminating fiber. The LED used is from Advanced Fiber Solutions, OS417N with an operating wavelength of 650 nm and output power measured, 6.475 mW. The power meter used is also from Advanced Fiber Solution, OM110N for detection of the received fiber at the back-end and forward-end of the receiving fiber. The power meter is set to 650 nm for calibration and the resolution of 1 mW or 0.01 dB.

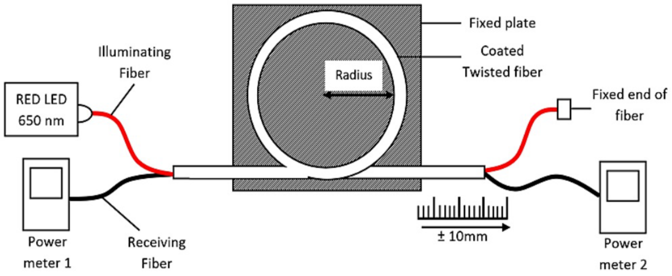

Figure 2: POF displacement sensor design structure.

For the main sensing part, a pair of twisted polymer optical fiber of SK-40 Bare Multimode POF is used and the fiber is coated with a black tube where in this experiment a black electrical shrink tube is used. The first fiber is connected to an LED source as an illuminating fiber. The second fiber is connected with a power meter to measure the received power both back-end and forward-end as receiving fiber. To test the sensor, the twisted fiber is bent to an initial 100 mm of bend radius, and adhesive tape is used to put the fiber at a fixed acrylic plate. The sensor is analyzed by using static measurement analysis with multiple variations of initial bend diameter.

During the experiment, the twisted fiber is manually pulled up to 100 mm for initial set loop with the changing of decreasing 10 mm displacement at each time. Each of the measurements is taken for both ends for scattered-bend and forward-end for macro-bend. From the result obtained, the losses of the light can be observed by the study of the graph of the received power. The tests are repeated three times to measure the repeatability of the reading for both the back-end and forward-end. The step will be repeated with setup loop of 80 mm and 60 mm loop. At the end of the experiment, the best result among the set loop of the sensor is characterized for the sensor parameter. The characterization of the sensor is based on performance parameters of resolution, sensitivity, repeatability error, and linearity of the reading and the obtained characteristic is compared with another studies.

3. Experimental Results

3.1 Coupling Power Ratio

Before the fabrication of the sensor, the coupling power response is studied and the result is being used as the reference element and for the verification of the sensor. Based on the coupling power ratio curve in Figure 3 and Figure 4, both losses in receiving fiber increase along with the decreasing bent diameter. This happened due to the increases of both losses in the illuminating fiber where with the side coupling effect, the light propagated from the illuminating fiber is radiated based on the evanescent wave theorem to receiving fiber. Most of the radiated power propagates parallel with the source but some of the power is refracted toward the back-end of the receiving fiber which is known as scattered-bend coupling power. When the fiber loop is pulled, the bend diameter is decreasing which causes the variation of coupling power.

Based on Table 1, the losses of the light in receiving fiber are decreasing at the forward end of the fiber from -44.06 dBm at 100 mm to -32.15 dBm at 20 mm. This also same goes to the power received at the back-end where the light losses also show a significant decrease from -51.50 dBm at 100 mm to -41.81 dBm at 20 mm. From observed Table 1, it is used for the displacement sensing and as guidance or reference to validate the sensor.

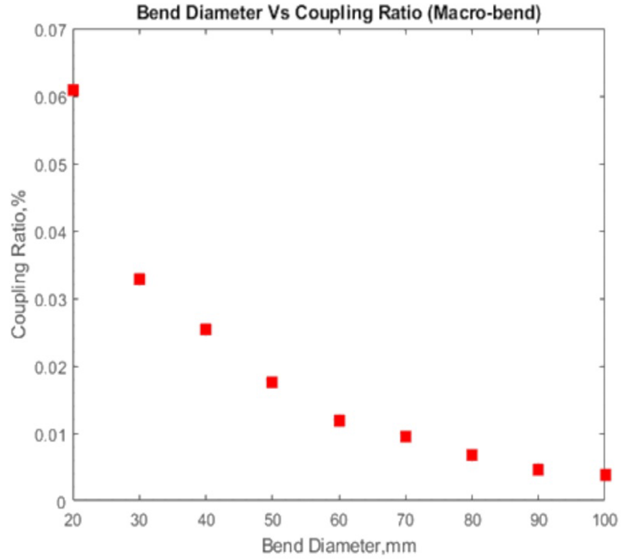

Figure 3: Macro-bend coupling power ratio.

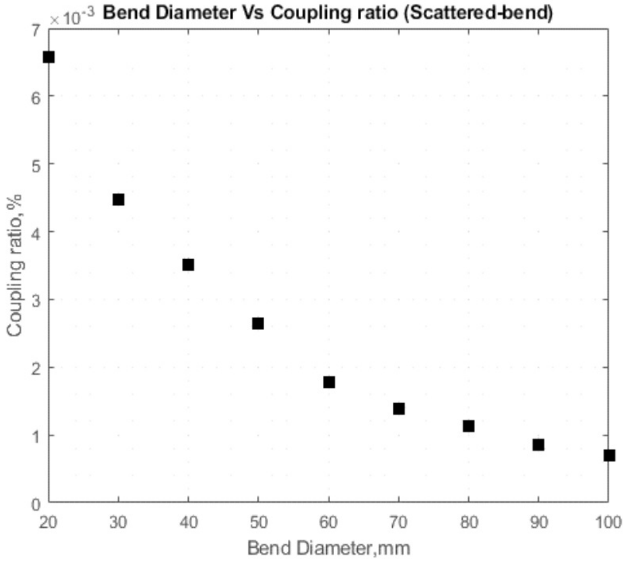

Figure 4: Scattered-bend coupling power ratio.

Table 1: Power losses from the reference power output.

	Power Received (dBm)		Total Power (dBm)	
Diameter (mm)	Macro-bend	Scattered-bend	Macro-bend	Scattered-bend
100	-35.95	-43.39	-44.06	-51.50
90	-35.18	-42.56	-43.29	-50.67
80	-33.60	-41.34	-41.71	-49.45

70	-32.08	-40.49	-40.19	-48.60
60	-31.16	-39.37	-39.27	-47.48
50	-29.46	-37.64	-37.57	-45.75
40	-27.85	-36.42	-35.96	-44.53
30	-26.72	-35.38	-34.83	-43.49
20	-24.04	-33.70	-32.15	-41.81

3.2 Displacement Sensing Test

Figure 5 shows the initial bending diameter of the twisted bend part at 100 mm, 80 mm, and 60 mm used in the sensor structure. The bending diameter of the structure decreased in 10 mm at each test which increases the coupled power received at receiving fiber.

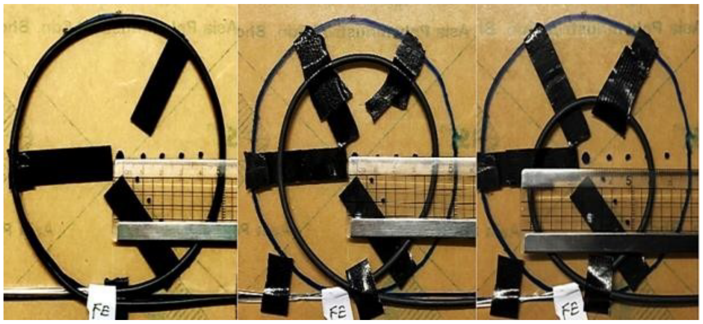

(a) (b) (c)

Figure 5: Initial bending diameter of sensor structure for (a) 100 mm, (b) 80 mm and (c) 60 mm

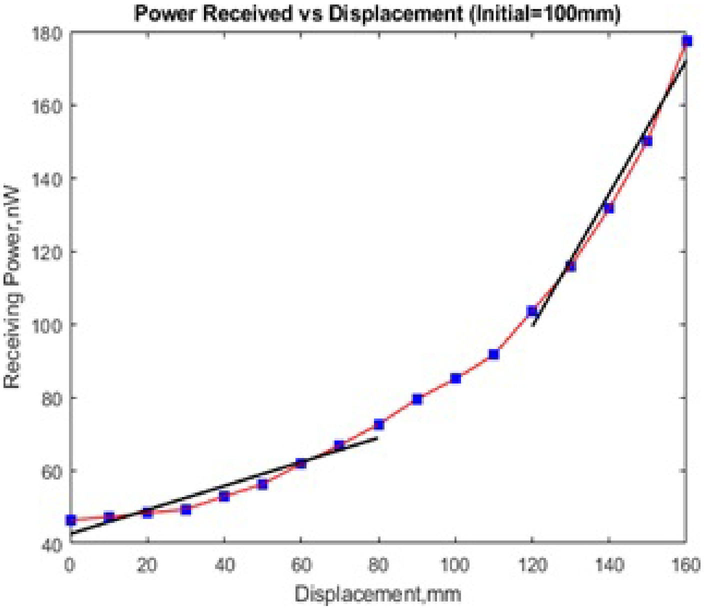

Figure 6: Received power at back-end of receiving fiber (Scattered-Bend coupling power).

Figure 6 showing the power received for the initial 100 mm bend diameter. It clearly shows that when the fiber is dragged 10 mm in each reading, the power received also increases. For macro-bend coupling power, it is producing an exponential curve relation as shown in Figure 7. From the experiment, both losses have producing good repeatability.

The step of the experiment is repeated by changing the loop bend diameter to 80 mm then 60 mm. As for a structure with an initial loop bend diameter of 100 mm, the smallest bend diameter at 160 mm displacement length is 50 mm. While the smallest diameter for initial loop bend of 80 mm is 30 mm at 160 mm displacement length, the smallest diameter for initial loop of 60 mm is 20 mm at 150 mm displacement length.

The result obtained can be verified by comparing the value of the power received of the tested sensor with the coupling power ratio graph.

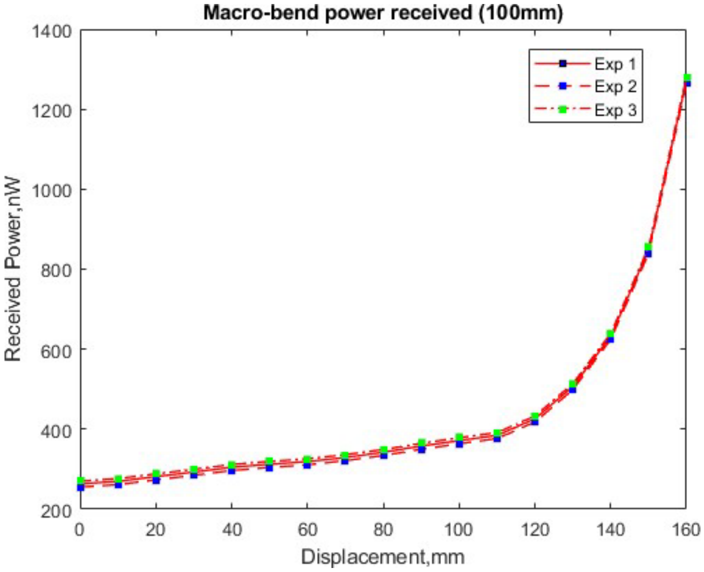

Figure 7: Macro-bend coupling received power at forward-end of receiving fiber.

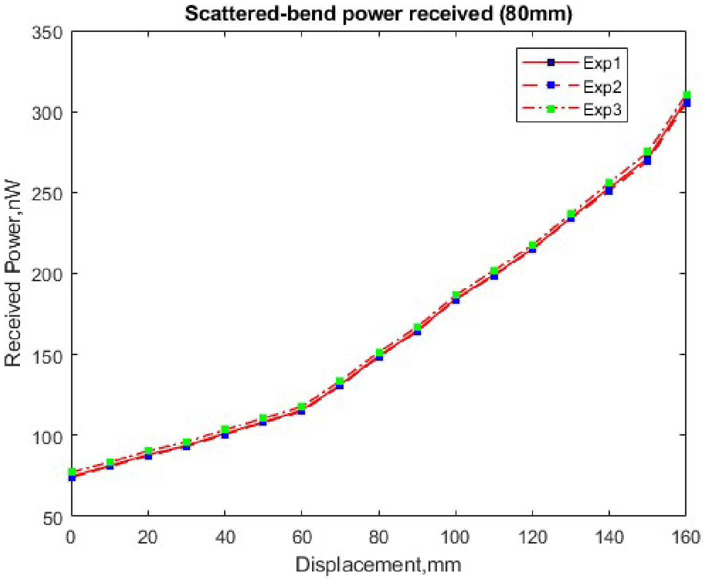

Figure 8: Scattered-bend coupling received power at forward-end of receiving fiber of 80 mm structure.

The power received should be in the range between the initial diameter and smallest diameter based on the coupling power ratio as shown in Figure 3 and Figure 4. The structure with 80 mm and 60 mm initial bend loop also shows a huge power gap between the changes of bend diameter for scattered-bend losses. This is because the characteristic of both losses is polynomial to exponential-like relation as in Figure 8 to Figure 11. This is also due to the increases of both losses at illuminating fiber which then transferred to receiving fiber by side coupling effect.

As in Figure 8 and Figure 9, both graphs showing the increases of the coupled power of scattered-bend for initial bend loop of 60 mm and 80 mm. In terms of the differences between received power, the coupling power of the macro-bend is particularly high compared to scattered-bend for all bending structures as shown in Figure 10 and Figure 11. This phenomenon happened because the macro-bending loss is producing a much higher loss due to the stress of the fiber which makes the refraction angle inside the fiber core is changes and then the light is radiated out from the core to the cladding. Due to the macro-bend is mostly propagate parallel with the light source the power received at the forward-end of the receiving fiber is higher compared to the back-end.

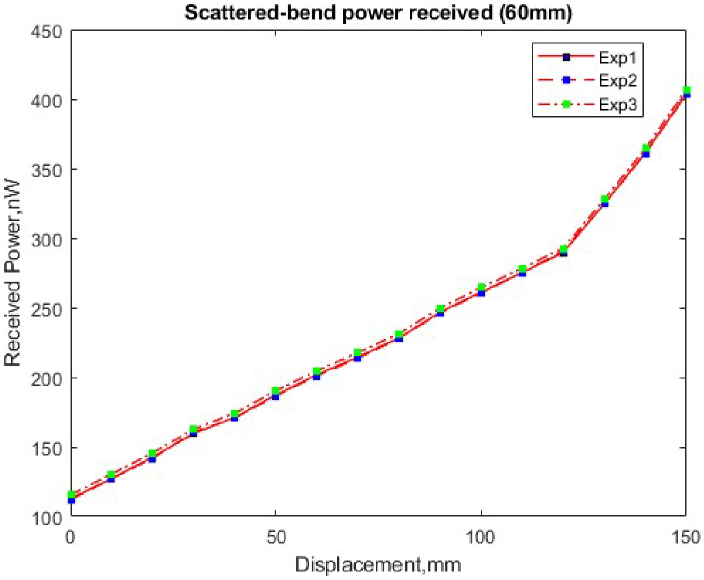

Figure 9: Scattered-bend coupling received power at forward-end of receiving fiber of 60 mm structure.

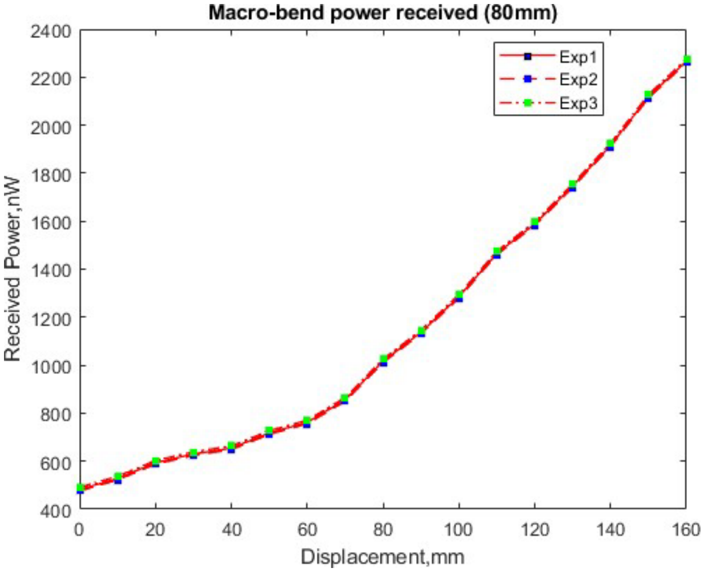

Figure 10: Macro-bend coupling received power at forward-end of receiving fiber of 80 mm structure.

While coupling power of scattering-bend loss is much lower because the scattering losses are considered a minor loss compared to macro-bend. This is because the scattering losses are caused by the density fluctuation and core defect which commonly ignore. Therefore, the coupled power of the scattered-bend in receiving fiber is very low.

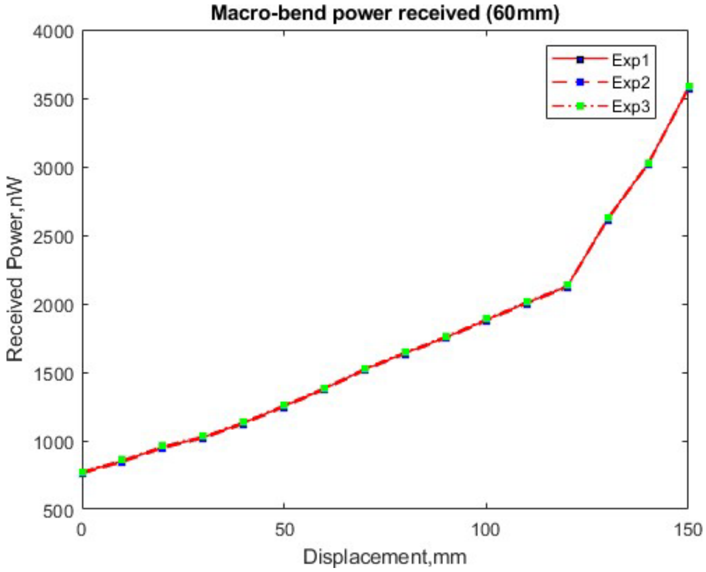

Figure 11: Macro-bend coupling received power at forward-end of receiving fiber of 60mm structure.

In comparison, the coupling power of scattered-bend loss is much stable, and the response showed by the scattered-bend loss coupling power towards the increases of displacement is much more suitable in displacement sensing application compared to macro-bend effect and characteristic of the proposed sensor has high reliability.

4. Sensor Characterization

The sensor characterization is a crucial part of sensing application. A sensor characterization is required to assess if the produced sensor is a good sensor [31]. In this experiment, the characterization parameters of the sensor that have been determined are sensitivity, linearity, resolution, and repeatability error as stated in Table 2. The characteristic will also be compared with other fiber-based displacement sensors in terms of the displacement range. The characterization is analyzed based on static measurement analysis. Based on the tested sensor, the best characteristic sensor is the structure that have an initial bend diameter of 100 mm, because the sensor is much more sensitive with the value of 0.817nW/mm, has a reasonable resolution value of 1.228 mm, and a small repeatability error of 1.858% compared to initial bend loop of 80 mm and 60 mm. Based on the comparison between techniques as in Table 3, the sensor proposed has one of the highest achieved displacement ranges which is up to 160 mm. If the tested sensor is compared with the linearity, the proposed sensor has good linearity at 0 mm to 80 mm and 120 mm to 160 mm where each linearity has a R^2 of 0.9182 and 0.9777. The sensitivity of the sensor is 0.817mW/mm which was calculated by using:

$$S = \frac{\Delta P_2}{\Delta d} \tag{3}$$

Where S is the sensitivity of the sensor, ΔP_2 is changes of received power at the back-end of the fiber, and Δd is changes of displacement. For the repeatability error, the sensor is tested three times at each test using the repeatability testing method where statistical mathematics is used by calculating the pooled standard deviation of the output.

Table 2: Fabricated sensor performance parameters.

Parameter	Measured Value	Reference Value
Range	0 mm – 160 mm	150mm -160mm
Sensitivity	0.817nW/mm	0.1nW/mm to 5nW/mm
Resolution	1.228mm	0.1mm to 1.5mm
Linearity	$y = 0.3282x + 42.55$ $R^2 = 0.9182$	$0.8 < R^2 \leq 1$
Repeatability Error	1.856%	2% to 1%

Table 3: Comparison between the technique in sensor structure.

Technique	Displacement Range
Twisted coupled macro-bend [32]	0mm – 140mm
Diffraction grating Ended [25]	4mm – 14mm
Dual-wavelength compensation [33]	0mm – 10mm
Twisted coupled scattered-bend	0mm – 160mm

5. Conclusions

In this research, a displacement measurement displacement sensor is designed by using a polymer optical fiber (POF) where the sensing part is utilizing the scattered-bend loss by side coupling method utilizing macro-bend effect. A scattered-bend loss is a combination of the scattering losses with the bending loss of the fiber where the losses are caused by density fluctuation and physical bending of the fiber. The measurement of the scattered-bend coupled power is measured at the back-end and the macro-bend coupled power at the forward-end of the receiving fiber. Most of the losses generated propagated parallel with the light source and some of the losses are refracted toward the back-end of the receiving fiber. This phenomenon explains the reason coupled power received at the forward-end of the receiving fiber is higher compared to the power received at the back-end of the fiber. The fabricated sensor can detect a measurement of displacement up to 160 mm with a sensitivity of 0.817 nW/mm, resolution of 1.228 mm, and repeatability error of 1.856%. The fabricated sensor also has a simple structure and analysis, low cost and easy to set up. The sensor also has a high potential advantages on the industrial application such as civil structuring, building surveyor, architecture, earth movement, landslides and medicine. The future works may include the utilization of IoT subsystem to be part of the system where the data collected can be analyzed beforehand and send to the users.

Conflict of Interest

The authors declare no conflict of interest.

Acknowledgment

This work would not have been possible without the financial and facility support of the Department of Electrical and Electronics Engineering, Faculty of Engineering, National Defence University of Malaysia.

References

[1] L.S. Supian, D.H.M. Razali, S.A. Syed Ali, "Investigation of Scattered-Bend Loss Coupling in Polymer Optical Fiber (POF) - Based Displacement Measurement Sensor," in 2022 IEEE 9th International Conference on Photonics (ICP), IEEE: 13–14, 2022, doi:10.1109/ICP53600.2022.9912445.

[2] A. Zendehnam, M. Mirzaei, A. Farashiani, L. Horabadi Farahani, "Investigation of bending loss in a single-mode optical fibre," Pramana, **74**(4), 591–603, 2010, doi:10.1007/s12043-010-0052-5.

[3] S. Addanki, I.S. Amiri, P. Yupapin, "Review of optical fibers-introduction and applications in fiber lasers," Results in Physics, **10**, 743–750, 2018, doi:10.1016/j.rinp.2018.07.028.

[4] A.W. Snyder, "Coupled-Mode Theory for Optical Fibers," Journal of the Optical Society of America, **62**(11), 1267, 1972, doi:10.1364/JOSA.62.001267.

[5] Z. Wang, H. Wu, X. Hu, N. Zhao, Q. Mo, G. Li, "Rayleigh scattering in few-mode optical fibers," Scientific Reports, **6**(1), 35844, 2016, doi:10.1038/srep35844.

[6] K. Tian, Y. Liu, Q. Wang, "Temperature-independent fiber Bragg grating strain sensor using bimetal cantilever," Optical Fiber Technology, **11**(4), 370–377, 2005, doi:10.1016/j.yofte.2005.03.001.

[7] W.J. Bock, J. Chen, P. Mikulic, T. Eftimov, "A Novel Fiber-Optic Tapered Long-Period Grating Sensor for Pressure Monitoring," IEEE Transactions on Instrumentation and Measurement, **56**(4), 1176–1180, 2007, doi:10.1109/TIM.2007.899904.

[8] G. Perrone, A. Vallan, "A Displacement Measurement System Based on Polymer Optical Fibers," in 2008 IEEE Instrumentation and Measurement Technology Conference, IEEE: 647–651, 2008, doi:10.1109/IMTC.2008.4547116.

[9] R. Correia, S. James, S.-W. Lee, S.P. Morgan, S. Korposh, "Biomedical application of optical fibre sensors," Journal of Optics, **20**(7), 073003, 2018, doi:10.1088/2040-8986/aac68d.

[10] N. Albakri, S. Abdullah, L.S. Supian, N. Arsad, S.D. Zan, A.A.A. Bakar, "Assessment of Palm Oil Fruit Bunch Maturity based on Diffuse Reflectance Spectroscopy Technique," in 2018 IEEE 7th International Conference on Photonics (ICP), IEEE: 1–3, 2018, doi:10.1109/ICP.2018.8533172.

[11] L.S. Supian, A.M.A. Amboalang, U.F.A. Rauf, K. Ismail, C.S. Ping, N.F. Naim, "Qualitative Assessment of Cooking Oil using Diffuse Reflectance Spectroscopy Technique," in 2022 International Conference on Green Energy, Computing and Sustainable Technology (GECOST), IEEE: 221–226, 2022, doi:10.1109/GECOST55694.2022.10010506.

[12] S. Thomas Lee, R. Dinesh Kumar, P. Suresh Kumar, P. Radhakrishnan, C.P.G. Vallabhan, V.P.N. Nampoori, "Long period gratings in multimode optical fibers: application in chemical sensing," Optics Communications, **224**(4–6), 237–241, 2003, doi:10.1016/S0030-4018(03)01597-9.

[13] A.B.L. RIBEIRO, J.L. SANTOS, J.M. BAPTISTA, L.A. FERREIRA, F.M. ARAÚJO, A.P. LEITE, "Optical Fiber Sensor Technology in Portugal," Fiber and Integrated Optics, **24**(3–4), 171–199, 2005, doi:10.1080/01468030590922722.

[14] W. Du, X.M. Tao, H.Y. Tam, C.L. Choy, "Fundamentals and applications of optical fiber Bragg grating sensors to textile structural composites," Composite Structures, **42**(3), 217–229, 1998, doi:10.1016/S0263-8223(98)00045-2.

[15] Y. Koike, T. Ishigure, M. Sato, E. Nihei, "Polymer optical fibers," in 1998 IEEE/LEOS Summer Topical Meeting. Digest. Broadband Optical Networks and Technologies: An Emerging Reality. Optical MEMS. Smart Pixels. Organic Optics and Optoelectronics (Cat. No.98TH8369), IEEE: III/13-III/14, doi:10.1109/LEOSST.1998.690041.

[16] L. Bilro, N. Alberto, J.L. Pinto, R. Nogueira, "Optical Sensors Based on Plastic Fibers," Sensors, **12**(9), 12184–12207, 2012, doi:10.3390/s120912184.

[17] W.E. van de Meent, EXPERIMENTAL DEMONSTRATION OF REDUCED BEND LOSSES IN LOW-CONTRAST POLYMER HYBRID WAVEGUIDES, 2015.

[18] D. Sartiano, S. Sales, "Low Cost Plastic Optical Fiber Pressure Sensor Embedded in Mattress for Vital Signal Monitoring," Sensors, **17**(12), 2900, 2017, doi:10.3390/s17122900.

[19] T. Eftimov, Sensor Applications of Fiber Bragg and Long Period Gratings, Springer Netherlands, Dordrecht: 1–23, doi:10.1007/978-1-4020-6952-9_1.

[20] K.O. Hill, B.S. Kawasaki, D.C. Johnson, Y. Fujii, Nonlinear Effects in Optical Fibers: Application to the Fabrication of Active and Passive Devices, Springer US, Boston, MA: 211–240, 1979, doi:10.1007/978-1-4684-3492-7_12.

[21] K. Kurihara, H. Ohkawa, Y. Iwasaki, O. Niwa, T. Tobita, K. Suzuki, "Fiber-optic conical microsensors for surface plasmon resonance using chemically etched single-mode fiber," Analytica Chimica Acta, **523**(2), 165–170, 2004, doi:10.1016/j.aca.2004.07.045.

[22] A.D. Kersey, T.A. Berkoff, W.W. Morey, "High-resolution fibre-grating based strain sensor with interferometric wavelength-shift detection," Electronics Letters, **28**(3), 236, 1992, doi:10.1049/el:19920146.

[23] D.S. Montero, C. Vázquez, "Polymer Optical Fiber Intensity-Based Sensor for Liquid-Level Measurements in Volumetric Flasks for Industrial Application," ISRN Sensor Networks, **2012**, 1–7, 2012, doi:10.5402/2012/618136.

[24] Polymer Optical Fiber-Based Sensors, EPFL Press: 365–408, 2011, doi:10.1201/b16404-14.

[25] M. Lomer, J. Zubía, J. Arrue, J.M.L. Higuera, "Principle of functioning of a self-compensated fibre-optical displacement sensor based on diffraction-grating-ended POF," Measurement Science and Technology, **15**(8), 1474–1478, 2004, doi:10.1088/0957-0233/15/8/007.

[26] L.S. Supian, M.S. Ab-Rahman, N. Arsad, "Polymer optical fiber tapering using chemical solvent and polishing," EPJ Web of Conferences, **162**, 01018, 2017, doi:10.1051/epjconf/201716201018.

[27] N. Uddin, M.R. M, S. Ali, "Performance Analysis of Different Loss Mechanisms in Optical Fiber Communication," Computer Applications: An International Journal, **2**(2), 1–13, 2015, doi:10.5121/caij.2015.2201.

[28] S. Savović, A. Djordjevich, I. Savović, "Theoretical investigation of bending loss in step-index plastic optical fibers," Optics Communications, **475**, 126200, 2020, doi:10.1016/j.optcom.2020.126200.

[29] C.-A. Bunge, R. Kruglov, H. Poisel, "Rayleigh and Mie scattering in polymer optical fibers," Journal of Lightwave Technology, **24**(8), 3137–3146, 2006, doi:10.1109/JLT.2006.878077.

[30] R.T. Schermer, J.H. Cole, "Improved Bend Loss Formula Verified for Optical Fiber by Simulation and Experiment," IEEE Journal of Quantum Electronics, **43**(10), 899–909, 2007, doi:10.1109/JQE.2007.903364.

[31] C.A.F. Marques, D.J. Webb, P. Andre, "Polymer optical fiber sensors in human life safety," Optical Fiber Technology, **36**, 144–154, 2017, doi:10.1016/j.yofte.2017.03.010.

[32] J. Liu, Y. Hou, H. Zhang, P. Jia, S. Su, G. Fang, W. Liu, J. Xiong, "A Wide-Range Displacement Sensor Based on Plastic Fiber Macro-Bend Coupling," Sensors, **17**(12), 196, 2017, doi:10.3390/s17010196.

[33] A. Vallan, M.L. Casalicchio, M. Olivero, G. Perrone, "Assessment of a Dual-Wavelength Compensation Technique for Displacement Sensors Using Plastic Optical Fibers," IEEE Transactions on Instrumentation and Measurement, **61**(5), 1377–1383, 2012, doi:10.1109/TIM.2011.2180975.

Advances in Science, Technology and Engineering Systems Journal Vol. 8, No. 2, 130-138 (2023)

www.astesj.com

Special Issue on Computing, Engineering and Multidisciplinary Sciences

ASTESJ

ISSN: 2415-6698

Detecting CTC Attack in IoMT Communications using Deep Learning Approach

Mario Cuomo, Federica Massimi, Francesco Benedetto*

Signal Processing for Telecommunications and Economics Lab., Roma Tre University, Rome, Italy

ARTICLE INFO

Article history:
Received: 28 December, 2022
Accepted: 05 April, 2023
Online: 28 April, 2023

Keywords:
Covert Timing Channel
TCP Protocol
Convolutional Neural Network
Siamese Neural Network
K-Nearest Neighbors
E-Health Security

ABSTRACT

Cyber security is based on different principles such as confidentiality and integrity of transmitted data. One of the main methods to send confidential messages is to use a shared secret to encrypt and decrypt them. Even if the amortized computational complexity of the hashing functions is O(1), there are several situations when it is not possible to use them due to the lack of computing power or the need to keep completely hidden the communication to other parties in the network. Covert Channels (CCs) are an excellent alternative in all these cases because they hide the private message in legitimate communication channels without the need to allocate additional resources to communicate. For this reason, they are difficult to identify because they are fully camouflaged in legitimate traffic. Unfortunately, CC technique is also used by hackers to exfiltrate network data and initiate cyber-attacks against devices in the system: Internet of Medical Things (IoMT) are one of the most vulnerable devices affected by this type of attack. It is therefore essential to create a system that can autonomously identify the presence of a malicious CCs to safeguard the health of patients. This paper describes an approach to create a Covert Timing Channel (CTC) based on TCP packets between client and server and how it is possible to detect the hidden communication using an innovative pipeline composed by several Machine Learning (ML) and Deep Learning (DL) models, such as Convolutional Neural Network (CNN), Siamese Neural Network (SNN) and K-Nearest Neighbors (K-NN). Considering 4 different message types exchanged in CTC, the proposed pipeline achieved 94% accuracy in identifying covert messages in the channel.

1. Introduction

In a world that is becoming increasingly and wirelessly connected, network security is now a critical task that must be seriously considered. It is necessary to avoid cybercriminals gaining illegal access to valuable data and sensitive information. It is important to note that the amount of data that devices produce, and the number of resources used, increase as more devices are connected. When an unauthorized user gets hold of data, he can cause several problems such as stolen assets, identity theft and reputational damage – not only to the individual but also to the entire network. A vulnerability can be described as a situation where a subject A (item, process or person) manages to exploit the privileges of a subject B to carry out operations not initially granted to him. Therefore, it is necessary to proactively manage risks, threats, and vulnerabilities.

Many studies have recently focused on Information Technology (IT) resilience. It describes the ability of a system to continue to deliver the expected results despite the occurrence of incidents, such as natural disasters and especially cyber-attacks.

In this scenario, Internet of Things (IoT) devices are particularly vulnerable to network attacks and the situation becomes extremely dangerous when we consider e-health devices. E-health data represents one of the most important personal information. It is important to design the system as confidential as possible, with high-level security policies. Even if various regulations for data management have been drafted over the years – such as the General Data Protection Regulation (GDPR, https://gdpr-info.eu/) – it is not uncommon to read news of improper exfiltration of data by unauthorized users: according to Protenus Breach Barometer, in 2022 there were 50M+ Patient records breached, 905 Incidents, 44% Increase in hacking incidents (https://www.protenus.com/breach-barometer-report).

---

*Corresponding Author: Francesco Benedetto, francesco.benedetto@uniroma3.it

https://dx.doi.org/10.25046/aj080215

The Internet of Medical Things (IoMT) [1] is that set of technologies aimed at using smart devices – connected to each other, even via the internet – in the medical field. If this technology guarantees an improvement in healthcare management, on the other hand new security challenges are expected: it is necessary to ensure correct authentication and authorization procedures (applying minimum privilege as much as possible), maintaining the confidentiality of data (both at rest and in transit, with encryption and obfuscation techniques) and integrity (making sure that the data is not modified by malicious users).

For obtain confidential communications, cryptography is used. It is a technique for encoding messages: symmetric encryption is based on sharing a shared secret; asymmetric cryptography is based on a pair of keys – public key and private key – used respectively to sign a message and to verify its integrity [2] . Given the low computing power, the encryption algorithms used in the IoMT are different from those used in servers, and they are classified into three categories: centralized (*i*), non-centralized (*ii*), low weight (*iii*) [3]. The centralized approach (*i*) uses a central node – often a server and not an IoT device – to encrypt the message. The sender sends the message in clear text over a secure channel to the centralized server which encrypts it and sends it over the potentially insecure channel to the receiver. The central node requires a lot of computing power, and it is a single point of failure (see Figure 1).

In the decentralized approach (*ii*) the encryption is distributed on the various link-by-link nodes: one node receives the encrypted message, decrypts it, re-encrypts it and transmits it to the next node. There is additional encryption level between end systems (see Figure 2).

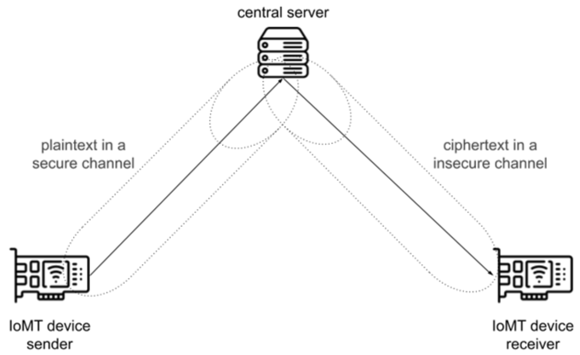

Figure 1: Centralized approach in IoMT cryptography

To minimize the effort of the devices, over the years various approaches have been proposed which are based on symmetric encryption in which each network node authenticates the others [4]. These algorithms belong to the low weight security approach (*iii*).

Obfuscation techniques, in accordance with the principles of least privilege, aim to make data inaccessible when it is not needed. Unlike encryption algorithms that use a key, to understand the plaintext you only need to know the algorithm for generating the obfuscated data [5]. More sophisticated techniques allow to completely anonymize the data, no longer allowing the re-identification of the data after anonymization [6].

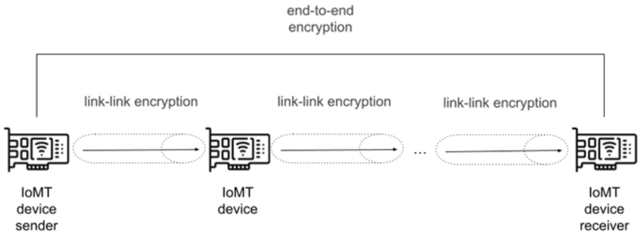

Figure 2: Decentralized approach in IoMT cryptography

The techniques and attacks used by hackers to compromise a system have become increasingly sophisticated so that human observation is less and less useful in identifying a compromise.

It is precisely here that Machine Learning (ML) in cybersecurity comes into play: in fact, the use of ML lends itself greatly to solving this type of problem. The systems can analyze patterns and learn from them to help prevent similar attacks and respond to behavior change. Generalization is the capacity of an ML model to fit correctly to additional, previously unobserved data taken from the same distribution as the model's original data. Because ML can learn from past data, it can recognize odd communications and user behaviors. As a result, it is possible to prevent threats and respond to active attacks in real time, not only reducing the amount of time spent on routine tasks but also allowing us to use the network's resources more strategically.

Artificial Intelligence (AI) approaches are widely used in healthcare: to preserve the privacy of health data from access by unauthorized users, several frameworks have been proposed for analyzing user behavior in a secure environment. Behavioral anomalies – such as unusual login and actions – are flagged by the system as suspicious and blocked [7]. Several vendors – e.g., Microsoft and Google – have implemented these security systems called Security Information and Event Management (SIEM). They are capable of monitoring and identify possible vulnerabilities and acting to mitigate them. Each SIEM is always composed of at least three main modules which are data collection (*i*), learning the normal flow without malicious actions (*ii*) and generating the classification report (*iii*) [8].

Over the years SIEM's training baseline has evolved, moving from using legacy Machine Learning models (e.g., Support Vector Machine, Decision Tree, K-NN [9]) to using Deep Learning (DL) models [10]: researchers have proposed systems running MLP-based Neural Networks [11], DNNs with optimization techniques (Principal Component Analysis and Gray Wolf Optimization) [12], Convolutional Neural Networks with Long Short-Term Memory [13].

Cyberattacks from malicious users are increasingly accurate and range across the entire ISO-OSI stack: Perception-level attacks can involve Denial of Service (DoD) of physical devices or RFID spoofing and cloning; Application layer attacks can create a Man in The Middle (active or passive) by sniffing network traffic by installing Malware or Medical information injections. At network level, attackers can invalidate DNS or ARP tables to redirect traffic to their destinations [14]. In this scenario, Covert Channels (CC) assume a great importance. Covert Channels are channels used to transmit information using existing system resources that were not designed to carry data. They make it possible not to show the communication taking place between two interlocutors in order not to alarm a third agent – potentially malicious and looking to exfiltrate data. The main characteristics of a CC are stealthies, low bandwidth and indistinguishability. Due to their ability to evade detection, they pose a serious threat to cyber security because attackers can use them for malicious scopes [15]. There are various types of Covert Channels: Covert Timing Channel (*i*), Covert Storage Channel (*ii*), Covert Behavioral Channel (*iii*). Covert Timing Channels (*i*) use a time measurement to signal the value to be sent on the channel; Covert Storage Channels (*ii*) encode information by hiding it in the fields of the network protocol used; Covert Behavioral Channels (*iii*) divide the hidden message to be sent and transmit it in smaller packets and generally using a lower-level protocol.

More recently, ML and statistical methods for detecting CTC attacks communications were presented such as temporal analysis (*i*), traffic analysis on the channel (*ii*), the observation of side channels (*iii*) and the study of entropy (*iv*).

In the temporal analysis (*i*), the computing times of the devices are analyzed to identify any anomalies: if the response time of a device varies abruptly, the presence of a CTC involving that device can be assumed. Unfortunately, this approach is subject to jitter: legitimate traffic on the channel stresses the devices and a false CTC alarm can be raised [16].

The traffic analysis on channel (*ii*) analyzes the traffic but takes into account factors like the frequency of packet sending, their volume, and occasionally even their content. By gathering the network traffic exchanged, a statistical model of the system is constructed in a secure environment, and from these the significant communication frequencies are discovered. The network traffic is evaluated in the detection phase, and the presence of a CTC can be suspected if there are several significant frequencies [17].

The execution of Covert Channels has unintended consequences for the systems; the variation of the side channels can be investigated (*iii*) to spot any network anomalies like CTC attacks. It is extremely challenging to isolate the various processes from one another in a system with highly interconnected components. A message exchange over unconventional channels is referred to as a CC when both the sender and the recipient are aware of it, and a SC when the message is sent by the sender involuntarily, such as through cache access, data movement between the CPU and memory, or the processor emitting electromagnetic waves. The identification of CCs by SC is still under study and there is no proof of its correctness [18].

The system's entropy can be affected by a CTC, and as a result, this measurement can offer helpful information for detection. Information Theory uses entropy as a metric to quantify the degree of disorder or uncertainty in a system. Entropy is a measure of how random and erratic messages are exchanged in the network about the problem of detecting a Covert Timing Channel. A legitimate communication system, as opposed to one that sends messages according to a set of rules and behaviors (such as the CTC-TR), is unpredictable and has a high degree of entropy. In [19], the authors demonstrate a method based on entropy (*iv*) using conditional entropy, which is an estimation of the system's entropy's value obtained from available data.

In recent years, ML models have been used in Covert Timing Channel identification systems: starting with network traffic that has been detected and then being cleaned up by removing unnecessary data, AI models are trained on the resulting data. KNN, SVM, and Naive Bayes are three of the most popular ML models [20].

With the aid of VGG-16 and Squeeze Net, the first instances of the application of DL approaches for the identification of CTCs and their validity can be seen [21].

In this paper, the hidden communication is embedded in the legitimate traffic by means of a CTC, obtained by modulating the inter-arrival packet delays. In practice, the malicious process modulates the inter-arrival delay of the transmitted e-health data, by transmitting one 0 bit (or 1 bit) when the delay is less (greater) than a pre-defined threshold. Here, we move one step further by proposing a type of CTC, based on the inter-arrival delays of TCP packets. In addition, we implement an ML and DL framework to detect what kind of message is transmitted on the channel in CTC (see Figure 3).

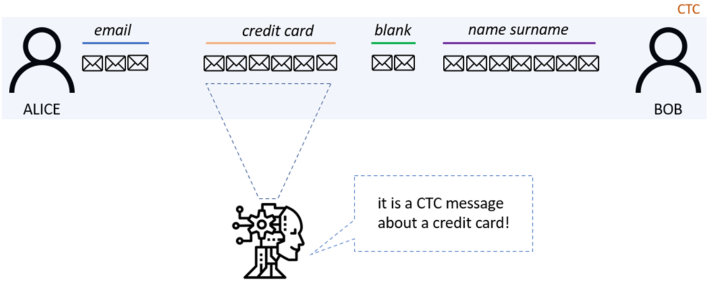

Figure 3: CTC scenario under consideration

The obtained results thus confirm the validity of such approach for ML and DL detection of hidden communications – the current State of Art in detecting CTCs is based on the analysis of the statistical variation of traffic on the network: as soon as this changes and exceeds a chosen threshold, an alert of a possible attack is sent; unfortunately this approach fails to detect highly stealthy traffic: a CTC uses the same throughput as the legitimate communication channel. For this reason, a DL model that can capture the insight hidden in the channel itself is needed.

The remainder of our work is organized as follows. Section 2 illustrates a Covert Timing Channel model and how the dataset of hidden communications is generated. Section 3 shows the ML and

DL methods used for the detection of illegitimate traffic, while Section 4 discusses the simulation results and shows the performance of the methods according to the main metrics used for evaluating the proposed pipeline.

2. Covert Timing Channel and Dataset Generation

For simplicity, we indicate two interlocutors as Alice and Bob. They establish a CTC communication. There is also a third user on the channel, Cindy, who is listening and has the aim of recovering the type of message that Alice and Bob are exchanging (see Figure 4). Let's consider Alice as a user with an active role in the communication: she is the only one who sends messages in the channel, while Bob is listening for them. It's not hard to think a real-life use case where an edge device sends messages to a central system hub to notify an event.

To understand how this channel works, it is necessary to start from a basic concept: what Alice sends on the channel is completely unrelated to what she is communicating. What's really related is how Alice is sending the message. As previously described, in a CTC the message is encoded in the packet interarrival time. We therefore distinguish between a covering message and a covered message: the first one is the message that Cindy recovers by sniffing the traffic, the second is the one that only Bob can reconstruct.

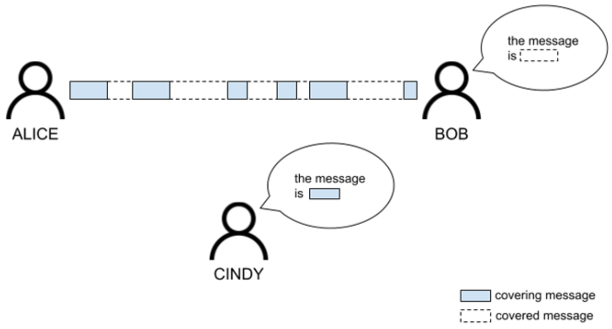

Figure 4: Scenario under consideration

Let's see how it is possible to encode the message that Alice wants to send using the packet interarrival times. Let x be the message to send. The first operation that Alice performs is the conversion of x into binary: each ASCII character can be represented using 7-bit sequence according to Table 1.

Table 1: Encoding ASCII to 7 bits string

	Leftmost three bits							
Righmost four bits	000	001	010	011	100	10 1	110	111
0000	NUL	DLE	Space	0	@	P	’	p
0001	SOH	DC1	!	1	A	Q	a	q
0010	STX	DC2	“	2	B	R	b	r
0011	ETX	DC3	#	3	C	S	c	s
0100	EOT	DC4	$	4	D	T	d	t
0101	ENQ	NAK	%	5	E	U	e	u
0110	ACK	SYN	&	6	F	V	f	v
0111	BEL	ETB	‘	7	G	W	g	w
1000	BS	CAN	(	8	H	X	h	x
1001	HT	EM	)	9	I	Y	i	y
1010	VF	SUB	*	:	J	Z	j	z
1011	VT	ESC	+	;	K	[	k	{
1100	FF	FS	,	<	L	\	l	|
1101	CR	GS	-	=	M	]	m	}
1110	SO	RS	.	>	N	^	n	~
1111	SI	US	/	?	O	_	o	DEL

Let $binaryx$ be the binary string representing x. Note that $binaryx$ will be 7 times the length of the initial string x. At this time $7|x|$ packets will be sent on the channel – one for each bit of $binaryx$. Each packet will be sent waiting a specifying time after the previous depending on whether we want to send a 0 bit or a 1 bit (e.g., 0 waiting 10 milliseconds, 1 waiting 50 milliseconds). It is necessary to have a specific packet to notify the beginning and the ending of the message.

The packets sent by Alice are simple TCP frame for communication at level 4 of the ISO-OSI stack and each of them contains a character of the covering message. It is obvious that the more the covering message makes sense, the less Cindy will be suspicious of the presence of a hidden communication between Alice and Bob.

$x =$ hello
$seed\_covert\_message =$ apple

$binaryx = 1101000\ 1100101\ 1101100\ 1101100\ 1101111$
$covert\_message$
$= appleappleappleappleappleappleappleapple$

Note that if the $seed\_covert\_message$ is shorter than the message to be sent, it must be repeated several times to cover completely it (see Figure 5).

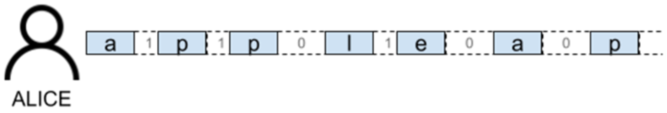

Figure 5: Example of CTC messaging packets

The use case we have considered is the one where an edge device notifies to a central hub several messages relating to events of 4 different kinds: the request to generate an access token for a user starting from the *email* or *name and surname*, checking the validity of a *credit card* or a *blank communication* used as heartbeat. For simplicity, both the edge device and the central hub are active on the same LAN by establishing a socket between them.

We created a dataset with 4 types of messages (see Table 2), developing the CTC described using python and sniffing communication using Wireshark.

Our analysis did not focus on internal packet analysis (known as Deep Packet Inspection) but rather we considered packet interarrival time as a classification vector. Considering the interarrival times of the packets we have created the representative spectrograms of the communications [22]. To produce the spectrograms, the packet interarrival times were collected and considered as sampling instants of a chirp signal. A chirp signal has the characteristic that its frequency varies - increasing or decreasing - over time. A linear increase was considered. The Short-Time Fourier Transform (STFT) was applied to the chirp signal, obtaining a matrix representation in which each column contains an estimate of the short-term frequency content located in the time of the signal itself. The matrix is the spectrogram of the communication encoded in RGB space. Each communication is therefore not represented by a flow of packets but by a single spectrogram which contains its characteristics (Figure 6).

Table 2. Number of instances for each class

MESSAGE CLASS	# INSTANCES
blank	500
credit_card	500
email	500
name_surname	500

The input for Deep Learning models described later will be images of the size $224 \times 224 \times 3$ and for our experiment we divided it in training set and test set with $1:4$ ratio.

Figure 6: Example of Spectrogram

3. Machine and Deep Learning Models

Over the years several Machine Learning models have been proposed for the classification task and some of them have been considered for our experiments.

We have implemented the following models.

- Random Forest (Figure 7)
- K-NN (see Figure 8)
- Convolutional Neural Network (Figure 9)
- Siamese Neural Network (Figure10)

The Random Forest (RF) model is based on the construction of several Decision Trees (DT) – other classification models - and the final output is obtained by combining the outputs of the individual DTs by applying the majority vote approach. A DT is a tree whose internal nodes represent feature splits, and the leaves represent classes. The idea is to traverse the tree from the root and based by values of the instance to classify and the node splits arrive on a leaf node and assign the corresponding class. To decide how to create the tree – such as which feature use at which level – are used different criteria such as entropy, information gain and Gini index.

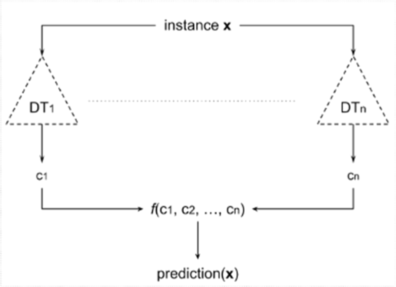

Figure 7: Schema of Random Forest model

To better understand how K-NN works it is necessary to introduce the Nearest Neighbour (NN). The idea of the NN is very simple: 2 instances of the same class are very similar to each other. Similarity can be calculated as the distance – consider the Euclidean distance – between the vectorial representations of the two instances. To classify an input, therefore, it is sufficient to retrieve the item closest to it and assign it the same class. KNN retrieves the K closest items and assigns to the input the class that has majority votes.

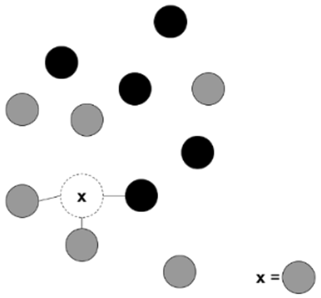

Figure 8: Example of K-NN prediction

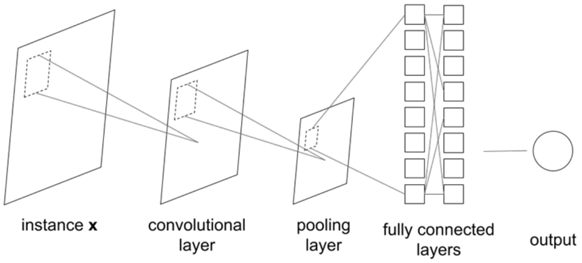

Figure 9: General schema of a CNN

A Convolutional Neural Network is a particular type of artificial neural network (ANN) widely used for many visual tasks such as image recognition, object classification and pattern recognition. It is composed in sequence of – at least – three types of layers: Convolution Layer (or Kernel), Pooling Layer and Fully Connected Layer. In the Convolutional Layer the image (a matrix of pixels) is input and a smaller matrix than the starting one is output. The output matrix is obtained by sliding an activation map over the input matrix and applying the dot product between it and the selected portion of the image. The goal of the pooling layer is to reduce the spatial dimension of the representation by extracting the dominant features. In the Fully connected layer, we try to learn non-linear combinations of the characteristics of the representation obtained. The Fully Connected level is trying to learn the nonlinear function that connects input to output.

A Convolutional Siamese Network [23] has two images as input and returns the similarity between them. Internally it is composed of two – or more – CNN that share the same weights. When classifying an image with a convolutional network the last layer is almost always a layer with a SoftMax function: we obtain a vector of k elements, and k[i] contains the probability of confidentiality in assigning class i to the image of inputs.

In a Siamese Network the last layer is eliminated, and another one is added to calculate the difference between the two representations. The last level is a single neuron with a sigmoid activation function (0 to 1).

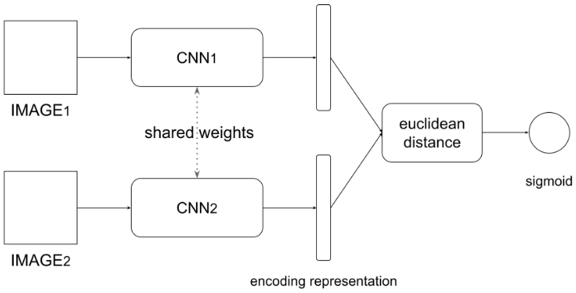

Figure 10: Siamese Network using CNNs

4. Results

To evaluate the performance of the system, some of the metrics mainly considered were used: Precision, Recall, F1-Score, Accuracy and Specificity, that are calculated using True (T) or False (F) Positive (P) or Negative (N). A correctly classified instance is a True Positive; a misclassified instance can be a False Negative or a False Positive. Considering the *credit_card* class as Positive class: a spectrogram of a credit card is a True Positive if the system assigns it the *credit_card* class; a spectrogram of a name and surname is a False Positive if the system assigns it the *credit_card* class; a credit card spectrogram is a False Negative if the system does not assign it the *credit_card* class. These values can be obtained by considering the confusion matrix in Table 3.

Table 3: Confusion Matrix of a binary classification

	Really positive	Really negative
Positive predicted	TP	FP
Negative predicted	FN	TN

Precision – as the name suggests – describes how accurate the system is in identifying true positives. If the system has high precision, it means that it is rarely wrong in identifying class of spectrogram: when the system claims the spectrogram is about email information, that is it.

$$\mathrm{Precision} = \frac{\mathrm{TP}}{\mathrm{TP} + \mathrm{FP}}$$

Recall indicates the ratio of positive instances that are identified by the system. If the system has high recall about *credit_card* messages, it means that almost all instances about this type of communication have been identified.

$$\mathrm{Recall} = \frac{\mathrm{TP}}{\mathrm{TP} + \mathrm{FN}}$$

F1-Score combines precision and recall into a single metric. This metric is the harmonic mean between the two.

$$\mathrm{F1} - \mathrm{Score} = \frac{\mathrm{TP}}{\mathrm{TP} + \frac{\mathrm{FN} + \mathrm{FP}}{2}}$$

Accuracy indicates how close a predicted value is to the actual one: informally, it is the fraction of predictions that are accurate.

$$\mathrm{Accuracy} = \frac{\mathrm{TP} + \mathrm{TN}}{\mathrm{TP} + \mathrm{TN} + \mathrm{FP} + \mathrm{FN}}$$

Specificity measures the proportion of true negatives and indicates the proportion of truly negative instances that are correctly identified. High specificity means that the model is correctly identifying most negative instances.

$$Specificity = \frac{TN}{FP + TN}$$

Using the elbow method, it was possible to identify the optimal value of K in the KNN algorithm. A similar method was applied to understand the maximum depth value (MD) of the decision trees constructed for the Random Forest model.

The best performances were achieved considering the application of an ensemble learning technique called Stacking (STC): the idea is to build a meta-classifier that learns from the classifications of the individual classifiers using a personal weight matrix. The meta classifier uses Logistic Regression [24].

The Convolutional Neural Network was built with a single convolutional layer inside it. The input of size $224 \times 224 \times 3$ first crosses the convolutional layer characterized by 16 feature maps of size 3×3. The new matrix is then computed by the MaxPooling layer characterized by matrices of size 2×2. To minimize overfitting a Dropout layer is then applied with a percentage of 20% - at each passage of the training data some random nodes are chosen, and they don't update their weights both in forward and backpropagation. The last layers are composed by a full Dense layer of 128 units which is converted to one of length 4 by the Softmax. Using this configuration, the following performances were achieved (see Figure 11).

The confusion matrix shows how generally the accuracy is high for all classes and there is no evidence of the imbalance between them. It is important to note the misclassification among *credit_card* and *name_surname* classes (see Figure 12).

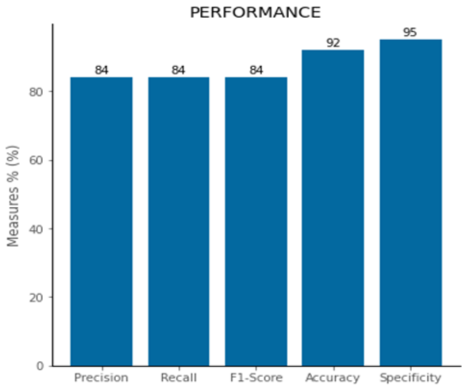

Figure 11: Performance of described CNN

Figure 12: Confusion Matrix of described CNN

Even if the performance of the Neural Network is slightly lower than the application of ensemble techniques, it is very robust to noise. Due to the construction of the Covert Timing Channel and the dataset, the communications are noise-free: we have applied Gaussian noise to the images (see Figure 13).

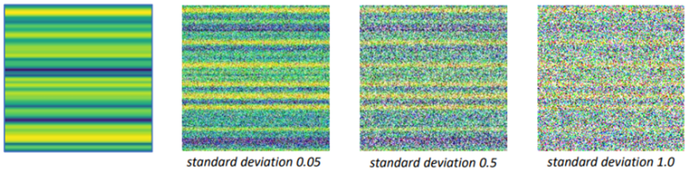
standard deviation 0.05

standard deviation 0.5

standard deviation 1.0

Figure 13: Noise effect with several Standard Deviation

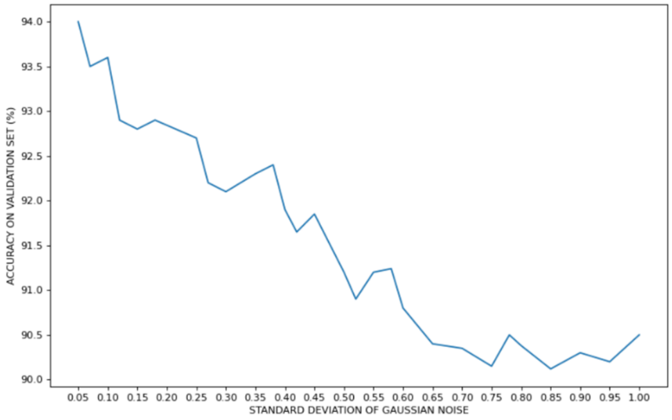

Figure 14: CNN Accuracy, based on Standard Deviation of Gaussian Noise

Gaussian noise is statistical noise having a probability density function equal to that of the normal distribution. We analysed how the performance varies as the standard deviation value of the noise varies (see Figure 14).

By testing the results of the various approaches introduced previously - RF, KNN, STC - the convolutional network is the one that maintains the highest accuracy value even in the case of spectrograms strongly affected by noise. It was therefore decided to use CNN as the first model in the classification pipeline (see Figure 15).

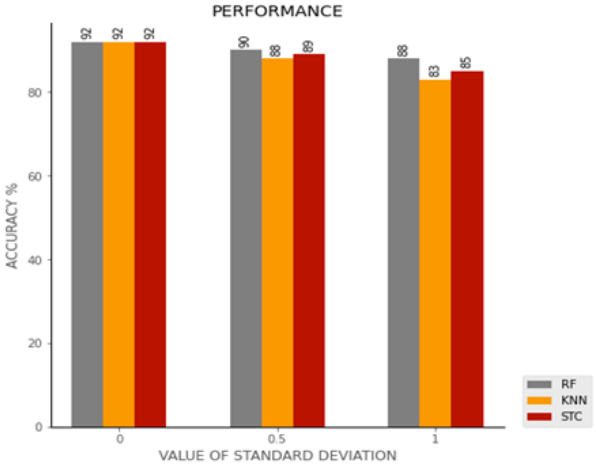

Figure15: Accuracy of ML and DL with several Standard Deviation

To try to improve the performance of Convolutional Neural Network we analysed a Siamese Neural Network. As we can check observing confusion matrix, the network didn't learn the difference between $credit\_card$ and $name\_surname$ instances. We trained the network using an input that is constituted by a pair of images. This network consists of two identical subnets that share weights during training. The idea is to train it to understand the level of similarity between two inputs. Internal networks feature a first layer of ReflectionPad2d which modifies the input tensor. Then, there are 3 convolutional layers characterized by a dimension of the convolutional kernel equal to 3×3 and pairs $(\mathrm{input\_size}, \mathrm{output\_size})$ respectively $(1,4)$, $(4,8)$ and $(8,8)$. Relu is used as activation function followed by two layers of batch normalization.

To easily understand how this network works it is sufficient to think in the following way: two images cross the two internal networks simultaneously and these produce a vectorial representation of them. We calculate the vector distance between them and with a sigmoid neuron we return 0 or 1 – 0 if the images are similar, 1 otherwise. There are several loss functions for training and in our case ConstrastiveLoss was used.

Once we obtained a very performing Siamese network to discriminate between two classes, it is used it in the following way [24]: we recovered the most significant spectrograms of each class by applying KMeans, and we built the dissimilarity space with which we trained a Random Forest model. The idea is to apply the Neural Network and this new model in cascade: when the CNN predicts in output that the instance is a `credit_card` or `name_surname`, then the RF and the Siamese Neural Network are asked for confirmation. Using this trick, accuracy improved by two percentage points (see Figure 16).

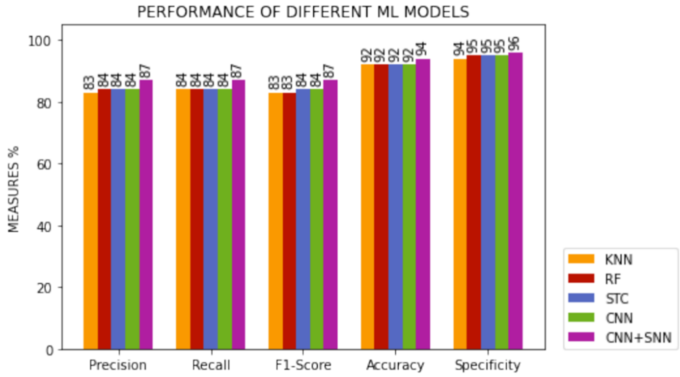

Figure 16: Performance of described ML and DL Models

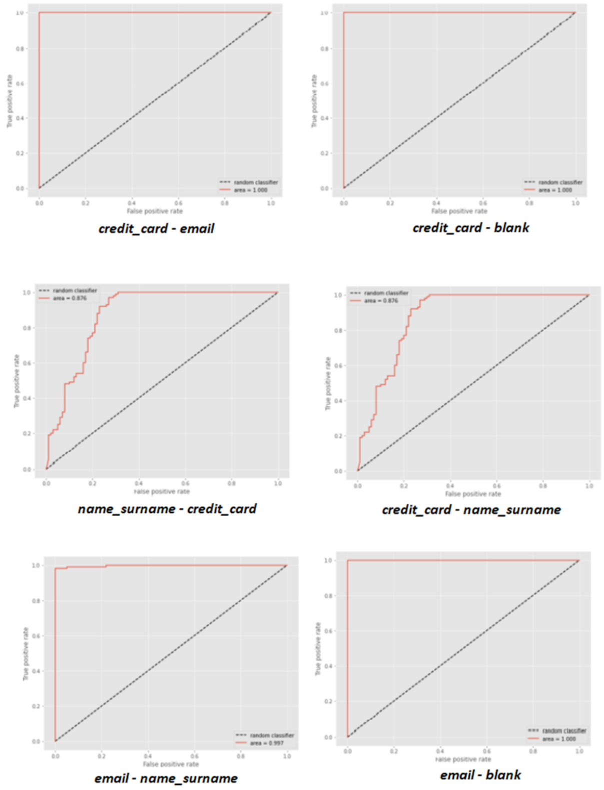

credit_card - email ***credit_card - blank***

name_surname - credit_card ***credit_card - name_surname***

email - name_surname ***email - blank***

Figure 17: Binary ROCs of proposed pipeline

The value of the AUC - Area Under the Curve - was examined in addition to the metrics previously mentioned. The area under the ROC curve (AUC) is a measurement of its size. The trend of True Positives as a function of False Positives is displayed on a ROC curve – Receiver Operating Characteristics – with different threshold values. In the case of a binary classification, a sigmoid CNN generates a real value in the range $[0, 1]$: based on a selected threshold, the network determines how to classify the input instance. AUC measures the classifier's ability to distinguish between Positive and Negative classes: the higher the AUC, the more effective the model. It is useful to understand how True Positives and False Positives change depending on the chosen threshold. TPR (True Positive Rate) and FPR (False Positive Rate) are the two metrics that are used: FPR is the decrease in Specificity compared to 1 while the TPR is the same as the Recall. Figure 17 shows ROC curves in binary classifications.

5. Conclusion

This paper showed how to create a simple CTC and how it is possible to apply Machine Learning (Random Forest and K-NN) and Deep Learning (Convolutional Neural Network and Siamese Network) approaches to classify hidden communications in TCP-based Covert Timing Channels in the e-health field. We proposed an innovative pipeline composed of a single CNN and a SNN to improve the accuracy of the classification. We have compared the performances of different methods and improved them with ensemble and combination techniques. The best performance was achieved by our pipeline with an accuracy of 94%. Even if the performances presented are slightly lower than those of the State of Art – which use ML and statistical models obtaining performances of 96% [20] - the work paves the way for the use of DL models for the identification of CTCs. The further contribution presented is the noise resistance of the pipeline: if there is noise, modelled with Gaussian distribution and different value of standard deviation applied to spectrograms, the pipeline performance remains efficient with 90% accuracy. The detection of the prototypes of each class demonstrates how it is possible to identify a representative spectrogram of each message in transit in the CTC. The prototype can be thought as a hashing of the attack and can be used in SIEM systems to compare the state of the network against each known hashed attack type.The current model has been tested on simple messages: as the number of classes increases, the size of the dissimilarity space increases, which could lead to longer training and identification times. At the same time, the simulated noise is only fictitious: it was inserted afterwards.

We are satisfied with the performances obtained in general but not so much with those relating to the Siamese network. Our future studies will focus on the study of this network and how to combine it with other DL models. Other studies are focusing on the internal analysis of the packets exchanged and using different CTCs.

References

[1] F. Hu, D. Xie, S. Shen, "On the Application of the Internet of Things in the Field of Medical and Health Care," in 2013 IEEE International Conference on Green Computing and Communications and IEEE Internet of Things and IEEE Cyber, Physical and Social Computing, IEEE: 2053–2058, 2013, doi:10.1109/GreenCom-iThings-CPSCom.2013.384.

[2] G.J. Simmons, "Symmetric and Asymmetric Encryption," ACM Computing Surveys, **11**(4), 305–330, 1979, doi:10.1145/356789.356793.

[3] S.K. Kharroub, K. Abualsaud, M. Guizani, "Medical IoT: A Comprehensive Survey of Different Encryption and Security Techniques," in 2020 International Wireless Communications and

Mobile Computing (IWCMC), IEEE: 1891–1896, 2020, doi:10.1109/IWCMC48107.2020.9148287.

[4] Y. Sun, F.P.-W. Lo, B. Lo, "Lightweight Internet of Things Device Authentication, Encryption, and Key Distribution Using End-to-End Neural Cryptosystems," IEEE Internet of Things Journal, **9**(16), 14978–14987, 2022, doi:10.1109/JIOT.2021.3067036.

[5] S.S. Albouq, A.A.A. Sen, A. Namoun, N.M. Bahbouh, A.B. Alkhodre, A. Alshanqiti, "A Double Obfuscation Approach for Protecting the Privacy of IoT Location Based Applications," IEEE Access, **8**, 129415–129431, 2020, doi:10.1109/ACCESS.2020.3009200.

[6] L. SWEENEY, "k-ANONYMITY: A MODEL FOR PROTECTING PRIVACY," International Journal of Uncertainty, Fuzziness and Knowledge-Based Systems, **10**(05), 557–570, 2002, doi:10.1142/S0218488502001648.

[7] A. Sundas, S. Badotra, S. Bharany, A. Almogren, E.M. Tag-ElDin, A.U. Rehman, "HealthGuard: An Intelligent Healthcare System Security Framework Based on Machine Learning," Sustainability, **14**(19), 11934, 2022, doi:10.3390/su141911934.

[8] J. Asharf, N. Moustafa, H. Khurshid, E. Debie, W. Haider, A. Wahab, "A Review of Intrusion Detection Systems Using Machine and Deep Learning in Internet of Things: Challenges, Solutions and Future Directions," Electronics, **9**(7), 1177, 2020, doi:10.3390/electronics9071177.

[9] C. Janiesch, P. Zschech, K. Heinrich, "Machine learning and deep learning," Electronic Markets, **31**(3), 685–695, 2021, doi:10.1007/s12525-021-00475-2.

[10] Y. Rbah, M. Mahfoudi, Y. Balboul, M. Fattah, S. Mazer, M. Elbekkali, B. Bernoussi, "Machine Learning and Deep Learning Methods for Intrusion Detection Systems in IoMT: A survey," in 2022 2nd International Conference on Innovative Research in Applied Science, Engineering and Technology (IRASET), IEEE: 1–9, 2022, doi:10.1109/IRASET52964.2022.9738218.

[11] H. Rathore, L. Wenzel, A.K. Al-Ali, A. Mohamed, X. Du, M. Guizani, "Multi-Layer Perceptron Model on Chip for Secure Diabetic Treatment," IEEE Access, **6**, 44718–44730, 2018, doi:10.1109/ACCESS.2018.2854822.

[12] S.P. R.M., P.K.R. Maddikunta, P. M., S. Koppu, T.R. Gadekallu, C.L. Chowdhary, M. Alazab, "An effective feature engineering for DNN using hybrid PCA-GWO for intrusion detection in IoMT architecture," Computer Communications, **160**, 139–149, 2020, doi:10.1016/j.comcom.2020.05.048.

[13] S. Khan, A. Akhunzada, "A hybrid DL-driven intelligent SDN-enabled malware detection framework for Internet of Medical Things (IoMT)," Computer Communications, **170**, 209–216, 2021, doi:10.1016/j.comcom.2021.01.013.

[14] A. Djenna, D. Eddine Saidouni, "Cyber Attacks Classification in IoT-Based-Healthcare Infrastructure," in 2018 2nd Cyber Security in Networking Conference (CSNet), IEEE: 1–4, 2018, doi:10.1109/CSNET.2018.8602974.

[15] H. Okhravi, S. Bak, S.T. King, "Design, implementation and evaluation of covert channel attacks," in 2010 IEEE International Conference on Technologies for Homeland Security (HST), IEEE: 481–487, 2010, doi:10.1109/THS.2010.5654967.

[16] A. Chen, W.B. Moore, H. Xiao, A. Haeberlen, L. Thi Xuan Phan, M. Sherr, W.Z. Zhou, Detecting Covert Timing Channels with Time-Deterministic Replay, USENIX Association, 2014.

[17] F. Chen, Y. Wang, H. Song, X. Li, "A statistical study of covert timing channels using network packet frequency," in 2015 IEEE International Conference on Intelligence and Security Informatics (ISI), IEEE: 166–168, 2015, doi:10.1109/ISI.2015.7165963.

[18] C. Shepherd, J. Kalbantner, B. Semal, K. Markantonakis, "A Side-channel Analysis of Sensor Multiplexing for Covert Channels and Application Fingerprinting on Mobile Devices," 2021.

[19] S. Gianvecchio, Haining Wang, "An Entropy-Based Approach to Detecting Covert Timing Channels," IEEE Transactions on Dependable and Secure Computing, **8**(6), 785–797, 2011, doi:10.1109/TDSC.2010.46.

[20] M.A. Elsadig, A. Gafar, "Covert Channel Detection: Machine Learning Approaches," IEEE Access, **10**, 38391–38405, 2022, doi:10.1109/ACCESS.2022.3164392.

[21] F. Massimi, F. Benedetto, "Deep Learning-based Detection Methods for Covert Communications in E- Health Transmissions," in 2022 45th International Conference on Telecommunications and Signal Processing (TSP), IEEE: 11–16, 2022, doi:10.1109/TSP55681.2022.9851366.

[22] S. Al-Eidi, O. Darwish, Y. Chen, G. Husari, "SnapCatch: Automatic Detection of Covert Timing Channels Using Image Processing and Machine Learning," IEEE Access, **9**, 177–191, 2021, doi:10.1109/ACCESS.2020.3046234.

[23] J. BROMLEY, J.W. BENTZ, L. BOTTOU, I. GUYON, Y. LECUN, C. MOORE, E. SÄCKINGER, R. SHAH, "SIGNATURE VERIFICATION USING A 'SIAMESE' TIME DELAY NEURAL NETWORK," International Journal of Pattern Recognition and Artificial Intelligence, **07**(04), 669–688, 1993, doi:10.1142/S0218001493000339.

[24] T.N. Rincy, R. Gupta, "Ensemble Learning Techniques and its Efficiency in Machine Learning: A Survey," in 2nd International Conference on Data, Engineering and Applications (IDEA), IEEE: 1–6, 2020, doi:10.1109/IDEA49133.2020.9170675.

Advances in Science, Technology and Engineering Systems Journal Vol. 8, No. 2, 139-147 (2023)

www.astesj.com

ASTESJ

ISSN: 2415-6698

Achieving a High Isolation for the Triple-band MIMO Antenna in 5G/ Wi-Fi 6 Applications using Symmetric Parasitic Structure

Nguyen Van Tan, Duong Thi Thanh Tu*, Nguyen Viet Hung, Hoang Minh Duc

Faculty of Telecommunication1, Posts and Telecommunications Institute of Technology, Hanoi, 100000, Vietnam

ARTICLE INFO

Article history:
Received: 04 January, 2023
Accepted: 26 April, 2023
Online: 28 April, 2023

Keywords:
triple-band
MIMO
Parasitic structure
Fibonacci

ABSTRACT

Recently, the Multiple-input multiple-output (MIMO) antennas have been used a lot and attracted many researchers in advanced high-speed wireless communication systems. MIMO antennas are an essential part not only in access points but also in end-user devices. This technology allows a significant increase in channel capacity, but also lead to a challenge of minimize mutual coupling and in the meantime reserved antennas' compact size. In this study, we propose a triple-band MIMO antenna design. By using a symmetric parasitic structure, isolation between radiation elements is significantly improved. Besides, each antenna element is designed using a combination of planar structure and 8 Fibonacci curves that makes it compact in size and easy to fabricate in the circuit board of 5G/ Wi-Fi 6 terminals. With a total dimension of 34.8 68.2*1.6mm^3, the proposed MIMO antenna design can operate at three bands of 2.4GHz, 3.5GHz, and 5GHz with wide bandwidths of 11.4%, 9.4%, and 14.58%, respectively. The results are analyzed based on simulation, measurement, and experiment.*

1. Introduction

Nowadays, the development of multimedia applications in end-user equipment such as portable devices, smartphones, and handheld gadgets is posing a great demand for high speed and reliability in wireless communication systems. MIMO technology is a great candidate to deal with this problem, which often requires implementation of MIMO antennas in both transceiver and receiver in wireless systems. Though this technology helps increasing channel capacity, it faces a challenge of depressing mutual coupling between close radiation elements [1]. There are several methods to obtain optimal isolation for MIMO antenna in end-user equipment that have been widely published. These methods increase isolation by using decoupling structure, parasitic element, neutralization line, orthogonal resonators, split ring resonator (SRR), and energy band gap [1]-[3]. These approach led to good isolation for UWB, single band, or dual band MIMO antenna. However, there are only a few publications with research for beyond dual-band MIMO antenna [4]-[17]. B. Bayarzaya et al. in [4] use a complex parasitic element to increase significantly isolation for triple-band MIMO antenna but the bandwidths are different at three bands and the radiation efficiencies are not detailed. The bandwidth is more uniform in the study [5]. However, the antenna's gain needs to be improved. In [6], the author used DGS and via to achieve high isolation but the second band of their antenna is rather narrow for modern wide-band equipment. Others triple-band MIMO antenna researches presented in [7]-[9] can also get low mutual coupling but their total dimensions are relatively large. In consequence, these designs are not easy to ensure high isolation when implemented in compact handheld gadgets. In [10], [11] achieved compact MIMO antennas in their studies but the isolation in some operating frequencies still get under 20 dB.

In this work, we proposed a compact 1x2 MIMO antenna with low mutual coupling. Combined with shorting pin, the total size radiation patch is reduced by 71.25% which compared to a traditional disk antenna. The proposed antenna resonate at three operating band. They are 2.3 GHz, 3.4 GHz, and 4.8 GHz. The bandwidths are wide-bands that are 11.47%, 9.40% and 14.58%, respectively. To improve the isolation between antenna elements, a structures of symmetric parasitic is proposed. This structure leads to a significant reduction in mutual coupling, which reach 32.8 dB at 2.3 GHz. On the other hand, other parameters of the antenna are not affected and remain adequate. Antenna's gain ranges from 2 to3.6 dBi, while radiation efficiency is kept in the range of 79-94%.

---

[*] Corresponding Author Duong T.T. Tu, Hanoi Vietnam, tudtt@ptit.edu.vn

https://dx.doi.org/10.25046/aj080216

The rest of our study is set up as follows. In Part II, we present the single and MIMO antenna designs. The simulation and measurement as well as their analysis are studied in Parts III and IV, respectively. In Part V, we show the experimental results, based on IEEE 802.11 system. Finally, the conclusion of our study is present in Part VI.

2. Antenna Design

2.1. Triple-Band Single Antenna Basing on Fibonacci Curve

In this work, we use a triple-band antenna as an element of a MIMO antenna design. This is designed for wide-band wireless application at three well-know bands for 5G and/or WiFi 6 applications. We usse FR4 substrate to design both sigle and MIMO antenna. The thickness is 1.6mm, the relative permittivity is 4.4. The single antenna structure is shown in Figure 1. It consists of three main parts. They are a radiation patch including eight Fibonacci spiral curve slots, a shorting pin, and a defected ground as shown in Figure 1.

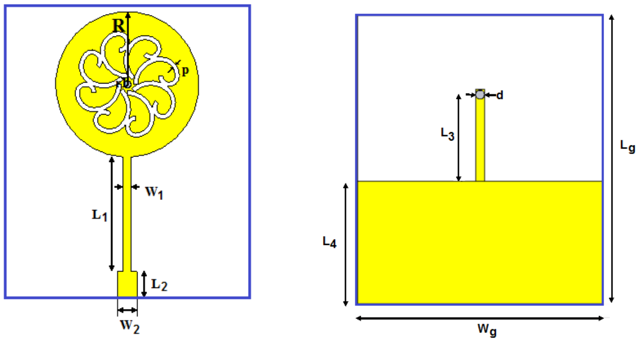

(a) Patch plane (b) Ground plane

Figure 1. Fibonacci antenna structure

The recursive procedure of forming Fibonacci spiral curve is presented in Figure 2 [17].

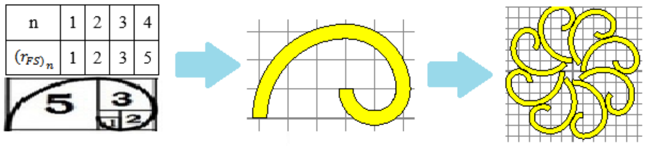

Fig 2. Fibonacci spiral curve for the proposed antenna

Each curve of Fibonacci sequence is calculated as follow:

$$(\mathrm{r_{FS}})_\mathrm{n} = \frac{(\phi^\mathrm{n} - (-\phi^\mathrm{n})}{\sqrt{5}} \tag{1}$$

where n is changed from 1 to 4 which equal the number of arcs in spiral curve, ϕ is golden ratio [6]. Value of ϕ is determined by equation (2):

$$\phi = \frac{1+\sqrt{5}}{2} = 1.618 \tag{2}$$

To get 2.4GHz band which is the lowest resonant frequency of the proposed antenna, we use the Equation (3) to calculate draft the radius of the circular radiation patch [12].

$$\mathrm{r} = \frac{\mathrm{F}}{\left\{1 + \frac{2\mathrm{h}}{\pi\varepsilon_\mathrm{r}\mathrm{F}}\left[\ln\left(\frac{\pi\mathrm{F}}{2\mathrm{h}}\right) + 1.7726\right]\right\}^{1/2}} \tag{3}$$

$$\mathrm{F} = \frac{8.791\mathrm{x}10^9}{\mathrm{f_r}\sqrt{\varepsilon_\mathrm{r}}} \tag{4}$$

To reduce the antenna size, a shorting pin is introduced in a form of a strip line. This via connects two sides of the proposed antenna as shown in Figure 1 [13]. Its length is determined approximately as follow:

$$L_s = \frac{3\mathrm{x}10^8}{\mathrm{f_r}\sqrt{\varepsilon_\mathrm{r}}} - 4\mathrm{r} \tag{5}$$

Table 1 presents the detail dimensions of the single antenna. It can be seen that, total antenna is 34.8*29.6 mm2 that is much compact comparing conventional 2.4GHz antenna.

Table 1. Dimension Values of Antenna

Parameter	**Value (mm)**	**Parameter**	**Value (mm)**
Lg	34.8	Wg	29.6
L_1	13.6	W_1	0.96
L_2	3	W_2	2.5
L_3	11.3	R	8.5
L_4	14	p	0.5
d	1	r	0.5

2.2. MIMO Fibonacci Antenna

Experiments with design of the unit cell of the parasitic structure using a basic square shape show reduction of mutual coupling for only one narrow band in MIMO antenna. To improve this the proposed unit cell structure includes a cross shape and four squares with gradual-changing-length slots as illustrated in Figure 3, Thus, this structure can reduce mutual coupling for multiple and wide bands.

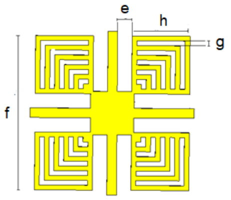

Figure 3. The proposed Symmetric Parasitic structure

In order to achieve significantly isolation of MIMO antenna for all three bands, the proposed 1x2 symmetric parasitic structure is placed as shown in Figure 4 with the close distance between elements of MIMO antenna. It is 9mm (0.072λ) from edge to edge or 36.1mm (0.288λ) from feeding point to feeding point.

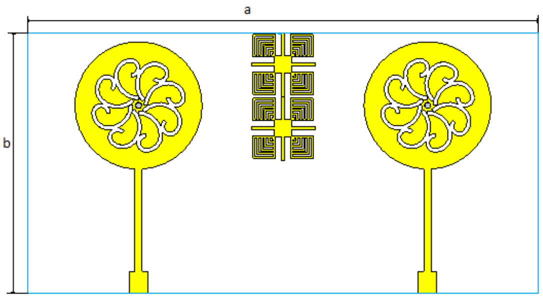

(a) Patch plane

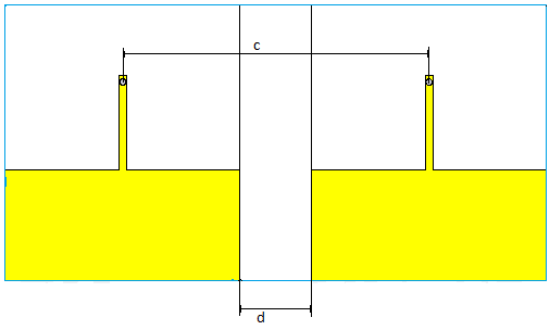

(b) Ground plane

Figure 4. The design of MIMO antenna using symmetric parasitic structure

Table 2 presents the detail dimensions of the MIMO antenna. It can be seen that the antenna gets a compact size 4.8 × 68.2 × 1.6mm^3.

Table 2. Detail Values of MIMO Antenna's dimension

Parameter	Value (mm)	Parameter	Value (mm)
a	68.2	e	0.75
b	34.8	f	8
c	36.1	g	0.25
d	9	h	2.88

3. Simulation results and analysis

3.1. Fibonacci Antenna

In this part, the characters of the Fibonacci antenna is validated by simulation using CST Studio 3D EM. Firstly, the S11 of the single antenna are presented following three steps of forming structure of triple-band Fibonacci antenna as shown in Figure 5.

One can observe that the disk antenna gets only one resonant frequency of 8 GHz. With the same antenna size, the antenna with inscribed Fibonacci curves achieves three resonant frequencies and the lowest one is 4.4 GHz. Thus the antenna at the second step has not only form the multiband antenna but also decreased its size by approximately 45% compared to the disk patch. To further the antenna's size reduction, a shorting pin like PIFA antenna that has lengthened on the ground plane is applied [13]. In this case, the lowest operation frequency of shorting-pin antenna is 2.2744GHz. It can be observed that there is a remarkable improvement of approximately 72% size decrease compared to the disk antenna. In additions, three bands of the proposed antenna are wide. They are 264MHz at 2.3GHz, 345MHz at 3.4GHz, and 815MHz at 4.6GHz. These bands are well-known bands of 5G and WiFi 6 applications.

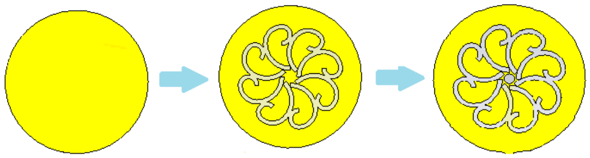

(a) Three step to form Fibonacci-PIFA antenna

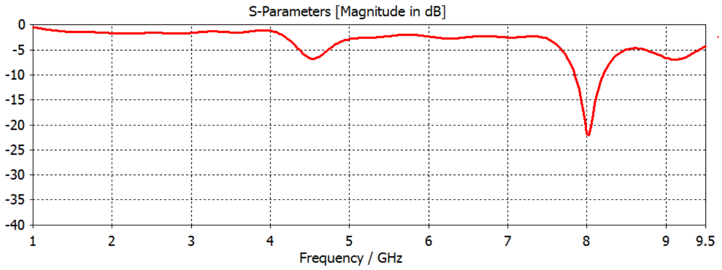

(b) The conventional circular antenna

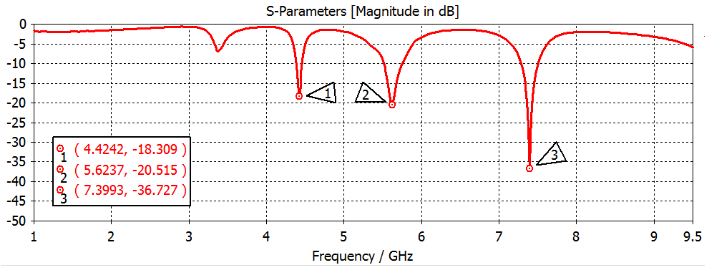

(c) The inscribed eight Fibonacci curve antenna

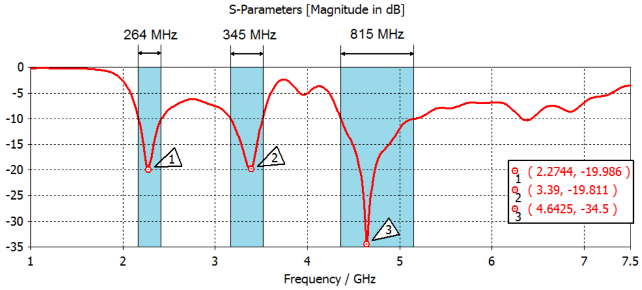

(d) The proposed Fibonacci antenna with shorting pin

Figure 5 The simulation results of S11 parameter in three steps of forming the proposed antenna

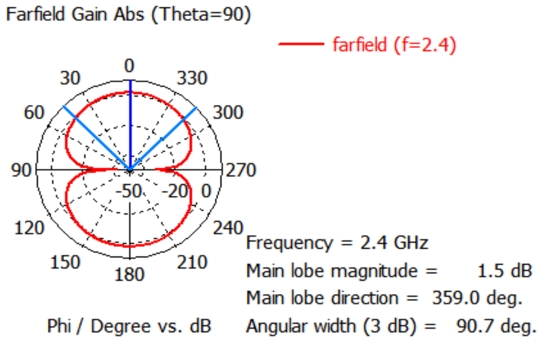

(a)At 2.4GHz

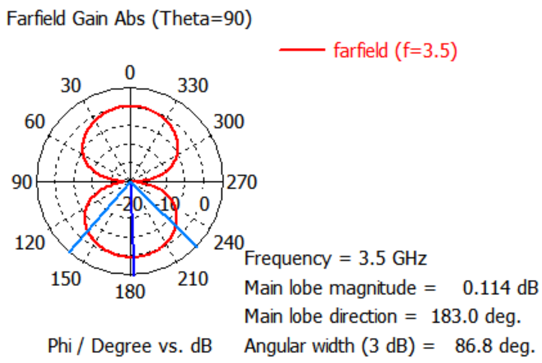

(b)At 3.5GHz

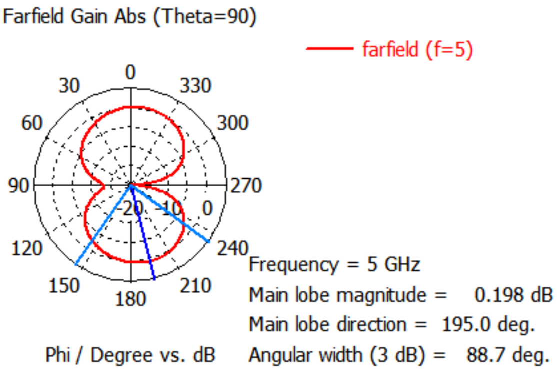

(c) At 5 GHz

Figure 6. The simulation results of radiation pattern

Figure 6 presents the 2D radiation patterns of the Fibonacci antenna. It is clearly seen that the proposed antenna gets a considerably stable pattern with a dipole-like shape at all frequencies. In addition, a rather good value of gain is achieved. They are 1.83dB, 2.41dB and 2.89 dB at 2.4 GHz, 3.5 GHz and 5 GHz respectively. Besides, radiation efficiency are relatively high of over 94% at 2.4 GHz, 81% at 3.5 GHz and nearly 87 % at 5GHz as illustrated in Figure 7.

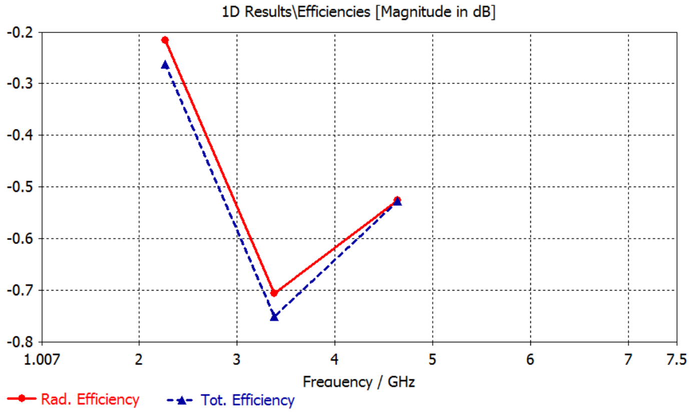

Figure 7. Radiation efficiency of Fibonacci antenna

3.2. The Triple-band MIMO Antenna

The simulation results of S11 and S12 parameters of triple-band MIMO antenna without symmetric parasitic structure are shown in Figure 8 with the distance of radiation patch of 9 mm. It can be observed that because of close distance between elements of MIMO antenna, the S12 of all operating bands are much above - 20 dB.

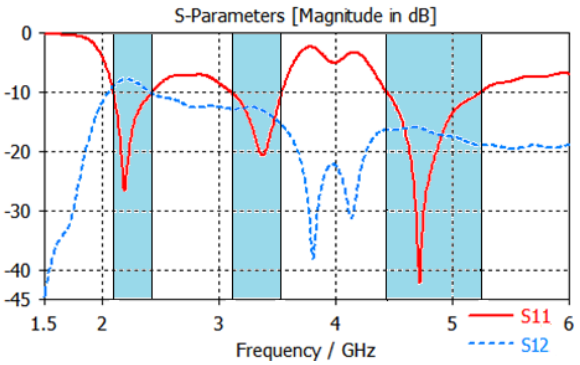

Figure 8. The value of S11 and S12 parameters without symmetric parasitic structure at 0.072λ distance

In addition, due to the effect of mutual coupling, there is a distortion of MIMO patterns without decoupling structure, their shape are shown in Figure 9.

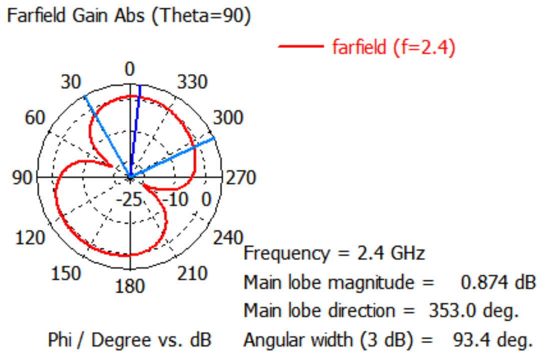

(a) At 2.4 GHz

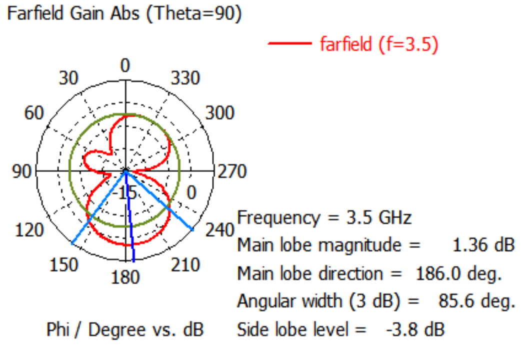

(b) At 3.5 GHz

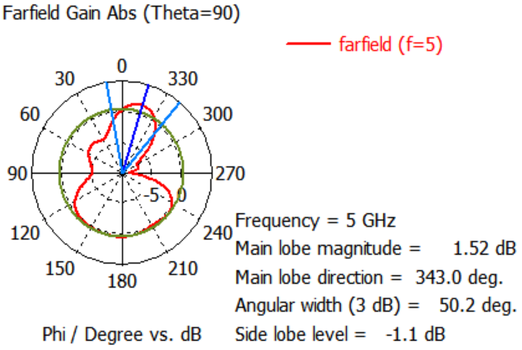

(c) At 5 GHz

Figure 9. MIMO antenna's pattern without symmetric parasitic structure

With the introduction of the proposed symmetric parasitic structure mentioned in section 2.2, the MIMO antenna's isolation is significantly improved, especially at the first operating band. On the other hand, this structure is simple and compact, therefore it can be easily placed in other positions in the MIMO antenna for experiments. It can also be applied in other MIMO antenna designs. The S parameters of the proposed MIMO antenna using the symmetric parasitic structure are shown in Figure 10. The distance between radiation elements is still kept at 9 mm. It can be observed that the isolation of the MIMO antenna using symmetric parasitic structure is increased at all of the three operating bands, especially at 2.4 GHz where S21 is reduced by 60 dB. Similarly, at the 3.5 GHz it is 13.8 dB and at 5 GHz it is 5.7 dB.

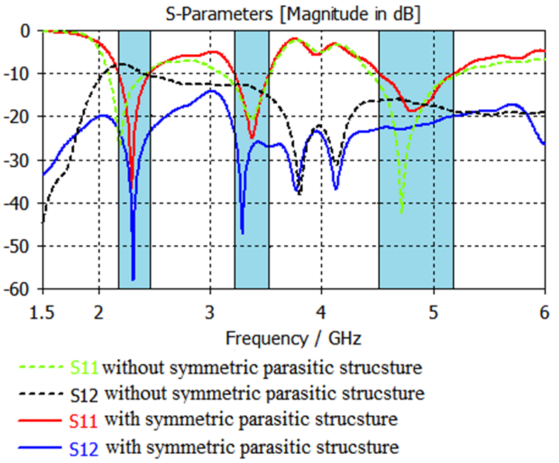

Figure 10. The value of S11 and S12 of MIMO antenna with and without symmetric parasitic structure

4. Measurement results

The proposed antennas are fabricate using FR4 substrate with thickness of 1.6mm and shown in Figure 11 and 12. The comparison of measurement and simulation results of both antenna's reflection coefficient are drawn using Matlab software as present in Figure 13 and 14.

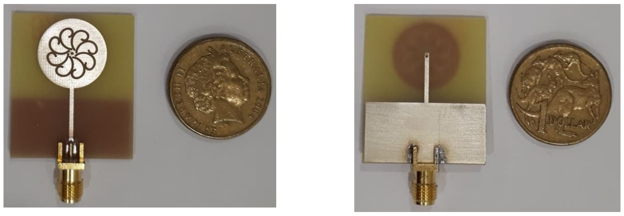

(a) Patch plane

(b) Ground plane

Figure 11. Fabricated single antenna

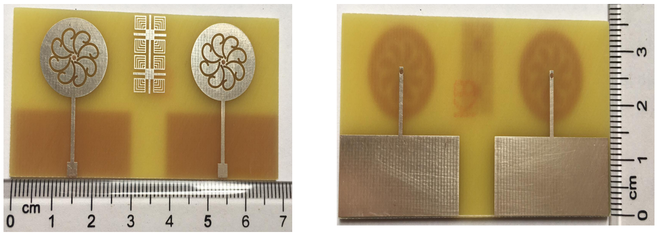

(a) Patch plane

(b) Ground plane

Figure 12. Fabricated MIMO antenna

It can be seen that both antennas achieve compact sizes of 34.8 x 68.2 x 1.6 mm^3 and 29.8 x 38.4 x 1.6 mm^3 for the MIMO and single antenna respectively. The circle patch's size is very small with the area of approximate 232 mm^2.

Measured results of S11 parameters show great similarity to the simulated ones as seen in Figure 13. Both single and MIMO antennas get the same resonant frequencies of around 2.4 GHz, 3.5 GHz and 4.8 GHz with large band width. They are over 10% at 2.4GHz, 9% at 3.5GHz, and 14% at 5GHz band. The measurement and simulation results agree well with each other. Besides, from Figure 14, the S12 parameter at all of three bands are under - 20 dB validated our proposed Symmetric Parasitic Structure. Thus the proposed decoupling structure can improve isolation for triple-band MIMO antenna.

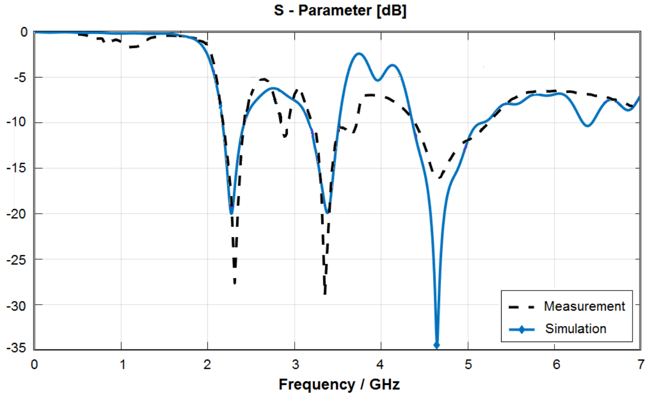

Figure 13. Comparison of measured and simulated S11 of single antenna

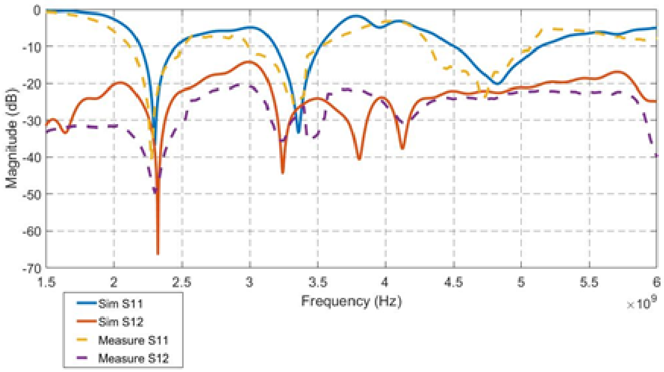

Figure 14. Comparison of measured and simulated S parameters of MIMO antenna with symmetric parasitic structure

5. Experiment results based on 802.11 systems

Two other performance parameters of the proposed antennas SNR (Signal to Noise Ratio) and RSSI (Received Signal Strength Indicator) are demonstrated by used Wi-Fi receiver as shown in Figure 15. These signal received by the proposed antennas will be compared with the result of a 2dB-gain dipole antenna which is commonly used for the Wi-Fi application. The test was held outdoors, with no obstructions in two weather conditions: sunny and light rain. Distance to signal source is from 0 to 100m (70m when it rains) with measuring positions 10m apart.

As showed in Figures 16 and Table 3 and Table 4, with sunny and dry weather, the proposed MIMO antenna has the best signal strength in both bands at close distances (from 0 to 30m) and the single antenna has better received signal strength at far distances.

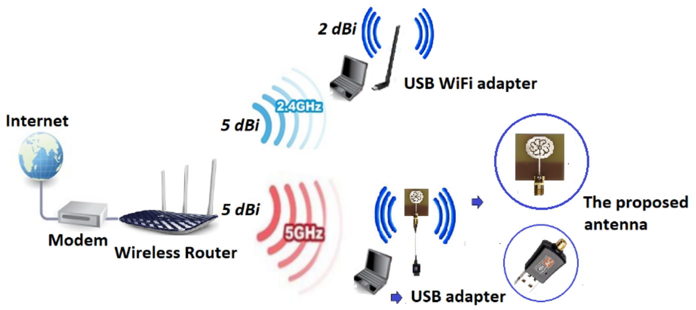

Figure 15. Test set up of the proposed antennas

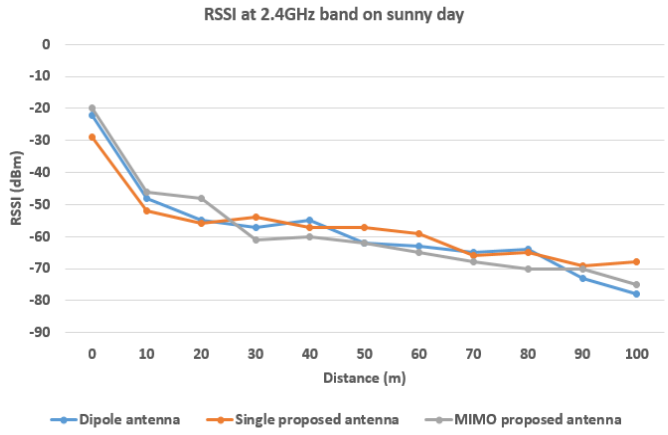

(a) At 2.4GHz

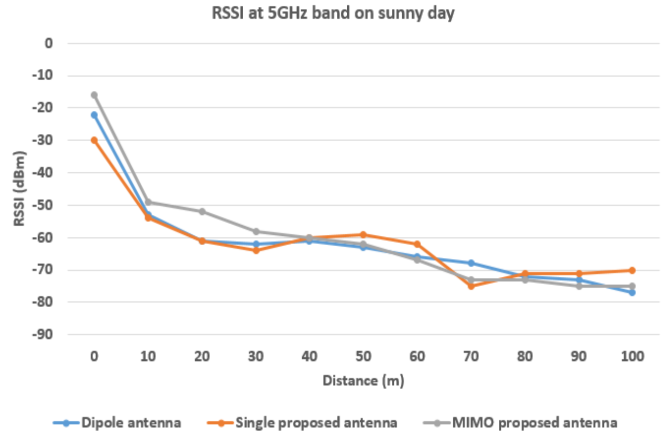

(b) At 5GHz

Figure 16. RSSI on sunny and dry weather

Table 3. RSSI (dBm) at 2.4GHz band on sunny day

Distance (m)	Dipole Antenna	Single Proposed Antenna	MIMO Proposed Antenna
0	-22	-29	-20
10	-48	-52	-46
20	-55	-56	-48
30	-57	-54	-61
40	-55	-57	-60
50	-62	-57	-62
60	-63	-59	-65
70	-65	-66	-68
80	-64	-65	-70
90	-73	-69	-70
100	-78	-68	-75

Table 4. RSSI (dBm) at 5GHz band on sunny day

Distance (m)	Dipole Antenna	Single Proposed Antenna	MIMO Proposed Antenna
0	-22	-30	-16
10	-53	-54	-49
20	-61	-61	-52
30	-62	-64	-58
40	-61	-60	-60
50	-63	-59	-62
60	-66	-62	-67
70	-68	-75	-73
80	-72	-71	-73
90	-73	-71	-75
100	-77	-70	-75

The results of the SNR in these two bands are presented in Figures 17 and Table 5 and 6. On 2.4GHz band, MIMO antenna's results are the same Dipole antenna's ones while the single Fibonacci antenna has better results. The SNR results at the 5GHz band are also the same RSSI results. Besides, the proposed MIMO antenna works well at close distances and the proposed single antenna works best at long distances. Thus, on sunny and dry weather, the two proposed antennas give quite similar and better results at some distances when compared to the Dipole antenna.

Table 5. SNR (dB) at 2.4GHz band on sunny day

Distance (m)	Dipole Antenna	Single Proposed Antenna	MIMO Proposed Antenna
0	100	100	100
10	100	100	100
20	100	100	100
30	92	100	92
40	84	92	84
50	74	92	74
60	74	88	74
70	70	84	68
80	68	80	64
90	58	74	62
100	58	64	60

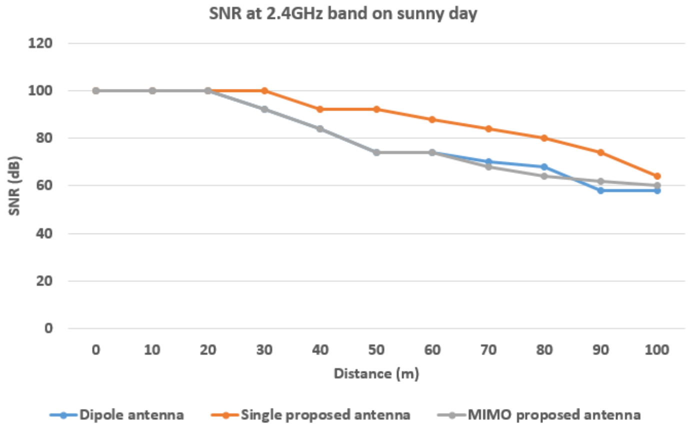

(a) At 2.4GHz

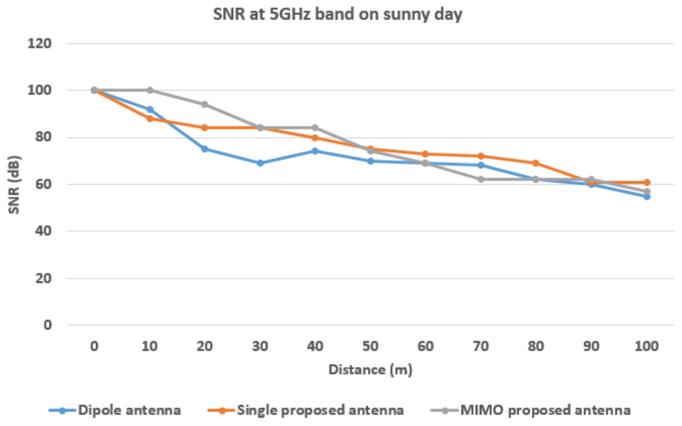

(b)At 5GHz

Figure 17. SNR on sunny and dry weather

Table 6. SNR (dB) at 5GHz band on sunny day

Distance (m)	Dipole Antenna	Single Proposed Antenna	MIMO Proposed Antenna
0	100	100	100
10	92	88	100
20	75	84	94
30	69	84	84
40	74	80	84
50	70	75	74
60	69	73	69
70	68	72	62
80	62	69	62
90	60	61	62
100	55	61	57

In rainy condition, the results of RSSI and SNR parameters are shown in Figures 18 and 19 and Tables 7, 8, 9 and 10. It can be seen that at both bands, the Dipole antenna has better signal strength than the two proposed antenna at close distances but worse at long distances.

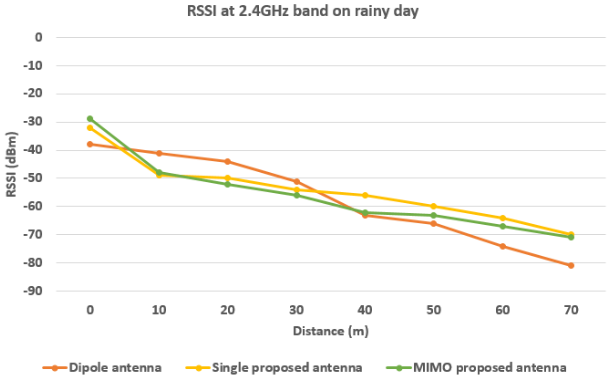

(a) At 2.4GHz

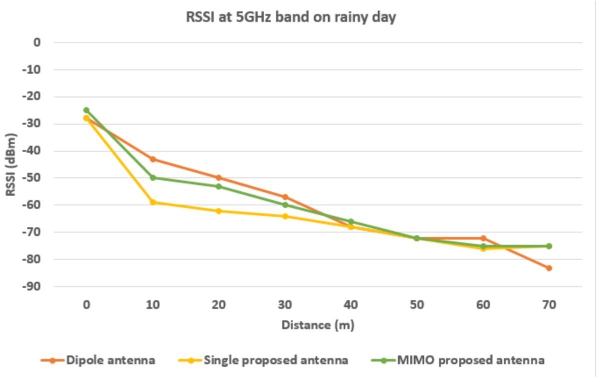

(b) At 5GHz

Figure 18. RSSI on rainy weather

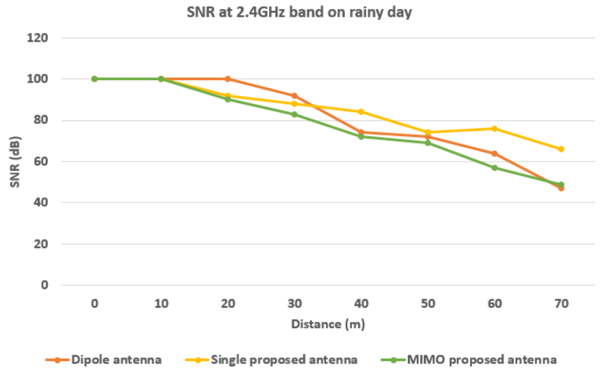

(a) At 2.4GHz

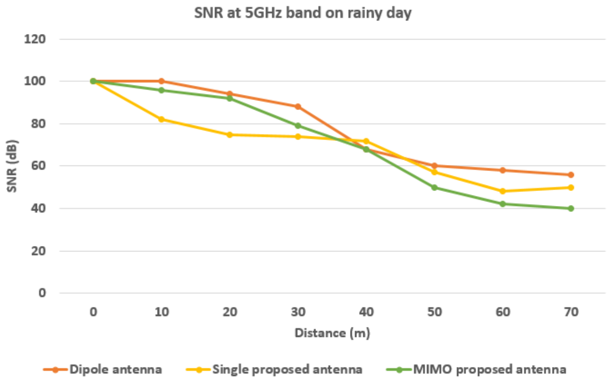

(b) At 5GHz

Figure 19. SNR on rainy weather

In the 2.4GHz band, the Dipole antenna has the best SNR results at close range, the single Fibonacci antenna achieves the best SNR at long distances and the MIMO Fibonacci one gets the worst results.

Table 7. RSSI (dBm) at 2.4GHz band on rainy day

Distance (m)	Dipole Antenna	Single Proposed Antenna	MIMO Proposed Antenna
0	-38	-32	-29
10	-41	-49	-48
20	-44	-50	-52
30	-51	-54	-56
40	-63	-56	-62
50	-66	-60	-63
60	-74	-64	-67
70	-81	-70	-71

Table 8. RSSI (dBm) at 5GHz band on rainy day

Distance (m)	Dipole Antenna	Single Proposed Antenna	MIMO Proposed Antenna
0	-28	-28	-25
10	-43	-59	-50
20	-50	-62	-53
30	-57	-64	-60
40	-68	-68	-66
50	-72	-72	-72
60	-72	-76	-75
70	-83	-75	-75

Table 9. SNR (dB) at 2.4GHz band on rainy day

Distance (m)	Dipole Antenna	Single Proposed Antenna	MIMO Proposed Antenna
0	100	100	100
10	100	100	100
20	100	92	90
30	92	88	83
40	74	84	72
50	72	74	69
60	64	76	57
70	47	66	49

Table 10. SNR (dB) at 5GHz band on rainy day

Distance (m)	Dipole Antenna	Single Proposed Antenna	MIMO Proposed Antenna
0	100	100	100
10	100	82	96
20	94	75	92
30	88	74	79
40	68	72	68
50	60	57	50
60	58	48	42
70	56	50	40

6. Conclusion

In this study, we proposed a compact triple-band MIMO antenna with eight Fibonacci slots and lengthened shorting pin with the symmetric parasitic structure. The overall MIMO antenna structure achieves a compact size of 34.8 x 68.2 mm^2 based on the FR4 substrate. Three bands of MIMO antenna achieve wide bandwidths. They are 277.5 MHz at 2.4 GHz, 315 MHz at 3.5 GHz, and 675 MHz at 5 GHz. This antenna design is therefore suitable for wireless communications of 5G and Wi-Fi 6 applications. Furthermore, by using symmetric parasitic structure, the antenna achieves both extremely high radiating efficiency and high gain. On the other, despite the narrow distance of 0.072λ at 2.4 GHz resonant frequency between two radiation elements, the mutual coupling is kept well under -20 dB for all three bands. The high agreement between simulation and measured results validated the performance of the design.

Conflict of Interest

The authors declare no conflict of interest.

Acknowledgment

This study is partly supported by Vingroup Innovation Foundation (VinIF) under Postgraduate Scholarships Program

References

[1] P. Sharma et al., "Review MIMO Antennas: Design Approaches, Techniques and Applications," Sensors, **2**(20), 7813, October 2022, doi:10.3390/s22207813.

[2] E. A. Andrade-González , J. A. Tirado-Méndez , H. Jardón-Aguilar , M. Reyes-Ayala , A. Rangel-Merino & Michael Pascoe-Chalke, "UWB four ports MIMO antenna based on inscribed Fibonacci circles," Journal of Electromagnetic Waves and Applications, 2021, DOI:10.1080/09205071.2021.1873196.

[3] M. M. H. Mahfuz et al.: "Wearable Textile Patch Antenna: Challenges and Future Directions," IEEE Access, 2022, **10**, doi: 10.1109/ACCESS.2022.3161564.

[4] B. Bayarzaya et al., "A Compact MIMO Antenna with Improved Isolation for ISM, Sub-6 GHz, and WLAN Application," Micromachines, 2022, 13, 1355, doi: 10.3390/mi13081355.

[5] X. Cao et al., "Tri-band MIMO antenna design based on characteristic modes manipulation," International Journal of Electronics and Communications, **2022**, 155, 154318 doi: 10.1016/j.aeue.2022.154318.

[6] S. Rao Pasumarthi, Jagadeesh Babu Kamili, Mallikarjuna Prasad Avala, "Design of Tri-Band MIMO Antenna with Improved Isolation using DGS and Vias," Wireless Personal Communications, 2019, doi: 10.1007/s11277-019-06799-9.

[7] J. Luo et al., "Design of Compact Tri-Band MIMO Antenna Using Decoupling Structures for 5G Mobile Terminals," 2021 Cross Strait Radio Science and Wireless Technology Conference (CSRSWTC), 43-45, 2021.

[8] B. Ahmed et al., "Design and Implementation of Super Wide Band Triple Band-Notched MIMO Antennas," Wireless Personal Communications, **2021**, 121:2757–2778, doi: 10.1007/s11277-021-08847-9.

[9] O. Faruque et al., "A Four-element Triple-band MIMO Antenna for 5G Smartphone Applications," 2nd International Conference on Sustainable Technologies for Industry 4.0 (STI),.2020.

[10] R. Liu *et al.*: "Neutralization Line Decoupling Tri-Band MIMO Antenna Design," IEEE Access, 2020, **8**, 27018 - 27026, doi: 10.1109/ACCESS.2020.2971038.

[11] M. Usman et al. , "Highly Isolated Compact Tri-Band MIMO Antenna with Trapezoidal Defected Ground Plane for 5G Communication Devices,." 2020 International Conference on UK-China Emerging Technologies (UCET), 2020.

[12] C.A. Balanis "Antenna Theory: Analysis and Design," Edition 3rd, Wiley, 2005.

[13] D. Tu et al., "4x4 Dual-Band MIMO Antenna with Low Mutual Coupling Using a Novel Structure of Neutral Line," International Conference on Advanced Technologies for Communications (ATC2017), 80-85, 18-20 October 2017, Quy Nhon, Vietnam

[14] M. Kaur, H. Shankar Singh, "Design and analysis of high isolated super compact 2 x 2 MIMO antenna for WLAN application," International Journal of RF and Microwave Computer-Aided Engineering, 2021, doi: 10.1002/mmce.22864.

[15] X. Yuan et al., "A Wideband PIFA-Pair-Based MIMO Antenna for 5G Smartphones," IEEE Antennas and Wireless Propagation Letters, 2021, **20**, 371 - 375, doi: 10.1109/LAWP.2021.3050337.

[16] B. Baloch et al., "Self-Decoupled Dual Band PIFA for Wi-Fi 6E Smartwatch MIMO Applications," Proceedings of 2022 19th International Bhurban Conference on Applied Sciences & Technology (IBCAST), 2022.

[17] D. Tu, Nguyen Van Tan, Nguyen Viet Hung, "Compact Triple-Band Antenna Based on Fibonacci Sequence for Wi-Fi/LTE-A/5G Below 6GHz Applications in IoT Devices," 2019 6th Naforted Conference on Information and ComputerScience (NICS), 309-313, 12-13 December 2019, Hanoi Vietnam.